

NASA CR-135256  
SSS-R-77-3367



(NASA-CR-135256) A THREE DIMENSIONAL  
DYNAMIC STUDY OF ELECTROSTATIC CHARGING IN  
MATERIALS Contractor Report, Jul. 1976 -  
Jul. 1977 (Systems Science and Software)  
334 p HC A15/MF A01

N78-13328

Unclas  
55188

CSSL 09C G3/33

## A THREE DIMENSIONAL DYNAMIC STUDY OF ELECTROSTATIC CHARGING IN MATERIALS

I. KATZ, D. E. PARKS, M. J. MANDELL, J. M. HARVEY,  
D. H. BROWNELL, JR., S. S. WANG AND M. ROTENBERG

REPRODUCED BY  
NATIONAL TECHNICAL  
INFORMATION SERVICE  
U.S. DEPARTMENT OF COMMERCE  
SPRINGFIELD, VA. 22161

SYSTEMS, SCIENCE AND SOFTWARE

PREPARED FOR

NATIONAL AERONAUTICS AND SPACE ADMINISTRATION

NASA LEWIS RESEARCH CENTER

CONTRACT NAS 3-20119

REPRODUCED BY  
NATIONAL TECHNICAL  
INFORMATION SERVICE  
U.S. DEPARTMENT OF COMMERCE  
SPRINGFIELD, VA. 22161



1. Report No. NASA CR-135256	2. Government Accession No.	3. Recipient's Catalog No.	
4. Title and Subtitle A THREE DIMENSIONAL DYNAMIC STUDY OF ELECTROSTATIC CHARGING IN MATERIALS		5. Report Date August 1977	6. Performing Organization Code
		8. Performing Organization Report No. SSS-R-77-3367	
7. Author(s) I. Katz, D. E. Parks, M. J. Mandell, J. M. Harvey, D. H. Brownell, Jr., S. S. Wang and M. Rotenberg		10. Work Unit No. YOS 7278	11. Contract or Grant No. NAS 3-20119
9. Performing Organization Name and Address Systems, Science and Software P. O. Box 1620 La Jolla, California 92038		13. Type of Report and Period Covered Contractor Report July 1976 - July 1977	
		14. Sponsoring Agency Code 6124	
12. Sponsoring Agency Name and Address National Aeronautics and Space Administration Lewis Research Center Cleveland, Ohio 44135		15. Supplementary Notes	
16. Abstract  This final report describes the physical models employed in the NASCAP (NASA Charging Analyzer Program) code, and presents several test cases. A NASCAP User's Manual is available under separate cover.  NASCAP dynamically simulates the charging of an object made of conducting segments which may be entirely or partially covered with thin dielectric films. The object may be subject to either ground test (electron gun) or space (magnetospheric) user-specified environments. The simulation alternately treats (1) the tendency of materials to accumulate and emit charge when subject to plasma environment, and (2) the consequent response of the charged particle environment to an object's electrostatic field.  Parameterized formulations of the emission properties of materials subject to bombardment by electrons, protons, and sunlight are presented. Values of the parameters are suggested for clean aluminum, Al <sub>2</sub> O <sub>3</sub> , clean magnesium, MgO, SiO <sub>2</sub> , kapton, and teflon. A discussion of conductivity in thin dielectrics subject to radiation and high fields is given, together with a sample calculation.			
17. Key Words (Suggested by Author(s)) NASCAP, Spacecraft charging, Secondary emission, Backscatter, Dynamical Charging, Computer simulation, Material testing		18. Distribution Statement  Publicly Available	
19. Security Classif. (of this report) Unclassified	20. Security Classif. (of this page) Unclassified	21. No. of Pages 345	22. Price*

\* For sale by the National Technical Information Service, Springfield, Virginia 22161



## ACKNOWLEDGMENT

The development of the NASCAP three-dimensional charging analyzer program was the result of help by many people. In particular the authors would like to acknowledge the encouragement and guidance of the NASA-LeRC project officer, James C. Roche. We would also like to thank N. J. Stevens and Carolyn Purvis of NASA-LeRC for their encouragement and helpful suggestions, and Dr. Andrew R. Wilson of S<sup>3</sup> for his contributions to the program management.

## TABLE OF CONTENTS

		Page
	SUMMARY . . . . .	1
1.	INTRODUCTION . . . . .	3
2.	NASCAP PLASMA MODEL . . . . .	6
2.1	INTRODUCTION TO NASCAP . . . . .	6
2.2	POTENTIAL CALCULATION . . . . .	17
2.3	FLUX CALCULATIONS . . . . .	21
2.4	DYNAMICAL MODEL . . . . .	24
3.	MATERIAL PROPERTIES . . . . .	26
3.1	GENERAL CONSIDERATIONS . . . . .	26
3.2	CHARGE DEPOSITION . . . . .	30
3.3	SECONDARY EMISSION . . . . .	33
3.3.1	Electron Impact . . . . .	33
3.3.2	Proton Impact . . . . .	44
3.3.3	Energy and Angle Distribution . . . . .	44
3.4	BACKSCATTERING AND REFLECTION . . . . .	44
3.4.1	Albedo for Electrons . . . . .	44
3.4.2	Energy and Angle Distribution of Backscattered Electrons . . . . .	47
3.4.3	Reflection of Protons . . . . .	47
3.4.4	Sputtering . . . . .	49
3.5	PHOTOEMISSION . . . . .	49
3.6	EFFECTIVE BOUNDARY CONDITIONS IN THIN DIELECTRIC MATERIALS . . . . .	50
3.7	SIMPLE MODEL FOR LEAKAGE CURRENTS AND FIELDS IN THIN DIELECTRIC FILMS . . . . .	52
3.8	KINETIC DESCRIPTION OF PROCESSES IN A DIELECTRIC . . . . .	56
3.9	ONE-DIMENSIONAL MODEL FOR DIELECTRIC EFFECTS IN A CHARGING ENVIRONMENT . . . . .	63

TABLE OF CONTENTS (Continued)

	Page
3.10 NUMERICAL METHODS FOR ONE-DIMENSIONAL DIELECTRIC CALCULATIONS . . . . .	68
3.10.1 Methods . . . . .	68
3.10.2 Results . . . . .	70
4. TEST CASES FOR THE NASCAP CODE . . . . .	77
4.1 GROUND TEST - FLOATING ALUMINUM PLATE . . . . .	77
4.2 GROUND TEST - TEFLON COATED PLATE . . . . .	81
4.3 GROUND TEST - SSPM . . . . .	87
4.4 ALUMINUM SPHERE SPACE TEST CASES . . . . .	100
4.4.1 Maxwell Probe Calculation. . . . .	100
4.4.2 Reverse Trajectory Simulation - Isotropic Flux . . . . .	101
4.4.3 Reverse Trajectory Simulation - Anisotropic Flux . . . . .	106
4.5 INSULATED SPHERES - MAXWELL PROBE CAL- CULATION . . . . .	106
4.6 COMPARISON OF DeFOREST DATA AND MAXWELLIAN . . . . .	106
4.7 ISOTROPIC SUN . . . . .	111
4.8 SPACE TEST OF SSPM . . . . .	113
4.9 CONCLUSIONS . . . . .	113
APPENDIX A - A PRELIMINARY SPECIFICATION OF THE ENVIRONMENT AT GEOSYNCHRONOUS ALTITUDE. . . . .	117
APPENDIX B - EXPERIMENTAL PLAN FOR THE TESTING OF SPACECRAFT CHARGING MODELS. . . . .	195
APPENDIX C - A VARIATIONAL/FINITE ELEMENT APPROACH FOR SATELLITE PROBLEMS OF ARBITRARY GEOMETRY . . . . .	275

TABLE OF CONTENTS (Continued)

	Page
APPENDIX D - POTENTIAL INTERPOLATION IN NASCAP . . .	285
D.1 LINEARLY BLENDED ELEMENTS . . . . .	285
D.2 ELEMENT TABLE CODES . . . . .	287
D.3 STANDARD VOLUME CELLS . . . . .	288
APPENDIX E - PAPER PRESENTED AT IEEE ANNUAL CON- FERENCE ON NUCLEAR AND SPACE RADIATION EFFECTS, WILLIAMSBURG, VIRGINIA, JULY 1977 . . . . .	295
APPENDIX F.1 - ELECTRON BACKSCATTER . . . . .	315
F.2 - DEPOSITION OF ELECTRONS IN MATERIALS . . . . .	321
F.3 - ANGULAR DEPENDENCE OF PHOTOEMISSION .	323
REFERENCES . . . . .	325

## LIST OF FIGURES

Figure No.		Page
2.1	Flow chart of NASCAP code . . . . .	7
2.2	Cross-section of grid, showing first four embedded meshes . . . . .	10
2.3	Four shapes of volume cells to be con- sidered by NASCAP code . . . . .	11
2.4	Six objects constructed by the NASCAP code . . . . .	12
2.5	A model for a geometrically complex object resembling ATS-6 . . . . .	13
2.6	Surface material composition of a model satellite . . . . .	15
2.7	To construct the distribution function $f(r_0, v_0)$ at a spacecraft surface. . . .	23
3.1	Schematic representation of charge density profile for a dielectric exposed to space environment . . . . .	31
3.2	Electron range in Si and SiO <sub>2</sub> and Al. .	36
3.3	Secondary emission coefficients for aluminum using Equation (3.9) (solid curves) and Equation (3.5) (dashed curves) . . . . .	39
3.4	Secondary emission coefficients for SiO <sub>2</sub> using Equation (3.9) (solid curves) and Equation (3.5) (dashed curves). . .	40
3.5	Secondary emission coefficients for MgO using Equation (3.9), with data from Table 3.2. . . . .	41
3.6	Secondary emission coefficients for Teflon using Equation (3.9), with data from Table 3.2 . . . . .	42
3.7	Secondary emission coefficients for Kapton using Equation (3.9), with data from Table 3.2 . . . . .	43

LIST OF FIGURES (Continued)

Figure No.		Page
3.8	Secondary emission by aluminum for proton impact at normal incidence . . .	45
3.9	Net albedo versus energy for isotropically incident electrons calculated from Equations (3.17) and (3.19). . . . .	48
3.10	Problem geometry for a one-dimensional system . . . . .	63
3.11	Surface potentials versus time . . . .	72
3.12	Dielectric potential difference ( $V^+ - V^-$ ) versus time . . . . .	74
3.13	Electric field versus distance at 210 seconds . . . . .	75
3.14	Charge density versus distance at 210 seconds . . . . .	76
4.1A	Particle trajectory plots (a-c) and current density contour plots (d-f) for uncharged (a,d), partially charged (b,e) and fully charged (c,f) aluminum plate subject to 2 keV electron beam. .	79
4.1B	Particle trajectory plots (a-c) and current density contour plots (d-f) for uncharged (a,d), partially charged (b,e) and fully charged (c,f) aluminum plate subject to 20 keV electron beam .	80
4.2	Peak incident flux (lower curves), net current (upper decreasing curves), and potential (increasing curves) versus time for an aluminum plate subject to an electron gun with energy 2, 5, 8, 20 keV . . . . .	83
4.3	Time development of potentials, net current, and peak incident flux for a 5 mil teflon-coated plate subject to a 10 keV electron beam . . . . .	85

LIST OF FIGURES (Continued)

Figure No.		Page
4.4	Time development of potentials, net current, and peak incident flux for a 5 mil teflon-coated plate subject to a 20 keV electron beam . . . . .	86
4.5	Potential contours at conclusion of 10 keV teflon plate tank test case. . .	88
4.6	Model of SSPM used for NASCAP test cases . . . . .	89
4.7	Current density contours to uncharged SSPM . . . . .	90
4.8	Potentials on the four SSPM material samples subject to a 5 keV electron beam . . . . .	92
4.9	Net and incident fluxes to the four SSPM samples subject to a 5 keV beam. . .	93
4.10	Potentials on the four SSPM material samples subject to an 8 keV electron beam . . . . .	94
4.11	Net and incident fluxes to the SSPM samples subject to an 8 keV beam. . . .	95
4.12	Potentials on the SSPM samples subject to a 10 keV beam . . . . .	96
4.13	Net and incident fluxes to the SSPM samples subject to a 10 keV beam. . . .	97
4.14	Potentials on the four SSPM material samples subject to a 20 keV beam. . . .	98
4.15	Net fluxes and incident fluxes to the four SSPM material samples subject to a 20 keV beam . . . . .	99
4.16	Potential and net flux for 3 m aluminum sphere in environment of Table 4.5 . . . . .	103

LIST OF FIGURES (Continued)

Figure No.		Page
4.17	Reverse trajectory simulations for 3 m aluminum sphere in environment of Table 4.5 . . . . .	105
4.18	Simulation of an aluminum sphere in an anisotropic plasma, with net flux to two representative surface cells . .	107
4.19	Net fluxes and potentials for di- electric-coated spheres in environ- ment of Table 4.5 . . . . .	109
4.20	Reverse trajectory calculations for 3 m Teflon sphere using DeForest data (hour 9.998 of day 73) and data of Table 4.5 . . . . .	110
4.21	Potential and net flux to a 3 m teflon sphere exposed to sunlight uniformly over its surface . . . . .	112
4.22	Potentials for SSPM material samples in environment of Table 4.5 and mounted on an aluminum plate fixed at -575 volts . . . . .	114
4.23	Net flux and incident electron flux to SSPM samples mounted on aluminum plate at -575 volts in environment of Table 4.5 . . . . .	115

## LIST OF TABLES

Table No.		Page
2.1	Orders of Magnitude Characterizing Satellite Charging in the Magneto- sphere. . . . .	8
3.1	Albedo and Range for Electrons in Materials . . . . .	32
3.2	Secondary Emission Data for Electron Impact Used to Calculate Figures 3.3 - 3.7 . . . . .	38
4.1	NASCAP Test Cases . . . . .	78
4.2	Results for the Aluminum Plate Ground Test Case . . . . .	82
4.3	Current Balance for the Teflon Plate Tank Test . . . . .	84
4.4	SSPM Ground Test Case Results . . . . .	91
4.5	Maxwellian Environment for Space Tests . . . . .	102
4.6	Current Balance for Aluminum Sphere - Maxwell Probe Calculation . . . . .	104
4.7	Current Balance for Insulating Spheres in Environment of Table 4.5 . . . . .	108



## SUMMARY

This final report describes the physical models employed in the NASCAP (NASA Charging Analyzer Program) code, and presents several test cases. A NASCAP User's Manual is available under separate cover.

NASCAP dynamically simulates the charging of an object made of conducting segments which may be entirely or partially covered with thin dielectric films. The object may be subject to either ground test (electron gun) or space (magnetospheric) user-specified environments. The simulation alternately treats (1) the tendency of materials to accumulate and emit charge when subject to plasma environment, and (2) the consequent response of the charged particle environment to an object's electrostatic field.

NASCAP is applicable when the Debye length in the plasma environment is long compared with body dimensions. Then particle trajectories are determined primarily by the charge on the satellite and only trajectories which begin or end on the object need be considered. For those cases in which photosheath effects are important, a first order explicit sheath calculation is provided.

NASCAP contains an object definition language which facilitates construction by the user of complex objects built of the basic cube, wedge, and tetrahedron elements, and allows specification of surface materials. The object definition output provides the information required by the conjugate gradient potential solver and by the various charging and emission routines.

Parameterized formulations of the emission properties of materials subject to bombardment by electrons, protons, and sunlight are presented. Values of the parameters are

suggested for clean aluminum,  $\text{Al}_2\text{O}_3$ , clean magnesium,  $\text{MgO}$ ,  $\text{SiO}_2$ , kapton, and teflon. A discussion of conductivity in thin dielectrics subject to radiation and high fields is given, together with a sample calculation.

Results of test cases run with the NASCAP code are presented. The test cases include bare aluminum and dielectric-coated plates under test tank conditions, aluminum and dielectric-coated spheres under space conditions, and the SSPM (aluminum plate with four material samples) under both ground test and space conditions.

## 1. INTRODUCTION

This final report describes the work performed during the past year at Systems, Science and Software under Contract NAS3-20119 to study the electrostatic charging in materials. The end result of our study is a computer code, NASCAP (NASA Charging Analyzer Program) which can simulate three dimensionally the dynamical charging of complex objects in either laboratory or space environments. This report describes the physical models employed in the code and presents the results of the first NASCAP calculations. A NASCAP User's Manual, which fully describes the operational details of the code, is available under separate cover.

NASCAP is able to predict how an object made of conducting sections which may be entirely or partially covered with thin dielectric films responds to a specified charged-particle environment. The environments of interest are those found in the earth's magnetosphere and in a ground-based test chamber designed to simulate spacecraft charging effects. NASCAP's approach is to divide the spacecraft charging problem into two sections: (1) the tendency of materials to accumulate and emit charge when subject to plasma environment, and (2) the consequent response of the charged particle environment to an object's electrostatic field. NASCAP treats both these sections in sufficient detail to simulate the charging of a complex satellite.

The objective of the materials study portion of our program has not been to break new ground in understanding fundamental material properties, but to review the existing literature and determine which processes are the most important ones to consider for the charging analyzer program. Much study has gone into the selection of which material processes are important so that the accuracy of any calculation would not be impaired due to the neglect of a dominant

mechanism. This study has also exposed voids in literature, where important relevant properties have not been adequately measured, and where there are no good theoretical values for necessary material parameters. In spite of such voids, we believe that the material properties are sufficient for NASCAP to be a useful dynamical charging model.

The response of the charged particle environment to an object's electrostatic field requires the calculation of the electric potentials on and near complex objects, and the determination of how those potentials influence charged particle trajectories. The electrostatic potential about the satellite or in the test tank is calculated by NASCAP using a finite element formulation of Poisson's equation. Under magnetospheric conditions, the Debye length  $\lambda_D = (kT/4\pi ne^2)^{1/2}$  is typically hundreds of meters, so that space charge can be ignored, except for a positively charged satellite which may develop a photoelectron sheath. The computational space consists of an arbitrarily large number of nested cubic meshes. The resulting set of several times  $10^4$  linear equations is solved using the Conjugate Gradient technique. The satellite or test object is defined within the innermost mesh and may have surfaces normal to any of the twenty-six cubic symmetry directions. It consists of one or more conductors which may be covered with thin dielectric layers. The conductors may be floating, held at fixed potentials, or biased relative to one another.

The net charge accumulation by each surface cell of the satellite is calculated in the presence of the electrostatic and magnetostatic fields about the satellite and specified environmental characteristics. In the ground test case, the incident flux is provided by a monoenergetic electron gun of specified beam profile. In the space case, the incident flux of electrons and ions at surfaces is determined using the reverse trajectory sampling method. The ambient plasma may

be isotropic and Maxwellian or may be represented by any of several sets of data from ATS-5 prepared by MAYA Development Corporation for  $S^3$ . Alternatively, a spherical probe approximation may be used. Optionally, a first-order photo-sheath calculation may be performed, but typically, because magnetospheric Debye lengths are large compared with spacecraft dimensions, space charge is neglected.

Section 2 of this report describes the potential and flux models used in NASCAP. The material property descriptions are discussed in Section 3 and Appendix E, while test case results are described in Section 4. Appendix A contains a description of the ambient space environment. An experimental plan for NASCAP verification is contained in Appendix B. Appendices C and D contain details of the finite element potential solver. Finally, a paper describing the charging of a materially complex spacecraft using NASCAP comprises Appendix F. This paper was presented at the IEEE conference on SPACE/RADIATION Physics held July 14-17, 1977, in Williamsburg, Virginia.

## 2. NASCAP PLASMA MODEL

### 2.1 INTRODUCTION TO NASCAP

Because it is bombarded by ions and electrons, a satellite will accumulate, emit and redistribute charge, as well as undergo material degradation. In addition, the flux of particles to the satellite will be substantially influenced by the satellite's own electromagnetic field. To describe this process, we have developed a three-dimensional dynamical computer code, NASA Charging Analyzer Program. This computer code, NASCAP, simulates the charging of geometrically, materially, and electrically complex objects in both ground test and magnetospheric environments. A block diagram of the code is shown in Figure 2.1. In this section, we discuss the physical models currently in the NASCAP code. More details of the NASCAP model can be found in Reference 1.

A summary of typical length and time scales involved is given in Table 2.1. A quick calculation shows that a one meter satellite subject to the full incident current of  $10^{-5}$  amperes/m<sup>2</sup> will charge at  $\sim 10^6$  volts/sec. If we suppose the satellite sufficiently near steady state that the net charging current is at least two orders of magnitude below the incident current and that ten volts per timestep will give sufficient accuracy, then the timestep for our computation will be  $\sim 10^{-3}$  seconds. During the differential charging process, a satellite is even closer to steady state. In such circumstances, NASCAP has been shown able to take timesteps of 100 seconds or longer.

A timestep of one millisecond or longer is long compared with any time characterizing the plasma, which can therefore be treated by the time-independent Vlasov equation. This allows us to calculate the flux to the satellite by the reverse trajectory technique described below. The electrostatic potential

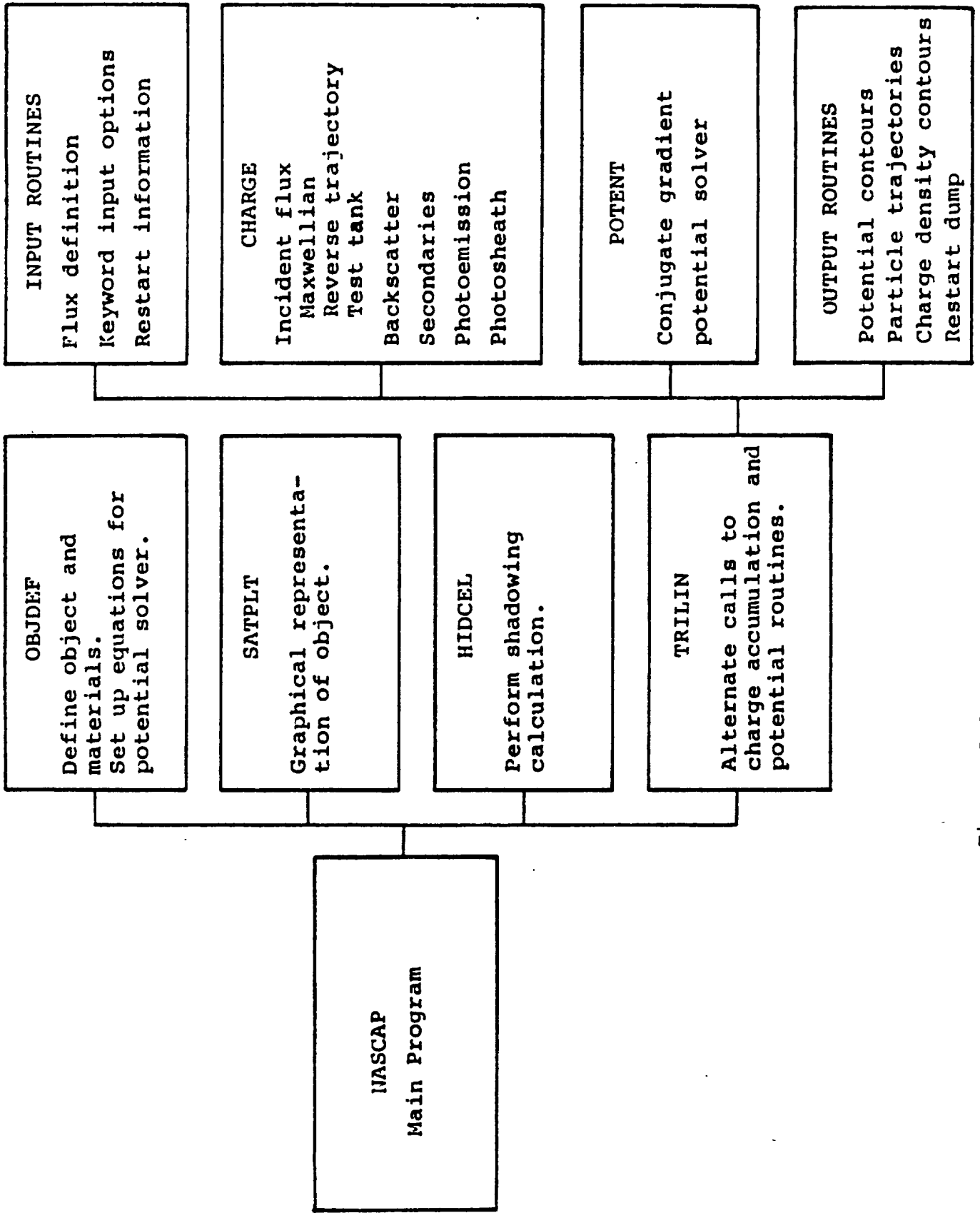


Figure 2.1. Flow chart of NASCAP code.

Table 2.1. Orders of Magnitude Characterizing Satellite Charging in the Magnetosphere

Object dimensions (L)	1-10 meters
Transit times:	
Light	$10^{-8}$ seconds
Hot electrons	$10^{-7}$ seconds
Hot ions	$10^{-5}$ seconds
Plasma frequency ( $\omega_p$ )	$10^5 - 10^6 \text{ sec}^{-1}$
Collision frequencies	$\ll \omega_p$
Incident current	$10^{-5}$ amperes/m <sup>2</sup>
Debye length	$10^2 - 10^3$ meters
Larmor radius	
Hot electrons	$10^4$ meters
Hot ions	$10^6$ meters
Time for	
Circuit element breakdown (arcing)	$10^{-8}$ seconds
Charging of bare conductor	$10^{-3}$ seconds
Differential charging of thin dielectric overlayer	$10^0 - 10^3$ seconds
Charge redistribution in a dielectric	$\sim 10^2$ seconds
Change in environmental conditions	$10^0 - 10^8$ seconds
Material degradation	$> 10^7$ seconds

is governed by Poisson's equation. Since the timestep is long compared with charge redistribution times associated with metallic conduction, conducting portions of the satellite may be treated as equipotentials. Differential charging, however, is governed by the large capacitances and low conductivities of dielectric films, so that a timescale of  $10^{-3}$  -  $10^{+3}$  seconds is suitable for its study.

While an entire satellite has a dimension of meters, adequate representation of its geometrical and compositional complexity requires a spatial resolution of 10 cm or better. Even this coarse resolution requires  $\sim 10^4$  mesh points in the immediate neighborhood of the satellite alone. NASCAP therefore uses a finite element, nested-mesh technique in order to achieve an accurate potential near the satellite while covering a substantial region of space with appropriately reduced resolution. NASCAP generates automatically a series of grids within grids as shown in Figure 2.2. All of the object is constrained to be within the innermost grid.

Objects are constructed from the four basic building blocks shown in Figure 2.3. These can be assembled in almost arbitrary fashion to generate the variety of objects in Figure 2.4. By adding these octagons, wedges, cubes, etc. together, one can construct an object as complicated as the primitive representation of ATS-6 shown in Figure 2.5. Some limitations of the present object definition routines are apparent in this figure. First, no object can be treated as a thin sheet. As a result, the solar panels, for example, are modeled to be a full cell in thickness. Secondly, booms must also be a cell in width.

The surface of the object may be covered with a thin layer of dielectric material, or may be exposed metal. The code automatically handles the electrical coupling between dielectric surfaces and underlying conductors. An example of

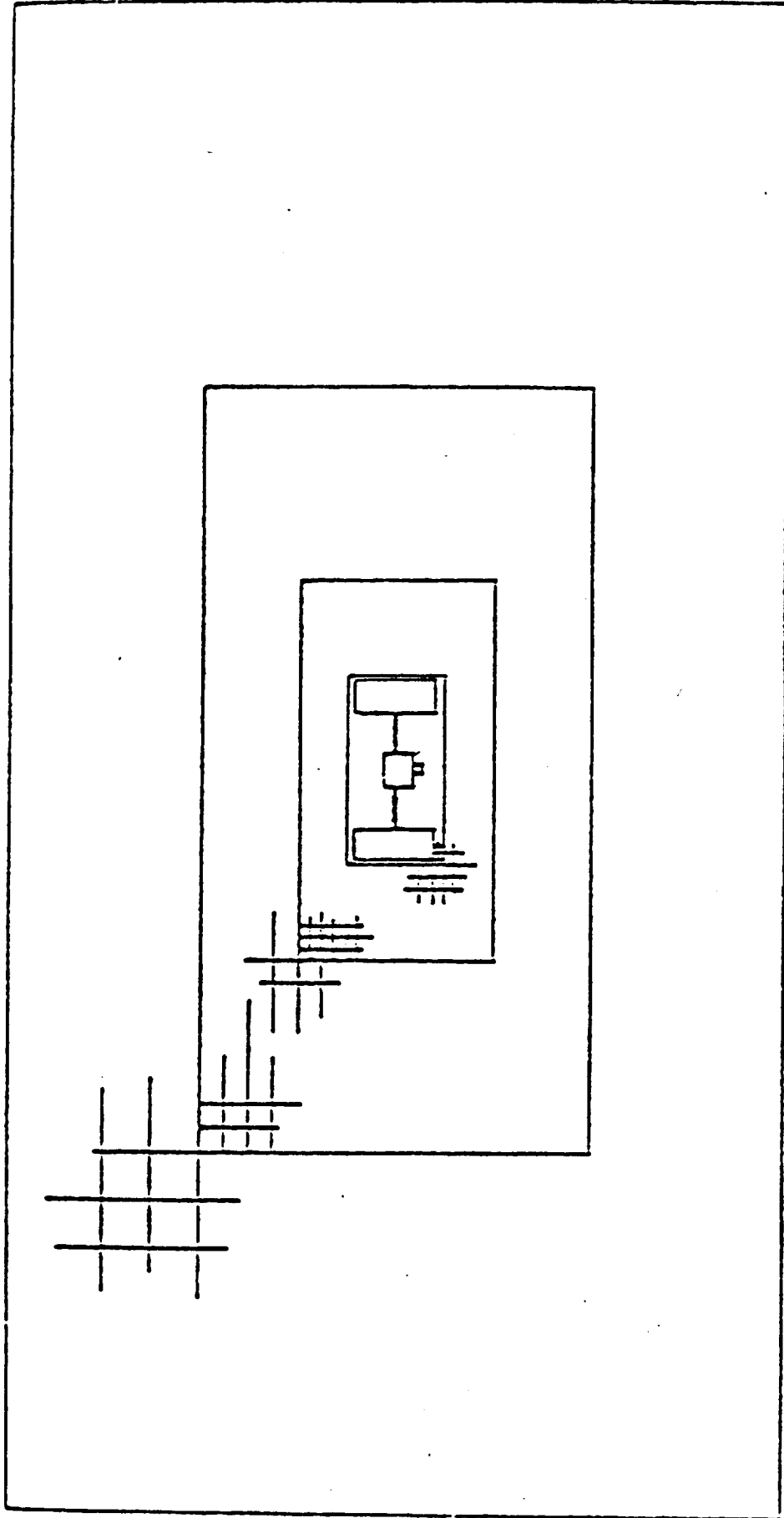
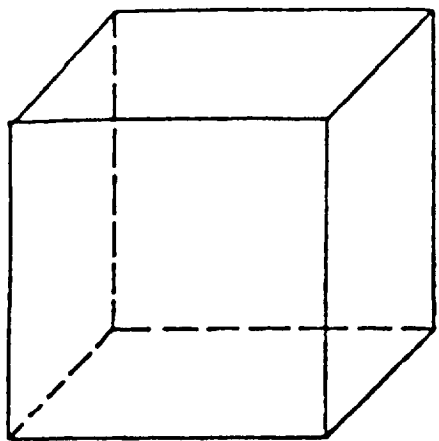
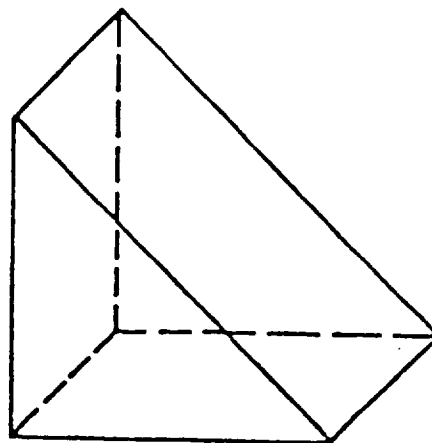


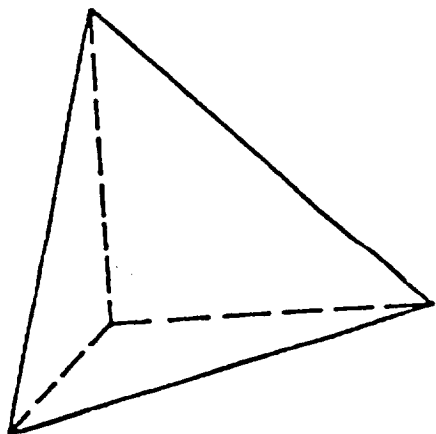
Figure 2.2. Cross-section of grid, showing first four embedded meshes.



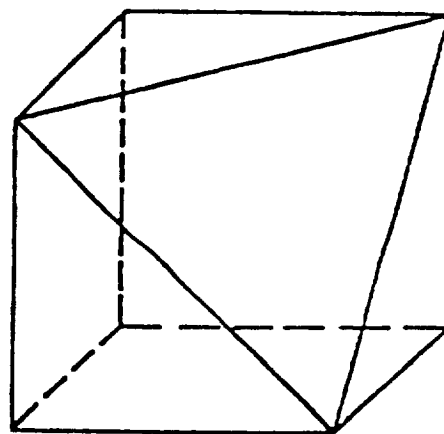
a



b



c



d

Figure 2.3. Four shapes of volume cells to be considered by NASCAP code: (a) empty cube; (b) wedge-shaped cell with 110 surface; (c) tetrahedron with 111 surface; (d) truncated cube with 111 surface.

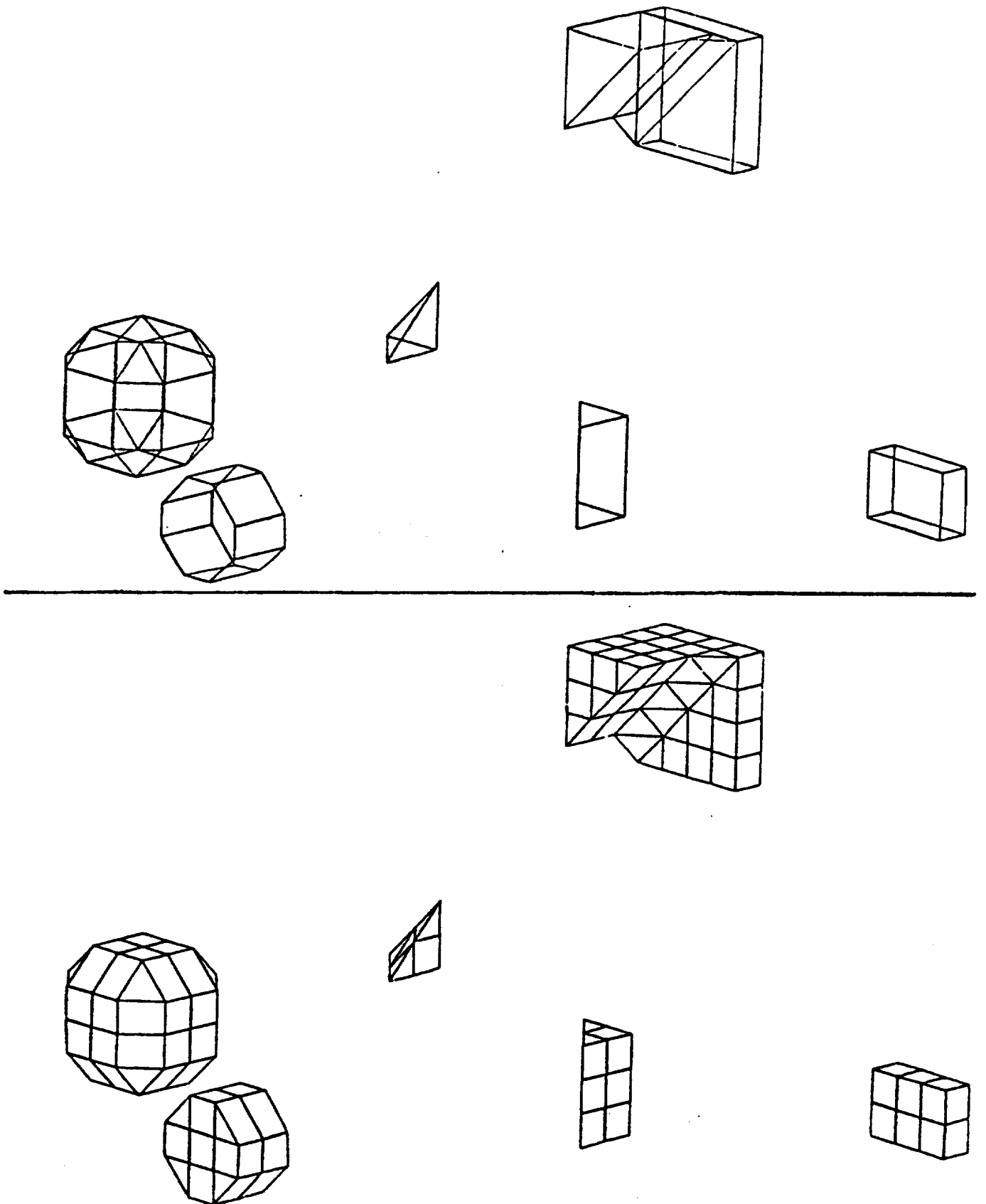


Figure 2.4. Six objects constructed by the NASCAP code. The top figure is drawn without hidden line elimination, and the lower is a full shadowing treatment showing individual surface cells.

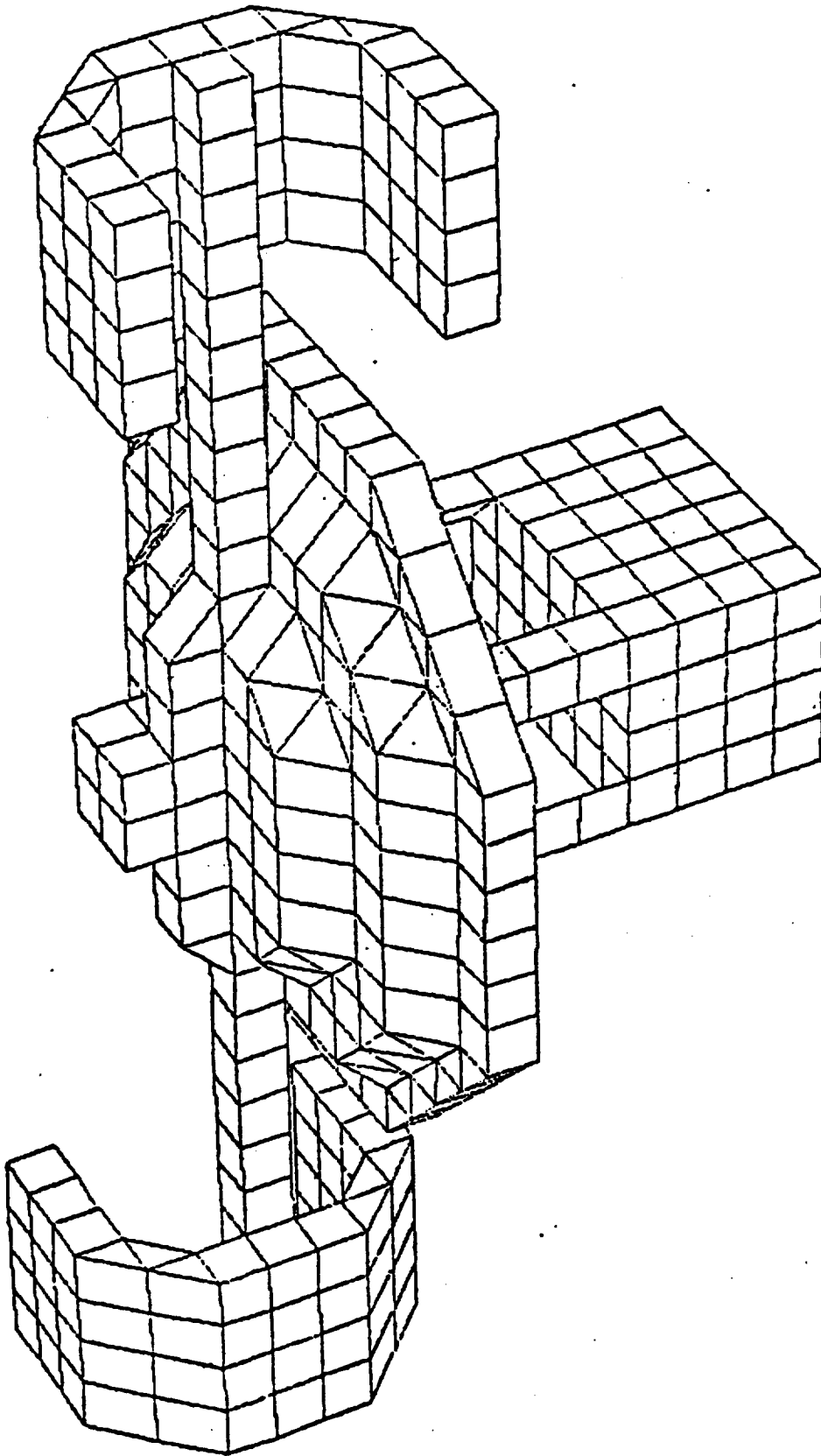


Figure 2.5. A model for a geometrically complex object resembling ATS-6. This model illustrates the geometrical capabilities of the current NASCAP code.

the variety of material surfaces possible is shown in Figure 2.6.

NASCAP is applicable when the Debye length in the plasma environment,  $\lambda_D$ , is long compared to body dimensions. In these circumstances, particle trajectories and the associated charging currents are determined primarily by the charge on the satellite and are nearly independent of the distribution of space charge around the satellite. In the absence of space charge effects, only those particle trajectories which begin or end on the object relate to spacecraft charging. Moreover, invariance under time reversal and the conservation of phase space volume along particle trajectories greatly simplifies the determination of the current of particles intercepted at object surfaces. Finally, when object dimensions,  $L$ , are small compared to  $\lambda_D$ , asymptotic potentials of the form  $Q/r$ , where  $Q$  is the object charge, are attained at distances  $r < \lambda_D$ ; consequently, the computational mesh required for numerical solutions is established by object dimensions rather than the much larger Debye length.

From the computational point of view, the long Debye length approximation reduces both storage requirements and the expense of the iterative process that would be required in the self-consistent determination of the potential and space charge distributions. Thus, there is a substantial economic incentive for NASCAP's utilizing the long Debye length approximation where the physical circumstances justify it.

The neglect of the effect of space charge on the potential distribution is valid in those circumstances in which the satellite is differentially charged to large negative potentials in the range of a few hundred to a few ten thousands of volts, such as can develop during magnetic substorms. However, secondary or photoelectrons can form sheaths with dimensions in the range from several centimeters to a few meters near surfaces.

SURFACE CELL MATERIAL COMPOSITION AS VIEWED FROM THE NEGATIVE Y DIRECTION

FOR Y VALUES BETWEEN 1 AND 17

MATERIAL LEGEND

1	
ALUMIN	
3	
SiO <sub>2</sub>	
4	
KAPTON	
11	
RPAIN	
12	
WFAINT	

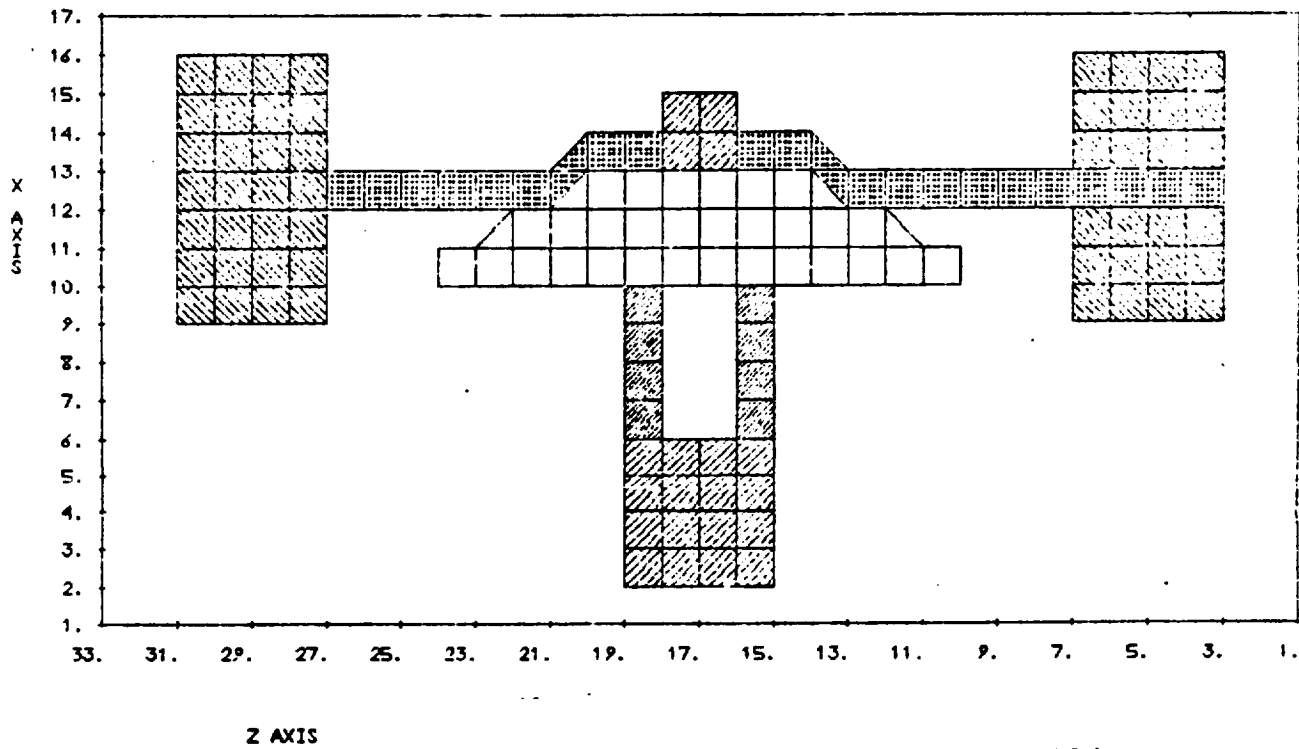


Figure 2.6. Surface material composition of a model satellite.

When the surface is at a large negative potential, the emitted electrons will be swept away; for positively charged surfaces, or for negative potentials in the range of a few volts or tens of volts, however, the space charge in such sheaths will strongly influence potential fields around the object.

The charges in the space surrounding a body consist not only of ambient particles, but also of charged particles emitted from surfaces as the result of impact of electrons, photons and positive ions, and in some cases, of electrons emitted prior to and during the process of dielectric breakdown. Emission processes and the trajectories of emitted particles play a prominent role in establishing the levels of charge and potential on both dielectric and conducting surfaces. Particle emission is taken into account by a first-order explicit sheath routine.

The equations that describe the plasma in the neighborhood of the satellite are the equilibrium Poisson-Vlasov equations:

$$\nabla^2 \phi = -e \int f \, d^3 \vec{v} / \epsilon_0 \quad (2.1)$$

$$0 = \frac{df}{dt} = \frac{\partial f}{\partial t} + \vec{v} \cdot \nabla f - \frac{e}{m} \nabla \phi \cdot \frac{\partial f}{\partial \vec{v}} \quad (2.2)$$

NASCAP uses an implicit equilibrium finite difference analogue to these equations:

$$\nabla^2 \phi^t = -e \int f^t \, d^3 \vec{v} / \epsilon_0 \quad (2.3)$$

$$\vec{v} \cdot \nabla f^{t+1} - \frac{e}{m} \nabla \phi^t \cdot \frac{f^{t+1}}{\partial \vec{v}} = 0 \quad (2.4)$$

The time dependence occurs in the boundary condition. In particular, the potential (Equation (2.3)) reflects charge buildup on the satellite in response to currents from the external plasma.

In the following sections of this chapter are presented the techniques used in NASCAP to solve the potential Equation (2.3) and the Vlasov Equation (2.4). In the final section, we briefly outline the time sequence of the code. Further details of the code can be found in the NASCAP User's Manual. [1]

## 2.2 POTENTIAL CALCULATION

In calculating the potential in three dimensions around an arbitrary object, a gridded method must be employed since the specification of the surface is far too general for analytical or multipole techniques. Since satellites are the order of meters in length, we need at least 10 cm resolution as an upper bound in the vicinity of the spacecraft. However, for determining particle orbits, the fields hundreds of meters away must also be known. In order to keep storage down to a reasonable level, some type of variable gridding must be employed. This precludes the use of any straightforward Fourier transform technique. One technique for achieving high resolution in the region around the object and still being able to handle vast quantities of space is through local mesh refinement. Finite difference approaches, however, have difficulty in mesh transition regions, especially when grid lines are terminated and generally lose an order of accuracy in such regions.

As a result of this, NASCAP employs a finite element approach using right parallelepiped elements and blended linear univariate edge interpolates. This permits the same degree of accuracy over the entire mesh, even though the mesh

elements differ in size. It results in the standard trilinear interpolation scheme for each element.

The fundamental approach is to solve Poisson's equation

$$\epsilon \nabla^2 \phi = -\rho / \epsilon_0 \quad (2.5)$$

by solving the associated variational principle

$$0 = \frac{\delta}{\delta \phi} \left\{ \int dV \left[ \frac{\epsilon}{2} (\nabla \phi)^2 + \frac{\rho \phi}{\epsilon_0} \right] \right\} + \int \left\{ \phi \nabla \phi \cdot \overline{dS} + \frac{\sigma}{\epsilon_0} dS \right\}. \quad (2.6)$$

The first term in the integrand corresponds to the Laplacian operator. The second term is the volume spacecharge contribution. The remaining terms are surface contributions, referring to the surface charge and electric field, respectively (see Appendix C).

In the variational calculation, we use locally defined basis sets, that is, trilinear interpolants within each cube-like element. Finite mesh volumes are given the correct variational weight, ensuring the maintenance of accuracy through mesh transition regions. The problem of local mesh refinement is approached by having grids within grids, that is, a chinese doll-like hierarchy of grids shown schematically in Figure 2.2. The theory of this technique is discussed in References 2 and 3. In order to have high computational speed, the linear equations resulting from the variational principle [Equation (2.6)] in the interface region were coded up explicitly in a series of thirteen subroutines. These same routines are used for interfacing any pair of the meshes.

The NASCAP code does not require that objects be composed solely of rectangular parallelepipeds; it allows surfaces

normal to any cubic symmetry direction, i.e., 110 and 111 as well as 100. This requires the treatment of surface elements shaped as right isosceles triangles, equilateral triangles, and  $\sqrt{2} \times 1$  rectangles, as well as squares, and three new shapes of volume elements in addition to the cube ( $0 < x < 1$ ,  $0 < y < 1$ ,  $0 < z < 1$ ) (see Figures 2.3-2.4).

$$(1) \quad 1 < x+y < 2, \quad 0 < z < 1$$

$$(2) \quad 1 < x+y+z < 3$$

$$(3) \quad 2 < x+y+z < 3$$

To meet the requirement that the potential be continuous, we have adopted the convention that the potential be bilinear on a square surface element, and linear on a triangular surface element or face. This results in a proliferation of "special cells" which have one or more square faces divided into two right triangles by the presence of surfaces in neighboring cells. Nonetheless, for any cell, we can write

$$\int_{\text{cell}} |\nabla\phi|^2 dv = \sum_{ij} W_{ij} \phi_i \phi_j \quad (2.7)$$

where  $i$  and  $j$  index the vertices of the cell. The coefficients  $W_{ij}$  are derived by "linear blending" techniques (see Appendix D). Thus, any "special cell" can be fit into the finite element scheme. NASCAP provides for a sufficient number of "special cells" to give the user reasonable flexibility in object specification.

A general derivation of the linear equations resulting from application of the finite element formalism to a system of charged conductors is given in Appendix C. In this section, we specialize this method to a cubic mesh with plane surfaces composed of thin dielectric layers.

NASCAP requires an object constructed so that mesh points lie on its dielectric surface. For each surface element, define nodes on the conductor immediately below each surface node. Taking the potential within the dielectric element to be a linear interpolant of the potentials of its eight (for a rectangular element, six for a triangle) vertices, (C.25) becomes:

$$\text{WPCOND}(I, n_c) = \epsilon_{FI} = -\sum_k \frac{A_k}{n_k} \frac{\epsilon_k}{d_k} + O(d_k) \quad (2.8)$$

where  $I$  is a surface point, the sum runs over those surface elements overlaying conductor  $n_c$  of which  $I$  is a vertex, and  $A_k$ ,  $\epsilon_k$ ,  $d_k$  and  $n_k$  are, respectively, the area, dielectric constant, thickness, and number of surface points associated with the  $k^{\text{th}}$  surface element. Terms proportional to the dielectric thickness are ignored. Equations (C.22a) can now be written

$$\left[ -\sum_J \text{WPCOND}(J, n_c) \right] \phi_{n_c} + \sum_J \text{WPCOND}(J, n_c) \phi(J) = \rho(n_c) + Q(n_c) \quad (2.9)$$

where  $Q(n_c)$  is the charge on conductor  $n_c$  and

$$\rho(n_c) = \sum_k A_k \sigma_k \frac{\bar{x}_k}{d_k} \quad (2.10)$$

where the sum runs over surface elements associated with  $n_c$ , and  $\sigma_k$  and  $\bar{x}_k$  are the surface charge density and mean deposition depth. (Similarly, the charge associated with a surface point  $J$  is

$$\rho(J) = \sum_k \frac{A_k}{n_k} \sigma_k \frac{d_k - \bar{x}_k}{d_k} \quad .) \quad (2.11)$$

Equations (C.22b) are written in the form

$$\text{WPCOND}(I, n_c) \phi_{n_c} + \sum_{J=1}^{27} W(J, I) \phi_J = \rho(I) \quad (2.12)$$

where the index J runs over I and the 26 points surrounding I in the 100, 110 and 111 symmetry directions. The coefficients W are given by

$$W(J, I) = \sum_k \epsilon_k \int_{\text{cell } k} \nabla N^I \cdot \nabla N^J \quad (2.13)$$

where k runs over all volume cells common to points I and J. The coefficients and interpolation functions associated with cell types implemented and the linear blending techniques used to obtain the weights and interpolation functions are described in Appendix D.

The resultant system of linear equations is solved using a conjugate gradient technique. This technique is a very efficient method for solving large systems of linear equations. It is necessary to use an iterative technique because of the large number (tens of thousands) of unknown potentials. The implementation of the conjugate gradient method in NASCAP is discussed in detail in the NASCAP User's Manual.

### 2.3 FLUX CALCULATIONS

The solution of the Vlasov equation is approached using the fact that phase space density is constant along a particle orbit. The numerical method used for this purpose is the time-symmetric, reversed trajectory method which enables us to bring the information in the velocity space from the undisturbed outer boundary to the spacecraft surface. Since  $\phi^{(n)}$ , the value of the potential distribution  $\phi$  at the nth stage of the

computational process is known, particle trajectories at the nth stage can be computed. The incident flux on any given surface element is determined by tracking time reversed orbits starting from an object surface element and invoking the principle of phase space volume invariance along particle trajectories in a collisionless plasma. If a particle starting at  $\vec{r}_0, \vec{v}_0$  on an object surface reaches  $\vec{r}, \vec{v}$ , then

$$f(\vec{r}_0, \vec{v}_0) = f(\vec{r}, \vec{v}) \quad (2.14)$$

where  $f$  is the phase space density. Thus, if  $\vec{r} = \vec{r}(\vec{r}_0, \vec{v}_0, t)$  is a point remote from the object, the orbit is one which a particle incident from remote distances can follow to the object; therefore, the flux of plasma particles incident on the surface can be determined from

$$f(\vec{r}_0, \vec{v}_0) = f(\vec{V}) \quad (2.15)$$

where  $f(\vec{V})$  is the distribution function of particles in the undisturbed plasma.

The procedure followed in connecting the spectrum of particles in a given element at  $\vec{r}_0$  to the unperturbed plasma spectrum is

1. Track particles with specified velocities  $\vec{v}_0$  from their point of origin  $\vec{r}_0$  along time reversed trajectories until they reach the outer boundary at  $\vec{r}_p$  of the computational mesh, or until it is clear that the particles will never reach the outer boundary. Here, the outer boundary is chosen so that the plasma beyond it is not significantly perturbed by the presence of the satellite.

2. Identify the incident particle spectrum at  $\vec{r}_0$  as

$$f(\vec{r}_0, \vec{v}_0) = f(\vec{V}) \quad (2.17)$$

where  $V$  is the velocity with which particles on their time reversed trajectories reach the outer boundary at  $r_p$ .

This process is illustrated in Figure 2.7. If  $\vec{v}_t$  is the terminal velocity at the outer boundary due to the backward trajectory tracing of a particle emitting with an initial velocity  $\vec{v}_i$  at the surface, then

$$f(\vec{r}_0, \vec{v}_i) = f(\vec{v}_t) \quad (2.17)$$

is the distribution function value at the point  $\vec{v}_i$ . By scanning these sampling points throughout the velocity space and completing their backward trajectory calculations, we can construct the whole distribution function  $f(\vec{r}_0, \vec{v}_0)$ .

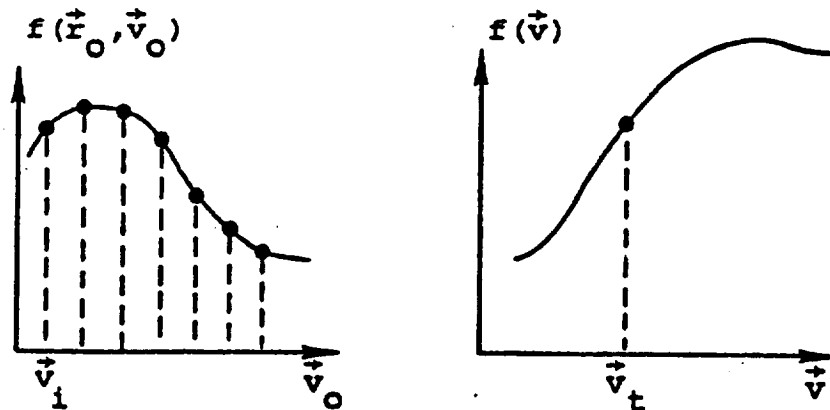


Figure 2.7. To construct the distribution function  $f(r_0, v_0)$  at a spacecraft surface.

In the general situation, we have to integrate the distribution function to obtain the charging current density for each species, that is

$$\vec{j}_c = \vec{n} \int_0^{2\pi} \int_0^1 \int_{v_m(\mu, \phi)}^{\infty} e v_o^3 f_o(v_o, \mu, \phi) dv_o \mu d\mu d\phi \quad (2.18)$$

where  $\mu = \cos\theta$ ,  $v_m(\mu, \phi)$  is the minimum escape speed of an electron emitted from the surface element with an angle  $(\theta, \phi)$  with respect to  $\vec{n}$ , and where  $f_o(v_o, \mu, \phi)$  includes anisotropy due to the magnetic field.

#### 2.4 DYNAMICAL MODEL

The dynamical model then consists of three parts:

1. The calculation of surface charging currents given potential distributions.
2. The calculation of dielectric, surface and space charge distributions given potentials and charging currents.
3. The calculation of potentials given charge distributions and boundary conditions.

In the typical one- or two-dimensional equilibrium code, the steps are iterated until a self-consistent solution is reached. However, the additional complexities introduced by the three-dimensional nature of the problem and the sophistication of the material properties treatment make iteration for each timestep prohibitive. Therefore, the solution sequence is a timestepping procedure from one quasi-static state to another. Initially, all potentials and charge distributions are specified. The dynamical parts of the problem are driven by charge accumulation on the body from external sources (ambient, plasma, electron gun, etc.), charge depletion (surface emission, etc.)

and conduction in dielectrics. Each timestep includes, in an explicit fashion, a fully three-dimensional electrostatic potential calculation time-staggered with a procedure in which incident charged particle fluxes, leakage currents, emission currents and emission current induced space charge effects are found according to the derived quasi-static equations.

### 3. MATERIAL PROPERTIES

#### 3.1 GENERAL CONSIDERATIONS

The interaction of charged particles at the surface of a geosynchronous satellite and the redistribution of charges in surface layers of the body are determinants of the electric stresses in satellite materials. The most important processes for satellite charging are charged particle deposition, photoelectron emission, secondary electron production by electron impact, electron backscattering and electron production by proton impact. The last process is generally of less importance than the others; in eclipse, however, where at electrical equilibrium electron and proton currents are nearly in balance, protonic and electronic emission processes are of comparable importance. NASCAP includes formulations for all of these processes. Other processes, such as electron emission by the impact of naturally occurring He and O ions, are not considered by NASCAP, but could readily be included if later judged to be important.

It is difficult to determine the particle emission properties of a given material accurately by laboratory experiments on well-characterized surfaces. For this application, the situation is still worse, since the surface properties of satellite materials are not carefully controlled; moreover, surface properties can be changed substantially by exposure to the magnetospheric environment. These factors should be viewed at this time as constituting a fundamental limitation on the quantitative accuracy with which electric potentials can be predicted.

Charged particles impacting a surface not only cause emission of other charged particles but also deposit charge beneath the surface. While charged particle deposition is not an important consideration for conducting materials, the

depth of deposition and the processes affecting it can have a profound effect on the strength and distribution of field within dielectric materials. Among the parameters affecting the internal electric fields are the intrinsic and field- and radiation-enhanced conductivities of the materials. Conductivity enhancement may occur by electron irradiation in a layer of thickness of the order of the electron range, by solar illumination to a depth depending on the optical absorption characteristics of the material, and by the production of charge carriers in strong electric fields ( $\sim 10^4$  volts/cm). Accurate determinations of the internal fields are rendered difficult not only because of the limited amount and quality of relevant data, but also because a complete and unambiguous theoretical description based upon the underlying physical processes is lacking for the materials of interest. Even if such a description were available, its incorporation into a three-dimensional computational scheme could seriously limit the efficiency of that scheme.

Based on the uncertainties inherent in material properties, as well as the high premium associated with the efficient operation of a three-dimensional code, a phenomenological approach to the charged particle transport within and emission from satellite materials is fully justified. Section 3.3 describes NASCAP's approach for the determination of electron emission resulting from electron, proton and photon bombardment. The approach described is comparable to state-of-the-art methods for estimating emission currents, and in addition it extends those methods to permit emission estimates over extended regimes of energy and angle of incidence. The parameters required to estimate emission currents from clean aluminum,  $Al_2O_3$ , clean magnesium,  $MgO$ ,  $SiO_2$ , kapton and teflon are presented.

We show in the following sections that secondary emission due to electron bombardment and electronic charge deposition are closely related to the range of the incident electron. A substantial simplification in the description of deposition profiles results if the energy and angle dependence of the incident electrons can be described a priori; such a simplification permits useful estimates of upper bounds on the electric field in the dielectric at its vacuum interface. One possibly useful description of the deposition is described in Section 3.2. The general validity of such simplified treatments of charged particle deposition as we consider here can best be established by calculations of incident particle spectra under a variety of charging conditions.

For conductors covered by a thin dielectric film, the region in which we seek solutions of Poisson's equation includes the dielectric. Boundary conditions are applied on conducting surfaces, but the charge on the conductor is determined not only by plasma currents, but also by leakage currents through the dielectric films. Except for extremely thin dielectric layers ( $\lesssim 0.1$  mil), the charge density and potential distributions within a dielectric into which charge is injected at one surface vary strongly as a function of position. Moreover, the injected charge is redistributed by charge transport processes which are not well understood, and in any case, are difficult to quantify.

We anticipate that in many practically occurring circumstances, the potential in the vacuum region depends only weakly on the charge distribution within the dielectric layer. In Section 3.6, we express the coupling between a conducting surface and vacuum through a dielectric film by means of an effective boundary condition at the dielectric surface. The basic approximation that leads to a computationally simple

boundary condition is that the thickness of the layer containing the injected charge is small relative to the film thickness. This approximation leads not only to a simple boundary condition, but also to the result that the electric field and leakage currents are independent of position throughout most of the depth within the dielectric. Under these circumstances, it is unnecessary to "zone" the dielectric. Therefore this simplified treatment is used by NASCAP.

While seeking to simplify the treatment of dielectric films, it is recognized that there are reasons for knowing the potential distribution in the dielectric and for understanding the processes which affect it. First, one should understand the limitations on our treatment of dielectrics in terms of an effective boundary condition. Second, knowledge of the electric field and charge density structure within the dielectric is likely to be of importance in the determination of conditions marking the onset of breakdown through the film.

Section 3.7 describes a simple field-dependent bulk conduction model for the transport of charge in a dielectric. There it is argued that the potential drop across a thin section of dielectric is insensitive to the detailed processes which govern charge migration and carrier production within the dielectric. This argument is considered in Section 3.8, the subject of which is a detailed one-dimensional treatment of charge migration that takes into account the production, mobility and trapping of a single species of charged carrier. Should the conclusion regarding the insensitivity of the potential drop have validity beyond the examples that demonstrate it, then separation of the calculation of surface potentials from the detailed calculation of field distributions within dielectric films would be valid. One can then invoke the surface potentials calculated in three-dimensions as boundary conditions for one-dimensional calculations of internal field distributions

that incorporate physically reasonable descriptions of the kinetics and transport of charged species.

### 3.2 CHARGE DEPOSITION

A good insulator will, with exposure to the space environment, develop a charge density profile similar to that shown in Figure 3.1. Within a few tens of angstroms from the surface a positively charged depletion layer forms due primarily to emission of secondary electrons and photoelectrons. Superimposed on this is a distribution of negative charge due to the stopped incident electrons. As indicated in Appendix F.2, this distribution can adequately be represented by a simple exponential, at least for the case of an isotropic, Maxwellian plasma:

$$N(x) = (1-A_0)/\bar{x} \exp(-x/\bar{x}) \quad (3.1)$$

where  $A_0$  is the net albedo (see Section 3.4 below),  $\bar{x}$  the mean deposition depth, and the energy dependence is based on Feldman's range formula.<sup>[4]</sup> For keV plasma temperatures,  $\bar{x}$  is a few hundred angstroms (see Table 3.1). The derivation of Equation (3.1) can be easily generalized to a non-Maxwellian, non-isotropic plasma.

Neglecting charge migration due to conduction processes (see section on dielectric properties), and treating the depletion layer as a surface charge, we have ( $q =$  electronic charge)

$$\rho(x,t) = \rho(x,0) + \int_0^t dt' \left\{ S(t') \delta(x) |q| \right. \\ \left. - \pi |q| f_e(t') \frac{1-A_0}{\bar{x}(t')} \exp(-x/\bar{x}(t')) + \frac{d}{dt'} \rho_i(t') \right\} \quad (3.2)$$

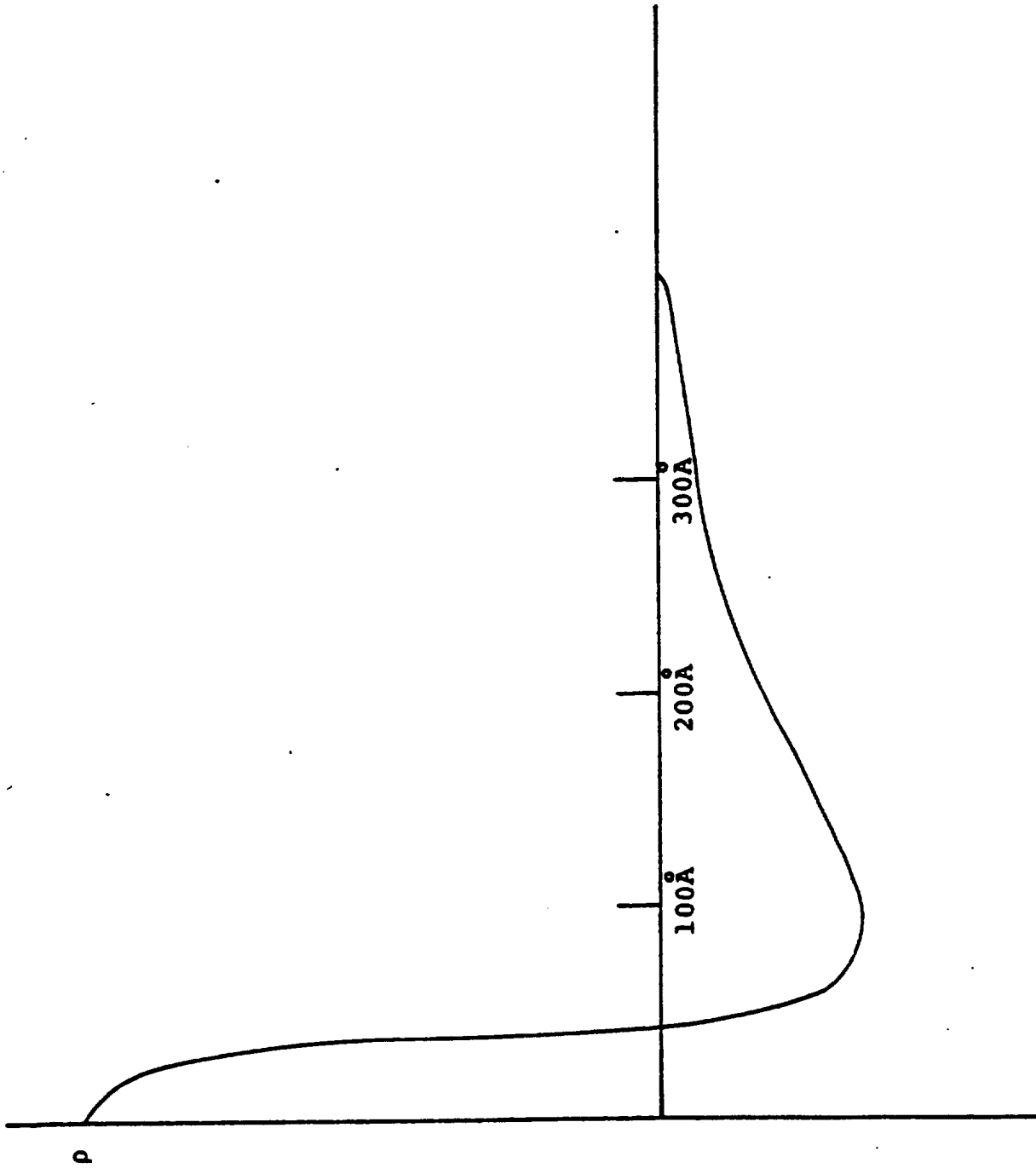


Figure 3.1. Schematic representation of charge density profile for a dielectric exposed to space environment.

Table 3.1. Albedo and Range For Electrons in Materials

<u>Material</u>	<u>A<sub>o</sub></u>	<u>n</u>	<u><math>\bar{x}T^{-n} (A\text{-keV}^{-n})</math></u>
Kapton	0.187	1.505	560
Teflon	0.235	1.63	400
SiO <sub>2</sub>	0.262	1.69	316
Al <sub>2</sub> O <sub>3</sub>	0.262	1.69	219
MgO	0.262	1.69	233
Al	0.299	1.77	313

for the charge density in the dielectric, where  $S$  is total secondary yield (due to electron and ion impact and photo-emission),  $f_e$  is the electron flux at the surface, and  $\rho_i$  is the charge density due to ion deposition. The NASCAP potential solver is in principle capable of handling the 0<sup>th</sup> moment,  $\sigma$ , and the first moment,  $\delta$ , of this distribution:

$$\sigma(t) = \sigma(0) + |q| \int_0^t dt' [S(t') - \pi(1-A_0)f_e(t') + \pi(1-A_{oi})f_i(t')]$$

$$\sigma(t)\delta(t) = \sigma(0)\delta(0) - |q|\pi \int_0^t dt' [(1-A_0)\bar{x}(t')f_e(t') - (1-A_{oi})\bar{x}_i(t')f_i(t')] \quad (3.3)$$

where we introduce  $f_i$ ,  $A_{oi}$ , and  $\bar{x}_i$  for the flux, albedo and mean deposition depth of ions. Because the ionic flux is small, an accurate representation of the ionic charge deposition profile is not essential. Furthermore, we anticipate that in most, and perhaps all interesting circumstances, the first moment  $\delta$  will have only a negligible effect on the external potential. The present version of NASCAP ignores the first moment,  $\delta$ .

### 3.3 SECONDARY EMISSION

#### 3.3.1 Electron Impact

The emission of low-energy electrons upon electron impact is one of the most important factors determining the sign of a spacecraft's charge. Unfortunately, the pool of experimental data characterizing this phenomenon is far from adequate.<sup>[5-8]</sup> It is therefore necessary to calculate secondary

emission using formulae which relate it to better characterized material parameters and which are general enough to accept future modification. Furthermore, the formulae must be applicable to non-normal incidence, for which the amount of available data is miniscule.

NASCAP uses a formulation based on the range and energy loss rate of the incident particles. Nearly all of the energy lost by an incident electron goes into electronic excitations, and we assume the probability of an electronic excitation resulting in an escaped secondary varies exponentially with depth. We then have

$$\delta = c_1 \int_0^R \left| \frac{dE}{dx} \right| e^{-c_2 x \cos \theta} dx \quad (3.4)$$

where  $\delta$  is the number of emitted secondaries per primary incident at angle  $\theta$ , and the range and energy loss rate are related by

$$\left| \frac{dE}{dx} \right| = \left( \frac{dR}{dE} \right)^{-1} \quad (3.5)$$

If the range function is known, the above expression can, in principle, be evaluated with the constants  $c_1$  and  $c_2$  determined from the energy of maximum yield,  $\epsilon_m$ , and the corresponding yield  $\delta_m$ .

For a general range expression, Equation (3.4) can be evaluated by assuming a constant  $dE/dx$ . This is reasonable since most of the secondary electrons originate in a thin surface layer. The upper limit of Equation (3.4) must be set to give the correct total energy loss (set  $c_1 = 1$  and  $c_2 = 0$ ). We then have

$$\begin{aligned} \delta(E, \theta) &= c_1 \int_0^{EdR/dE} \left(\frac{dR}{dE}\right)^{-1} e^{-c_2 x \cos \theta} dx \\ &= \frac{c_1 [1 - \exp(-c_2 \cos \theta EdR/dE)]}{c_2 \cos \theta dR/dE} \end{aligned} \quad (3.6)$$

The angle averaged yield then becomes

$$\bar{\delta}(E) = 2c_1 E (Q - 1 + \exp(-Q)) / Q^2 \quad (3.7)$$

where

$$Q = c_2 EdR/dE \quad (3.8)$$

NASCAP, in fact, evaluates (3.4) by assuming  $dE/dx$  is linear in  $x$ :

$$\frac{dE}{dx} = \left(\frac{dR}{dE_0}\right)^{-1} + \frac{d^2R}{dE_0^2} \left(\frac{dR}{dE_0}\right)^{-3} x \quad (3.9)$$

The range is represented by the sum of two exponentials:

$$R = r_1 E^{n_1} + r_2 E^{n_2} \quad (3.10)$$

For such data as is available this gives a good representation of the range for  $100 \text{ eV} < \epsilon < 100 \text{ keV}$ . (See Figure 3.2.) The upper limit,  $R_u$ , on the integral Equation (3.4) is taken as the lesser of the solutions of

$$\left. \frac{dE}{dx} \right|_{R_u} = 0 \quad (3.11a)$$

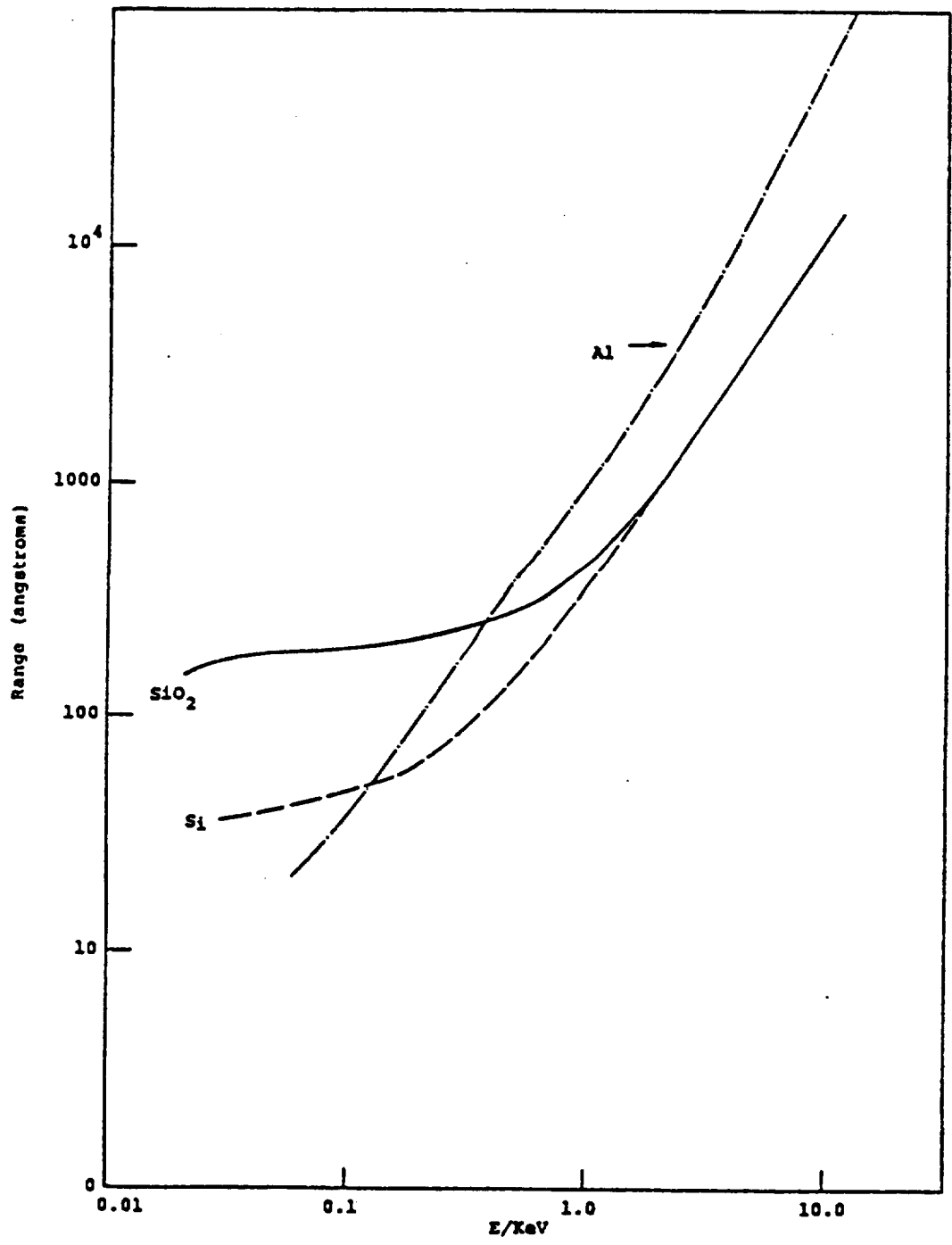


Figure 3.2. Electron range in Si and SiO<sub>2</sub><sup>[9]</sup> and Al. [10-11]

$$\int_0^{R_u} \left| \frac{dE}{dx} \right| dx = E \quad (3.11b)$$

Then, letting  $Q = c_2 R_u \cos \theta$ , we have

$$\begin{aligned} \delta(E, \theta) = c_1 \left[ R_u \left( \frac{dR}{dE_0} \right)^{-1} \frac{1 - \exp(-Q)}{Q} \right. \\ \left. + R_u^2 \frac{d^2 R}{dE_0^2} \left( \frac{dR}{dE_0} \right)^{-3} \frac{1 - (Q+1) \exp(-Q)}{Q^2} \right] \end{aligned} \quad (3.12)$$

$$\begin{aligned} \bar{\delta}(E) = 2c_1 \left[ R_u \left( \frac{dR}{dE_0} \right)^{-1} (Q-1 + \exp(-Q)) / Q^2 \right. \\ \left. + z R_u^2 \left( \frac{d^2 R}{dE_0^2} \right) \left( \frac{dR}{dE_0} \right)^{-3} \right] \end{aligned} \quad (3.13a)$$

where, in (3.13)  $Q$  is evaluated for normal incidence and

$$z = \int_0^1 u du \frac{1 - (Qu+1) \exp(-Qu)}{Q^2 u^2} \quad (3.13b)$$

which may be expanded for large and small values of  $Q$ .

NASCAP uses this formulation of secondary emission to evaluate the constants  $c_1$  and  $c_2$  from user input parameters  $\delta_m$ ,  $E_m$ .

Figures 3.3 through 3.7 show illustrative curves generated by the electron-secondary subroutines. These curves are based on the parameters given in Table 3.2.

Table 3.2. Secondary Emission Data for Electron Impact Used to Calculate Figures 3.3 - 3.7

The range data for SiO<sub>2</sub> and aluminum approximate the curves of Figure 3.2; others are based on Feldman's formula. [4] Energies are given in keV and distances in Å.

<u>Material</u>	<u>δ<sub>max</sub></u>	<u>E<sub>max</sub></u>	<u>E<sub>I</sub></u>	<u>E<sub>II</sub></u>	<u>Range</u>
Aluminum [5-7]	0.97	0.3			260E <sup>1.3</sup> +240E <sup>1.73</sup>
Al <sub>2</sub> O <sub>3</sub> [5-7]	1.5-9	0.35-1.3			187E <sup>1.69</sup>
MgO [5-7]	4.0	0.4			198E <sup>1.69</sup>
SiO <sub>2</sub> [7]	2.4	0.4			250E <sup>.12</sup> +360E <sup>1.63</sup>
Teflon [8]	3.0	0.3	0.05	1.85	350E <sup>1.63</sup>
Kapton [8]	2.1	0.15	0.03	0.5	514E <sup>1.5</sup>
Mg	0.92	0.25			377E <sup>1.75</sup>

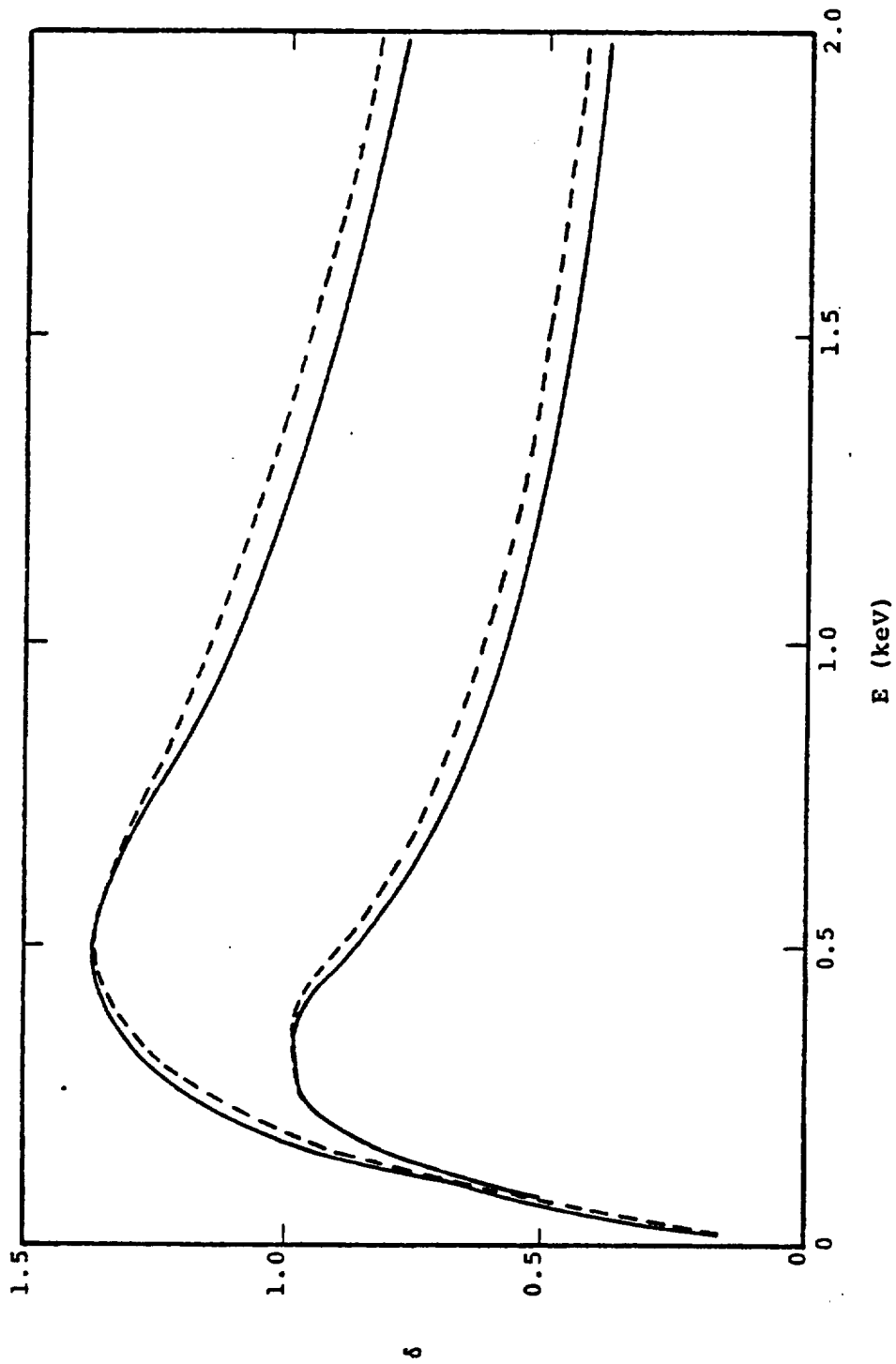


Figure 3.3. Secondary emission coefficients for aluminum using Equation (3.9) (solid curves) and Equation (3.5) (dashed curves). Upper curves are for isotropic flux and lower curves for normal incidence. Range,  $\delta_{\max}$  and  $E_{\max}$  are taken from Table 3.2.

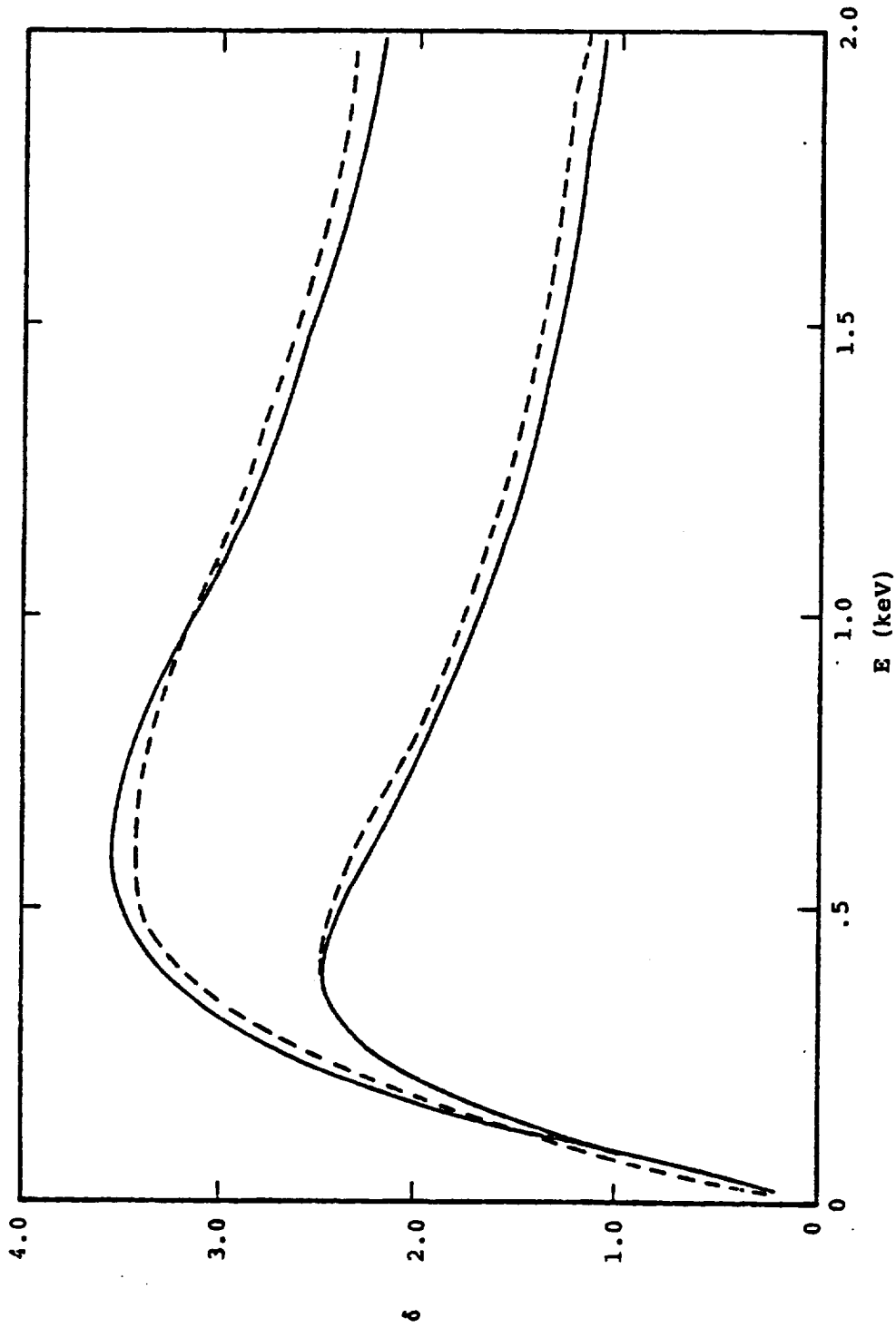


Figure 3.4. Secondary emission coefficients for  $\text{SiO}_2$  using Equation (3.9) (solid curves) and Equation (3.5) (dashed curves). Upper curves are for isotropic flux and lower curves for normal incidence. Range,  $\delta_{\text{max}}$  and  $E_{\text{max}}$  are taken from Table 3.2.

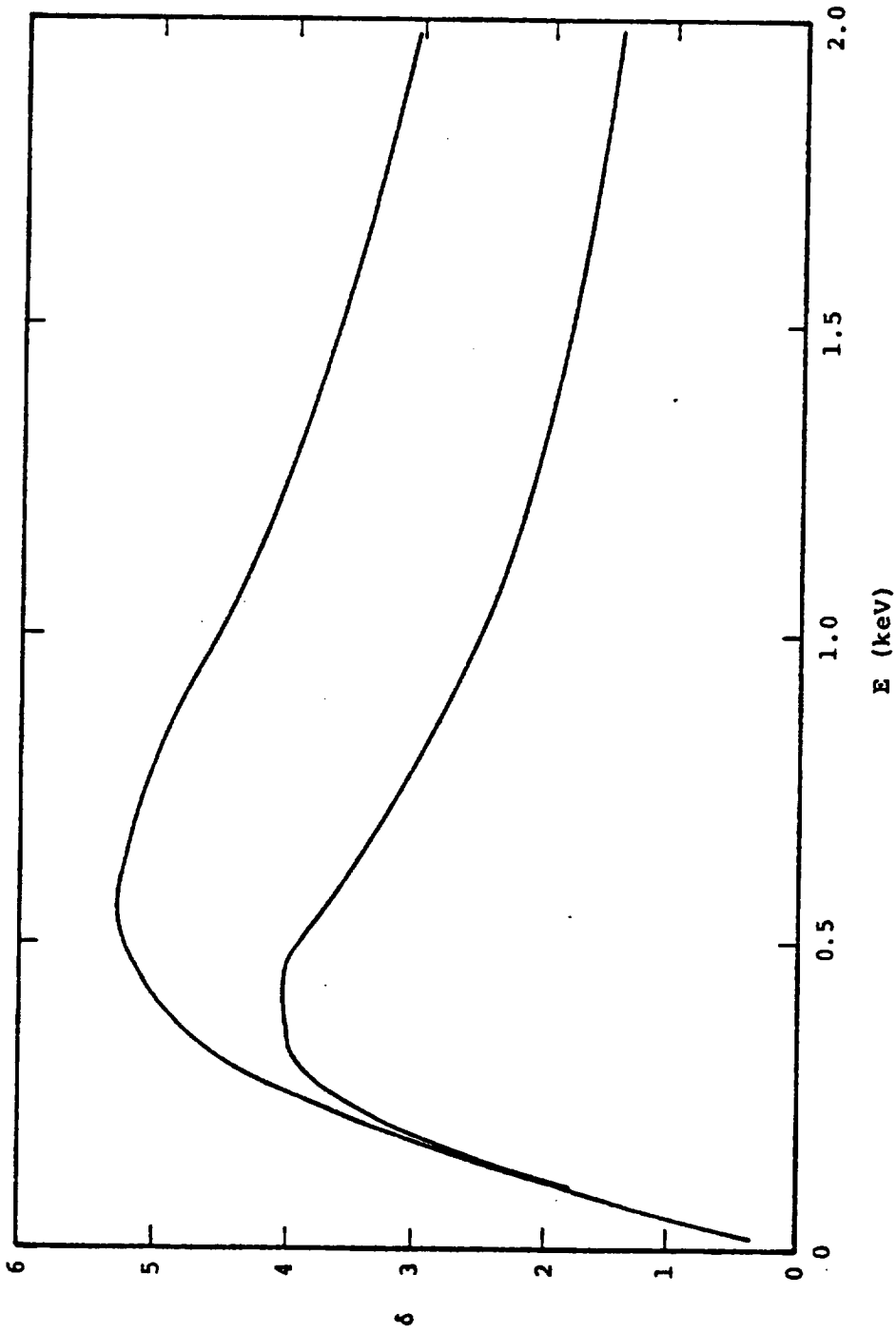


Figure 3.5. Secondary emission coefficients for MgO using Equation (3.9), with data from Table 3.2.

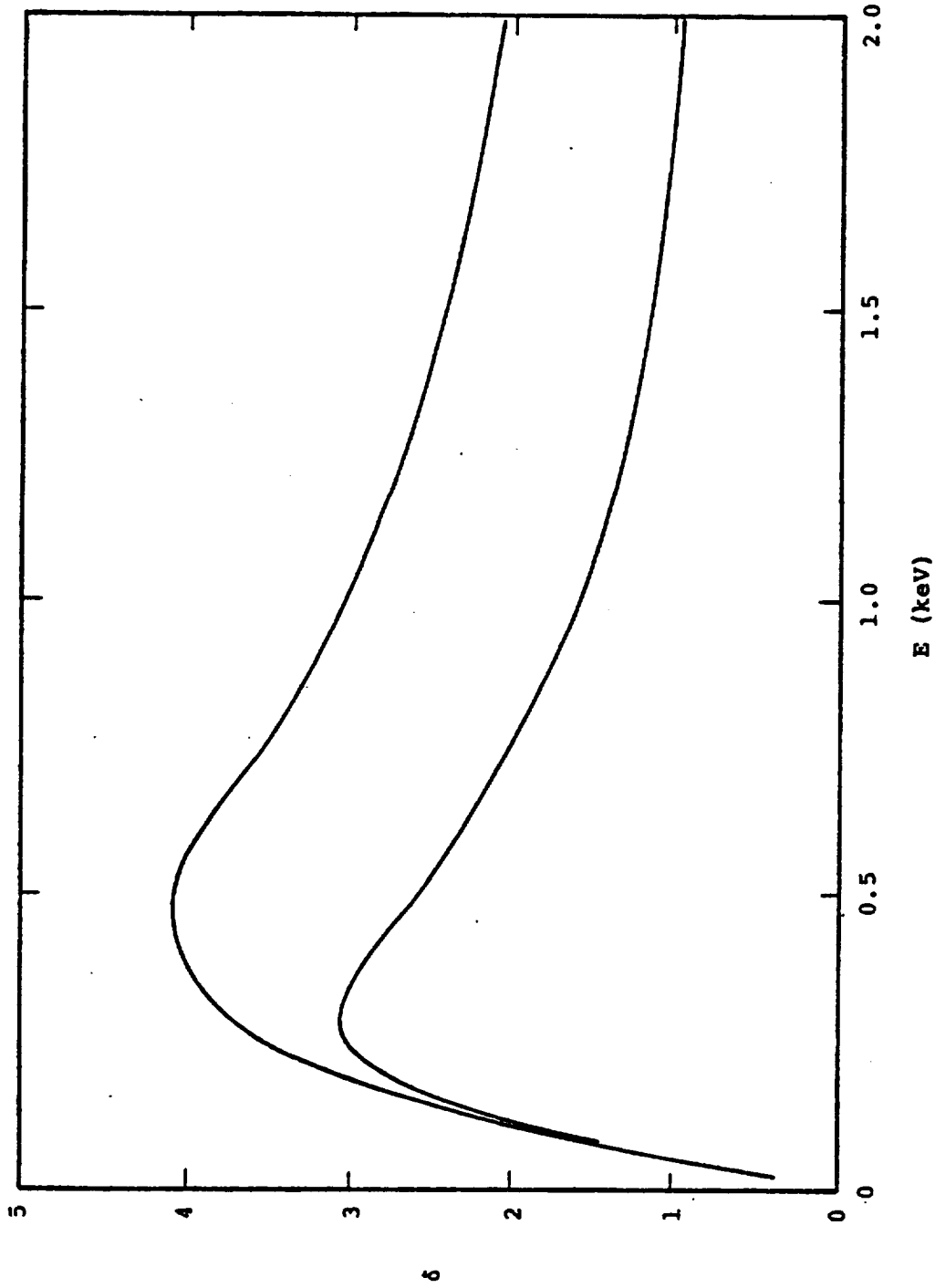


Figure 3.6. Secondary emission coefficients for teflon using Equation (3.9), with data from Table 3.2.

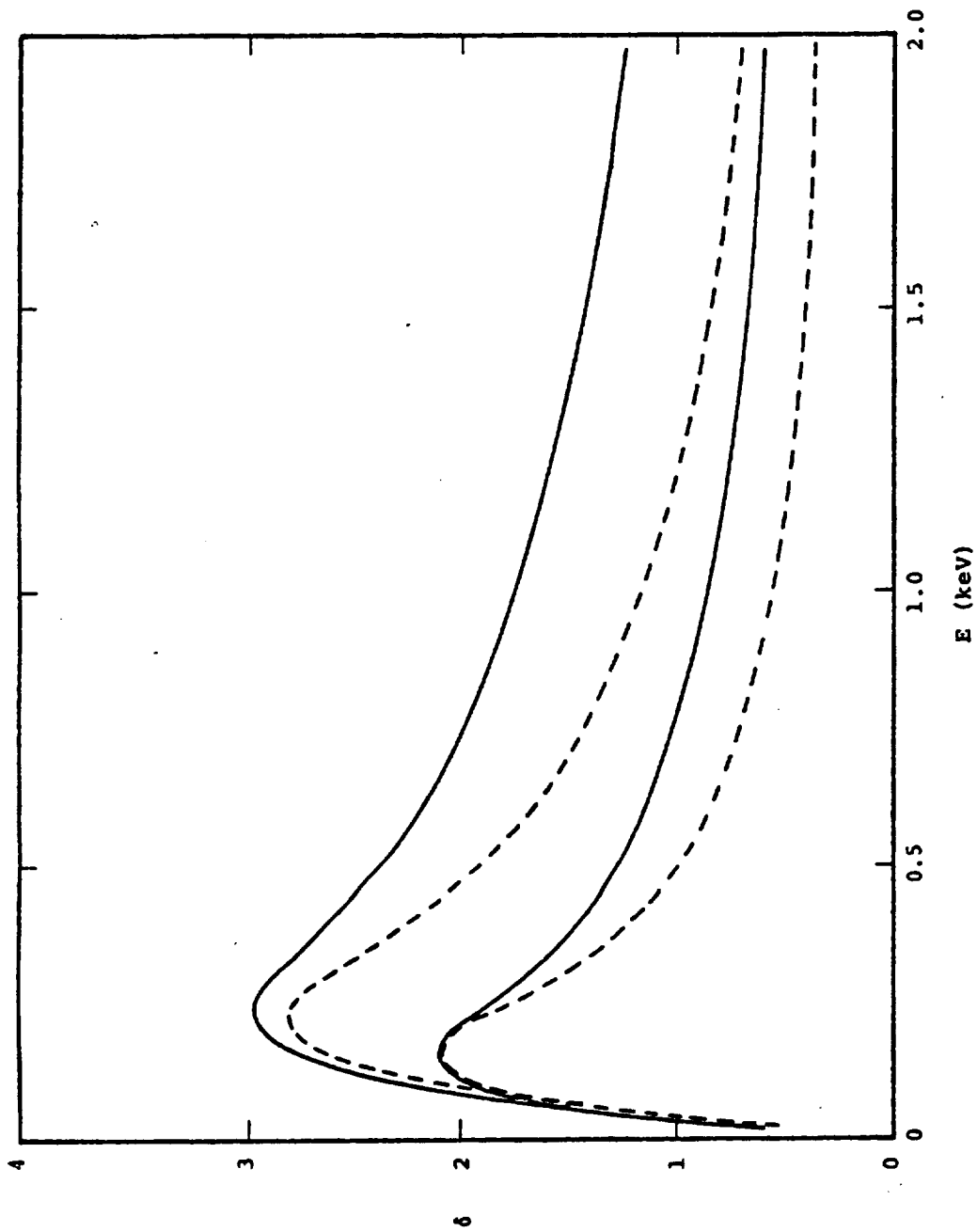


Figure 3.7. Secondary emission coefficients for kapton using Equation (3.9) with data from Table 3.2 (solid curves). Dashed curves were obtained by changing range exponent from 1.50 to 1.75 to fit value of  $E_{II}$ .

### 3.3.2 Proton Impact

Secondary emission due to proton impact<sup>[12-17]</sup> is treated by NASCAP in similar fashion to the electron case. A difference is that the energy loss is well represented by

$$\left| \frac{dE}{dx} \right| = cE^{1/2} / (1 + E/E_{\max}) \quad , \quad (3.14)$$

where  $E_{\max} \sim 50$  keV. Proton secondary emission can be large in the 10-100 keV energy range. Below 1 keV, the "potential emission" process comes into play. However, the potential emission coefficient is seldom as large as 0.1 and can probably be ignored. Because energetic protons travel long distances in straight lines, and because emission by ions is generally less important, Equation (3.5) is used in the formulation, and the angular dependence is taken to be simply  $\sec \theta$ . Secondary emission by aluminum on proton impact is indicated in Figure 3.8.

### 3.3.3 Energy and Angle Distribution

The energy distribution of secondary electrons is peaked at a few volts. Either a Maxwellian or a uniform distribution provides an adequate representation for spacecraft charging purposes.

A small emitting surface emits secondary electrons into a unit solid angle at  $\theta$  at a rate proportional to  $\cos \theta$ . This results in an isotropic flux of secondaries above an extended emitting surface.

## 3.4 BACKSCATTERING AND REFLECTION

### 3.4.1 Albedo for Electrons

Backscattering of electrons is discussed in Appendix F.1. We describe a large-angle scattering theory similar to

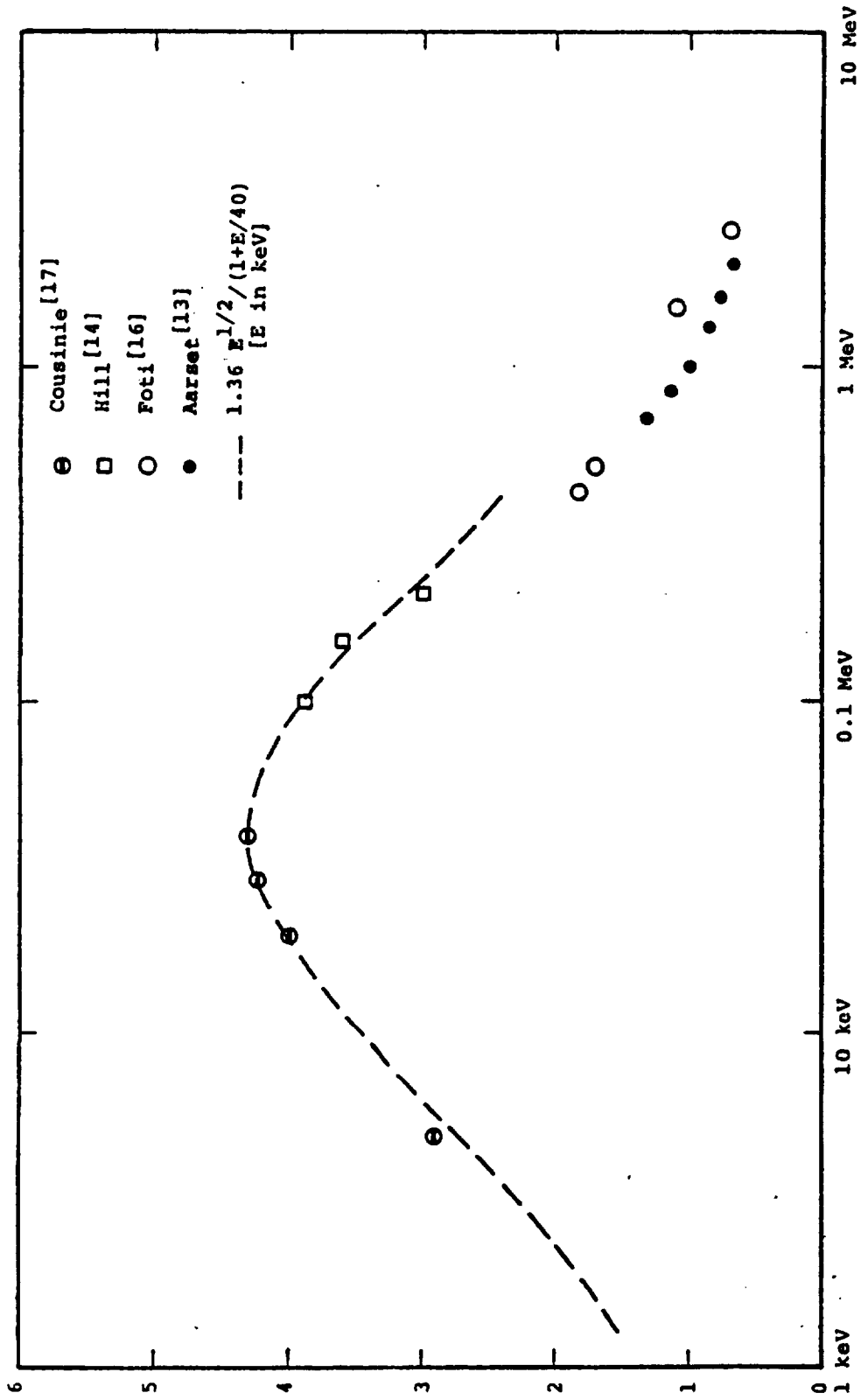


Figure 3.8. Secondary emission by aluminum for proton impact at normal incidence. Curve is Equation (3.10). Experimental points as indicated.

that of Everhart, [18] but generalizable to arbitrary angles of incidence. (Large-angle-scattering approximations are known to be superior to diffusion approximations for low  $z$  materials.) For normal incidence, and assuming the Rutherford scattering cross-section and the Thomson-Widdington slowing down law  $dE/dx \propto E^{-1}$ , this theory can be integrated to yield

$$\eta = 1 - \left(\frac{2}{e}\right)^a \quad (3.15)$$

where  $a$  renormalized exponent  $a = 0.037Z$  gives backscattering coefficients in good agreement with experiment. This result is expected to be valid for  $10 \text{ keV} < E < 100 \text{ keV}$ .

The large-angle scattering theory, together with Monte-Carlo (ELTRAN) data and experiments by Darlington and Cosslett, [19] indicate that the angular dependence of backscattering is well described by

$$\eta(\theta) = \eta(0) \exp[\eta_1(1-\cos\theta)] \quad (3.16)$$

where the value of  $\eta_1$  is, within the uncertainty in the data, what would be obtained by assuming total backscattering at glancing incidence, viz.  $\eta_1 = -\log \eta_0$ . The net albedo for an isotropic flux is then

$$A_0 = 2[1 - \eta_0(1 - \log \eta_0)] / (\log \eta_0)^2 \quad (3.17)$$

As the energy is decreased below 10 keV the backscattering increases. Data cited by Shimizu [20] indicate an increase of about 0.1, almost independent of  $Z$ . NASCAP approximates this component of backscattering by

$$\delta\eta_0 = 0.1 \exp[-E/5 \text{ keV}] \quad (3.18)$$

At very low energies the backscattering coefficient becomes very small and, below 50 eV, backscattering and secondary emission are indistinguishable. NASCAP takes account of this by a factor of  $\log(E/50 \text{ eV}) \theta(E - 50 \text{ eV}) / \log(20)$ . The formula for energy-dependent backscattering, incorporating these assumptions, is then

$$\eta_0 = \{[\log(E/0.05)\theta(E - 0.05)\theta(1.0-E)/\log(20)] + \theta(E-1.0)\} \\ \times [0.1 \exp(-E/5) + 1 - (2/e)^{.037Z}] \quad (3.19)$$

where energies are measured in keV. Resultant curves for the net albedo are shown in Figure 3.9.

#### 3.4.2 Energy and Angle Distribution of Backscattered Electrons

Monte-Carlo (e.g., ELTRAN) data as well as several approximate theories indicate that the energy and angle distributions of backscattered electrons are smooth and exhibit surprisingly weak dependence on incident angle. The mean energy of backscattered electrons in the 10 keV - 100 keV range is about two-thirds the incident energy, while the angular distribution is roughly  $\cos\theta$  for all but the most glancing angles. Accordingly, the energy and angle distribution of backscattered electrons may be approximated as

$$f_B(E, \theta) = 2A_0 \int_E^\infty dE_i f(E_i) (E/E_i^2) \cos\theta \quad (3.20)$$

where  $f(E_i)$  is the angle-averaged incident flux at energy  $E_i$ .

#### 3.4.3 Reflection of Protons [12,21]

There is little data on reflection of protons from solids. Indications are that the net reflection from low- $z$  materials is no more than 10 percent. However, many protons are reflected as neutrals or negative ions, so that the charge reflection coefficient is surely small. NASCAP neglects reflection of protons.

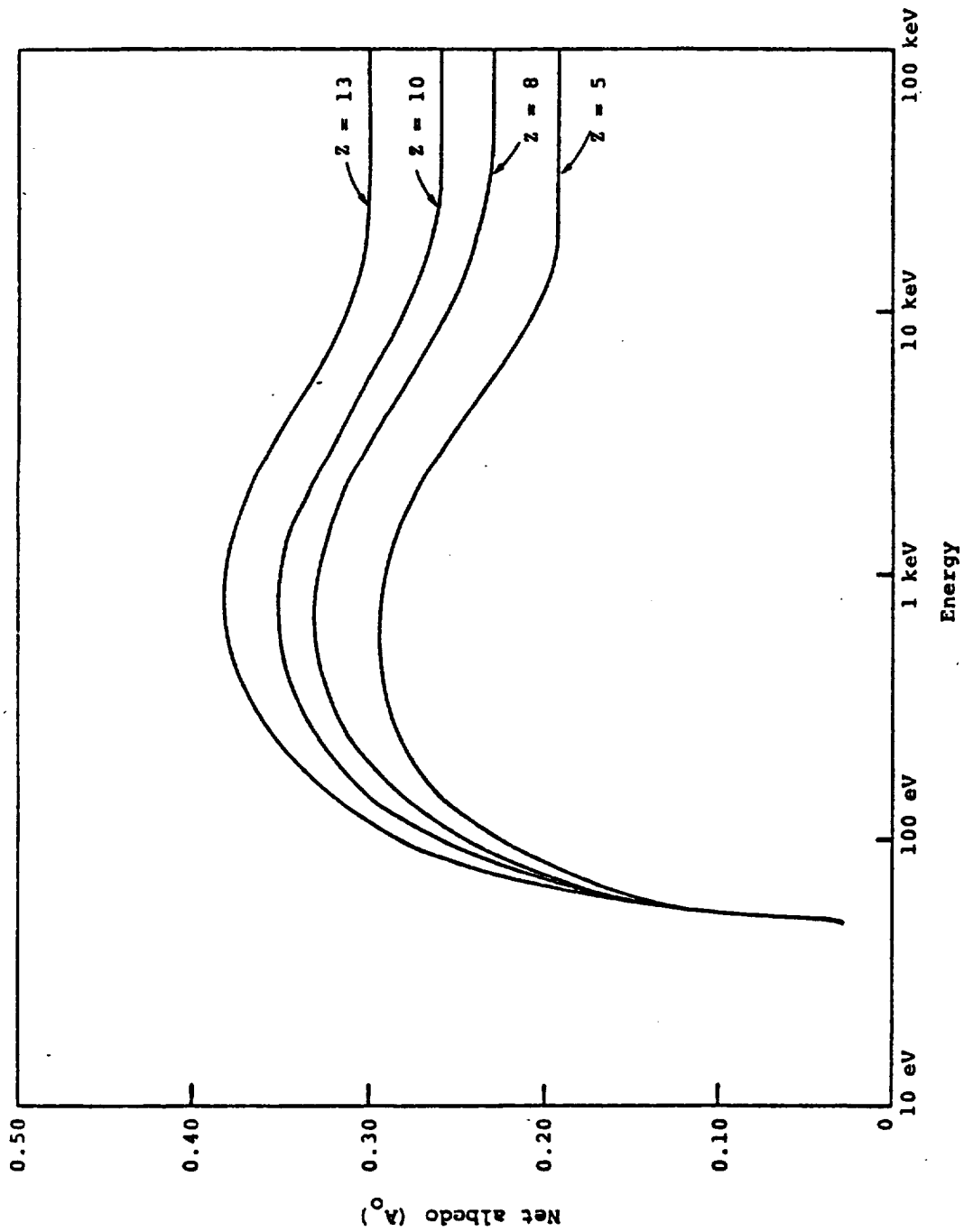


Figure 3.9. Net albedo versus energy for isotropically incident electrons calculated from Equations (3.17) and (3.19).

#### 3.4.4 Sputtering

Kaminsky<sup>[12]</sup> indicates that sputtering coefficients for metals under proton bombardment seldom exceed 0.1 atoms/ion. Furthermore, the charge distribution of sputtered particles is unknown. In view of the low proton fluxes, sputtering should be a negligible factor for spacecraft charging, except insofar as it results in surface degradation. NASCAP does not treat sputtering.

#### 3.5 PHOTOEMISSION

In a sense, photoemission is a relatively simple process to treat, since the spectrum of incident particles is unique and fairly well characterized, viz. the solar spectrum.<sup>[22,23]</sup> However, few measurements of photoelectric yield or optical properties have been made in the vacuum ultraviolet. Furthermore, the photoyield is strongly dependent on surface condition.

NASCAP expects the user to enter a number (based, say, on the work of Feuerbacher and Fitton<sup>[24]</sup>) for the photoyield in amps/m<sup>2</sup> under normally incident sunlight. The program will then correct for angle by assuming a constant yield per incident photon.

If more data were available, the yield could be calculated by:

$$Y(\theta) = \int d\epsilon y(\epsilon) f(\epsilon) h(\epsilon, \theta) \cos\theta \quad (3.21)$$

where  $y(\epsilon)$  is the yield (el/photon for normally incident monochromatic light at energy  $\epsilon$ ,  $f(\epsilon)$  is the solar flux (photons/cm<sup>2</sup>-sec), and  $h(\epsilon, \theta)$  is the ratio of the monochromatic yield at angle  $\theta$  to the normally incident yield. As discussed in Appendix F.3,  $h(\epsilon, \theta)$  depends only on the optical properties of the material, and is given by

$$h(\epsilon, \theta) = \sec \theta \frac{|E(\theta)|^2}{|E(o)|^2} \times \frac{1+2\alpha(o)L}{1+2\alpha(\theta)L} \quad (3.22)$$

where  $E(\theta)$  is the electric field just inside the solid calculated using the usual electromagnetic boundary conditions,  $\alpha(\theta)$  is the  $\vec{E}$ -field attenuation coefficient normal to the surface, and  $L$  is the escape depth for photoelectrons, which may be taken as the inverse of the constant  $c_2$  appearing in the preceding discussion of secondary emission.

### 3.6 EFFECTIVE BOUNDARY CONDITIONS IN THIN DIELECTRIC MATERIALS

For conductors covered by a thin dielectric film, it is convenient to express the potential drop across the film by means of an effective boundary condition at the dielectric vacuum interface. The desired relation between the potential,  $\phi_o$ , at the vacuum-dielectric interface ( $x = 0$ ) and the potential,  $\phi_c$ , at the dielectric-metal interface ( $x = d$ ) follows from the definition

$$\phi_c - \phi_o = - \int_0^d E_-(x) dx \quad (3.23)$$

and the boundary condition

$$\kappa(o)E_+(o) - E_-(o) = \frac{\sigma^s}{\epsilon_o} \quad (3.24)$$

by integrating Poisson's equation

$$\frac{d}{dx} (\kappa E) = \frac{\rho}{\epsilon_o} \quad (3.25)$$

through the dielectric material. Here,

$$\epsilon_o \approx \frac{1}{36\pi} \times 10^{-7} \text{ farad/meter} , \quad (3.26)$$

$E_+(0)$  and  $E_-(0)$  are the electric fields at  $x = 0^+$  and  $x = 0^-$ , respectively,  $\kappa(x)$  is the relative static dielectric constant at the position  $x$ ,  $\rho$  is the charge density, and  $\sigma^s$  is the density of surface charge. For a single dielectric layer, the effective boundary condition takes the form

$$\vec{n} \cdot \nabla \phi - \kappa \frac{(\phi_o - \phi_c)}{d} = - \frac{1}{\epsilon_o} \{ \sigma^s + \sigma_v (1 - \frac{\bar{x}}{d}) \} \quad (3.27)$$

where

$$\sigma_v = \int_0^d \rho(x) dx \quad , \quad (3.28)$$

$$\bar{x} = \sigma_v^{-1} \int_0^d x \rho(x) dx \quad , \quad (3.29)$$

and  $\vec{n}$  is the unit normal vector directed from the dielectric into vacuum. It follows that if  $\bar{x} \ll d$ , that is if the excess charge injected into the dielectric remains near the vacuum-dielectric interface, it is a good approximation to consider the net injected charge as a surface charge,

$$\sigma_s^{\text{eff}} = \sigma^s + \sigma_v \quad .$$

This conclusion, however, applies only for the purpose of computation of potentials in the space outside the dielectric. Clearly, the determination of the electric field within the dielectric, particularly near the vacuum-dielectric boundary, requires a knowledge of the charge distribution in the dielectric.

### 3.7 SIMPLE MODEL FOR LEAKAGE CURRENTS AND FIELDS IN THIN DIELECTRIC FILMS

The mathematical treatment of charge leakage through an ohmic medium is extremely simple. Consider a beam of electrons incident onto one face of a thin dielectric slab, and denote by  $j_b$  the current of beam electrons within the medium. The charge deposition profile is given by  $q(\partial j_b / \partial x)$ , where  $q$  is the electronic charge. If  $\rho$  is the charge density,  $E$  the electric field,  $\sigma$  the constant conductivity of the medium and  $\epsilon$  the dielectric constant, the equations governing the electrical behavior within the dielectric are

$$\epsilon \frac{\partial E}{\partial x} = \rho \quad (3.30a)$$

$$\frac{\partial \rho}{\partial t} = -\sigma \frac{\partial E}{\partial x} - q \frac{\partial j_b}{\partial x} = -\frac{\sigma}{\epsilon} \rho - q \frac{\partial j_b}{\partial x} \quad (3.30b)$$

with solution

$$\rho(x, t) = \rho(x, 0) e^{-\frac{\sigma}{\epsilon} t} - \int_0^t \frac{\partial j_b}{\partial x} e^{-\frac{\sigma}{\epsilon}(t-t')} dt' \quad (3.31)$$

For a deposition profile of time invariant shape

$$j_b(x, t) = j_b^0(t) f(x) \quad (3.32)$$

the spatial dependence of the charge distribution of an initially uncharged dielectric is also time invariant. Moreover, if the range of electrons in the dielectric medium is less than its thickness, the electric field in the region beyond the range of the incident electrons is independent of position. Typically, the thickness of the layer of dielectric

adjacent to the "vacuum" is greater than 1 mil ( $2.5 \times 10^{-3}$  cm) whereas the range of 10 keV electrons in teflon is only about  $10^{-4}$  cm, so that the electric field varies spatially only in a small region near the surface at which electrons are incident. In such circumstances, one can suppose that the deposited charge resides on the surface so that the electric field is spatially uniform through the dielectric layer. The approximation would be a good one for the calculation of the electric fields everywhere except within the deposition zone.

As long as deposited electrons are treated as a surface charge, the electric field is spatially uniform through the dielectric even for a field dependent conductivity. If the conduction current is  $j_c = j_c(E)$ , then

$$\frac{\partial \rho}{\partial t} = - \frac{\partial j_c}{\partial x} = - \frac{\partial j_c}{\partial E} \frac{\partial E}{\partial x} = - \frac{\rho}{\epsilon} \frac{\partial j_c}{\partial E} . \quad (3.33)$$

Thus if  $\rho$  vanishes initially it vanishes for all times and  $\partial E / \partial x = 0$ . On the other hand, within the deposition zone the form of the charge density profile would be modified by the effects of conduction.

As long as we maintain the assumption that any excess charge in the dielectric remains in a surface layer, the problem of calculating dielectric leakage currents is mathematically straightforward. It still remains, however, to describe the manner of dependence of conduction currents on electric field strength.

Many authors have advanced models for electrical conduction by dielectrics at high fields based on the classical ideas of Schottky<sup>[25]</sup> and Frenkel.<sup>[26]</sup> These models have been summarized by Adamec and Calderwood.<sup>[27]</sup> The latter authors have also proposed a model for polymeric insulating materials which yields a relationship between conductivity

and field strength in good agreement with experimental values for a number of polymers (including polyimide at 250°C) over a range of field strengths ranging from  $10^4$  to  $10^6$  volts/cm. According to their model, the field dependence of conductivity may be expressed as

$$\sigma = \frac{\sigma_0(T)}{3} (2 + \cosh(\beta_F E^{1/2}/2 kT)) \quad (3.34)$$

for fields less than about  $10^8$  volts/m. Here, in mks units,

$$\beta_F = \left( \frac{|q|}{\pi \epsilon_0 \kappa} \right)^{1/2} \quad (3.35)$$

is the Frenkel parameter,  $\kappa$  the relative dielectric constant at high frequency,  $k$  is Boltzmann's constant,  $T$  the absolute temperature,  $\epsilon_0 = 1/36 \times 10^{-9}$  farad/meter and  $\sigma_0$  is the intrinsic low field conductivity, which may depend on the temperature.

The precise values of parameters to be used in Equation (3.34) are not at all certain. Nominal values of resistivity have been given for kapton,<sup>[28]</sup> teflon<sup>[29]</sup> and fused silica;<sup>[30]</sup> presumably, the measured nominal values of resistivity are determined from a resistance which is obtained by dividing an applied voltage by the observed current through the sample. The values of resistivity so obtained depend, in general, on the applied voltage, sample thickness and temperature, and quite possibly the measurements also reflect electrode and space charge effects. There is also some uncertainty concerning the behavior of the conductivity at high fields. Equation (3.34) gives a high field conductivity which varies as  $\exp(\beta_F E^{1/2}/2 kT)$ . Models proposed by Johnscher<sup>[31]</sup> and by Mead<sup>[32]</sup> give field conductivities varying as  $\exp(\beta_F E^{1/2}/kT)$ ,

that is, with the exponents having an argument twice as large as that in Equation (3.34).

Let us consider the magnitude of field enhanced conductivity. For a material with  $\kappa = 3.5$  at  $T = 300^\circ\text{K}$ , the quantity  $\beta_F/2kT$  has the numerical value

$$\frac{\beta_F}{2kT} = 7.8 \times 10^{-4}$$

when fields are given in volts/meter, then

$$\sigma \approx \frac{1}{6} \sigma_0 \exp(7.8 \times 10^{-4} E^{1/2})$$

$$\approx 407 \sigma_0 \text{ for } E = 10^8 \text{ volts/meter.}$$

Such enhancement of the conductivity in kapton by fields in the megavolt/cm range are consistent with the measurements of Hoffmaster and Sellen. [33] For kapton, the nominal value of  $\sigma_0$  at  $T = 300^\circ\text{K}$  is of the order of  $10^{-15} - 10^{-16}$  mho/m.

At fields of order  $10^8$  volts/meter, the dielectric is able to support steady state currents in the range from a few hundredths to a few tenths of nanoamps/cm<sup>2</sup>. It is also interesting to observe that a dielectric relaxation time defined by

$$t = \frac{\kappa \epsilon_0}{\sigma}$$

is reduced from days to minutes in going from low fields to fields of one megavolt/cm. In Section 3.8, we will include field enhanced conductivity in the determination of the field structure in the interior of a dielectric.

### 3.8 KINETIC DESCRIPTION OF PROCESSES IN A DIELECTRIC

Numerous experiments over the years<sup>[34,35]</sup> have demonstrated that polymers such as teflon conduct small, but significant currents with applied fields of the order of  $10^5$  v/cm, and are capable of storing charge for long periods of time (days at low temperatures). Moreover, for high applied fields,  $>10^5$  v/cm, currents increase in a roughly linear manner on a Schottky ( $\log I$  versus  $V^{1/2}$ ) plot. These facts indicate the presence of a species of "free" carrier with some mobility,  $\mu$ , the presence of deep traps, and probably the existence of field assisted excitation of charge from trapped sites. Below, we construct one simple model which incorporates these important features of insulating materials used in space applications. For simplicity, we assume that electrons are the only carriers of electricity.

Our purpose here is to examine properties that are required to model the charge migration and field buildup in a dielectric. Such a description will allow

1. A better understanding of the material parameters influencing charge transport.
2. A basis for assessing the approximations of the simple phenomenological description of leakage currents given in the preceding section.

For the present, we consider bulk effects in the absence of radiation-induced effects.

The temporal evolution of the charge and field distribution in a dielectric is governed by Equation (3.30a) and

$$\frac{\partial \rho}{\partial t} = -\nabla \cdot \mathbf{j} \quad (3.36)$$

where  $\rho$  is the charge density and  $j$  the current density. To complete the description, we must relate the current density  $j$  to  $\rho$  and  $E$ .

The particle current density  $j_p$  (and electric current density  $j$ ) is the sum of the plasma electron current penetrating into the dielectric,  $j_b$ , and a drift current  $j_c = -n_c \mu E$

$$j = qj_p = q(j_b + j_c) \quad (3.37)$$

Here  $n_c$  is the density of free carriers and  $\mu$  their mobility. In addition, the capture and release of charge from traps is governed by<sup>[36]</sup>

$$\frac{\partial n_c}{\partial t} = -n_c \langle \sigma v \rangle [N_t - n_t] + \nu n_t - \nabla \cdot j_c \quad (3.38)$$

where  $\langle \sigma v \rangle$  is the capture rate,  $\nu$  is the trap release frequency,  $N_t$  is the trap density, and  $n_t$  is the density of occupied traps. For low fields, release from traps is thermally activated and

$$\nu = \nu_0 e^{-\frac{\Delta \epsilon}{\theta}} \quad (3.39)$$

where  $\Delta \epsilon$  is the depth of the trap measured from the "conduction band" and  $\theta$  the temperature in energy units. For the trap population, we have

$$\frac{\partial n_t}{\partial t} = n_c \langle \sigma v \rangle [N_t - n_t] - \nu n_t \quad (3.40)$$

The charge density given by

$$\rho = q(n_c + n_t - n_{c0} - n_{t0}) \quad (3.41)$$

where  $n_{c0}$  and  $n_{t0}$  are the thermal equilibrium values of free and trapped carrier density, satisfies Equation (3.36).

Typically,  $n_t$  in space insulating materials is substantially less than  $N_t$ , at least before the onset of dielectric breakdown. The density of free carriers is small compared with the trapped charge density, both in thermal equilibrium and for a dielectric containing a space charge, and the free time,  $\tau = [N_t \langle \sigma v \rangle]^{-1}$ , is short ( $\leq 10^{-9}$  sec) compared with the time scale of macroscopic variation. Then it is a good approximation to set  $\partial n_c / \partial t = 0$ . If additionally,  $\nabla \cdot j_c$  is neglected, one obtains a component of current of the form  $\rho \mu_{\text{eff}} E$ , but with a mobility  $\mu_{\text{eff}} \neq \mu$ . Although neglecting  $\nabla \cdot j_c$  in Equation (3.38) may not be a valid approximation for all conditions of interest, it is nonetheless useful to examine its consequences.

We find

$$\frac{n_c}{n_t} \approx v\tau = \frac{n_{c0}}{n_{t0}} \ll 1 \quad (3.42)$$

$$\rho \approx q(n_t - n_{t0}) \quad (3.43)$$

$$\begin{aligned} j &= qj_p = qn_c \mu E = qn_c^0 \mu E + \rho(\mu v \tau) E \\ &= \sigma_0 E + \rho \mu_{\text{eff}} E . \end{aligned} \quad (3.44)$$

Thus, transport of excess charge is proportional to the net charge density, but with a trap modulated mobility

$$\mu_{\text{eff}} = (\mu v \tau) \ll \mu , \quad (3.45)$$

a quantity frequently appearing in the literature on charge storage, and the object of many experimental observations. Gross, et al., [37] have used Equation (3.44) in the analysis of experiments on the transport of charge injected into a dielectric. In the context of modeling the electrical behavior of insulators in the space environment, it is important that we understand the significance of the experimentally observed mobilities.

The preceding theory also permits treating field enhanced thermal activation of occupied traps. Assuming that trapped sites are neutral when occupied and invoking a Poole-Frenkel ionization mechanism, [38] the required modification consists in replacing  $v_0$  by  $v_0 e^{\alpha E^{1/2}}$  where the coefficient  $\alpha$  is related to the dielectric constant and temperature of the medium. Provided that space charge effects are not pronounced, this leads to the frequently observed linear relationship between  $\ln(J)$  and  $E^{1/2}$  at high fields.

The theory, as elaborated so far, does not admit the effects of conductivity induced by electron or solar irradiation. Typically, under constant irradiation with a dose rate  $\dot{D}$ , the material acquires a steady state conductivity following Fowler's law [39]

$$\sigma = k(\dot{D}/\dot{D}_0)^\Delta \tag{3.46}$$

where  $\dot{D}_0$  is a reference dose rate, usually taken as 1 rad/sec, and  $\Delta$  is a material parameter with values between 0.5 and 1 depending on the energy level distribution of traps in the material. A simple model with a single trapping level is not expected to be a good model for radiation-induced conductivity (RIC). Nevertheless, RIC can be simulated by adding to Equation (3.38) and subtracting from Equation (3.40) a term  $Rn_t$ , where  $R$  determines the rate of trap ionization by the impressed

radiation field. The effect of RIC on field structure within the dielectric is determined in this manner in Section 3.10.

To place the foregoing considerations into the context of the entire spacecraft charging model, it is important to have some notion of the relative time scales involved in the problem. The important characteristic times for the dielectric are  $\tau$  and  $l/v$ , as previously defined, the dielectric relaxation time

$$t_d = \frac{\epsilon}{\sigma}, \quad (3.47)$$

where  $\sigma$  is the conductivity, and the transit time  $t_{tr}$  across the thickness of dielectric. These times should be compared with body charging time  $t_c$ ; for an initially uncharged body of dimension  $R$ , the latter time scale is estimated by

$$4\pi R^2 j t_c = C\theta \quad (3.48)$$

where  $j$  is the one-sided plasma electron current density,  $\theta$  is the plasma temperature in volts and  $C$  the capacitance relative to the zero of potential. For  $R$  of order one meter, ( $C \sim 10^{-10}$  farad),  $j \sim 10^{-5}$  amps/m<sup>2</sup>,  $\theta \sim 10^3$  volts,

$$t_c \approx 10^{-3} \text{ sec.}$$

Dielectric relaxation times for good insulators are much longer than this, even for levels of conductivity that may be induced by the radiation levels at geosynchronous altitudes. The trap residence time is highly variable, depending on temperature and field strength, and can be larger or smaller than  $t_c$ . Transit times are very long,

$$t_{tr} \approx L/\mu_{eff} E ;$$

for a thickness  $L \sim 10^{-2}$  cm, a trap modulated mobility  $\mu_{\text{eff}} \sim 10^{-10}$  cm<sup>2</sup>/volt-sec and a field strength  $E \sim 10^5$  v/cm,

$$t_{\text{tr}} = 10^3 \text{ sec} .$$

The carrier free time  $\tau_f$  is much shorter than  $t_c$ , so that the free carrier concentration relaxes instantaneously to a quasi-steady value  $\partial n_c / \partial t \approx 0$ .

The important consequence of the foregoing considerations is that while the body charges to a quasi-equilibrium characterized by a vanishing net current in the space around the body, charges in the dielectric hardly move at all. This suggests that the problem of spacecraft charging separates into two rather distinct parts; one being the overall charging equilibrium, followed by redistribution of charges on the body.

Before attempting numerical calculations based on the carrier kinetics, it is worthwhile to relate the kinetic description to the simple model described in Section 3.7. First we observe that at low fields and in the absence of buildup of excess charge,  $n_c$  and  $n_t$  have their thermal equilibrium values  $n_{c0}$  and  $n_{t0}$ , respectively, which are related by

$$n_{c0} \langle \sigma v \rangle [N_t - n_{t0}] = v n_{t0} ,$$

with a dark conduction current

$$j_0 = n_{c0} \mu q E .$$

Thus experimental knowledge of the dark conductivity

$$\sigma_0 = n_{c0} \mu_0 e$$

constrains the product  $n_{CO} \mu_O$ . Field enhanced conductivity is introduced by allowing the trap ionization rate coefficient  $\nu$  to depend on the electric field. The Adamec and Caldwood model of Section 3.7 may be obtained by replacing  $\nu_O$  in Equation (3.39) by

$$\frac{\nu_O}{3} [2 + \cosh(\beta_F E^{1/2}/2 kT)] .$$

### 3.9 ONE-DIMENSIONAL MODEL FOR DIELECTRIC EFFECTS IN A CHARGING ENVIRONMENT

Calculations have been performed on the charging of a one-dimensional system consisting of a conductor coated with a thin layer of dielectric. The problem geometry is schematized in Figure 3.10. The conductor is assumed negligibly thick.

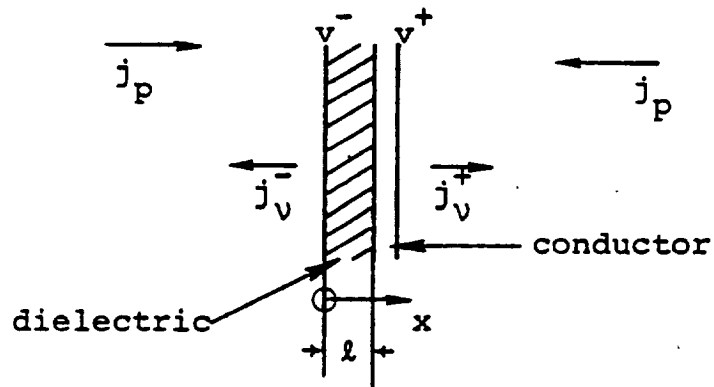


Figure 3.10

Here,  $j_p$  is the undisturbed plasma current, part of which is reflected if the surface potentials  $V^-$  or  $V^+$  are negative; in that case, the current incident on the dielectric surface is

$$j^- = j_p e^{-\frac{V^-}{\theta_p}}$$

where  $\theta_p$  is the temperature of the assumed Maxwellian plasma. A similar result applies for the current incident on the conductor. The photo-currents emitted by the dielectric and conductor are denoted by  $j_v^-$  and  $j_v^+$ , respectively. Secondary emission caused by impact of a single electron is represented

by  $\delta^\pm$ . Here no attempt is made to account for the energy dependence of  $\delta^\pm$ , even though it would not be difficult to do so.

The total particle currents incident on the slab are

$$j_p^- = j_p f\left(\frac{v^-}{\theta_p}\right) + \left[ j_v^- + \delta^- j_p f\left(\frac{v^-}{\theta_p}\right) \right] f\left(-\frac{v^-}{\theta_e}\right), \quad x < 0$$

$$j_p^+ = -j_p f\left(\frac{v^+}{\theta_p}\right) + \left[ j_v^+ + \delta^+ j_p f\left(\frac{v^+}{\theta_p}\right) \right] f\left(-\frac{v^+}{\theta_e}\right), \quad x > l \quad (3.49)$$

where  $\theta_e$  is the "temperature" of the emitted electrons, and

$$f(y) = 1, \quad y \geq 0$$

$$= \exp(y), \quad y < 0.$$

In addition to the kinetic equations describing charge transport in the dielectric, we have (by differentiating Equation (3.30a) with respect to  $t$  and integrating with respect to  $x$ )

$$\epsilon \frac{\partial E}{\partial t}(x, t) + qj(x, t) = J(t) \quad (3.50)$$

with

$$q = -1.6 \times 10^{-19} \text{ coulomb}$$

$$j(x, t) = j_p^- \quad x < 0$$

$$= j_p^+ \quad x > l \quad (3.51)$$

$$= j_d(x, t) = j_b(x, t) + j_c(x, t) \quad 0 \leq x \leq l$$

where  $j_b$  is the current of plasma electrons penetrating into the dielectric,  $j_c$  is the dielectric particle current, and

$J(t)$  is an integration constant. In the plasma, we neglect space charge so that if the plasma "ground planes" are at  $x = -D$  and  $x = D + \ell$ , then the space fields are independent of position:

$$\begin{aligned} E(x,t) = E^- &= -\frac{V^-}{D} & x < 0 \\ E(x,t) = E^+ &= \frac{V^+}{D} & x > \ell . \end{aligned} \tag{3.52}$$

Integrating Equation (3.50) over space from  $x = -D$  to  $x = D + \ell$ , using the boundary condition  $V = 0$  on the plasma ground planes, gives

$$J = q \left( 2D + \frac{\ell}{\kappa} \right)^{-1} \left[ D(j_p^+ + j_p^-) + \frac{1}{\kappa} \int_0^{\ell} j_d(x,t) dx \right] \tag{3.53}$$

where  $\kappa = \epsilon/\epsilon_0$  is the relative dielectric constant of the material.

The body charging time  $t_c$  discussed earlier is in general very short in relation to the time scale for development of potential differences across the thickness of dielectric. In the present circumstances  $t_c$  is determined by the capacitance per unit area of the dielectric metal slab relative to the plasma and is proportional to  $1/D$ . If the time  $t$  elapsed after commencement of charging is much greater than  $t_c$ , then we expect that the plasma electric field will vary slowly, so that it is a good approximation to neglect the vacuum displacement currents  $\epsilon_0 \partial E/\partial t$  in Equation (3.50), and obtain from Equations (3.49) - (3.50) algebraic relations between the surface voltages  $V^\pm$  and the circuit current  $J$ . Thus, for example, if  $V^\pm < 0$ ,

$$v^+ = \theta_p \ln \frac{j_v^+ - J/q}{j_p(1-\delta^+)} \quad (3.54)$$

$$\frac{\partial v^+}{\partial t} = \frac{\theta_p}{J - qj_v^+} \frac{\partial J}{\partial t} \quad (3.55)$$

and

$$\frac{\partial v^-}{\partial t} = \frac{\theta_p}{J + qj_v^-} \frac{\partial J}{\partial t} \quad (3.56)$$

Now, integrating Equation (3.50) over the dielectric gives

$$\frac{\partial}{\partial t} (v^- - v^+) = \frac{1}{\epsilon} \left[ J\ell - \int_0^\ell j_d(x,t) dx \right] \quad (3.57)$$

or, using Equations (3.55) - (3.56),

$$\frac{\partial J}{\partial t} = - \frac{\ell}{\epsilon \theta_p} \frac{[J - q\bar{j}_d][J + qj_v^-][J - qj_v^+]}{q(j_v^+ + j_v^-)} \quad (3.58)$$

where

$$\bar{j}_d = \frac{1}{\ell} \int_0^\ell j_d(x,t) dx \quad (3.59)$$

Equation (3.57) shows that a steady state for the system occurs when  $J/q = \bar{j}_d$ . Equation (3.58) shows that, if  $|J| \ll |qj_v^\pm| \sim qj_v$  this steady state is approached with a time constant

$$t_d = \frac{\epsilon \theta_p}{\lambda q j_v} \quad (3.60)$$

This is the time constant associated with development of a potential difference across a dielectric. With  $\epsilon = 3 \times 10^{-11}$  farad/meter,  $\theta_p \sim 10^4$  volts,  $q j_v \sim 10^{-5}$  amp/meter<sup>2</sup>, and  $\lambda = 10^{-4}$  meters

$$t_d \approx 300 \text{ sec.}$$

Such differential charging time scales enter together with the time constants associated with the kinetics of the charge carriers in the determination of the electric fields within the dielectric medium.

A further useful relation is obtained by using the field equations to eliminate  $j_p^+$  and  $j_p^-$  from Equation (3.53);

$$J = - \frac{\kappa \epsilon_0}{\lambda} \frac{\partial}{\partial t} (V^+ - V^-) + q \bar{j}_d \quad (3.61)$$

The field in the dielectric then satisfies

$$\epsilon \frac{\partial E}{\partial t} = q(j_d - \bar{j}_d) - \frac{\kappa \epsilon_0}{\lambda} \frac{\partial}{\partial t} (V^+ - V^-) \quad (3.62)$$

### 3.10 NUMERICAL METHODS FOR ONE-DIMENSIONAL DIELECTRIC CALCULATIONS

#### 3.10.1 Methods

The results of numerical calculations reported in this section are obtained from difference approximations to equations developed in the preceding two sections. The difference equations will not be displayed, but we will discuss briefly means for efficiently obtaining solutions through several minutes of charging time. The basic limitations on a practical numerical scheme are imposed by the large disparity between the various time scales that occur in the defining equations; the potentially most stringent limitation is associated with the drift current in Equation (3.38). The code used to perform these calculations has not been incorporated into NASCAP, but has been delivered separately to NASA/LeRC.

Equations (3.36), (3.38) and (3.41) are taken as defining equations in the dielectric. In Equation (3.38) however we neglect  $\partial j_c / \partial x$ , which in the examples to be considered is small in comparison with the remaining terms on the right hand side of the equation. One extremely useful consequence of this approximation is that it permits a substantially larger time step in the numerical scheme than would otherwise be possible.

The algorithm for the particle conduction current at the grid point  $k$  ( $x = k\Delta x$ ) is

$$j_c(k) = \frac{1}{2} \mu E(k) (n_c(k+1) + n_c(k)) - \frac{1}{2} \mu |E(k)| [n_c(k+1) - n_c(k)] \quad . \quad (3.63)$$

If  $n_c$  and  $E$  are staggered on a uniform spatial grid, this algorithm is first order accurate in  $\Delta x$ ; without the term proportional to  $|E(k)|$  it would be second order accurate. The latter term, together with a Courant restriction on the time step, which is required for stability, assures that the difference equations maintain the particle densities as positive quantities. If the term  $\partial j_c / \partial x$  were retained in Equation (3.38), the condition

$$\Delta t < \Delta t_1 = \frac{1}{2} \frac{\Delta x}{\mu E}$$

would be sufficient for stability. Neglecting  $\partial j_c / \partial x$ , the sufficiency condition is relaxed to

$$\Delta t \lesssim \Delta t_2 = \frac{1}{2} \frac{\Delta x}{\mu_{\text{eff}} E} .$$

Using  $\mu = 10^{-3} \text{ cm}^2/\text{volt sec}$ ,  $\mu_{\text{eff}} = 10^{-10} \text{ cm}^2/\text{volt sec}$ ,  $\Delta x = 2 \times 10^{-3} \text{ cm}$  and  $E = 10^5 \text{ volts/cm}$ , gives

$$\Delta t_1 = 10^{-5} \text{ sec}$$

$$\Delta t_2 = 10^2 \text{ sec} .$$

A time step limitation as small as  $\Delta t_1$  would be impractical for calculations which extend over several minutes of charging time.

Other time step limitations which could occur in an explicit time-differencing scheme are for all practical purposes removed with an implicit scheme. For example, the time scale

$$t_\sigma = N_t \langle \sigma v \rangle$$

does not limit the stability of the difference scheme when the first term in the difference analogue of Equation (3.38) is evaluated at the advanced time.

### 3.10.2 Results

Three sets of calculations were performed with the following parameters

$$D = 10 \text{ cm}$$

$$l = 10^{-2} \text{ cm}$$

$$j_p = 10^{-10} \text{ amp/cm}^2$$

$$j_v^+ = 0.75 \times 10^{-10} \text{ amp/cm}^2$$

$$j_v^- = 0.50 \times 10^{-10} \text{ amp/cm}^2$$

$$\delta^- = 0.1$$

$$\delta^+ = 0$$

$$N_T = 10^{18} \text{ cm}^{-3}$$

$$\theta_p = 10^4 \text{ volts}$$

$$\theta_e = 2 \text{ volts}$$

$$\kappa = 2$$

The dielectric was divided into 50 spatial zones, each having  $\Delta x = 2 \times 10^{-4}$  cm. The beam current profile within the dielectric was assumed to be linear, dropping to zero in a distance of  $10^{-3}$  cm.

The three cases considered were (1) a passive dielectric, (2) a dielectric with natural and field enhanced conductivity, and (3) a dielectric identical to that in Case 2 but having in addition a radiation induced conductivity in the deposition zone.

In the passive dielectric, charge deposited in trapping sites remains in the deposition layer, giving a

charge density profile which is spatially uniform in the deposition zone, and which vanishes beyond.

The additional parameters required to define Case 2 are

$$\mu = 10^{-4} \text{ cm}^2/\text{volt sec}$$

$$v = 3 \times 10^3 \text{ sec}^{-1}$$

$$\langle \sigma v \rangle = 10^{-9} \text{ cm}^3 \text{ sec}^{-1}$$

$$\beta = .021 \text{ cm}^{1/2}/(\text{volt})^{1/2}$$

$$n_{co} = 6.25 \times 10^4 \text{ cm}^{-3}$$

$$n_{to} = 2.083 \times 10^{11} \text{ cm}^{-3}$$

corresponding to a dark conductivity

$$\sigma_o = n_{co} \mu E = 10^{-18} \text{ mho/cm}$$

and an effective mobility

$$\mu_{\text{eff}} = \frac{v}{N_T \langle \sigma v \rangle} \mu = 3 \times 10^{-10} \text{ cm}^2/\text{volt sec.}$$

Case 3 is identical to Case 2 except for addition of a "radiation induced conductivity" in the deposition zone. The ionization rate ( $\text{cm}^{-3} \text{ sec}^{-1}$ ) is taken to be

$$10^{-3} j_b(x,t) n_t(x,t)$$

where  $j_b$  is electron flux ( $\text{cm}^{-2} \text{ sec}^{-1}$ ) and  $n_t$  ( $\text{cm}^{-3}$ ) is the density of occupied traps. The induced conductivity when  $qj_b \approx 10^{-10} \text{ amps/cm}^2$ ,  $n_t = 2 \times 10^{11} \text{ cm}^{-3}$  is approximately  $\sigma_r \approx 2 \times 10^{-15} \text{ mho/cm}$ .

The surface potentials  $V^-$  and  $V^+$  as a function of time, plotted in Figure 3.11, are very nearly equal for all

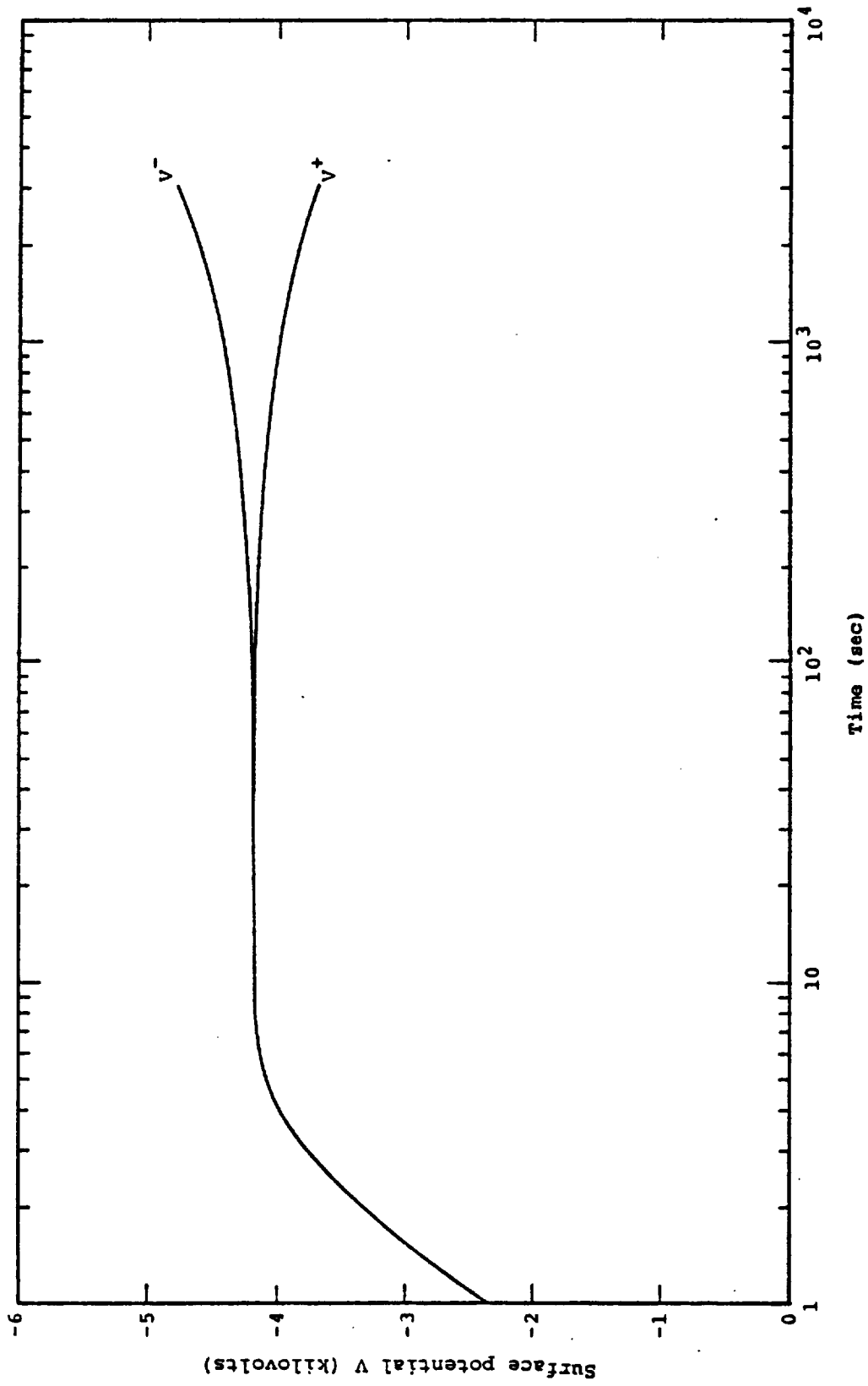


Figure 3.11. Surface potentials versus time.

three cases for  $t \leq 230$  sec, the maximum time for which Cases 2 and 3 were run. The small differences between the dielectric potential drop in the three cases is illustrated by Figure 3.12. There does however appear a trend toward a departure from Case 1 for times larger than a few hundred seconds. That this might be expected is indicated by comparing the electric field and charge density profiles given in Figures 3.13 and 3.14, respectively. The latter figure for Cases 2 and 3 shows a substantial charge migration away from the region of deposition.

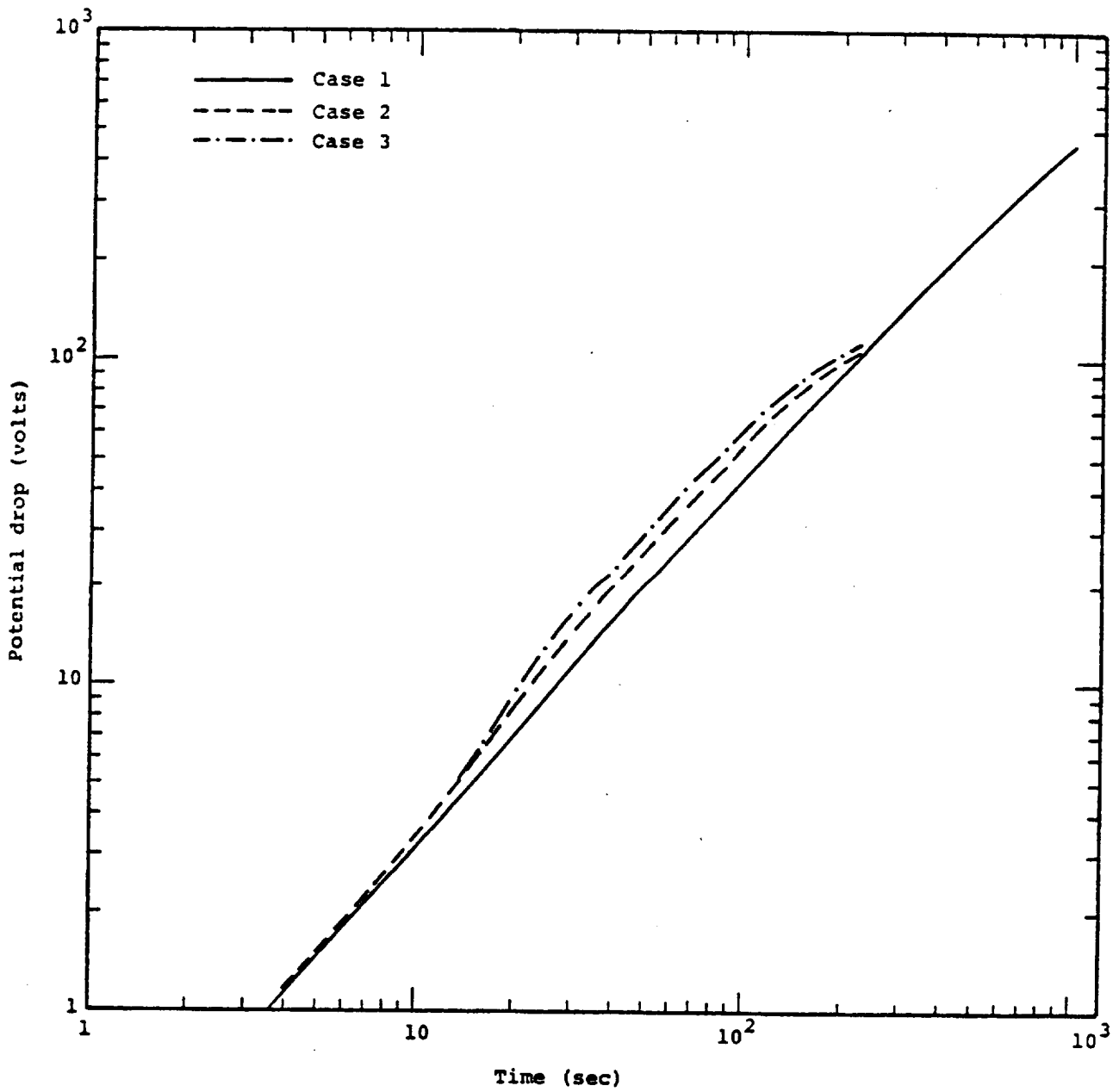


Figure 3.12. Dielectric potential difference ( $V^+ - V^-$ ) versus time.

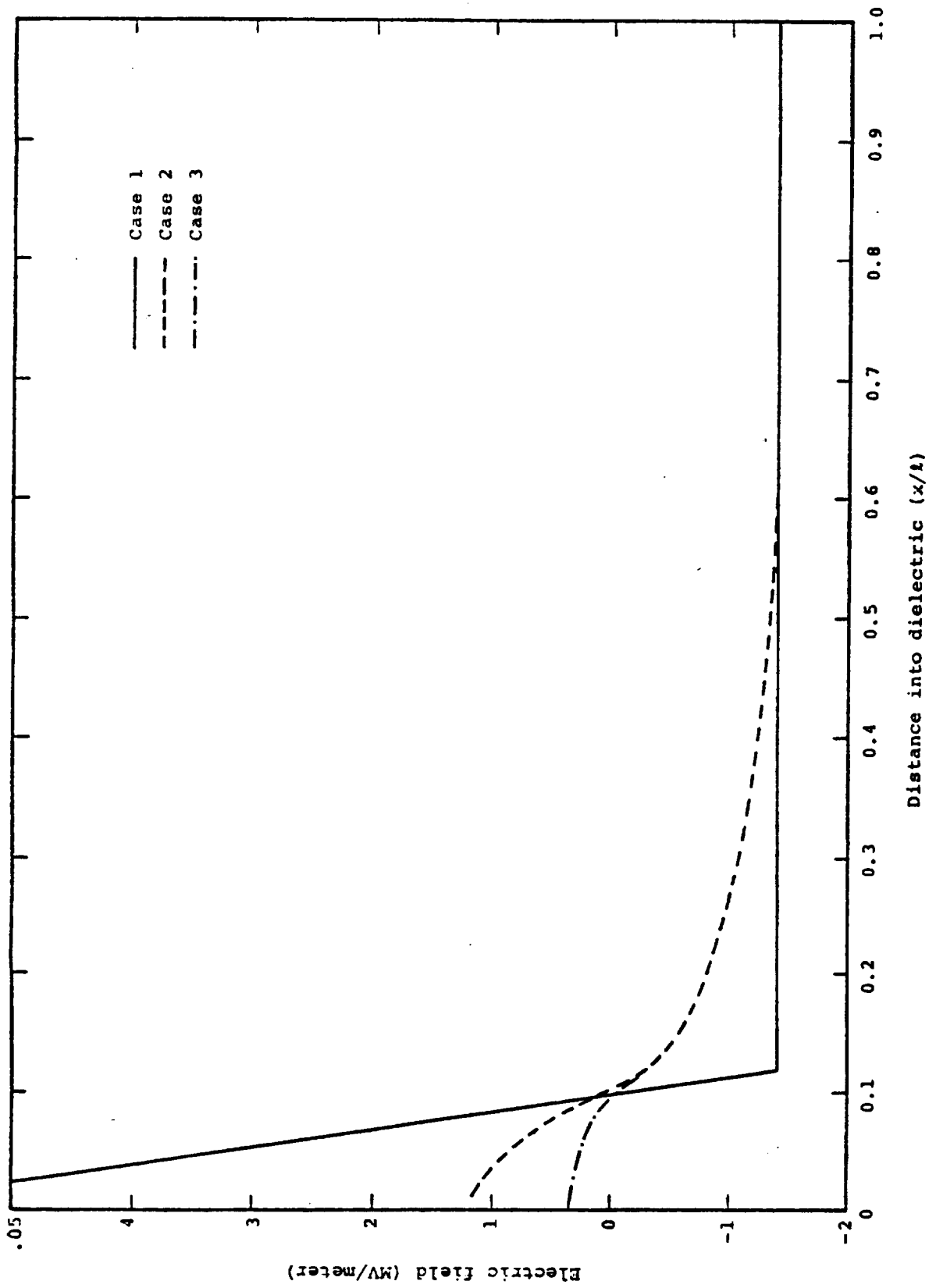


Figure 3.13. Electric field versus distance at 210 sec.

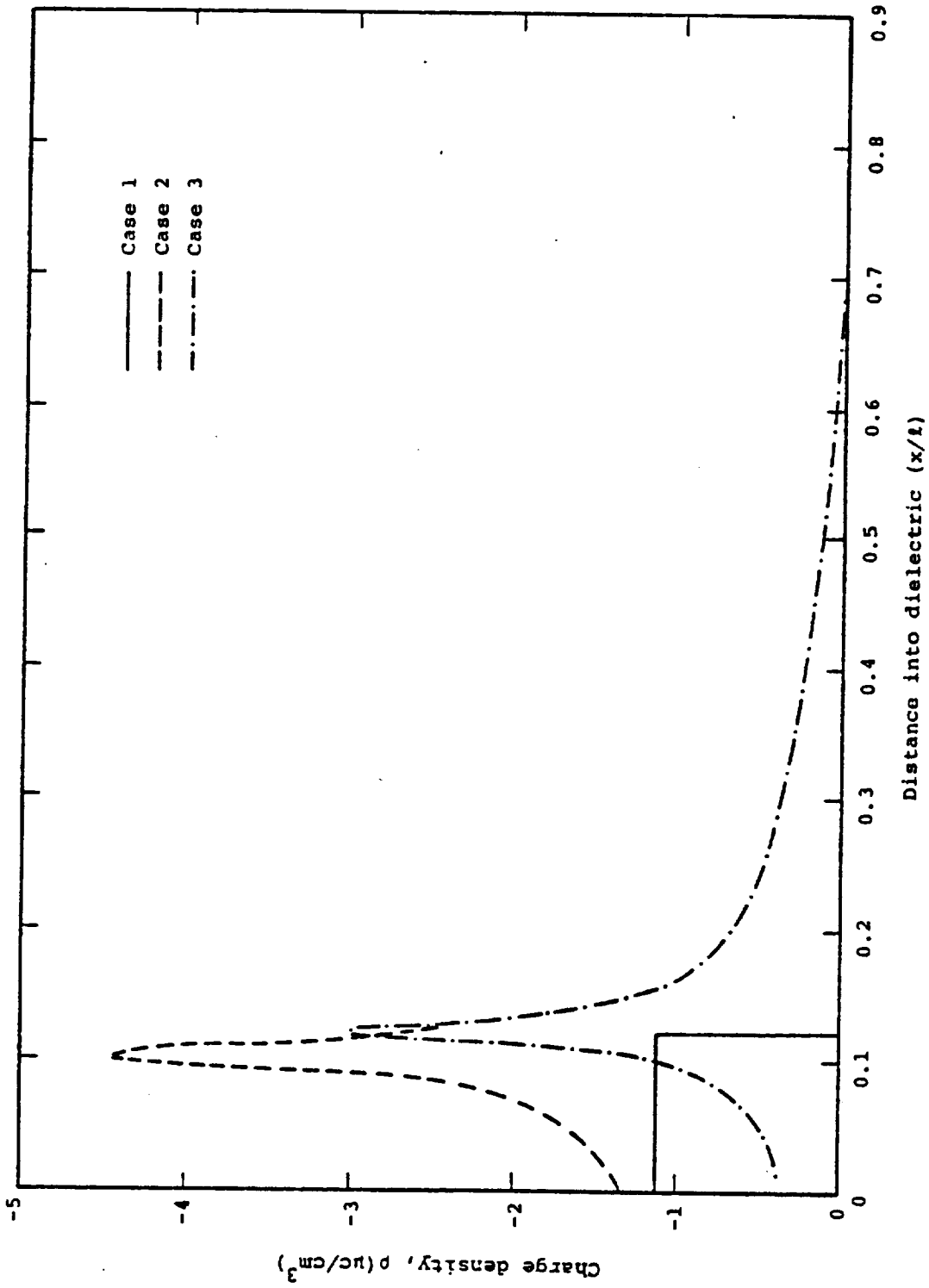


Figure 3.14. Charge density versus distance at 210 sec.

#### 4. TEST CASES FOR THE NASCAP CODE

For the purposes of illustrating, error-checking and verifying the NASCAP code, test cases were run in all three NASCAP operating modes (see Table 4.1). The first sequence of problems were designed to simulate the electrostatic charging of material samples in a laboratory test facility. These ground test model test cases were done with one inch resolution in a computational space with dimensions in rough correspondence with those of the LeRC facility. An electron beam profile similar to one measured at LeRC was used. The last sequence of problems were designed to simulate the charging of an object in a plasma with parameters similar to those found in the earth's magnetosphere. These space model test cases, with two exceptions, were spheres in isotropic environments. The material properties were those suggested in the NASCAP User's Manual.

##### 4.1 GROUND TEST - FLOATING ALUMINUM PLATE

This set of test cases were entirely successful. No problems were encountered concerning length of time step, and, because the potential scales with total charge, repeated potential calculations were not required. The computer costs involved were quite modest.

The electron gun emitted a current of  $0.37 \mu\text{A}$  and had a profile similar to that supplied to  $S^3$  by NASA-LeRC (see Figure 4.1d). The peak flux was slightly greater than  $1.0 \text{ nA/cm}^2$ . The sample was a 6 inch by 8 inch plate, 1 inch thick, located 40 inches from the electron source. A magnetic field comparable to the earth's field ( $B_x = 0$ ,  $B_y = 0.52$  gauss,  $B_z = -0.19$  gauss, where y is vertical and z is the beam propagation direction) was assumed present. Simulations were carried out for beam energies of 2, 5, 8 and 20 keV.

Table 4.1. NASCAP Test Cases

<u>Operating Mode</u>	<u>Object</u>	<u>Environment</u>
1. Ground Test	6" x 8" aluminum plate; floating	a. 2 keV electron beam b. 5 keV c. 8 keV d. 20 keV
2. Ground Test	6" x 8" teflon-coated aluminum plate; grounded	a. 10 keV electron beam b. 20 keV
3. Ground Test	14" x 14" grounded aluminum plate with 4 material samples (SSPM)	a. 2 keV electron beam b. 5 keV c. 8 keV d. 10 keV e. 20 keV
4. a. Maxwell Probe	3 meter aluminum sphere	a. Plasma with different electron and ion temperatures: $\theta_e = 4.1 \text{ keV}; \theta_i = 430 \text{ eV}$
b. Reverse Trajectory		b. Same as (a).
c. Reverse Trajectory		c. Anisotropic flux from ATS-5 data
5. Maxwell Probe	a. Teflon-coated sphere b. Kapton-coated sphere	Same as 4a.
6. a. Reverse Trajectory	3-meter teflon-coated sphere	a. From ATS-5 data
b. Reverse Trajectory		b. Same as 4a.
7. Maxwell Probe	3-meter teflon-coated sphere	Isotropic sunlight
8. Maxwell Probe	SSPM (as in (3) above) with aluminum plate fixed at -575 volts	Same as 4a above.

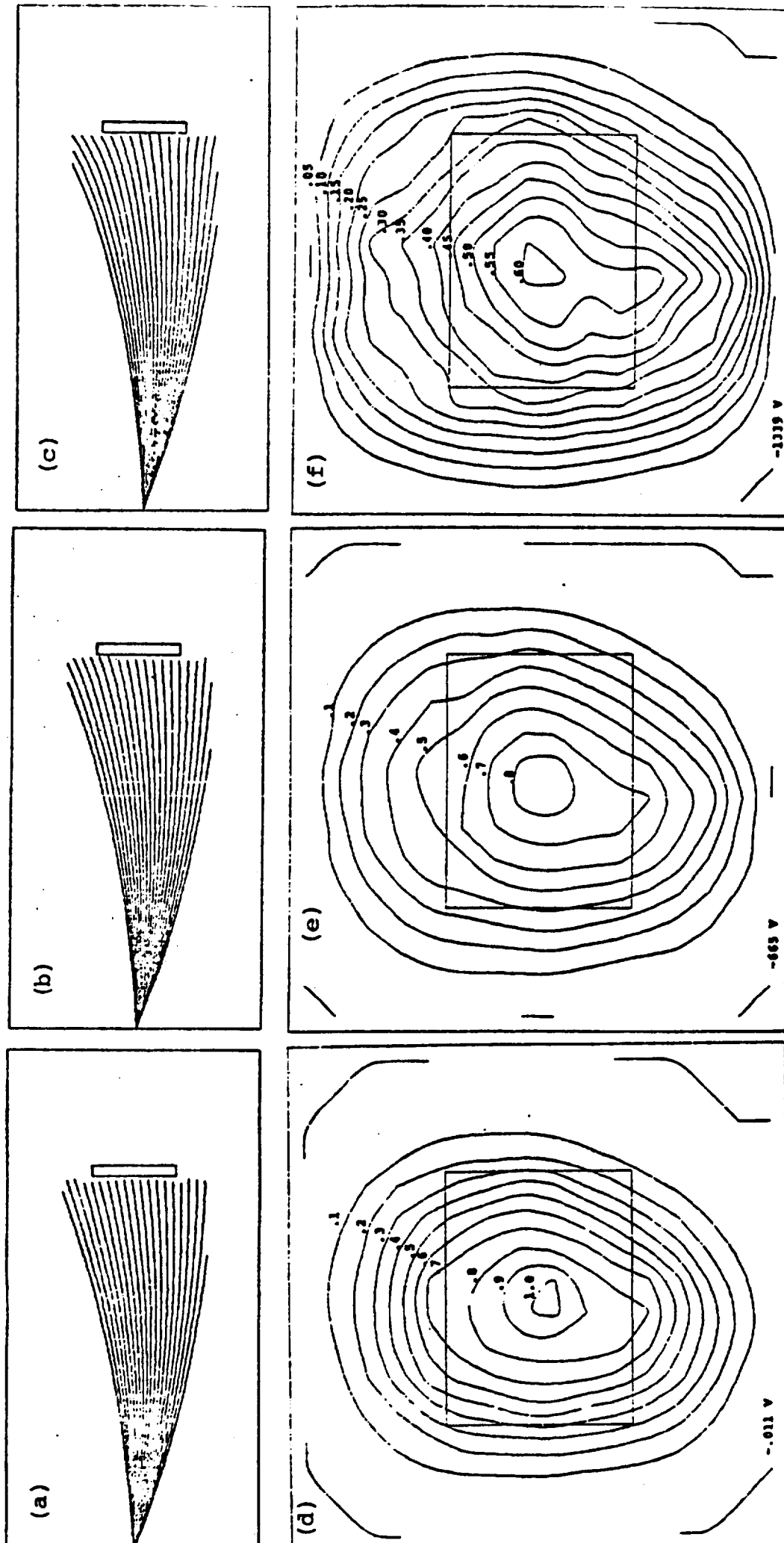


Figure 4.1A. Particle trajectory plots (a-c) and current density contour plots (d-f) for uncharged (a,d), partially charged (b,e) and fully charged (c,f) aluminum plate subject to 2 keV electron beam. The numbers indicate current densities in nA/cm<sup>2</sup>.

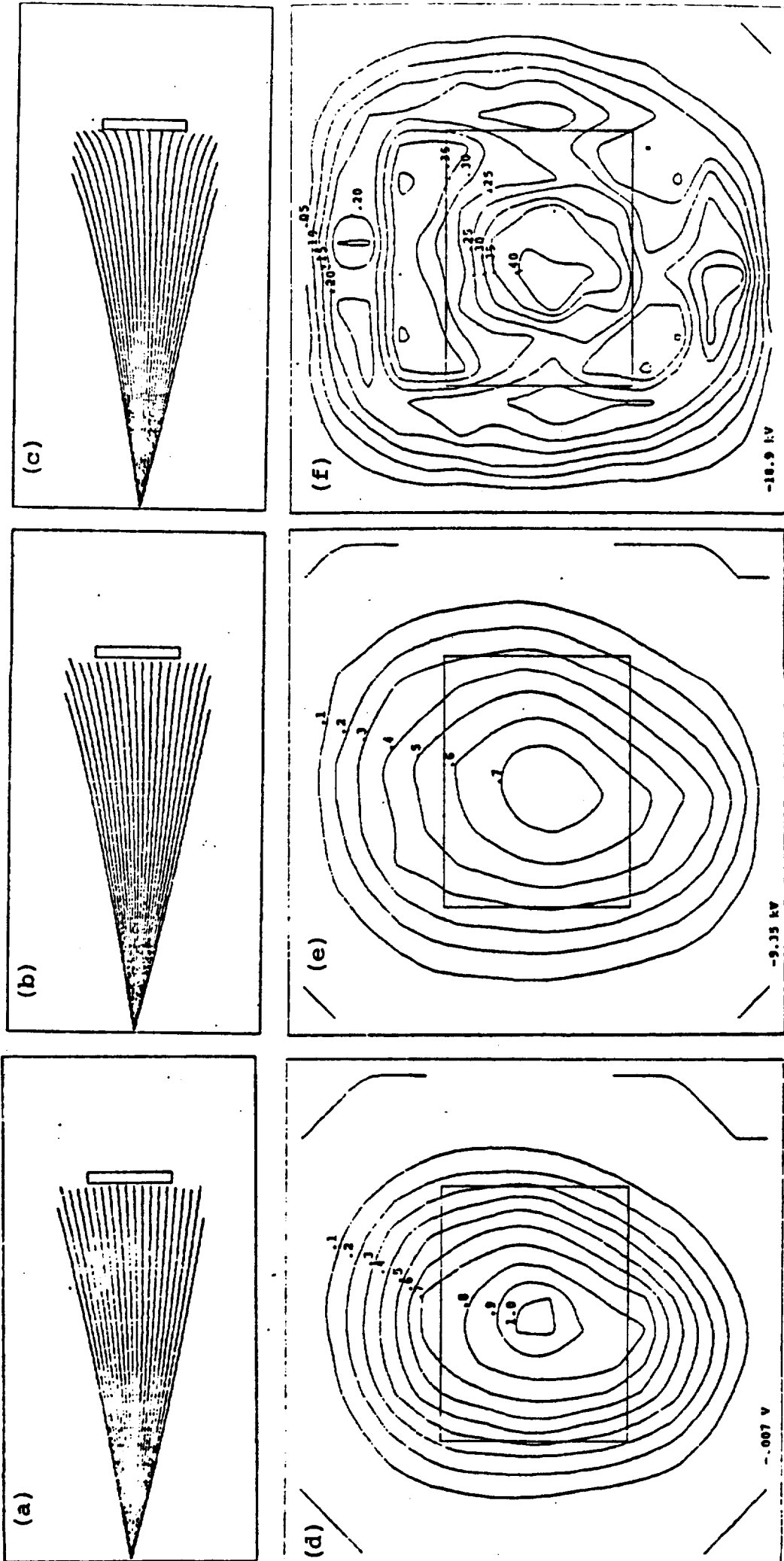


Figure 4.1B. Particle trajectory plots (a-c) and current density contour plots (d-f) for uncharged (a,d), partially charged (b,e) and fully charged (c,f) aluminum plate subject to 20 keV electron beam. The numbers indicate current densities in nA/cm<sup>2</sup>.

The simulation proceeds at each cycle by first tracking particles forward in the tank (Figure 4.1a-c) and thus determine the current density and incident angle at the sample (Figure 4.1d-f). The curvature due to magnetic field is apparent at the low energies. The charge on the plate is adjusted in accordance with the net current, the potentials scaled accordingly, and the next cycle is begun.

For each beam energy the plate charged to its final value in a time roughly proportional to the beam voltage (Figure 4.2). The difference between the beam voltage and the final plate potential increased somewhat with increasing energy. Final current balance was achieved by a decrease in incident current to about half its uncharged value, and a substantial increase in secondary emission ratio, attributable in part to non-normal incidence. Decrease in incident electron flux was more important at higher energies (Figure 4.2, Table 4.2).

#### 4.2 GROUND TEST - TEFLON COATED PLATE

Another sequence of ground tests was performed with a 5 mil teflon coating on a grounded aluminum plate. The beam characteristics, experimental geometry, and magnetic field were identical to the previous case. Since simple potential scaling is not appropriate, 10-30 potential iterations were performed each cycle following use of the "DSCALE" option.

This case differs from the previous in that (1) because the charging is across a larger capacitance the time scale is  $\sim 10^2$  times as long, and (2) the potential varies with position on the insulating teflon surface. The results are given in Table 4.3 and Figures 4.3 and 4.4. The central area of the sample charged to  $-1.8 \times 10^4$  volts for the 20 keV beam, and  $-7.8 \times 10^3$  volts for the 10 keV beam. In both cases the periphery of the sample initially charged at about half the

Table 4.2. Results for the Aluminum Plate Ground Test Case

Beam Energy		Time	Potential (volts)	Incident Flux (nA/cm <sup>2</sup> )	Backscatter (nA/cm <sup>2</sup> )	Secondary (nA/cm <sup>2</sup> )
2 keV	Initial		0	0.81	0.17	0.31
	Final		-1353	0.41	0.08	0.31
5 keV	Initial		0	0.81	0.14	0.18
	Final		-4266	0.45	0.10	0.33
8 keV	Initial		0	0.81	0.13	0.14
	Final		-7173	0.39	0.10	0.28
20 keV	Initial		0	0.81	0.11	0.08
	Final		-18,940	0.23	0.08	0.18

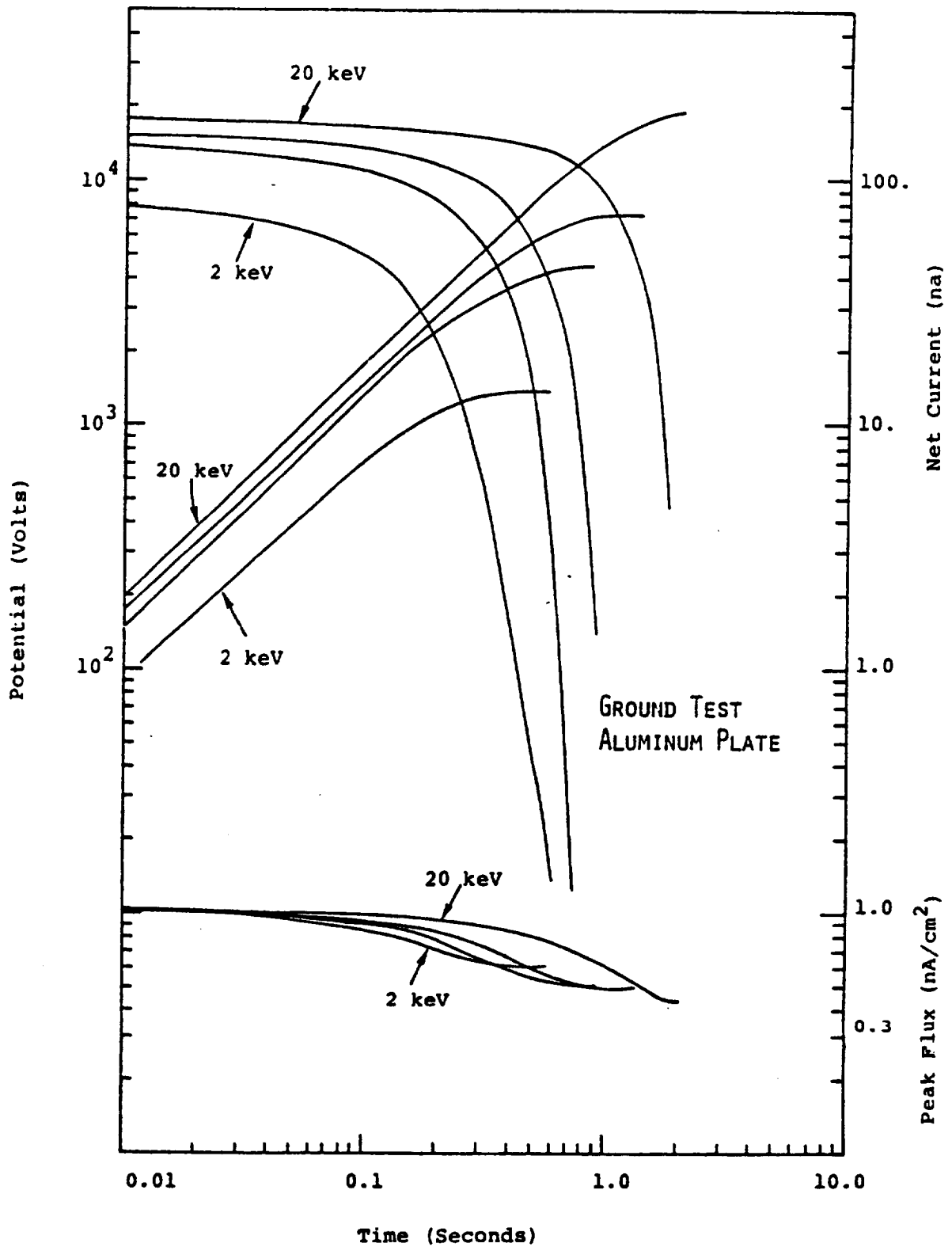


Figure 4.2. Peak incident flux (lower curves), net current (upper decreasing curves), and potential (increasing curves) versus time for an aluminum plate subject to an electron gun with energy 2, 5, 8, 20 keV.

Table 4.3. Current Balance for the Teflon Plate Tank Test

<u>Beam Energy</u>	<u>Time</u>	<u>Potential (volts)</u>	<u>Incident Flux (nA/cm<sup>2</sup>)</u>	<u>Backscatter (nA/cm<sup>2</sup>)</u>	<u>Secondary (nA/cm<sup>2</sup>)</u>
10 keV (cell 55)	Initial	0	1.02	0.12	0.30
	Final	-7757	0.51	0.09	0.43
20 keV (cell 9)	Initial	0	0.81	0.09	0.15
	Final	-15,790	0.46	0.09	0.29

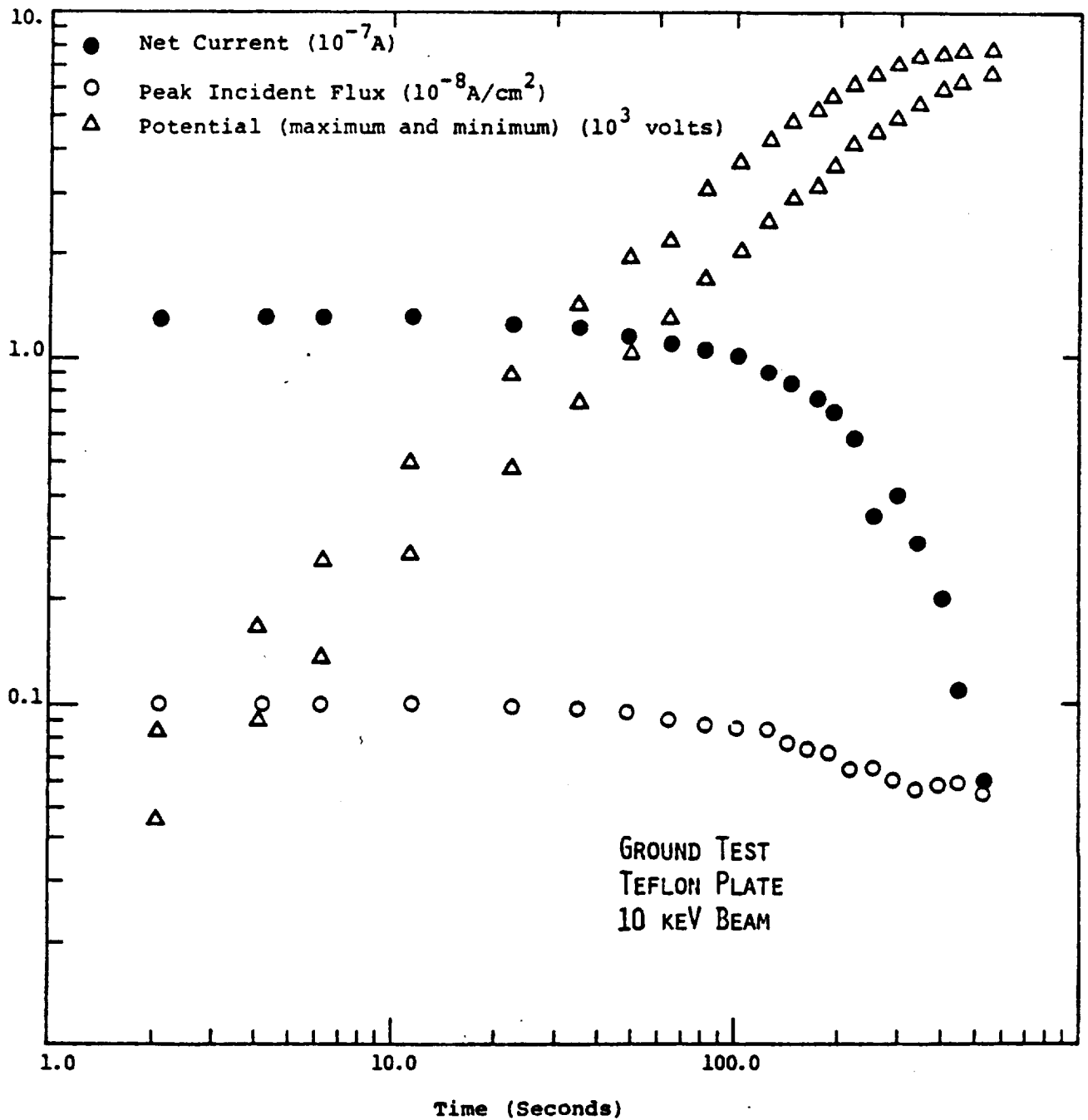


Figure 4.3. Time development of potentials, net current, and peak incident flux for a 5 mil teflon coated plate subject to a 10 keV electron beam.

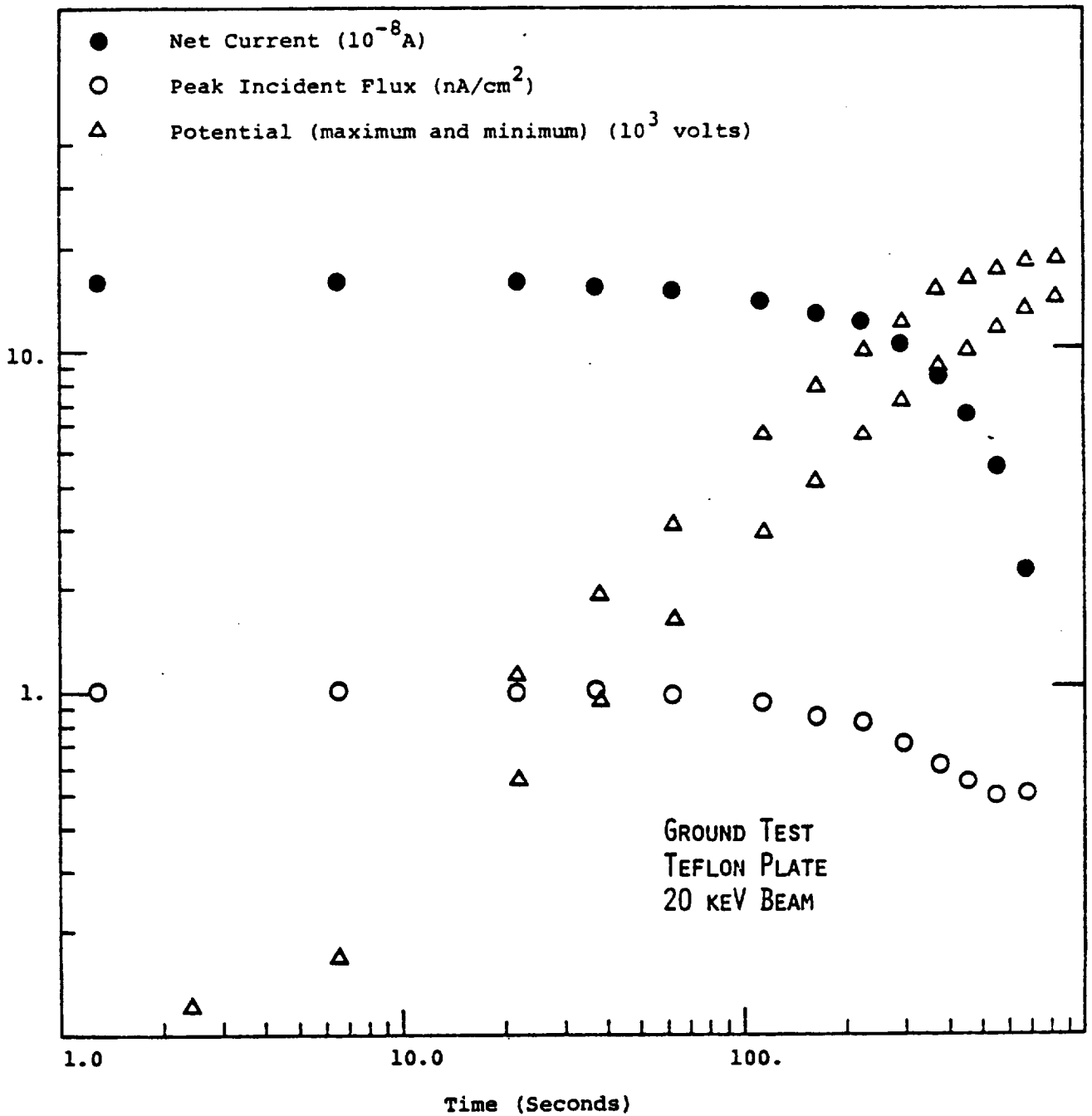


Figure 4.4. Time development of potentials, net current, and peak incident flux for a 5 mil teflon coated plate subject to a 20 keV electron beam.

rate of the center, and tended to catch up later in the simulation. The incident current was reduced to about half its initial value at the end of both simulations. Space potential contours at the end of the 10 keV simulation are shown in Figure 4.5.

#### 4.3 GROUND TEST - SSPM

The final set of ground test cases exposed to the electron beam a complex object (Figure 4.6) resembling the Spacecraft Surface Potential Monitor (Experiment SC1) scheduled to be flown on the SCATHA satellite. The object consisted of a 14 inch x 14 inch x 1 inch aluminum plate with four 5 inch x 5 inch material samples: teflon, kapton,  $\text{SiO}_2$ , and clean magnesium. The properties of these surfaces were those suggested in the NASCAP User's Manual. The insulators were 5 mils thick, and the magnesium sample was mounted on an insulating spacer with a capacitance of 347 pf. These test cases were run in similar fashion to the teflon plate cases, except that a wider beam profile was used, and the beam current was increased to 0.84  $\mu\text{A}$  to maintain a 1.0  $\text{nA}/\text{cm}^2$  flux at the beam center (Figure 4.7). The potentials and fluxes at the central surface cell of each sample were monitored.

The results are shown in Table 4.4 and Figures 4.8 to 4.15. For the 2 keV case it is seen that the teflon and  $\text{SiO}_2$  initially charge positive, while the kapton and magnesium charge negatively. This suggests the presence of a photoelectron current between the surfaces. NASCAP could have completed this case through the use of a very short time step, but the cost would have been excessive.

For the 5, 8, 10 and 20 keV cases all surfaces charged negatively, with the magnesium surface charging most rapidly due to its smaller capacitance to the aluminum. Often the

POTENTIAL CONTOURS ALONG THE Y-Z PLANE OF X = 9

ZMIN = -.77850+04 ZMAX = -.88532+01 ΔZ = .50000+03

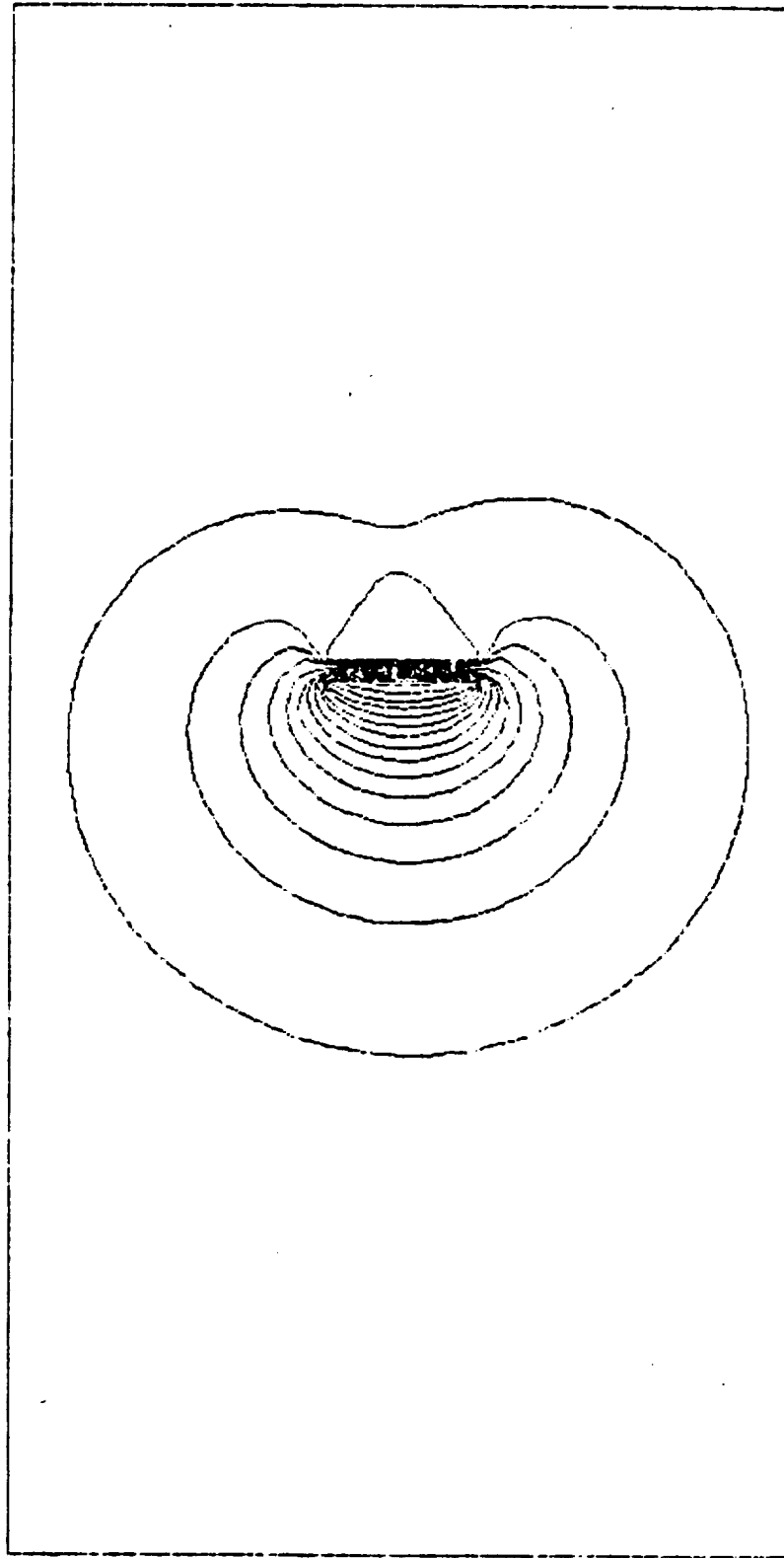


Figure 4.5. Potential contours at conclusion of 10 keV teflon plate tank test case. The potential contours are plotted in intervals of 500 volts.

SURFACE CELL MATERIAL COMPOSITION AS VIEWED FROM THE NEGATIVE Z DIRECTION

FOR Z VALUES BETWEEN 1 AND 33

MATERIAL LEGEND

- 1 ALUMIN 
- 2 TEFLON 
- 3 KAPTON 
- 4 MAGNES 
- 5 SiO2 

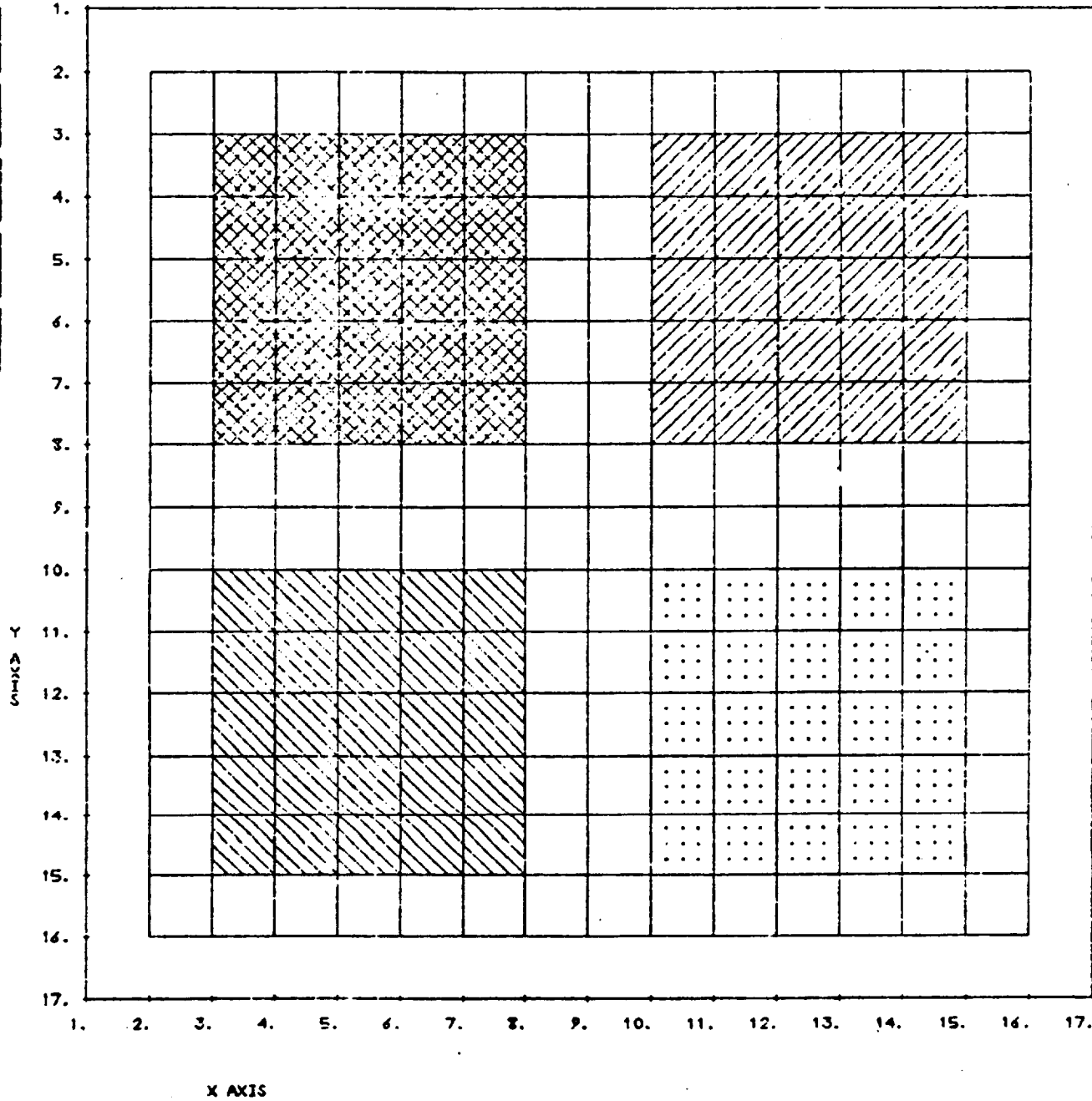


Figure 4.6. Model of SSPM used for NASCAP test cases.

THE CURRENT DENSITY CONTOURS OF E BEAM AT THE SAMPLE WITH UNIT AMP-M<sup>2</sup>

ZMIN = .00000 ZMAX = .10078-04 ΔZ = .10000-05

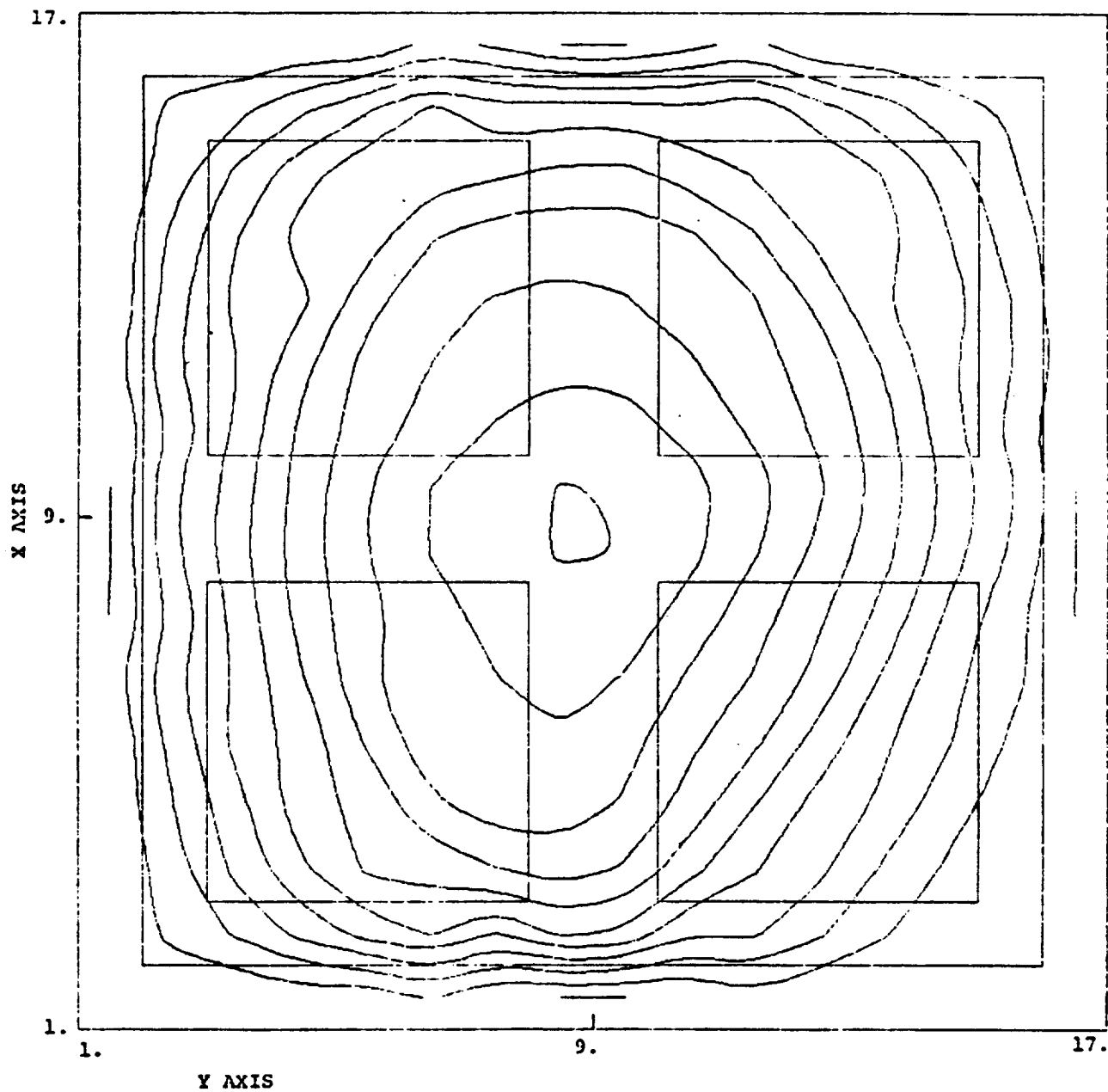


Figure 4.7. Current density contours to uncharged SSPM.  
(Note change of axes relative to Figure 4.6.)

Table 4.4. SSPM Ground Test Case Results (Current Balance, nA/cm<sup>2</sup>)

(I - Incident Electron Flux)  
 (B - Electron Backscatter)  
 (S - Secondary Electron Emission)  
 (N - Net Flux)

Beam Energy	Time (sec)	Teflon				Kapton				SiO <sub>2</sub>				Magnesium			
		I	B	S	N	I	B	S	N	I	B	S	N	I	B	S	N
2 keV	0	0.74	0.13	0.67	0.06	0.66	0.09	0.41	-0.16	0.59	0.11	0.63	0.17	0.48	0.09	0.10	-0.28
5 keV	0	0.74	0.11	0.35	-0.28	0.68	0.07	0.27	-0.35	0.59	0.09	0.36	-0.14	0.48	0.08	0.05	-0.35
	292	0.50	0.09	0.39	0.01	0.46	0.07	0.30	-0.08	0.38	0.07	0.31	0.002	0.14	0.02	0.13	0.01
8 keV	0	0.74	0.10	0.25	-0.39	0.68	0.05	0.21	-0.42	0.59	0.08	0.27	-0.24	0.48	0.07	0.04	-0.38
	219	0.55	0.09	0.33	-0.13	0.53	0.06	0.22	-0.25	0.50	0.08	0.28	-0.15	0.19	0.04	0.07	-0.08
10 keV	0	0.74	0.09	0.22	-0.43	0.68	0.05	0.19	-0.45	0.59	0.07	0.23	-0.28	0.48	0.07	0.03	-0.38
	290	0.49	0.08	0.28	-0.13	0.51	0.05	0.19	-0.27	0.48	0.07	0.24	-0.18	0.08	0.01	0.05	-0.02
20 keV	0	0.74	0.09	0.22	-0.43	0.68	0.05	0.19	-0.45	0.59	0.07	0.23	-0.28	0.48	0.07	0.03	-0.38
	364	0.50	0.07	0.16	-0.28	0.58	0.04	0.14	-0.40	0.53	0.07	0.16	-0.30	0.12	0.03	0.05	-0.03

Potentials at Run Termination, Volts

5 keV	292	-2421	-2720	-1563	-4803
8 keV	219	-4151	-3057	-1645	-6880
10 keV	290	-5856	-4195	-2384	-9895
20 keV	364	-10,600	-6622	-4380	-19,060

ORIGINAL PAGE IS  
 OF POOR QUALITY

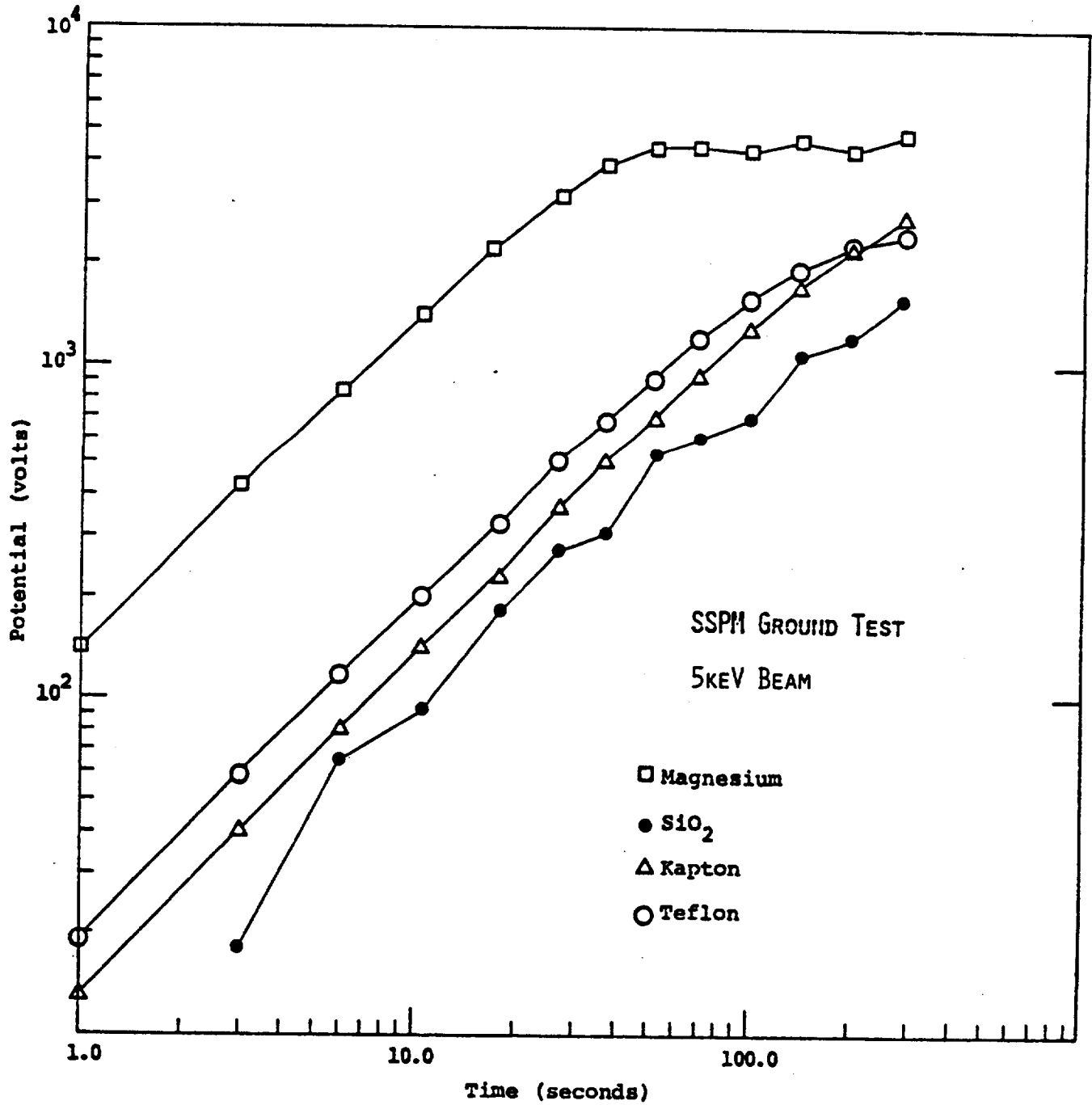


Figure 4.8. Potentials on the four SSPM material samples subject to a 5 keV electron beam.

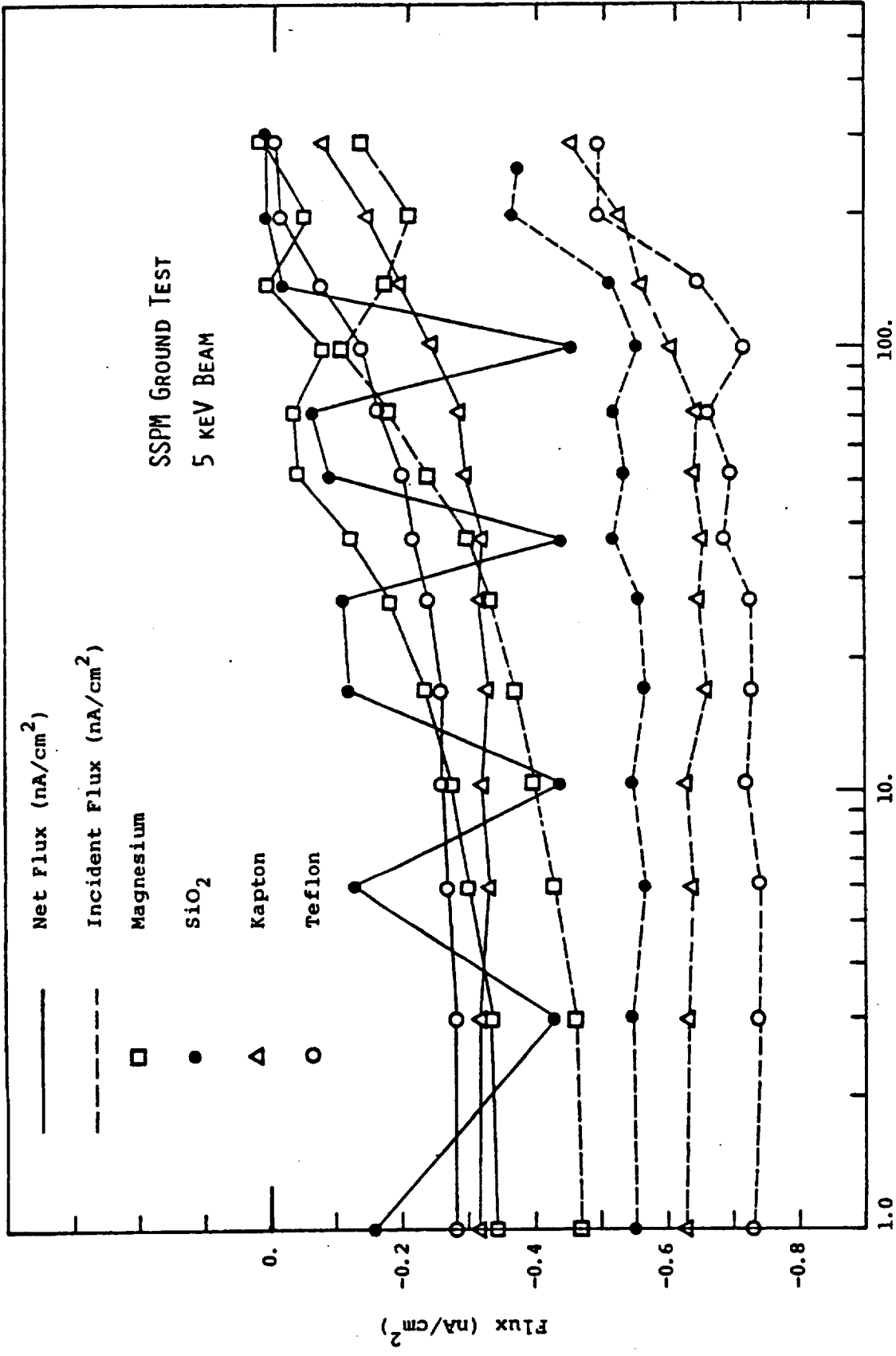


Figure 4.9. Net and incident fluxes to the four SSPPM samples subject to a 5 keV beam. Note the oscillation in the SiO<sub>2</sub> flux due to nonlinear suppression of secondary emission by the external field.

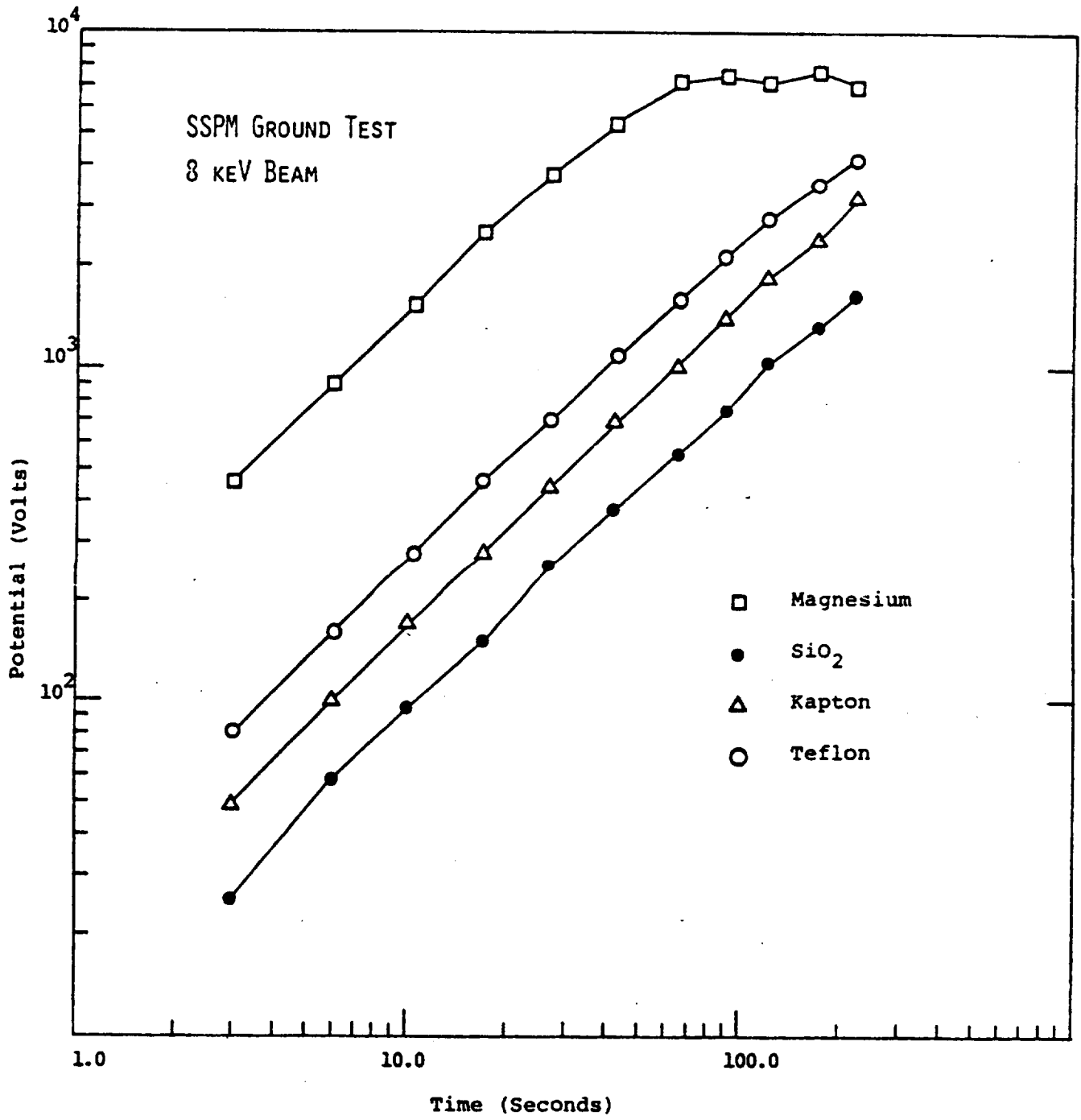


Figure 4.10. Potentials on the four SSPM material samples subject to an 8 keV electron beam.

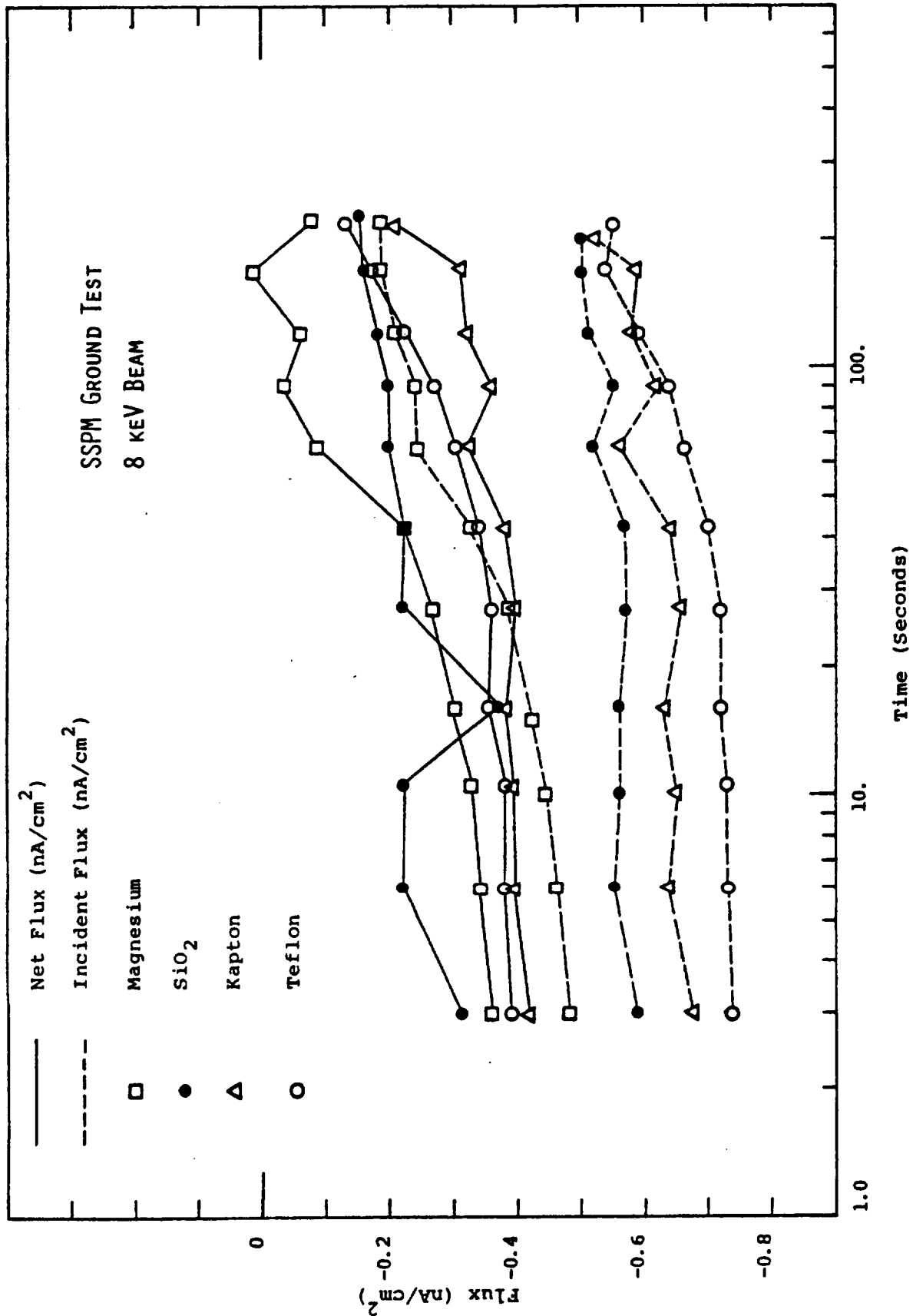


Figure 4.11. Net and incident fluxes to the SSPM samples subject to an 8 keV beam.

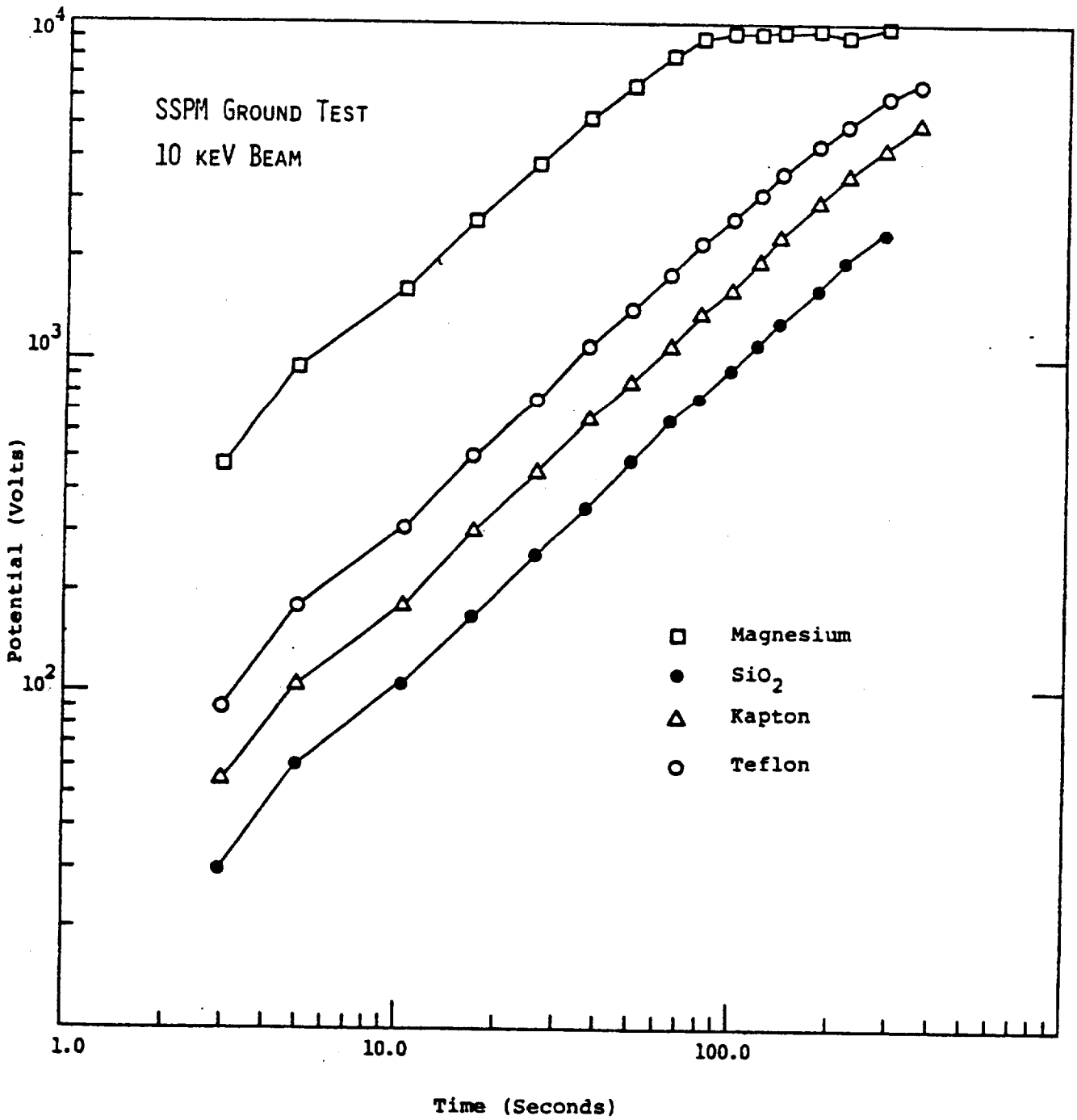


Figure 4.12. Potentials on the SSPM samples subject to a 10 keV beam.

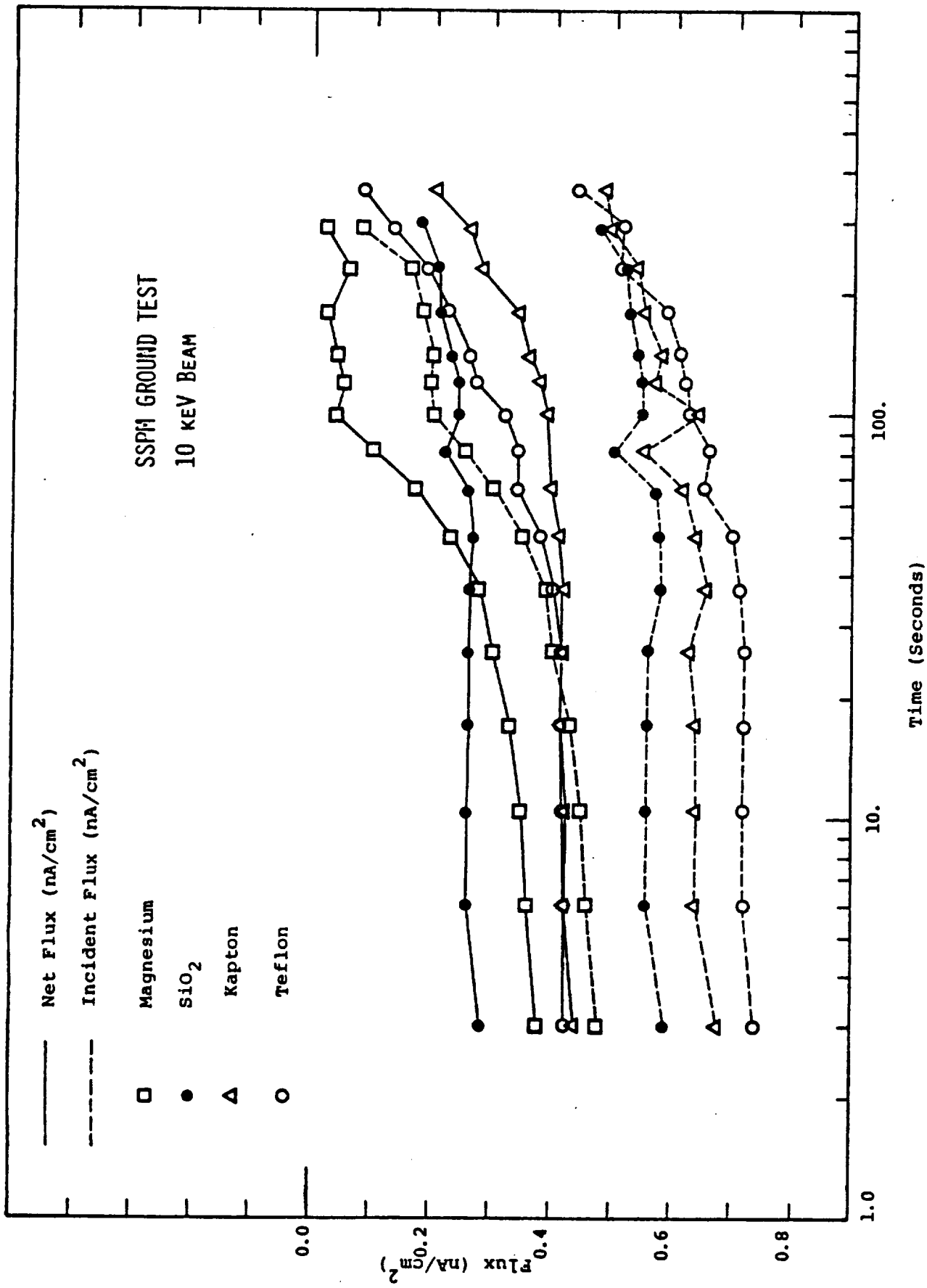


Figure 4.13. Net and incident fluxes to the SSPM samples subject to a 10 keV beam.

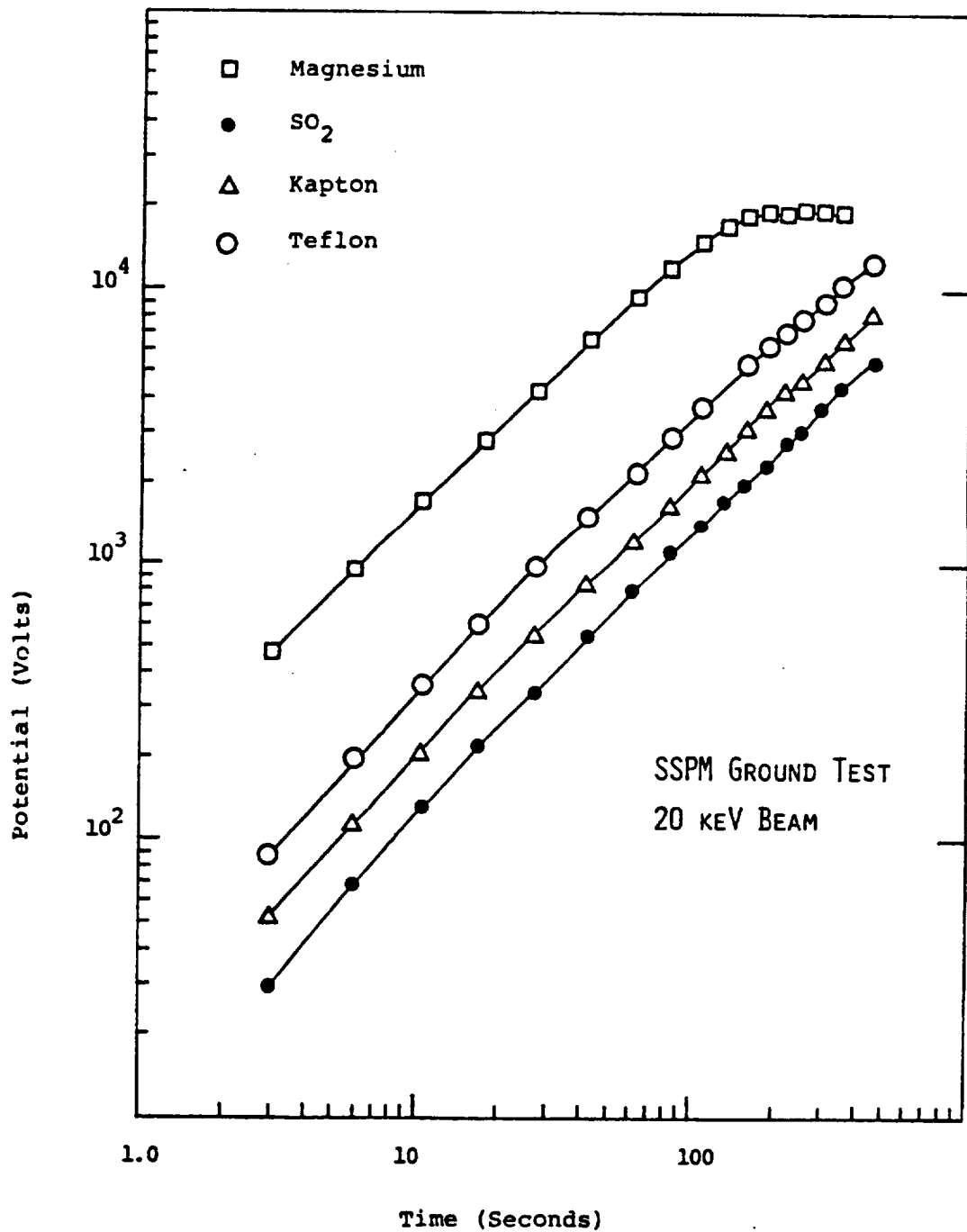


Figure 4.14. Potentials on the four SSPM material samples subject to a 20 keV beam.

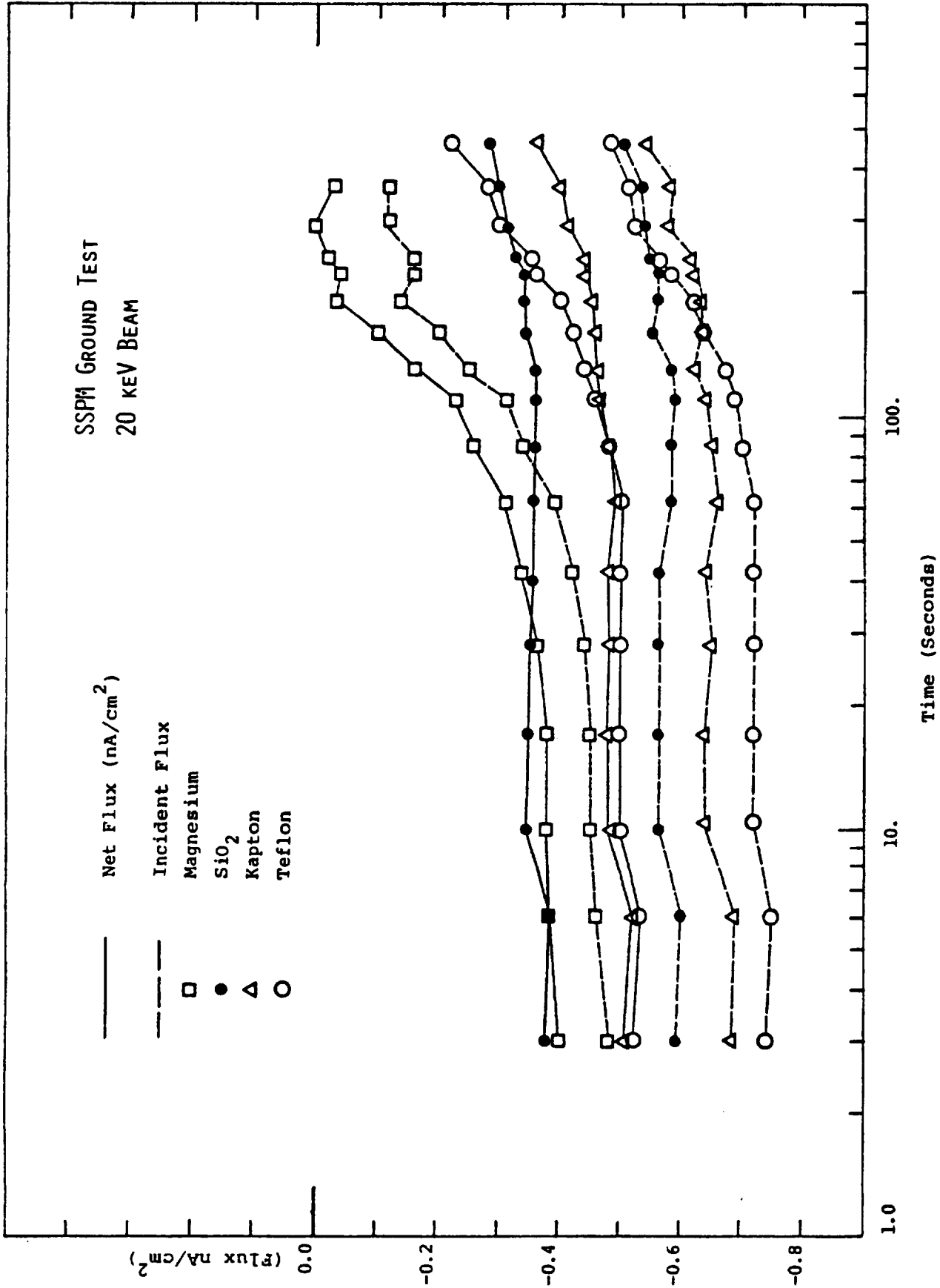


Figure 4.15. Net fluxes and incident fluxes to the four SSPM material samples subject to a 20 kev beam.

field due to the magnesium was sufficient to reverse the sign of the field in front of the other samples, suppressing their secondary emission. The simulations were carried out well beyond saturation of the magnesium potential. The oscillatory behavior seen in many of the plots is due to having taken excessively long time steps in order to minimize computer costs. Because of this problem, the runs were stopped before the insulating samples became fully charged.

#### 4.4 ALUMINUM SPHERE SPACE TEST CASES

Several tests were performed on an aluminum sphere of nominal diameter 3 meters. The actual object was the smallest quasisphere definable by NASCAP, having one facet in each of the 26 symmetry directions. The effective diameter (from capacitance calculation) was 3.19 meters. Because of its symmetry and because it is a simple conductor, the aluminum sphere is a particularly simple object for a charging simulation.

##### 4.4.1 Maxwell Probe Calculation

The Maxwell probe formulation used in NASCAP is, in principle, exact for a sphere in an isotropic, Maxwellian plasma, and thus nearly exact for a quasisphere in such an environment. This formulation writes the differential particle flux per unit area to the satellite as

$$\frac{d^2 f}{dE d\Omega} = \rho \left( \frac{kT}{2\pi m} \right)^{1/2} E \exp[-(E + qV)/kT] \frac{\cos\theta}{\pi}$$

where  $E$  is the energy of incidence,  $q$  the particle charge, and  $V$  the surface voltage. (The formula requires  $E + qV > 0$ .) The incident flux is then given by

$$\rho \left( \frac{kT}{2\pi m} \right)^{1/2} \exp(-qV/kT) \quad qV > 0$$

$$\rho \left( \frac{kT}{2\pi m} \right)^{1/2} (1 - qV/kT) \quad qV < 0.$$

The secondary emission and backscatter are calculated as

$$\Gamma = \int_{E_{\min}}^{\infty} dE \times 2\pi \int_0^1 d(\cos\theta) \gamma(E, \theta) \frac{d^2 f}{dE d\Omega}$$

where  $\gamma$  is the relevant coefficient. (The angular integral has been performed analytically, whereas the energy integral is done using Simpson's Rule.)

In the environment shown in Table 4.5 the sphere reached an equilibrium potential of 1415 volts in a time of 0.2 seconds (Figure 4.16). The initial and final current balances are shown in Table 4.6. Note the important role played by the cold ions and the resulting secondary electrons in establishing the final current balance.

#### 4.4.2 Reverse Trajectory Simulation - Isotropic Flux

Three reverse trajectory simulations were carried out using successively finer grids of incident energy and angle. The environment was identical to the previous case (Table 4.5). The potentials reached after 0.81 seconds were -1720 volts, -1640 volts, and -1600 volts for  $(n_E, n_\theta) = (3,3), (4,4),$  and  $(5,5)$  respectively (Figure 4.17). The degree of charging is overestimated due to underestimation of the secondary emission. A more nearly optimal choice of incident angles would serve to ameliorate this situation.

Table 4.5. Maxwellian Environment for Space Tests

Species	$e^-$	$H^+$
Temperature	4.11 keV	430 eV
Density	$0.53 \text{ cm}^{-3}$	$0.60 \text{ cm}^{-3}$

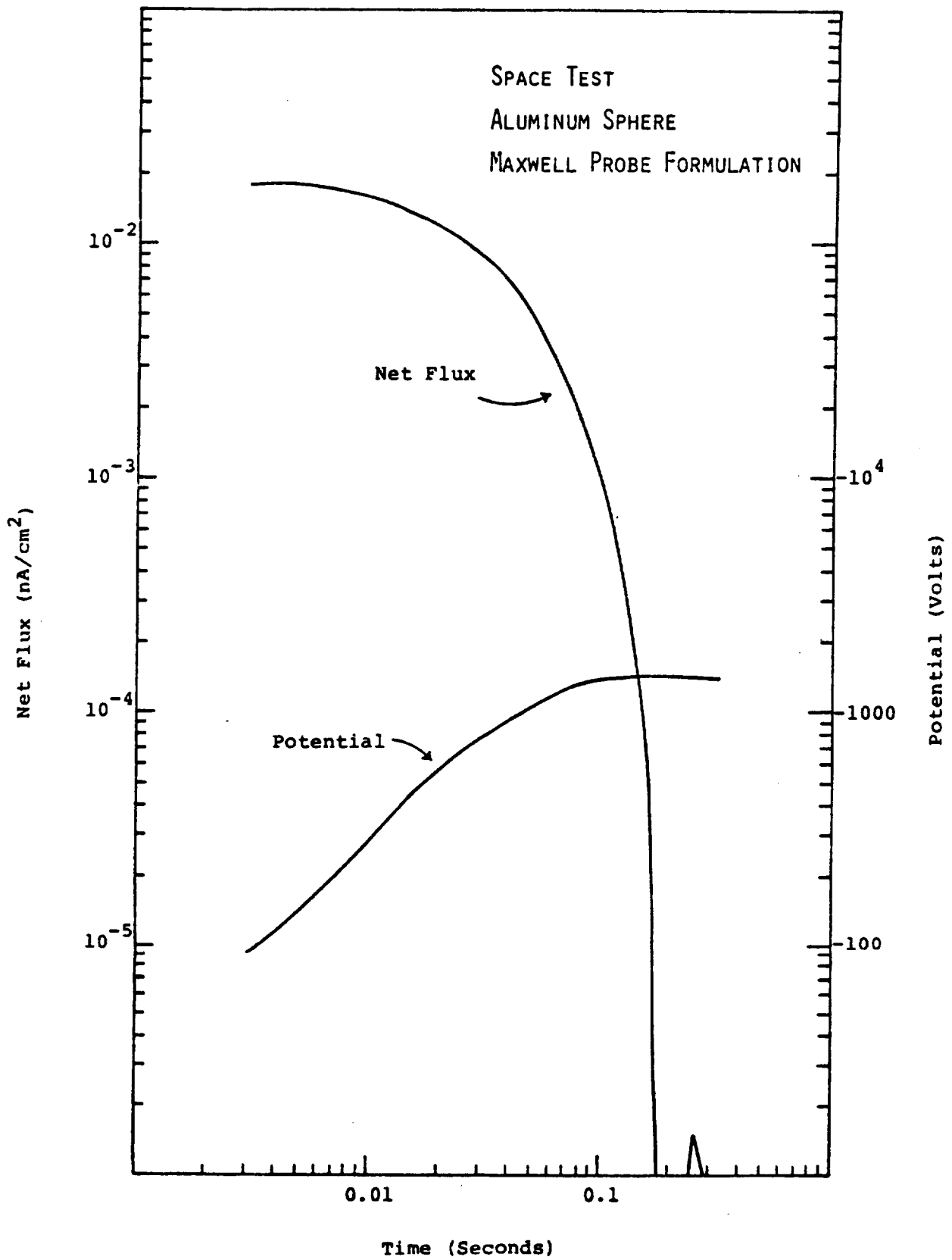


Figure 4.16. Potential and net flux for 3 m aluminum sphere in environment of Table 4.5.

Table 4.6. Current Balance for Aluminum Sphere -  
Maxwell Probe Calculation

	<u>Initial</u>	<u>Final</u>
Potential (volts)	0	-1415
Incident Electrons (nA/cm <sup>2</sup> )	-0.0909	-0.0645
Backscatter (nA/cm <sup>2</sup> )	0.0303	0.0215
Secondaries (nA/cm <sup>2</sup> )	0.0388	0.0277
Incident Protons (nA/cm <sup>2</sup> )	0.0008	0.0033
Secondaries (nA/cm <sup>2</sup> )	0.0018	0.0120
Net Flux (nA/cm <sup>2</sup> )	-0.0192	0

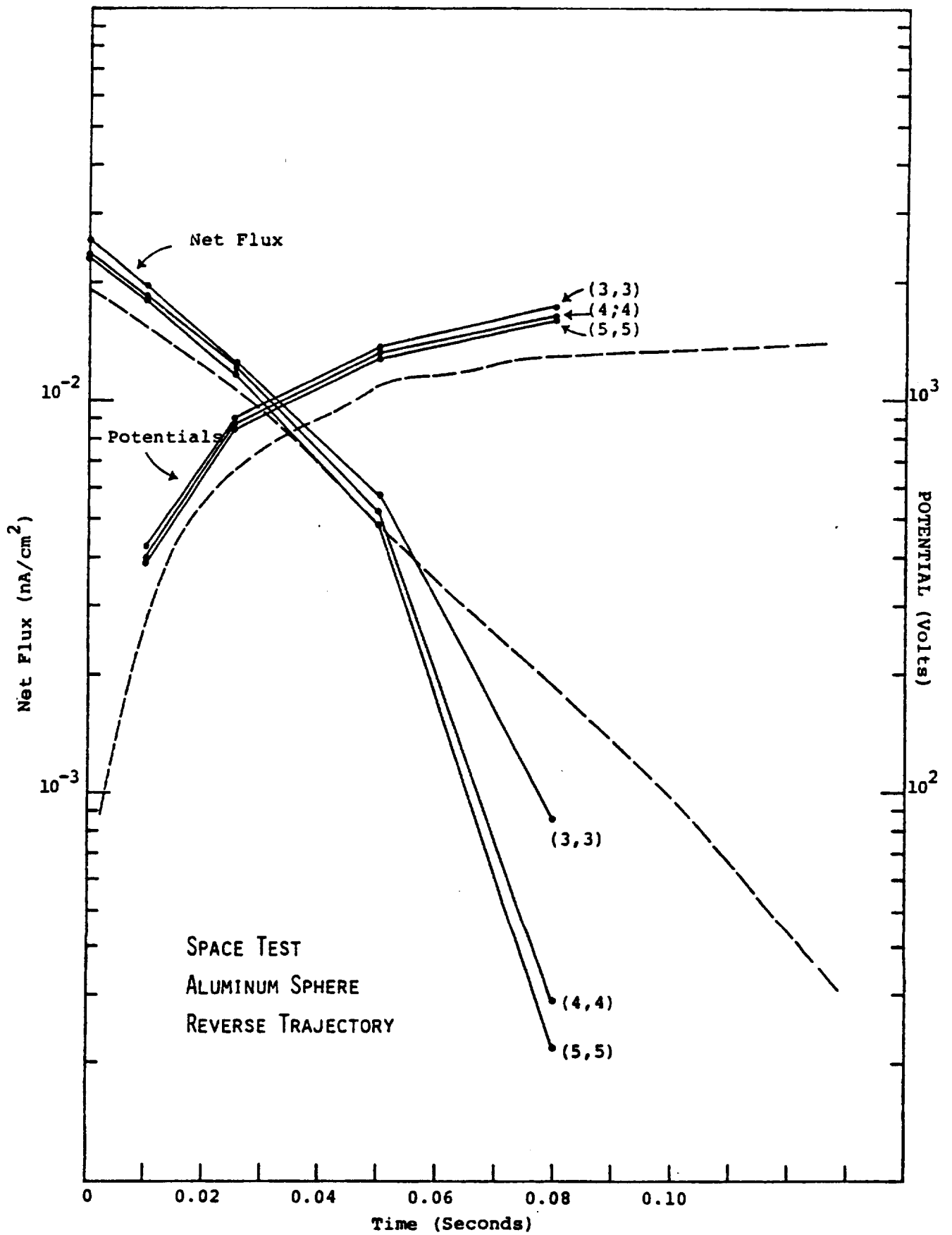


Figure 4.17. Reverse trajectory simulations for 3 m aluminum sphere in environment of Table 4.5. Figures in parentheses indicate numbers of incident energies and angles used. The dashed lines are the results of the Maxwell probe simulation.

#### 4.4.3 Reverse Trajectory Simulation - Anisotropic Flux

The final aluminum sphere space test case uses a reverse trajectory treatment for an anisotropic plasma based on ATS-5 data for hour 9.998 of day 73. The plasma temperatures were similar to those of Table 4.5, but the electron density was somewhat lower and the proton density much higher. The incident particle matrix was  $5 \times 5 \times 5$  (energies, polar angles, azimuthal angles).

The results are shown in Figure 4.18. The final potential was -280 volts, with a nonuniform flux (averaging to zero) over the surface of the sphere.

#### 4.5 INSULATED SPHERES - MAXWELL PROBE CALCULATION

Kapton and teflon both tend to achieve positive potentials in the environment of Table 4.5. Since the electric field just outside the surface suppresses low energy electron emission, the maximum potentials are only a few volts and are achieved in  $\sim 10^{-4}$  seconds. The results of these simulations are given in Table 4.7 and Figure 4.19.

#### 4.6 COMPARISON OF DeFOREST DATA AND MAXWELLIAN

Reverse trajectory calculations (Figure 4.20) were done for a 3 m teflon sphere subject to the ATS-5 data for hour 9.998 of day 73, and the similar environment of Table 4.5. Despite an overshoot in the Maxwell simulation, both charge to  $\sim 1.2$  volts in  $\sim 10^{-4}$  seconds.

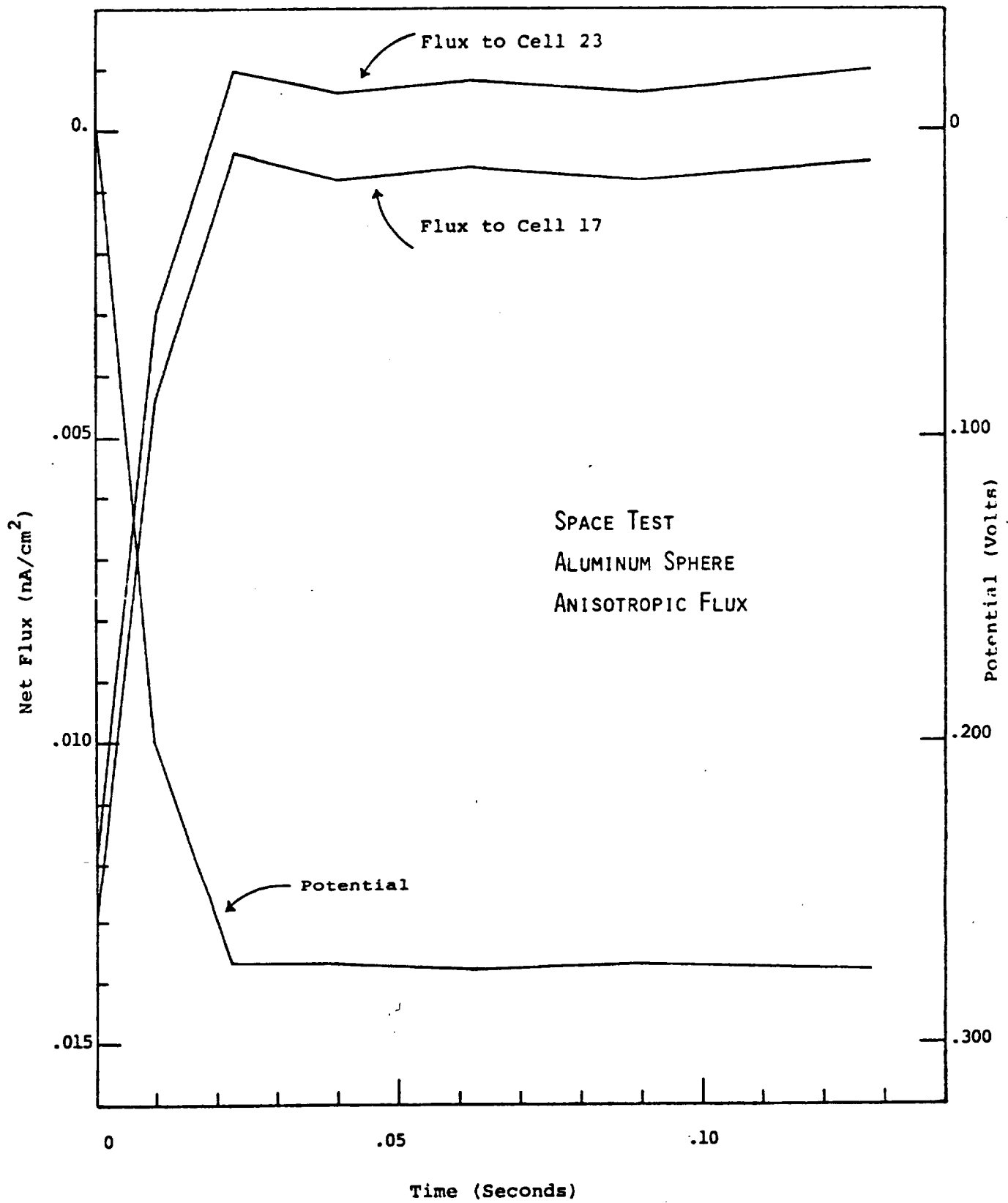


Figure 4.18. Simulation of an aluminum sphere in an anisotropic plasma, with net flux to two representative surface cells.

Table 4.7. Current Balance for Insulating Spheres in Environment of Table 4.5

	<u>Teflon</u>		<u>Kapton</u>	
	<u>Initial</u>	<u>Final</u>	<u>Initial</u>	<u>Final</u>
Potential (volts)	0	1.6	0	0.024
Incident Electrons (nA/cm <sup>2</sup> )	-0.0909	-0.0910	-0.0909	-0.0909
Backscatter (nA/cm <sup>2</sup> )	0.0272	0.0272	0.0210	0.0210
Secondaries (nA/cm <sup>2</sup> )	0.0862	0.0603	0.0673	0.0673
Incident Protons (nA/cm <sup>2</sup> )	0.0008	0.0008	0.0008	0.0008
Secondaries (nA/cm <sup>2</sup> )	0.0019	0.0013	0.0019	0.0019
Net Flux (nA/cm <sup>2</sup> )	0.0250	-0.0014	< 10 <sup>-4</sup>	< 10 <sup>-4</sup>

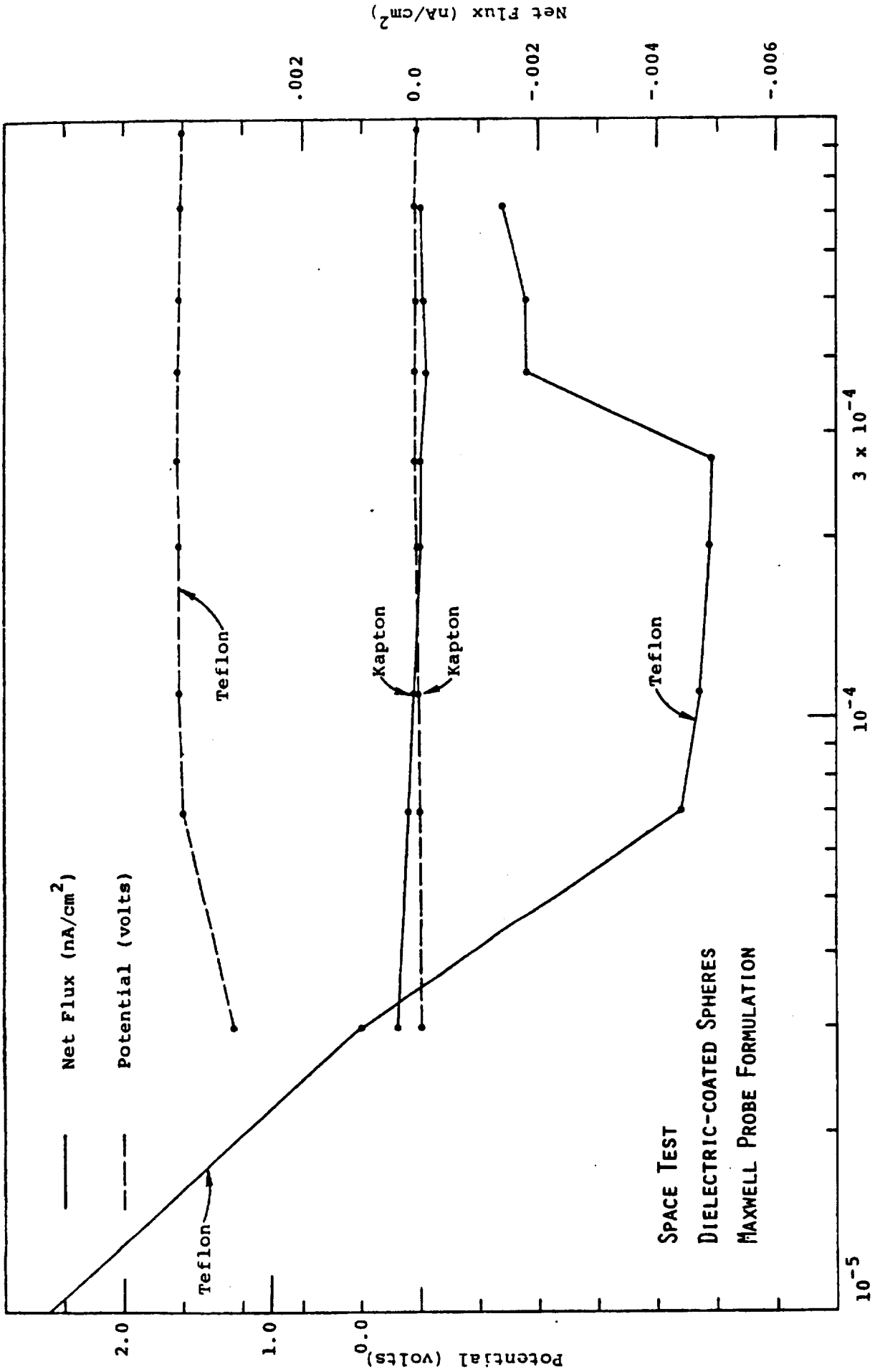


Figure 4.19. Net fluxes and potentials for dielectric-coated spheres in environment of Table 4.5.

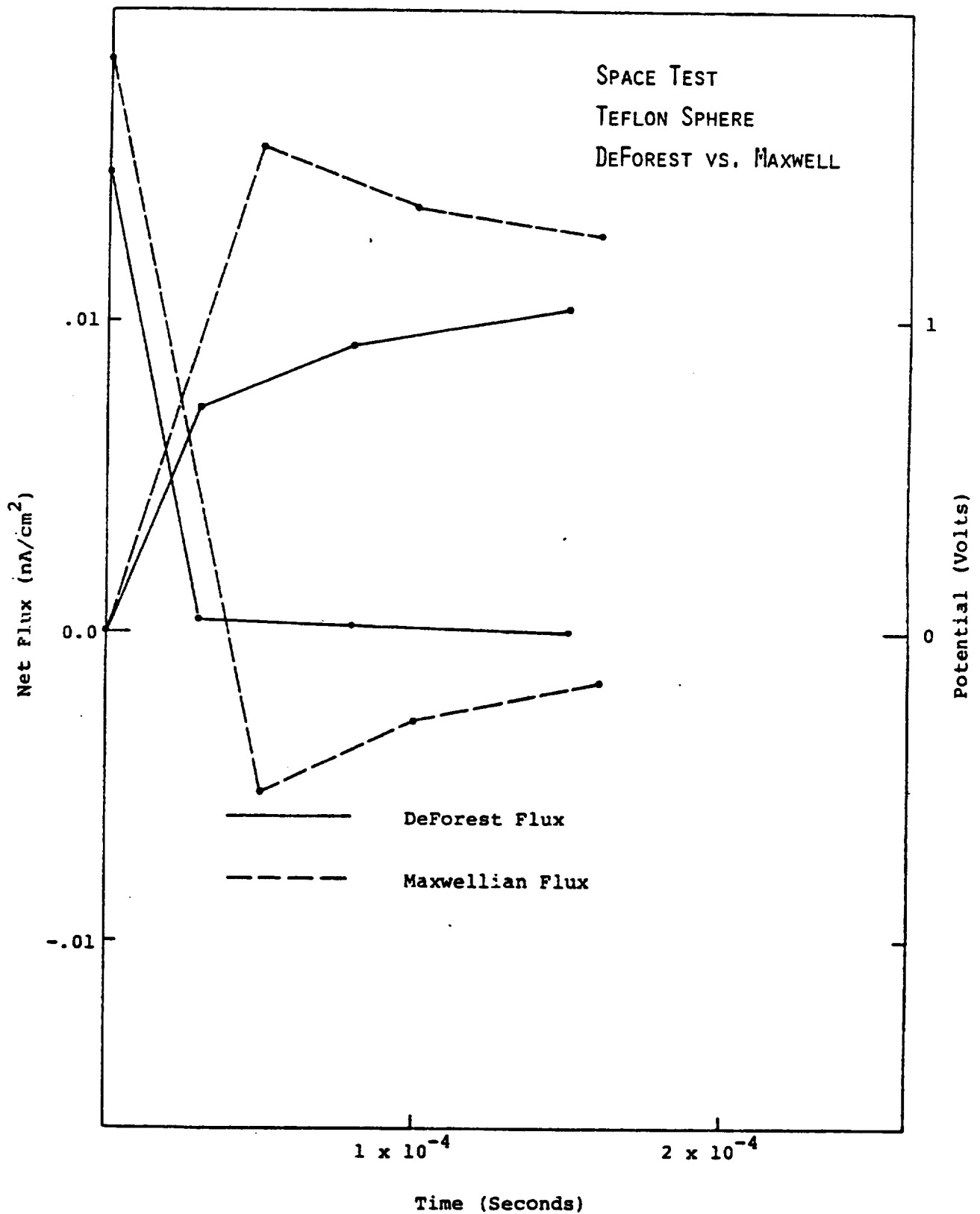


Figure 4.20. Reverse trajectory calculations for 3 m teflon sphere using DeForest data (hour 9.998 of day 73) and data of Table 4.5.

#### 4.7 ISOTROPIC SUN

A special version of NASCAP was mapped for which the sun shone on a 3 m teflon sphere uniformly from all directions. (Normally, NASCAP does a full shadowing calculation for photoemission.) The flux was dominated by the photocurrent of  $2 \text{ nA/cm}^2$ . The sphere charged to 16 volts in a few times  $10^{-5}$  seconds (Figure 4.21).

The reason the sphere was charged to well above the 2-volt characteristic energy of secondary- or photo-electrons is worth some explanation. This run was performed using the default "NOSHEATH" option to avoid tracking secondary electrons. Under these conditions, the low energy electron current emitted by an electron attracting surface is reduced by a factor

$$f(\vec{E}) = \begin{cases} \exp(-|\vec{E}|/2) & |\vec{E}| < 10 \\ 0 & |\vec{E}| > 10 \end{cases}$$

where  $|\vec{E}|$  is the electric field normal to the surface in volts/mesh unit. Thus the satellite charged to the point where its surface field was approximately 10 volts/mesh unit, the mesh unit in this case being 1 m. Had the "SHEATH" option been invoked, 2 eV electrons would have been emitted from the sphere and tracked in the electrostatic field. When the surface potential exceeded 2 volts positive, these electrons would have returned to the sphere. NASCAP would then have cancelled the emitted and return currents, thus giving an equilibrium potential slightly in excess of 2 volts.

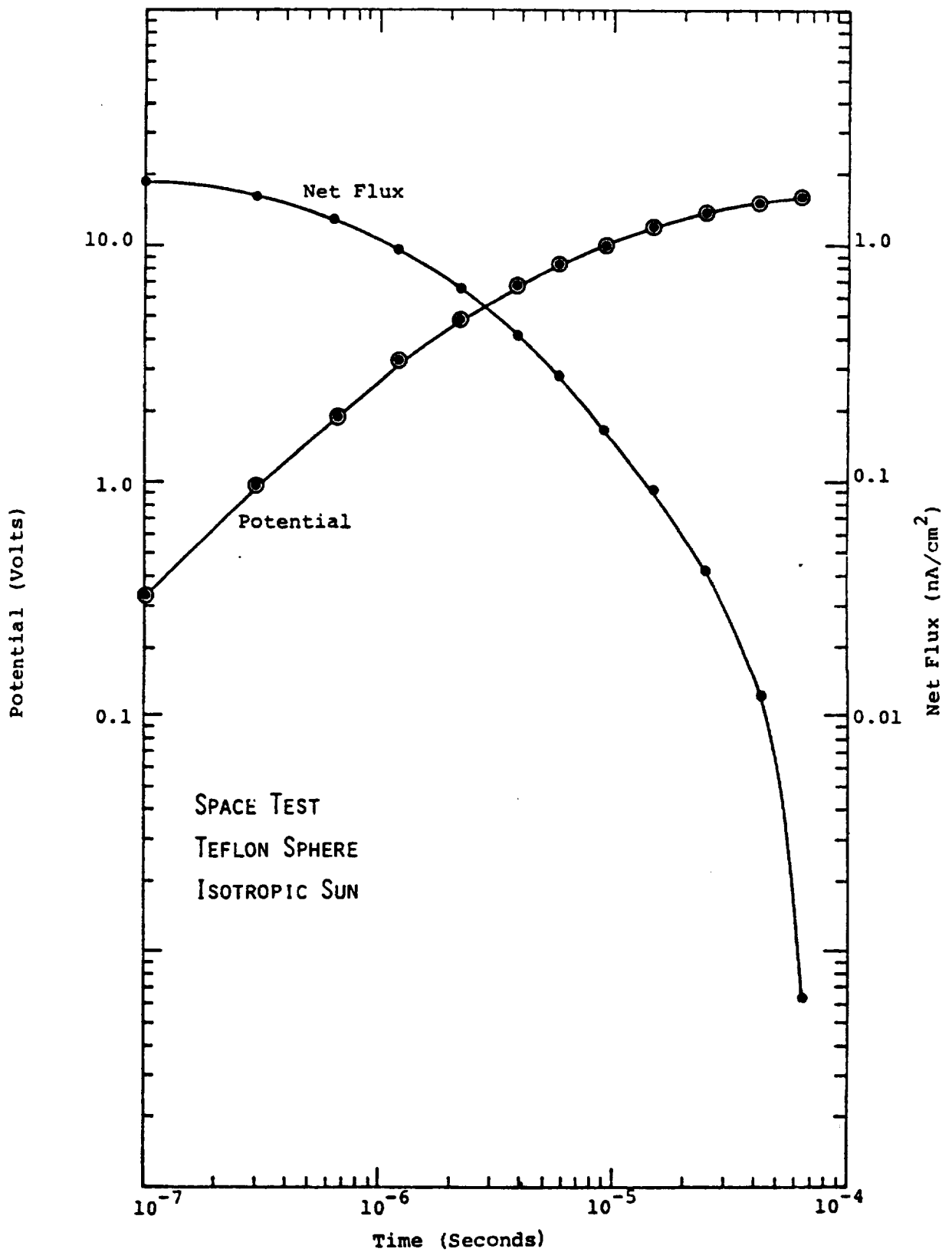


Figure 4.21. Potential and net flux to a 3 m teflon sphere exposed to sunlight uniformly over its surface.

#### 4.8 SPACE TEST OF SSPM

The final test case was the SSPM (Figure 4.6) in the environment of Table 4.5 and mounted on an aluminum plate with potential fixed at -575 volts. (This was the potential achieved in a test run of a SCATHA-like satellite. See Appendix E.) The potentials and fluxes are shown in Figures 4.22 and 4.23. After 100 seconds, the potentials were: magnesium at -1500 volts, kapton at -500 volts, SiO<sub>2</sub> at -410 volts, teflon at -380 volts. Beyond this time, the magnesium (which eventually reached -2200 volts) was sufficiently negative to suppress low energy electron emission from the insulators, and the simulation became unstable to the long time step which was taken, again for cost considerations.

#### 4.9 CONCLUSIONS

The variety of cases presented here, together with that presented in Appendix F, comprise the first tests of the NASCAP program. They were designed to exercise much of the modeling capability within the code and to point out the strengths and weaknesses of the techniques employed in NASCAP. These calculations were performed at the end of this contract period and there was little time remaining to modify the analytical models to improve speed or accuracy. No attempt was made to obtain improved output by re-performing a test case after analysis of the first simulation.

In general the code worked remarkably well. That is, the collection of physical models which comprise NASCAP were able, without modification, to calculate the charging processes and yield physically reasonable results. Both ground test and space models worked smoothly in almost all instances. Flux, potential, material, and electrical

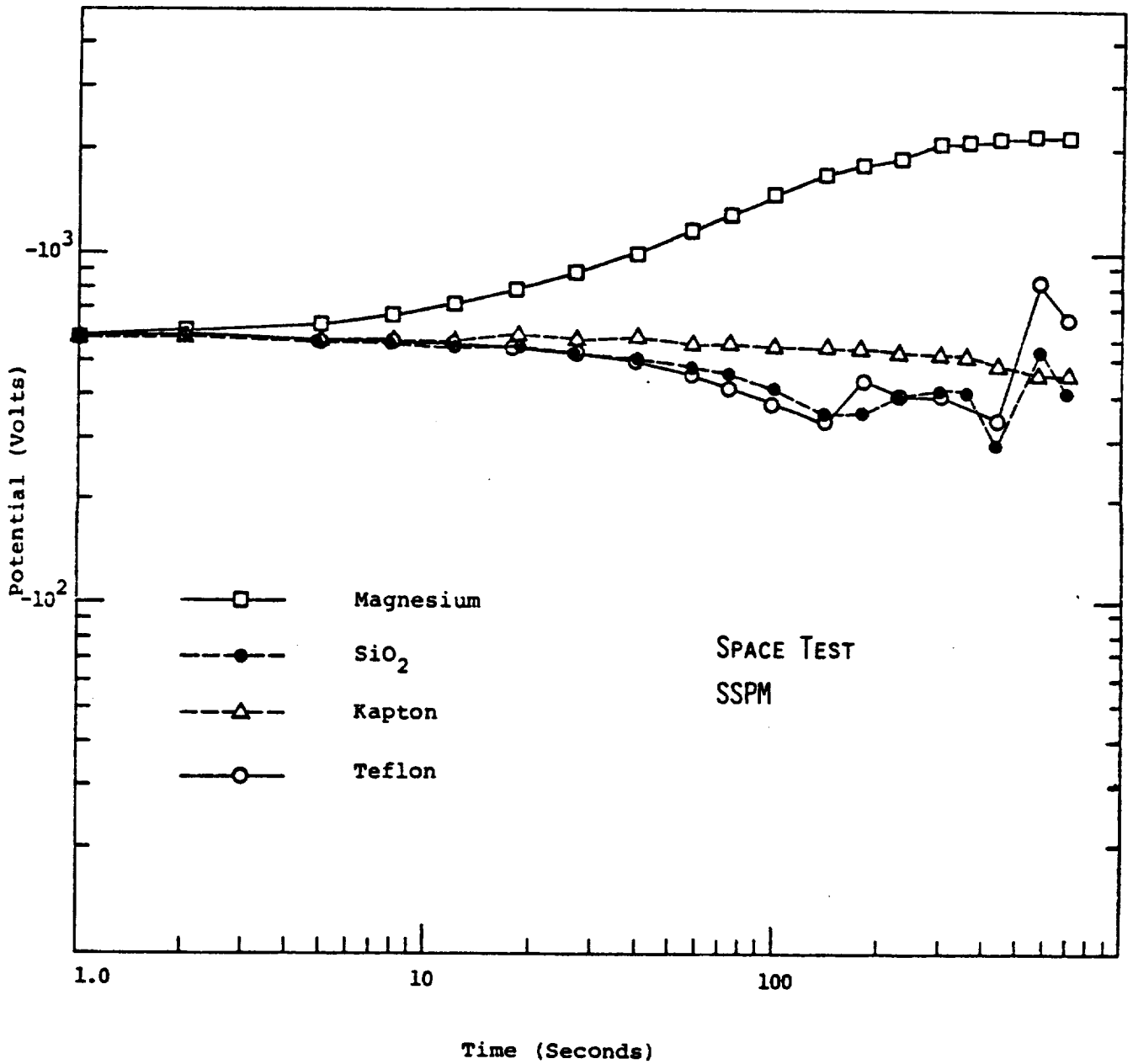


Figure 4.22. Potentials for SSPM material samples in environment of Table 4.5 and mounted on an aluminum plate fixed at -575 volts.

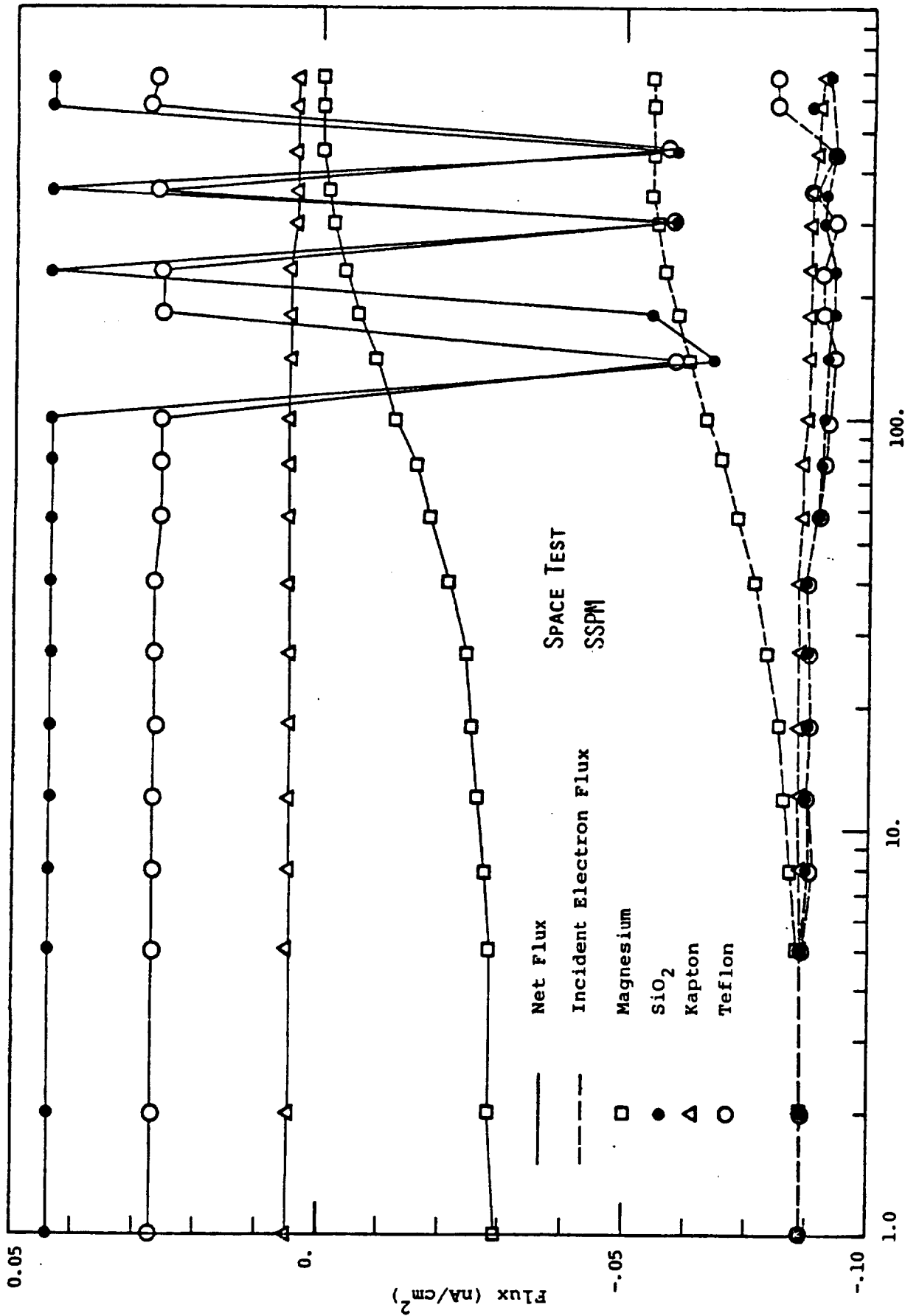


Figure 4.23. Net flux and incident electron flux to SSPM samples mounted on aluminum plate at -575 volts in environment of Table 4.5.

models functioned extremely well. Only one test case offered any difficulty; that was the 2 keV SSPM tank test. In that case the extremely large secondary currents from the dielectrics along with the magnesium negative potential created an electron sheath situation that the present NASCAP sheath treatment could calculate only by using extremely short time steps. However, on account of budgetary constraints it was decided not to rerun the case, but to present it as a limitation on the current version of NASCAP, something that simple sheath model modifications could eliminate.

These tests demonstrate that NASCAP can calculate successfully almost all aspects of the three-dimensional electrostatic charging of materials both in ground test and space environments. It should have great value as a design and analysis tool for scientific and engineering applications.

APPENDIX A

A PRELIMINARY SPECIFICATION OF THE ENVIRONMENT  
AT GEOSYNCHRONOUS ALTITUDE

Prepared by

MAYA DEVELOPMENT CORPORATION

for

SYSTEMS, SCIENCE AND SOFTWARE

August 1976



## 1.0 MAGNETOSPHERIC ENVIRONMENT

The magnetic field of the earth is confined to a finite volume by the pressure of the solar wind plasma which distorts the field into a teardrop-like shape with a tail of indefinite length (see Figure 1.1). Within this volume, called the magnetosphere, satellites encounter a wide variety of plasma physical phenomena. During the almost two decades since the initiation of space exploration a truly enormous amount of information on the magnetospheric plasma, its dynamics and its effects upon the earth, have been collected. From this vast array of data we have selected a data base from the geosynchronous satellites ATS5,6 which will be used to describe the magnetospheric environment. The last ten years has seen the development of theoretical models of the magnetospheric plasma which also guide our interpretation of the data. With this data and these models we can adequately describe the magnetospheric "weather" which is likely to cause spacecraft charging to occur.

The magnetosphere is a vast relaxation oscillator gradually distorting and storing some  $10^{22}$  ergs drawn from solar wind and earth's rotation and then explosively releasing the stored energy into the polar atmosphere where visible auroras occur. This phenomenon is known as a magnetospheric substorm. In general the substorm reaches its peak within 15-20 minutes and then gradually subsides. Auroral activity follows this pattern of growth and decay and also indicates the concentration of most substorm activity between local midnight and dawn.

The visual aurora is but one of many manifestations of the magnetospheric substorm. Observations from the ground, from balloons and from rockets have shown that negative bays in the horizontal magnetic component, enhanced absorption of cosmic radio noise, the production of millisecond



X-ray bursts, the occurrence of VLF hiss and chorus, the pattern of micro-pulsation observation, are all correlated with the onset of a magnetospheric substorm. Direct measurements from rockets and satellites have shown the visual aurora to result from fluxes of electrons and protons that occur during the early phases of a substorm. The ground based data and general description of the magnetospheric substorm are best reviewed in Akasofu (1968).

Satellite observations provided new insight into the phenomenology and dynamics of the magnetospheric substorm. Using data from Ogo 1,3 and Vela, Vasylunas (1968) demonstrated the existence of an intense low energy flux of electrons (the plasma sheet). The inner boundary of this plasma sheet was found to move inward with the onset of a substorm as indicated by ground based magnetic data. Lezniak and Winkler (1971) used ATS-1 electron data in energy ranges 50-150 keV, 150-500 keV, and 500-1000 keV to demonstrate the convective injection of energetic electrons into synchronous orbit. These concepts were extended and the data base to support them was vastly enlarged by the work of DeForest and McIlwain (1971) who used electron and proton data from ATS-5 differential analyzers that measured some 64 energy levels between 50 eV and 50 keV. This satellite provides much of the data base which we propose to use.

The theoretical understanding of plasma flow at geosynchronous orbit was further extended by McIlwain (1972) who used static electric and magnetic fields to model the magnetosphere (see Figures 1.2 and 1.3). Tracing particle orbits in these fields enabled him to explain many of the features observed in the ATS-5 data. In particular he was able to explain the shapes of boundaries which are often observed between particles of different energies. This work also demonstrated that intense fluxes correspond to particles which have been convected in from regions of low magnetic field ( $<40 \gamma$ ).

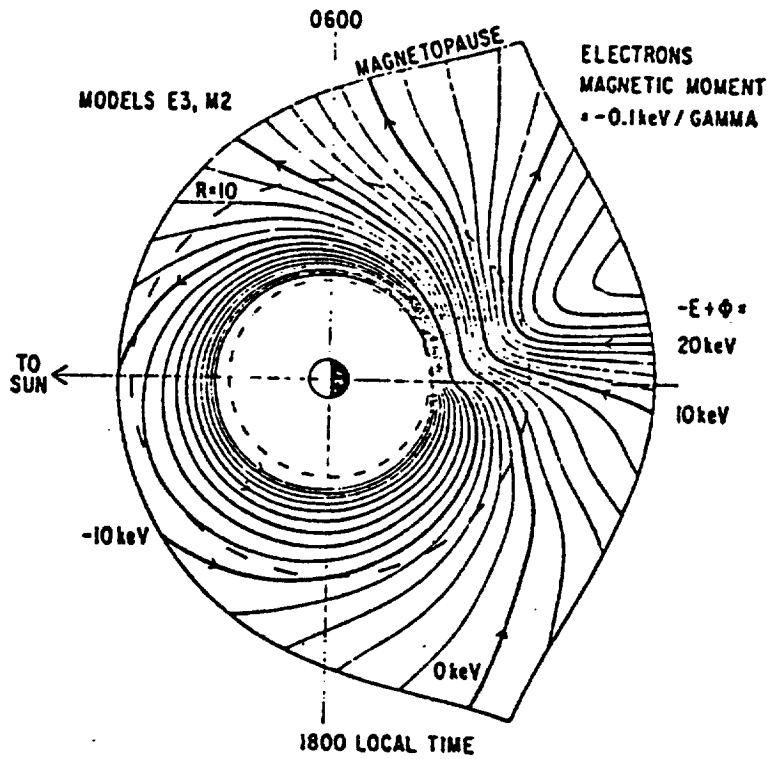


Figure 1.2 - McIlwain Model Electric Field.

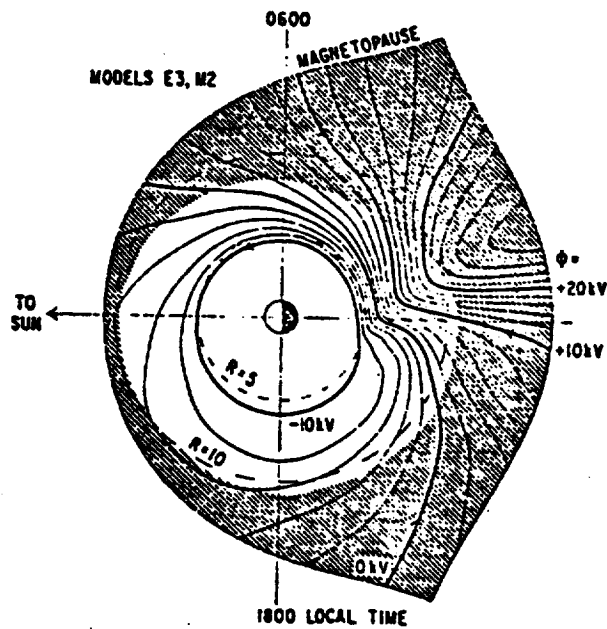


Figure 1.3 - Trajectories of electrons with magnetic moments of  $-0.1 \text{ keV}/\gamma$  in the model fields.

Extensions of this work were presented by McIlwain (1974) and by Mauk and McIlwain (1974). In this work the concept of an "injection boundary" similar in many ways to the plasma sheet boundary of Vasyunas (1968) was added to the models of the earlier work. By tracing the trajectories of particles backward through the model fields one is able to determine the inner boundary of the fresh plasma. The injection boundary was found to be related to  $K_p$ , the universal index of magnetic disturbance, and is given by

$$R_b = \frac{122 - 10 K_p}{\phi - 7.3}, \quad (1)$$

when  $\phi$ , the local time, lies between 18 and 24 hours. The concepts have been examined most recently by Konradi, et al (1975), who have found that the injection boundary and McIlwain field model explain their observation of 1-35 keV protons and 1-300 keV electrons from Explorer 45.

The launching of ATS-6 again added to the measuring capability of satellite plasma analyzers. The instruments on ATS-6 enable one to measure electrons and protons over the range of 1 eV to 80 keV and can in addition be scanned mechanically to look at different azimuthal and pitch angles. With these detectors new phenomena inaccessible to study with ATS-5 are being examined. In particular, McIlwain (1975) has found intense field aligned fluxes of electrons. These fluxes usually occur shortly after the onset of a magnetospheric substorm. They are characterized by an energy spectrum which is flat out to a break point energy usually between .1 keV and 10 keV. Those beams with break point energies above 2 keV seem only to occur within the first 10 minutes after the onset of plasma injection associated with a substorm. These beams will require further study and could be particularly effective in producing differential charging.

The charging of spacecraft to kilovolt potentials was first

discovered in ATS-5 data and reported by DeForest (1972). The problem of spacecraft charging had been recognized early in the design of the ATS-5 instruments. Before launch, the research group at San Diego under the direction of S. E. DeForest and C. E. McIlwain had insisted that conducting collars be placed around the apertures of the low energy particle detectors. In addition some concern was expressed about the fact that the viewing cones of two instruments looked out through a cylinder of solar cells which could charge to high potential.

At the time of the initial discovery of kilovolt charging potentials, only a few volts were expected. Thus the large potentials were somewhat surprising. DeForest (1972) was able to piece together an elementary theory which explained the observed high potentials.

The prelaunch worries about charging of the solar cells proved well founded. Differential charging, indicated by a spin modulation of the parallel detector fluxes, could only be caused by local electric fields. Thus DeForest (1973) demonstrated experimentally the possibility of kilovolt differential charging. Further work on this subject was presented at a joint AGU/AIAA special session on spacecraft charging in 1975. An especially useful paper, which we shall use to help select environmental data, was presented by Reasoner, et al (1975). It discussed the statistical relationship between the ATS-6 spacecraft charging events and the encounter of warm plasma clouds associated with the onset of a magnetospheric substorm.

## 2.0 DATA SELECTION

Environmental data obtained by plasma spectrometers on board the Advanced Technology Satellite 5 (ATS-5) from September 1969 through the vernal equinox of 1971 has been analyzed to provide input spectra for use in SSS spacecraft charging programs. Representative data from six days is presented in the following forms:

- 24 hr Spectrogram
- Integrals,  $n_e$ ,  $n_i$ ,  $j_e$ ,  $j_i$ , the number densities and energy fluxes respectively based on 2.3 minute averages for the selected 24 hour periods
- Plots of six selected spectra for each 24 hour period
- Printouts and punched cards containing the selected spectra

The data has been selected to typify several broadly different categories of magnetospheric weather which occur at geosynchronous orbit. While representative of the magnetospheric conditions the data is not extensive. It is meant to provide useful input for the development of spacecraft charging codes. A complete meteorological survey is being sponsored by Air Force Cambridge Research Laboratories. Data for this report has been provided under Defense Nuclear Agency Contract No. DNA001-76-C-0121.

## 2.1 BACKGROUND INFORMATION FOR DATA SELECTION

Previous studies provide background information which is useful in the selection of data for the study of spacecraft charging. Facts which should be considered include:

### 2.1.1 SPACECRAFT PERFORMANCE FEATURES

- Spin up anomalies on the DSCS-II spacecraft are well correlated with geomagnetic substorms (TRW SCA II, 1975)
- There is a strong association of unexplained satellite performance with the midnight to dawn sector of local time (McPherson, et al (1975)). (See Figure 2.1)
- The local time distribution of spacecraft charging events is found to maximize between local midnight and dawn (Reasoner, et al (1975)). (See Figure 2.2)

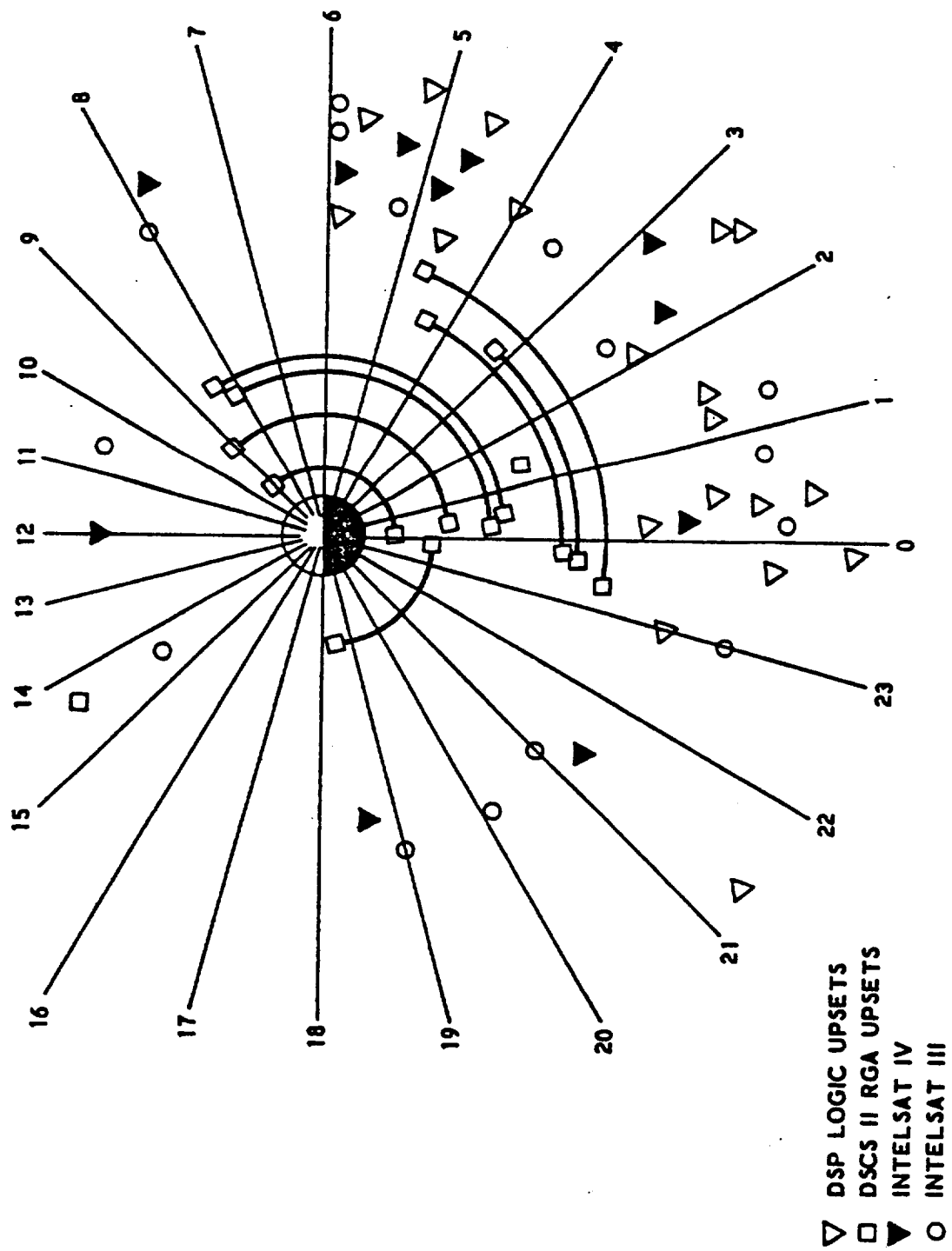


Figure 2.1 Unexplained Satellite Performance Correlates with Local Time.

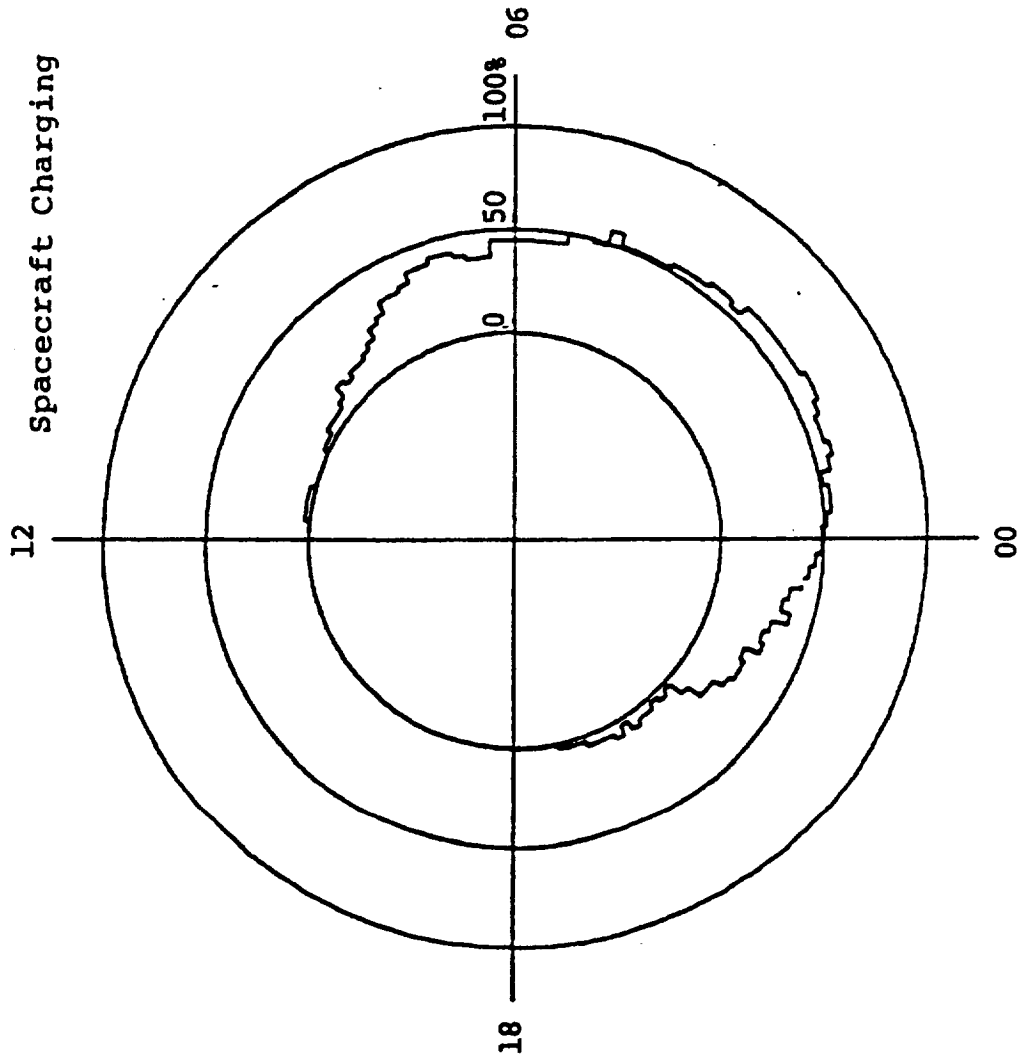


Figure 2.2 Local Time Distribution of Spacecraft Charging Events.

### 2.1.2 MAGNETOSPHERIC WEATHER FEATURES

- Equatorial observations by the geostationary satellite ATS-5 of charged particles on auroral lines of force reveal the frequent injection of plasma clouds into the magnetosphere. These intrusions of hot plasma are found to have a one to one correspondence with magnetospheric substorms. (DeForest and McIlwain, 1971)
- The electromagnetic fields surrounding the earth act to separate the injected plasma clouds on the basis of both charge and energy. (McIlwain, 1972). Electric fields attempt to bring about corotation of low energy electrons and protons as one moves inward toward the earth. Magnetic field gradients cause high energy electrons to drift toward the dawn side of the magnetosphere while high energy protons are caused to drift toward dusk. Effects of importance which follow are first, the spectra in the midnight to dawn sector are characterized by high electron energies and thus tend to induce spacecraft charging (DeForest, 1972)  
Second, field aligned fluxes are set up in order to maintain overall charge neutrality. (McIlwain, 1975). These fluxes can make important contributions to differential charging of spacecraft surfaces. (DeForest, 1973)
- The plasmasphere shrinks during periods of high magnetic activity (Chappel, 1970). At geosynchronous orbit encounters with the plasmasphere are concentrated in the local noon to local evening sector as shown in Figure 2.3. Plasmasphere encounters are anti-correlated with spacecraft charging.

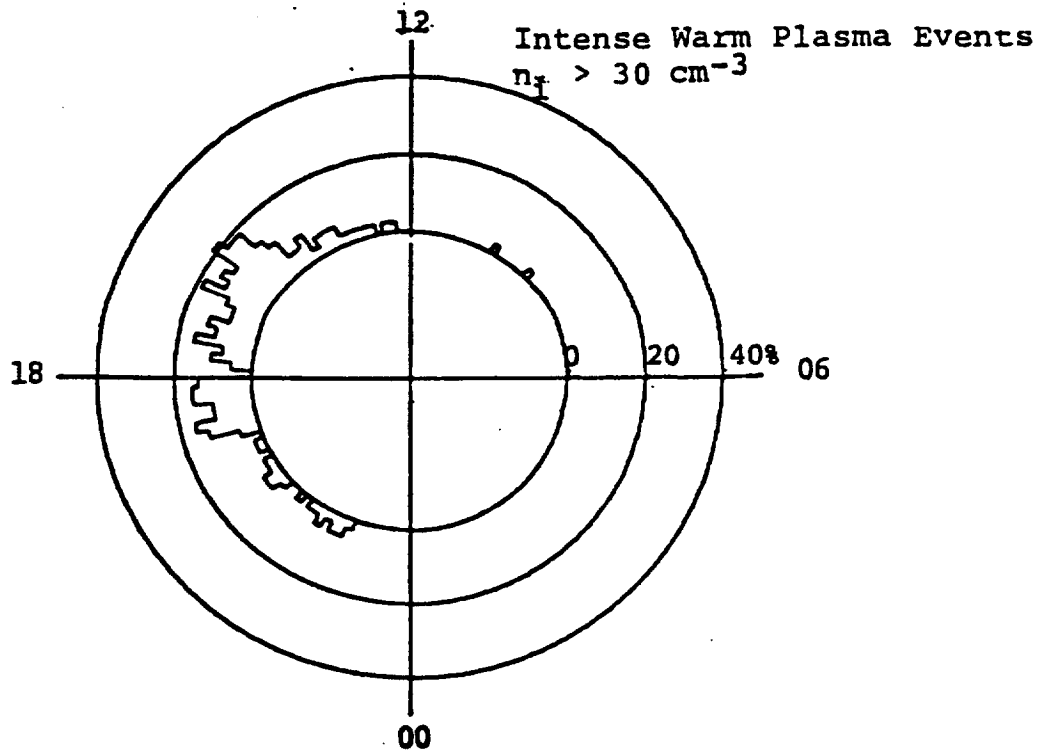
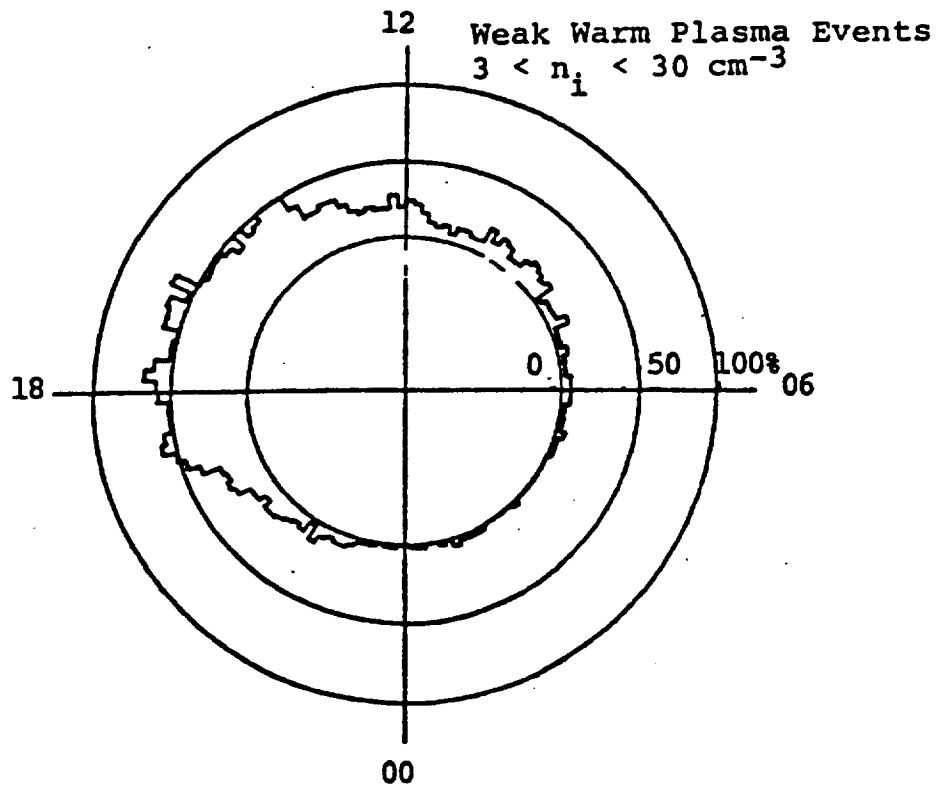


Figure 2.3 Local Time Distribution of Warm Plasma Encounters.

There are two reasons for this. First, the high density low energy plasma provides a grounding current to the spacecraft thus preventing large potential buildups. Second, plasmasphere encounters are more common during quiet times when substorm activity is low.

## 2.2 TYPICAL CONDITIONS REPRESENTED

With these facts in mind data from the year 1970 gathered by the UCSD plasma spectrometers on ATS-5 was analyzed. From this data the six representative days were chosen to typify the following magnetospheric weather conditions.

- A quiet day with no substorm activity
- A moderately active day with a single substorm of low intensity
- Two days with intense localized post midnight substorms
- A premidnight substorm
- A day when spacecraft charging occurred in the sunlight

## 2.3 SPECIAL CONDITIONS

Several special conditions can occur which we have designed into the total distribution functions which are to be used in this study (See Appendix C).

- 2.3.1 ECLIPSE OF THE SUN - the spacecraft charging phenomena was first discovered on ATS-5 during eclipse. The loss of the large photo-electron flux from the satellite surfaces allows the satellite to float up to high potentials (DeForest, 1972)
- FIELD ALIGNED FLUXES - usually encountered during the intense early phases of a substorm and of importance because they can cause differential charging.

### 3.0 DATA AND FORMAT

The data presented in this section consists of four types in addition to sets of punched cards for easy computer use. For each day or event presented, a 24-hour spectrogram is used to establish the context. Following that, selected spectra are shown which illustrate significant events. Instruction for reading both the spectrograms and the average plots are provided in the appendix. Punched cards containing the same data are provided with this report with instructions for their use. The printouts of the detailed spectra are also provided. Note that these detailed spectra are produced from 6.8 minute averages. This gives good statistics without smoothing rapid time fluctuations.

The final form of data presentation is a table of various integrals taken over 2.3 minute periods for the whole day. These might prove useful for studies where analytical approximations to the spectral shape is more useful than the actual spectra. The whole day is provided for possible future use in time-varying codes.

### 3.1 MODERATE ACTIVITY

2/ 1/70 The activity on this day was limited to two early morning injections at approximately 0110 and 0500 UT. The effect was to bathe the spacecraft in a moderate flux of 3000 volt electrons. From previous experience, we can estimate that had the spacecraft gone into eclipse on this day, it would have charged to approximately 1000 volts.

The fluxes associated with this injection were insufficient to cause charging in the sunlight. [For purposes of this report a potential of less than about 50 volts will be neglected since the ATS-5 detectors do not sense lower energies]. Furthermore, isolated substorms of this type have never been seen to charge ATS-5 significantly. However, from ATS-6 data we

can estimate that a potential of at least -5 volts occurred and that by simply renormalizing the total flux by a factor of 2-10 while keeping the same spectral shape, we can simulate the conditions under which daylight charging of -100 volts would happen.

Detailed spectra are provided for 0300 to see the pre-electron encounter conditions. The next spectra are at 0400 when the high-energy protons had been encountered, but not the associated electrons. The next three sets of spectra are taken at different points in the main part of the substorm. At 0530 ATS-5 experiences the greatest flux of high energy electrons. By 0630 the average energy of the electrons has fallen slightly due to gradient drifting while the average energy of the ions has increased slightly. At 0730 the ion chasm is well developed, and a notch has developed in the electron spectra. This feature is common and will persist for the entire day. A final set of spectra taken at 1200 is provided simply to complete the story. The spectra at 0530 and 0630 are probably the most hazardous to the spacecraft.

In summary, 2/1/70 is a good example of isolated, moderate activity which could be used to study the response of a spacecraft to a normal environment.

### 3.2 INTENSE LOCALIZED POST MIDNIGHT SUBSTORM

2/11/70 On this day we were fortunate enough to find an intense substorm occurring right at the spacecraft location. This day is particularly valuable because of the lack of complicating activity at other times, and because no corrections for daylight charging are needed.

The injection took place at 0850 when ATS-5 was located in the hazardous midnight-to-dawn sector. The total fluxes at 0900 were quite close (within a fraction of 2) of charging the spacecraft in sunlight.

The first set of spectra are taken in the quiescent plasma at 0700. The next spectra taken at 0900 show the first encounter with this event. The low-energy spike seen in both electron detectors is not due, as might be suspected, to charging positively, but rather is most likely the locally produced secondaries being reflected from a suddenly enhanced plasma sheath about the spacecraft (see discussion by Whipple, 1976). This event could easily have produced charging in excess of 10,000 volts if the spacecraft had been eclipsed at this time. Such a sharp, localized event was probably responsible for the main power supply failing on a non-NASA spacecraft. (Note both ATS-5 and ATS-6 are research craft and are somewhat better built than operational craft. Therefore one is not surprised that they can sail through disturbances that would sink weaker vehicles).

Spectra at 1000 and 1100 document the evolution of the event in the normal manner. The predominant spectral changes are again caused by gradient drifts.

Spectra at 1400 and 1700 show the complex spectra that can result from the combination of injected particles, particle losses (the chasm in the protons, and loss of high-energy electrons), and multiple encounters with the high-energy particles as they circle the earth. These spectra would be useful for studying spacecraft conditions near noon. However, a low-temperature plasma must be assumed to be present in both sets (see previous section.) (See also the description of day 12/3/70 for a similar event.)

### 3.3 QUIET DAY

2/12/70 This day was chosen to illustrate a quiet period partly because it is one of the longest quiet times normally seen, and because it fortunately followed the intense event already described on 2/11/70.

Therefore we have a single two-day period of uncommon interest for this

project. Note that we have small data gaps at both the start and end of the day. These are of no consequence since the activity is so low.

The spectra for this day is simply spaced throughout to sample uniformly. Any use of these spectra must assume the presence of copious cold (or "warm") plasma with densities of at least 30/cm.

#### 3.4 POST-MIDNIGHT SUBSTORM

3/18/70 The event shown on this day actually consists of two closely spaced injections occurring after a large quiet period. The activity starts at about 1040 VT. This is sufficiently past midnight that the plasma response is very different than the case shown for 2/11/70. In particular, the main body of protons do not reach the spacecraft until about 1330 after travelling around the world to the west. This situation could produce hazardous charging.

The first set of spectra taken at 0900 set the stage for the later injection. The next three sets are spaced somewhat closer than the nominal minimum of one hour followed in the rest of this report. This was necessary because of the rapid development and the desire to show all phases of the event. The set at 1000 shows some electron enhancement over the earlier spectra. The 1050 spectra shows the leading edge of the injection. [Note the apparent oscillations in the electron spectra in this and the following set are an unavoidable artifact due to the particular operating mode chosen that day and the relatively rapid changes taking place]. At 1112 we see significant changes in both the low-energy electrons and the shape of the protons. But at 1200 we see even hotter electrons instead of the effective cooling we would expect normally. The explanation is easily seen in the spectrogram: another injection has followed this first. This is common and does not affect the usefulness of this day for the report.

The final set of spectra follow the injection development. Only

now we see that the electrons have experienced rapid depletion (by probably precipitating into the atmosphere) and the arrival of the protons from their trip around the world has given us a spike in the distribution.

### 3.5 PRE-MIDNIGHT SUBSTORM

12/3/70 The main feature of this day is the surplus of high-energy protons early in the day. Although this condition is probably not hazardous to spacecraft from the point of view of charging, it is a common occurrence, and the vehicle's response should be studied. Spectra are provided for 0200, 0400, 0600, 0700, 0800, and 1200 LT. The first four are of prime interest for the study of the effect of high-energy protons. The 0800 spectra can be used in a way similar to those of 2/11/70 for intense localized substorms. The main difference between the two being the higher energies, but lower fluxes seen on 12/3/70. The last set of spectra (1200 LT) are provided simply to show the time development of the storm.

### 3.6 ECLIPSE AND SUNLIGHT CHARGING

3/14/71 Although the intent of this report is to provide isolated examples of various types of events at synchronous altitude, we realize that for many purposes this is not sufficient. Therefore we also present an active day which has both charging in eclipse and a good example of charging in sunlight. As can be seen from the spectrogram, this day is very different from the other examples. Several distinct substorms follow one after the other. The plasma conditions change so quickly that obtaining good averages is difficult. The charging events are easily identified by the bright bands in the low energy protons. The eclipse is always centered about local midnight, and the sunlight charging on ATS-5 is always observed between midnight and dawn.

The first spectra taken at 0600 is pre-eclipse. The next two are at different phases of the eclipse. The 0800 set in post-eclipse. The last two sets of spectra are preceding and during sunlight charging.

The parallel electrons in the last two cases show the effects of differential charging.

Persons using this set of data might want to correct the fluxes to what they would be if there were no charging. The cookbook method for doing this assumes that the instrument is a differential detector. Then by Liouville's theorem,

$$J_p(E) = [E^2/(E - q\phi)^2] J_m(E - q\phi)$$

where  $J_p$  is the predicted flux at energy  $E$ ,  $J_m$  is the measured flux, and  $\phi$  is the potential. The sign of the charge,  $q$ , is positive for ions and negative for electrons.

For the one sunlight charge case shown,  $\phi$  is -80 volts. Therefore corrections above a few thousands of volts are unnecessary. For the eclipse cases essentially all channels should be corrected.

The lowest energy fluxes of electrons and the highest energy ions will be missing from the corrected spectra.

## APPENDIX A

### DESCRIPTION OF ATS-5 SPECTROGRAMS

#### Format

The spectrograms are produced in pairs: one showing the spectra from the perpendicular proton and the perpendicular electron analyzers and one showing the spectra from the parallel proton and electron analyzers. They are labeled by a large  $\perp$  or  $\parallel$  on the middle left side. The proton part is always below the electron part. The day of the year (January 1 equals day 1) and year is given at the bottom. The month, day in month, and year are also given at the left just above the  $\perp$  or  $\parallel$  label. The times at the beginnings and ends of the spectrograms can be arbitrarily set, and can cover any desired time span. Time scales covering as little as 10 minutes and as great as 4 days have been used. When more than one day is encompassed, either negative hours or hours greater than 24 are used to prevent any ambiguity. Grey scales are located at the right. Six different integrals are plotted in grey coded bands in the upper part along with magnetic field quantities. At the very top are two data quality indicators.

#### Grey Scale Interpretation

The primary value of spectrograms is their ability to reveal patterns in the energy-time plane. The determination of actual flux levels from them is of secondary importance. For this reason, and because of the loss in time resolution, the option which produces a coded pattern with which accurate flux values can be obtained is now rarely used. Color coding also permits accurate values to be obtained, but is more

expensive than grey coding. In the present case, color is reserved for adding another dimension: by superimposing the perpendicular and parallel spectrograms with color filters limiting each to one-half of the visible spectrum, the energy and time dependence of the pitch angle anisotropies are clearly displayed as patterns of different shades of color.

Should one desire to estimate the flux at a given point on a spectrogram, first locate the corresponding level on the grey scale at the lower right and determine the value of "G" on the scale marked 0 to 3. The differential energy flux in  $\text{ev/cm}^2 \text{ sec sr ev}$  is then given by

$$(10^G - 1) 10^b + 4.367$$

where b is given by "EL" in the lower left corner of the spectrogram for the electron fluxes or "PR" for the proton fluxes. The value of "ST" in the lower left corner gives the change in G between each of the 33 discrete grey levels available.

One option available is to let the grey scale recycle repeatedly instead of simply saturating. This option with a small value of "ST" is used to reveal small variations over a wide dynamic range of fluxes.

### Energy Scales

The computer program which generates the spectrograms can utilize any arbitrary function of energy for the energy scales for exhibiting all or any part of the measured spectra. The entire range from 50 ev to 50 kev is usually plotted with one of the two types of scales:

1. logarithmic with 50 ev at the bottom for both protons and electrons.
2. proportional to  $1/(E + 3 \text{ kev})$  with the electron part inverted and sharing the same point with the protons at zero energy. The bias of 3 kev was arbitrarily chosen to give a good presentation of the 50 ev to 50 kev energy range. If the scale, S, is taken to be 0.0 at infinite proton energy, 1.0 at zero electron and proton energy and 2.0 at infinite electron energy, then

$$S = \frac{E(1-q) + 3 \text{ kev}}{E + 3 \text{ kev}} \quad \text{where } E \text{ is the particle energy in kev}$$

$q = \pm 1$  depending on the sign of the particle's charge.

Note that at low energies,  $S \simeq 1 + qE/3 \text{ kev}$ . Time tic marks are located at  $S = 0, 1,$  and  $2$ . The extrapolation of dispersion curves back to the time marks (at  $S = 0$  or  $2$ ) yields the time infinite energy particles would have arrived, and therefore, the time of the event responsible for the dispersing particles. The slopes of the high energy parts of dispersion curves give a measure of the distance of the satellite from the regions in which the particles were perturbed, but it is apparently necessary to include electric field effects to obtain useful accuracy.

## Subsidiary Data

A number of useful quantities are given in the lower left hand corner.

The analyzers in the "master" and "mate" channels are identified by numbers following "MASTR" and "MATE" according to the scheme:

1. perpendicular electron analyzer
2. perpendicular proton analyzer
3. parallel electron analyzer
4. parallel proton analyzer

TA = averaging time for the spectra in minutes.

TS = time between spectral averages in minutes.

TM = averaging time for the magnetic data in minutes.

The seven bit command word is given immediately below "COMMAND".

The first three bits give the channel assignments and are therefore redundant to the master and mate identifications given above. Bits 4 and 5 specify the operating mode according to the scheme:

<u>bit</u>	<u>4</u>	<u>5</u>	<u>Mode</u>
	0	0	track-scan
	0	1	single step scan only
	1	0	track only
	1	1	double step scan only

Bits 6 and 7 not set to zero correspond to other modes which are rarely used.

"ST", "EL", and "PR" are described above.

"PSNG" specifies the quantity being plotted in the spectrogram according to the scheme:

1. differential energy flux
2. differential number flux
3. ratios of the flux averaged over "TS" minutes to the flux averaged over the previous "TA" - "TS" minutes.
4. ratios of adjacent energy steps.

Options other than the first are used only in special studies.

If the option to make the background black rather than white has been used, then "PSNG" will be negative. A black background is preferred for slides that are to be projected.

#### Magnetic Field

Data from the ATS-5 magnetometer have been kindly supplied by T. Skillman of the Goddard Space Flight Center and are plotted above the spectral data along with lines at 0, 50, 100 and 150 gammas. The data are not corrected for the effects of time changes in the spacecraft current systems. These perturbations can be as large as 15 gammas. The absolute value of the magnetic field component parallel and perpendicular to the spin axis is given by the darker and lighter points respectively (and usually the upper and lower respectively) with the spectrograms of the perpendicular analyzers. The perpendicular component is obtained using only the coarse (33 gamma step size) data and is thus uncertain by at least  $\pm 10$  gammas. Most of the scatter in this component is due to using only the coarse data.

The magnitude of the field and the angle of the field to the spin axis are given by the lighter and darker points respectively (and usually the upper and lower respectively) with the spectrograms of the parallel

analyzers. The angle to the spin axis is given in degrees. Both the magnitude and angle are subject to the additional uncertainties in the perpendicular component.

### Integrals

Above and below the magnetometer data are six strips in which various quantities are logarithmically encoded in a grey scale such that a ratio of about 2000 to 1 is covered in going from black to white.

In the 1st, 2nd, 3rd, and 5th strips, the following integrals from the perpendicular and parallel analyzers are plotted with perpendicular and parallel spectra respectively:

<u>Label</u>	<u>Quantity</u>	<u>Value at Midpoint of Grey Scale</u>
PR N DEN	proton number density	1.0 proton/cm <sup>3</sup>
EL N DEN	electron number density	1.0 electron/cm <sup>3</sup>
E E FLX	electron energy flux	1.0 erg/cm <sup>2</sup> sec sr
PR E FLX	proton energy flux	1.0 erg/cm <sup>2</sup> sec sr

In the 4th strip labeled "PRESSURE", the total perpendicular electron plus proton pressure is plotted with the spectrogram of the perpendicular detectors with a midpoint value of  $10^{-8}$  dynes/cm<sup>2</sup>. In the 4th strip with the parallel data, the magnetic field pressure is plotted with a midpoint value of  $2 \times 10^{-8}$  dynes/cm<sup>2</sup>.

In the 6th strip (near the top) labeled "PAR NFLX" the parallel electron number flux is plotted with the spectrogram of the perpendicular detectors with a midpoint value of  $10^8$  electron/cm<sup>2</sup> sec sr. In the top strip with the parallel data, the parallel proton number flux is plotted with a midpoint value of  $10^7$  protons/cm<sup>2</sup> sec sr.

## Data Quality Indicators

At the very top of the spectrogram is a line which increases in breadth with an increasing percentage of missing data. In the track-scan mode, about 73 percent of the potential data is usually "missing" since 75 percent of the time is spent tracking a peak in a narrow spectral region. When data are not available, previous data are used unless the time gap is greater than 30 minutes in which case the spectrograms are left blank. The top line, of course, goes to its maximum width during gaps in the data. The magnetometer data is not plotted during such gaps. Care must be exercised to avoid false interpretations of spectrograms containing data padded in from an earlier time.

Just below the missing data line is a line which becomes darker and thicker with increasing numbers of bad points. Often the quality of data transmission is such that over one percent of the data points are bad. Even the highest quality data being obtained are usually incorrect more than 0.1 percent of the time. This corresponds to over 800 bad data points per day of data. A data editing scheme has been devised which eliminates approximately 99 percent of the bad data and rarely removes data later judged to be good. Failure to remove bad points usually occurs when the false data happen to form a self-consistent context. This type of failure to edit properly is responsible for the two white areas in the lower right of Figure 4. The bad data indicating line reaches its maximum thickness when there are more than 10 bad points in the four spectra measured during the time covered between averages (equal to "TS").

## APPENDIX B

### DESCRIPTION OF ATS-5 SPECTRAL AVERAGE PLOTS

#### Format

The spectra from the two electron and the two proton analyzers are plotted in adjoining log-log plots with borders at 30 ev and 100 kev. The range of the vertical scale is variable and depends upon whether the differential energy flux or the differential number flux is being plotted. The parallel electron spectrum is shifted down by a factor of 100 (i.e.  $\times 0.01$ ) and the perpendicular proton spectrum is shifted up by a factor of 100 (i.e.  $\times 100$ ). These shifts usually provide adequate separation and place the perpendicular spectra above the parallel spectra in each case.

The universal time at the midpoint of the data being averaged over is given twice at the top of the plots. On the left hand (electron) side, the time is given in hours, minutes, tenths of minute, month, day of month, and year, and is followed by the averaging time in minutes. On the right hand (proton) side, the time is given in hours (to the nearest one thousandth of an hour), day of year (January 1 equals day 1), and the year. The local time in hours and minutes is sometimes added on the left side.

Also given near the top are four different integrals over each of the four spectra. The integrals for the perpendicular data are given above the integrals for the parallel data. Following two of these sets of integrals will be found the words "MASTER" and "MATE" to indicate which analyzers are occupying the two non-subcommutated data channels.

When in the track mode, the "master" analyzer controls the peak tracking system. The operating mode (for example the scan only or track-scan modes) of the system is given on the right side.

#### Error Bars

Vertical bars which encompass the middle 68.26 percent of the Poisson distribution are given at each data point. At high rates, they correspond to plus and minus one standard deviation. The approximation  $N_{\pm} = N \pm \sqrt{N} (1.0 - 0.17/N)$  is used where N is the total number of counts accumulated at the point.

When in the track-scan mode, there are about four times the number of accumulations at the points near the energy of the peak being tracked than at other energies. Also the spectra from the "Master and "Mate" channels will have about twice the accumulation time as the other two (subcommutated) spectra.

When in the single step scan only mode, every other data point in the subcommutated spectra will be missing. This under-sampling of the spectra can lead to substantial errors in the smooth line drawn through the data points since structure as sharp as the instruments' resolution is frequently observed.

If zero counts are obtained, then the error bar is replaced by a triangle pointing up to the line which is placed at one-half the flux corresponding to one count being accumulated.

If no data are available for a point during the time period being averaged over, then the flux obtained during a preceding time period is inserted. In this case, the error bar is replaced by a triangle pointing down to the data point.

## Integrals Over the Spectra

The four integrals given for each analyzer at the top of the plots are of course intrinsically directional quantities. The parallel cases correspond to pitch angles  $\alpha \sim 0$  ( $\alpha$  = the angle of the spin vector to the magnetic field vector) and the perpendicular cases correspond to averages over the pitch angle range of  $90 \pm \alpha$  degrees. The integrals are taken only over the measured range of 50 ev to 50 kev and are, therefore, lower limits.

The number densities in particles/cm<sup>3</sup> are labeled "DEN" and correspond to  $4\pi$  times the directional number densities in particles/cm<sup>3</sup> sr.

The particle pressures in  $10^{-9}$  dynes/cm<sup>2</sup> are labeled "PRES". They correspond to  $8\pi/3$  times the directional energy densities in ergs/cm<sup>3</sup> sr. The multiplication by  $8\pi/3$  simplifies computation of the total particle pressure perpendicular to the magnetic field vector.

The directional energy fluxes in ergs/cm<sup>2</sup> sec sr are labeled "E FLX".

The directional number fluxes in  $10^6$  particles/cm<sup>2</sup> sec sr are labeled "N FLX".

## REFERENCES

- Akasofu, S. I., Polar and Magnetospheric Substorms, D. Reidel Publishing Company, Dordrecht, Netherlands (1968).
- Chappel, C. R., "A study of the Influence of Magnetic Activity on the location of the plasmopause as measured by OGO 5", J. Geophys. Res. 75, 50 (1970).
- DeForest, S. E. and C. E. McIlwain, Plasma Clouds in the Magnetosphere, J. Geophys. Res. 76, 3587, (1971).
- DeForest, S. E., Spacecraft Charging at Synchronous Orbit, J. Geophys. Res. 77, 651, 1972 (U).
- DeForest, S. E., Electrostatic Potentials developed by ATS-5, Photon and Particle Interactions with Surfaces in Space, pp 263-276, D. Reidel Publishing Co., Dordrecht, Holland, 1973 (U).
- Konradi, Andrei, C. L. Semar and T. A. Fritz, Substorm-Injected Protons and Electrons and the Injection Boundary Model, J. Geophys. Res., 80, 543, (1975).
- Lezniak, T. W. and J. R. Winkler, Experimental Study of the Magnetospheric Motions and the Acceleration of Energetic Electrons during Substorms, J. Geophys. Res., 75, 7075, (1971).
- Mauk, Barry and C. E. McIlwain, Correlation of Kp with the Substorm-Injected Plasma Boundary, J. Geophys. Res., 79, 3193, (1974).
- McIlwain, C. W., Plasma Convection in the Vicinity of the Geosynchronous Orbit, in Earth's Magnetospheric Processes, D. Reidel, Dordrecht, Netherlands (1972).
- McIlwain, C. E., Substorm Injection Boundaries, in Magnetospheric Physics, edited by B. M. McCormack, p. 143, D. Reidel, Dordrecht, Netherlands (1974).
- McIlwain, C. E., Auroral Electron Beams Near the Magnetic Equator, in Physics of the Hot Plasma in the Magnetosphere, Edited by B. Hultquist and L. Stenflo, Plenum, New York, (1975).
- McPherson, D. A., D. P. Cauffman and Capt. W. Schober, AIAA 13th Aerospace Meeting, January 1975 (U).
- Meulenberg, A., Evidence for a New Discharge Mechanism for Dielectrics in a Plasma, COMSAT Laboratories (1976).
- Reasoner, D. L., W. Lennartsson and C. R. Chappel, The Relationship between the ATS-6 Spacecraft Charging Occurrences and Warm Plasma Encounters, AIAA/AGU Proceedings on Spacecraft Charging, December (1975).

- Rosen, Alan, Spacecraft Charging: Environment Induced Anomalies, AIAA Paper 75-91, AIAA 13th Aerospace Sciences Meeting, Pasadena, Ca., January 20-22, 1975 (U).
- Scarf, F. L. and R. W. Fredricks, Findings regarding Correlation of Satellite Anomalies with Magnetospheric Substorms, TRW Systems Group, February 1972 (U).
- Shaw, R. R., Electrical Discharges caused by Satellite Charging at Synchronous Altitudes, Orbital Data Analysis Report No. 5078-01, July 1974 (U).
- Stevens, John N., Robert R. Lovell and Victore Gore, Spacecraft Charging Investigation, NASA Technical Memorandum, Lewis Research Center, NASA TM X-71795 (1975).
- Vasyliunas, V. M., A survey of Low Energy Electrons in the Evening Sector of the Magnetosphere with Ogo 1 and Ogo 3, J. Geophys. Res., 73, 2839, (1968).
- Whipple, E. C., Observation of Photoelectrons and Secondary Electrons Reflected from a Potential Barrier in the Vicinity of ATS-6, J. Geophys. Res., 81, 715 (1976).

## APPENDIX C

### Construction of Complete Spectra

The data presented in the main report can be combined with experience gained in the ATS-6 program to construct a most probable set of total spectra. This consists of adding other components to the measured fluxes.

Let  $dN$  = number density between  $E$  and  $E + dE$ ,  $\Omega$  and  $\Omega + d\Omega$ , then for the magnetospheric plasma at geosynchronous orbit one has

$$dN = dN_{\text{cold}} + dN_{\text{iso}} + dN_{\text{field aligned}}$$

where

1) COLD

$$dN_{\text{cold}} = N_{\text{cold}} \frac{1}{2\pi^{3/2}} (KT_{\text{cold}})^{-3/2} \sqrt{\epsilon} e^{-(\epsilon/KT_{\text{cold}})}$$

for  $0 \leq \epsilon \leq 50 \text{ ev}$

2) ISOTROPIC

$$dN_{\text{iso}} = \sqrt{\frac{m}{2}} \mathcal{E}^{-3/2} dj$$

for  $50 \text{ ev} \leq \epsilon \leq 50 \text{ kev}$

where  $dj$  = energy flux /  $\text{cm}^2$ -sec-ster = data

3) FIELD ALIGNED

$$dN_{\text{F.A.}} = N_{\text{F.A.}} \left( \frac{m}{2\pi KT_{\text{F.A.}}} \right)^{3/2} \sqrt{\epsilon} e^{-[(\epsilon - 2\sqrt{\epsilon}\sqrt{\epsilon_0} \cos \alpha + \epsilon_0)/KT_{\text{F.A.}}]}$$

for  $0 \leq \epsilon \leq \infty$ ,  $\alpha$  = pitch angle

The total number density

$$N = \int dN \approx N_{\text{cold}} + N_{\text{ISOTROPIC}} + N_{\text{F.A.}}$$

Charge neutrality requires that

$$\sum_i q_i N_{e,i} = 0$$

The temperature chosen for  $T_{\text{cold}}$  should probably be a few volts to a few tens of volts. The density of the cold component can be estimated from Reasoner's work (1975) and figure 2.3 to be about  $30/\text{cm}^3$ .

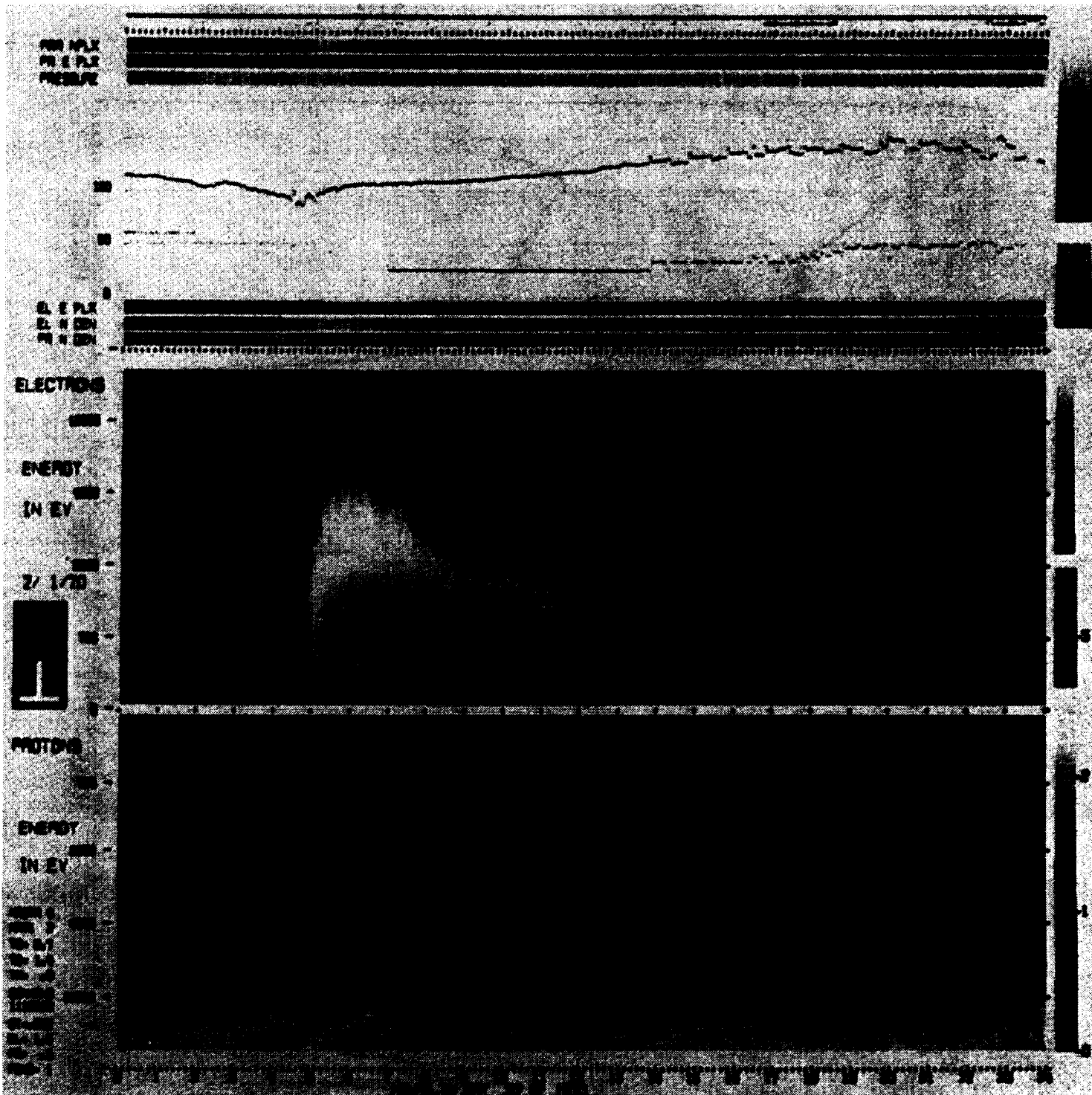
The form for the field-aligned component was derived from the assumption of a displaced maxwellian plasma falling through a potential well of  $\epsilon_0$ . If we assume that these particles have their origins in the ionosphere, then we can estimate  $100 < \epsilon_0 < 10,000$  electron volts and that  $kT_{\text{F.A.}}$  is a few electron volts. The density is more difficult to estimate, but a few percent of the ambient would be consistent with measurements.

Note that the field-aligned component is probably only important for the study of differential charging since it only influences the charge state at locations where the bulk of the plasma is excluded (i.e., in properly oriented cavities on the vehicle).

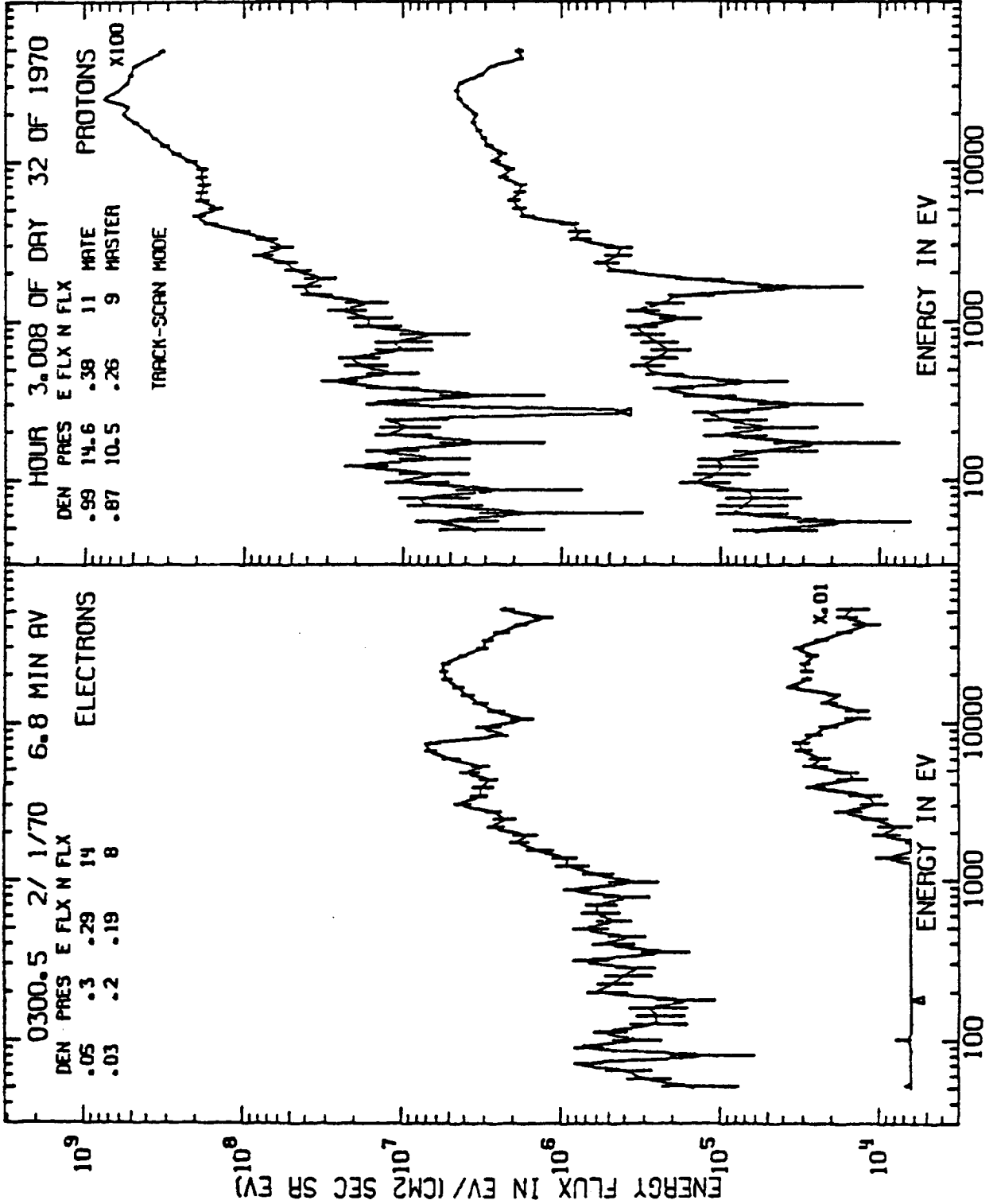
APPENDIX D

DATA

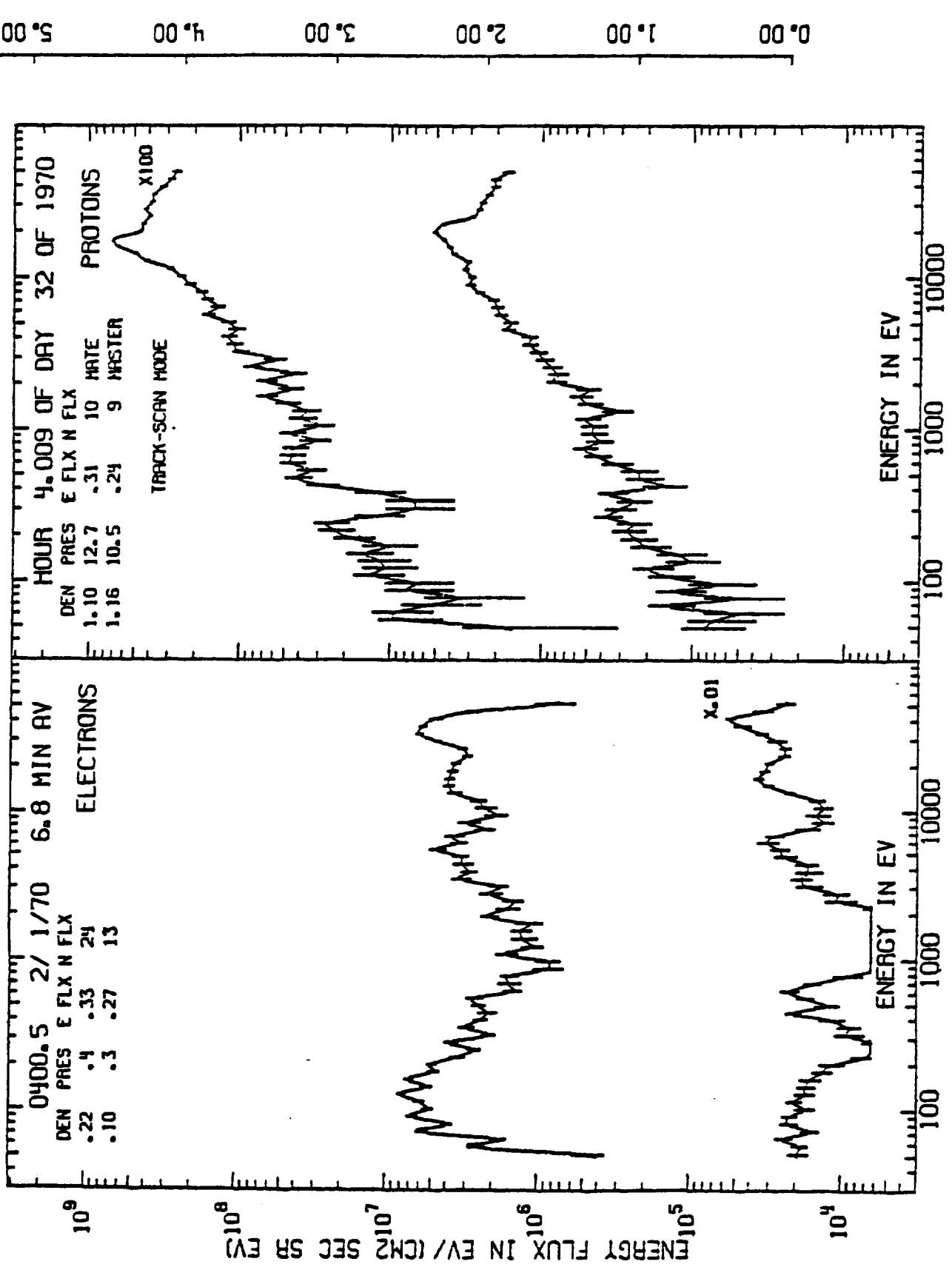
ORIGINAL PAGE IS  
OF POOR QUALITY



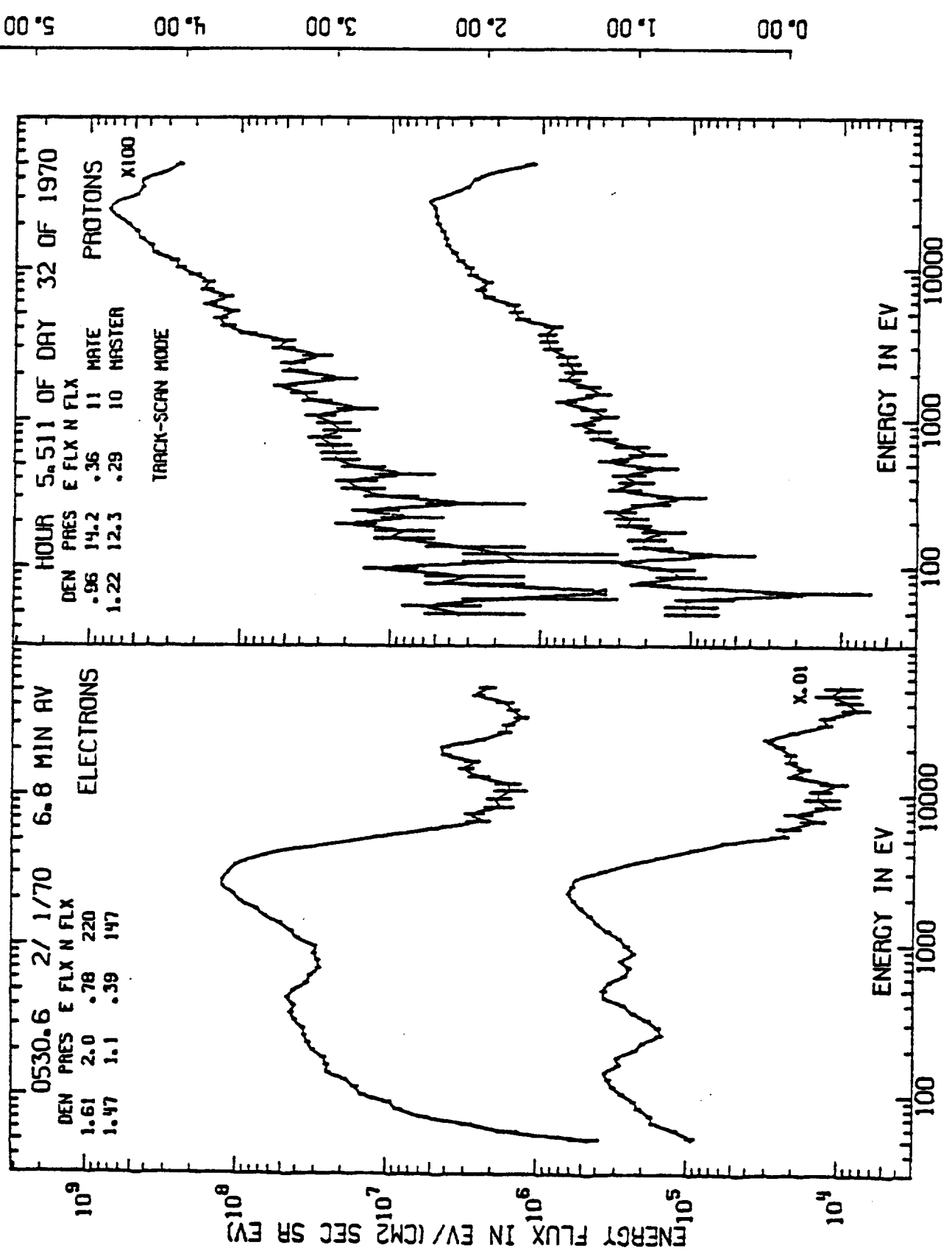
Spectrogram for 2/1/70 - Moderate activity.



0.00 1.00 2.00 3.00 4.00 5.00

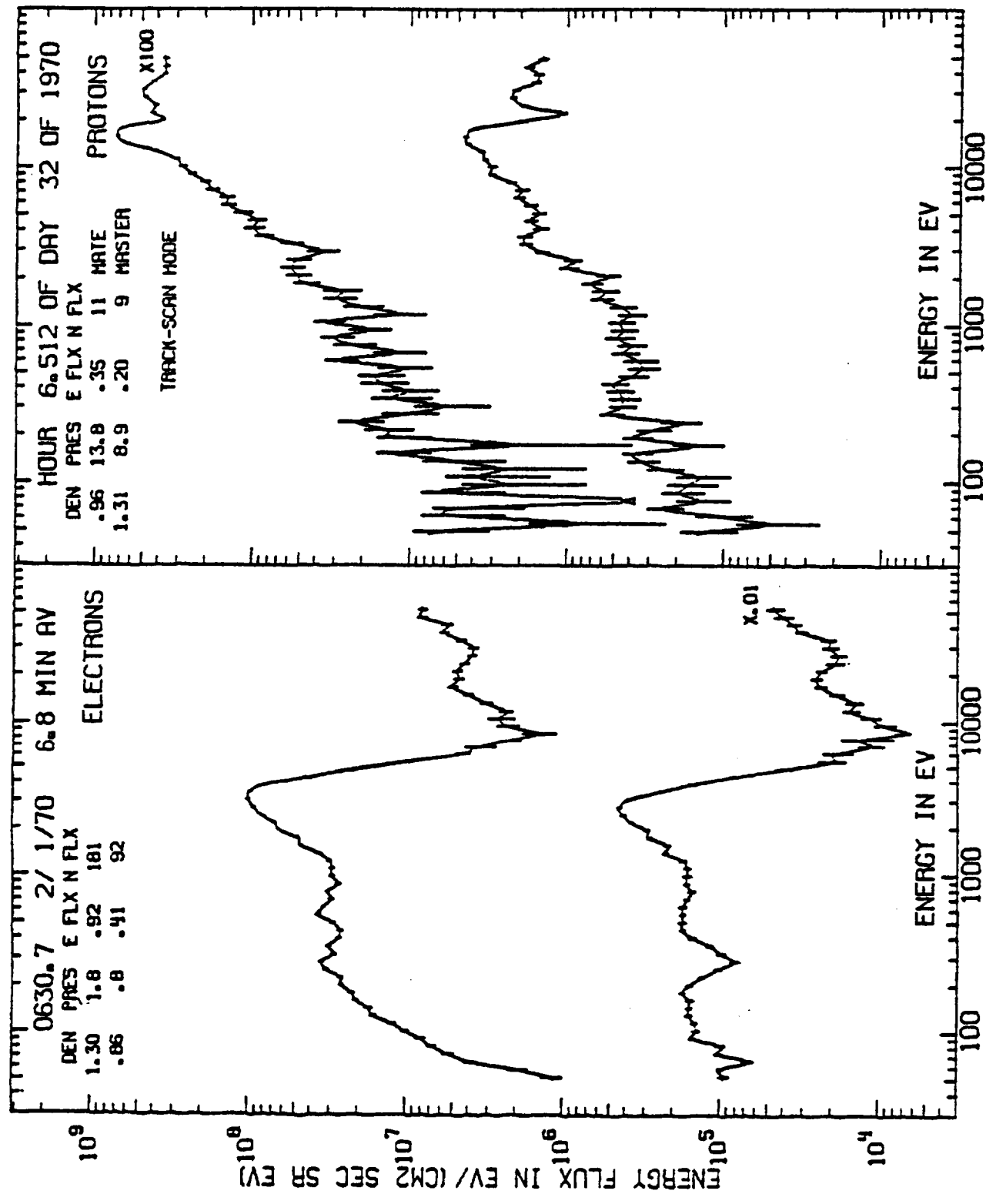


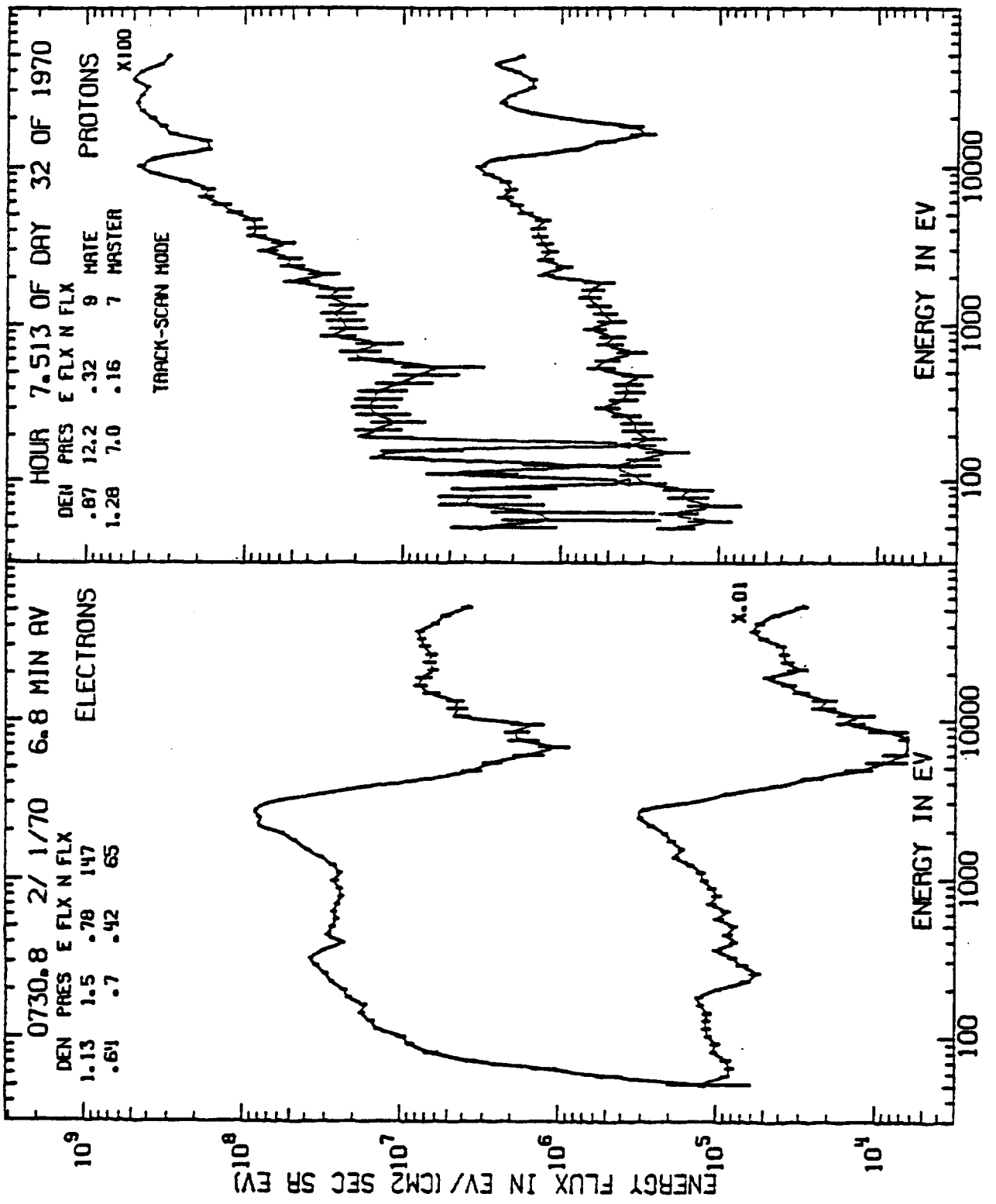
0.00  
1.00  
2.00  
3.00  
4.00  
5.00



0.00  
1.00  
2.00  
3.00  
4.00  
5.00

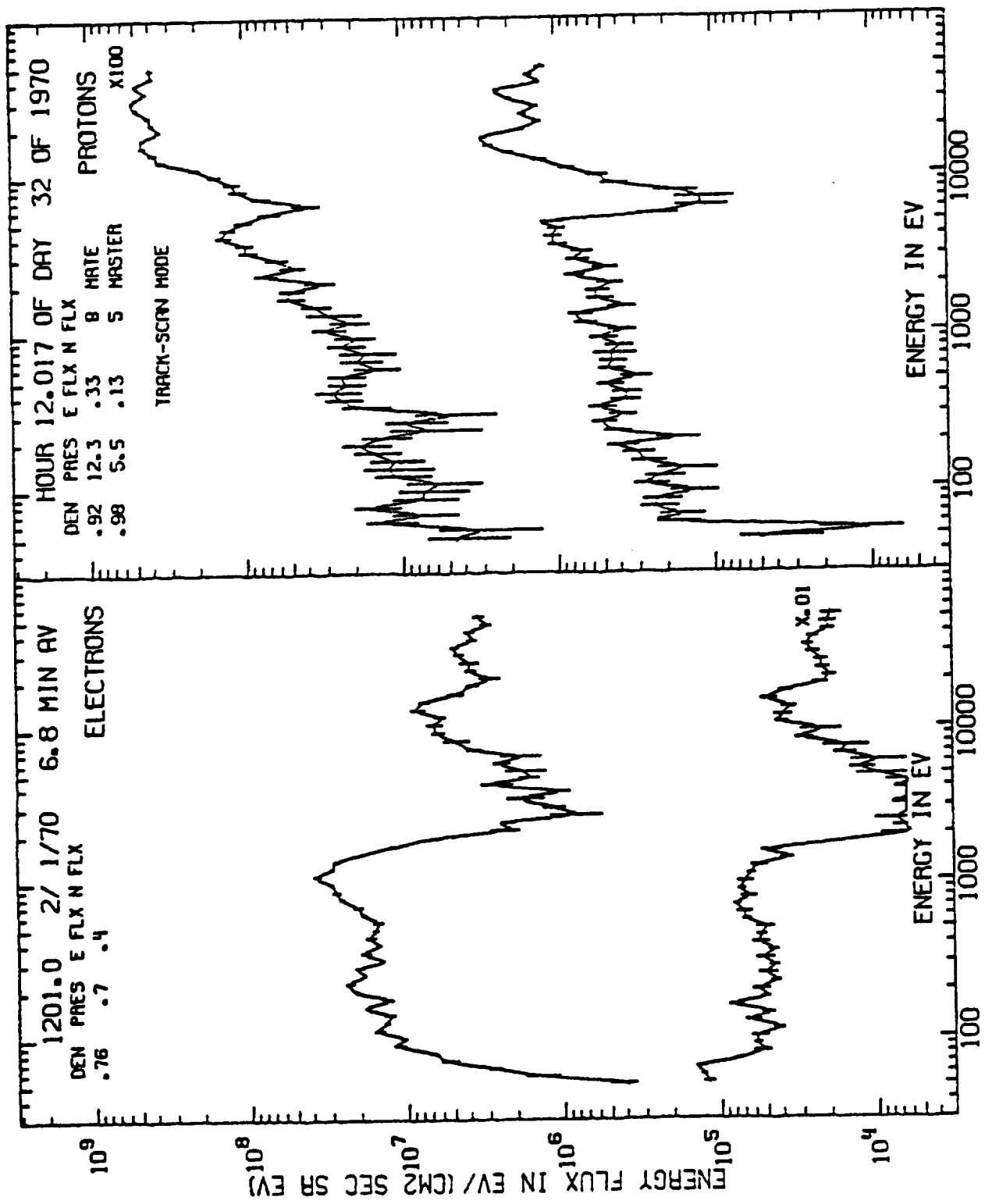
0.00 1.00 2.00 3.00 4.00 5.00



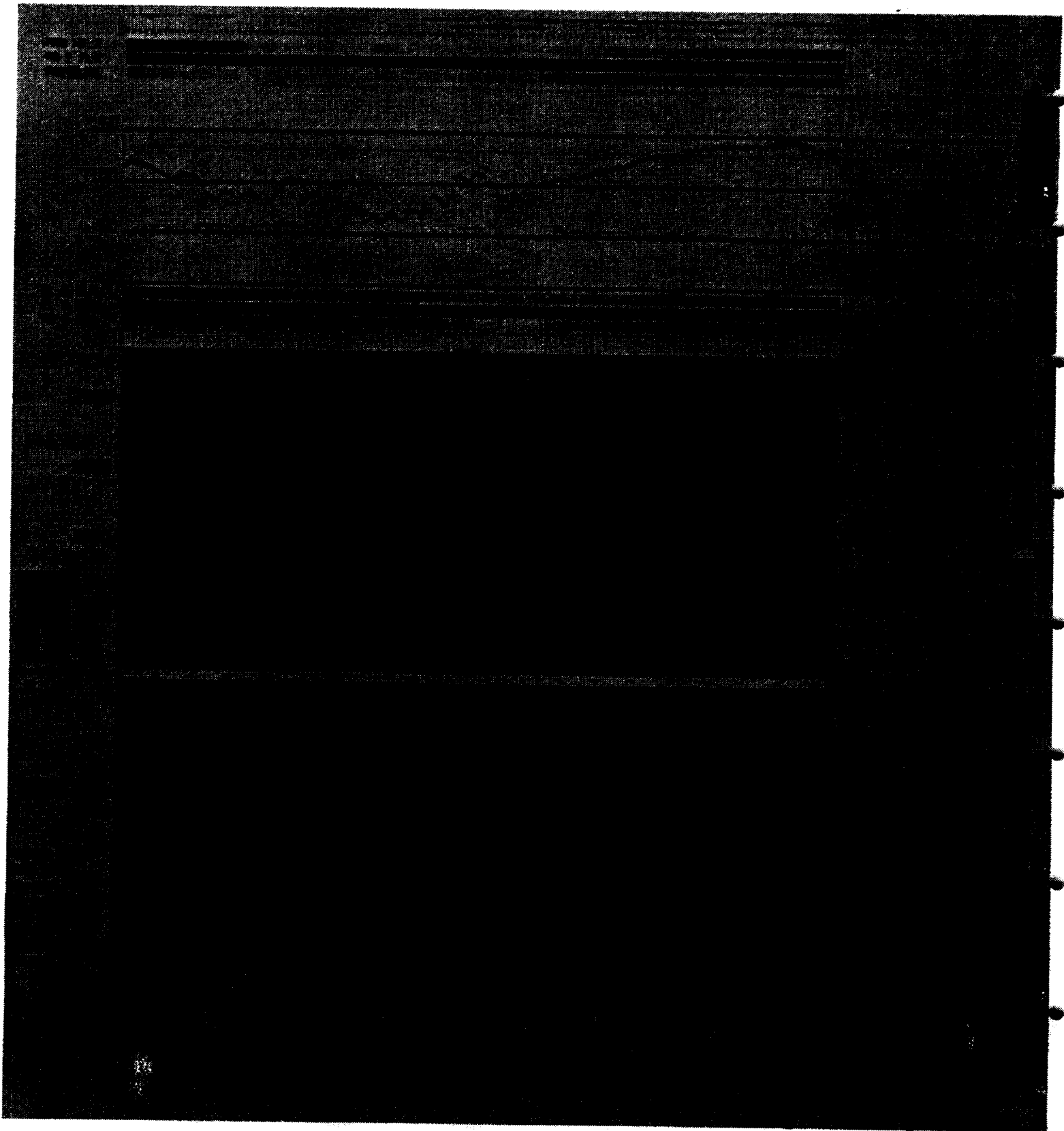


0.00 1.00 2.00 3.00 4.00 5.00

0.00  
1.00  
2.00  
3.00  
4.00  
5.00

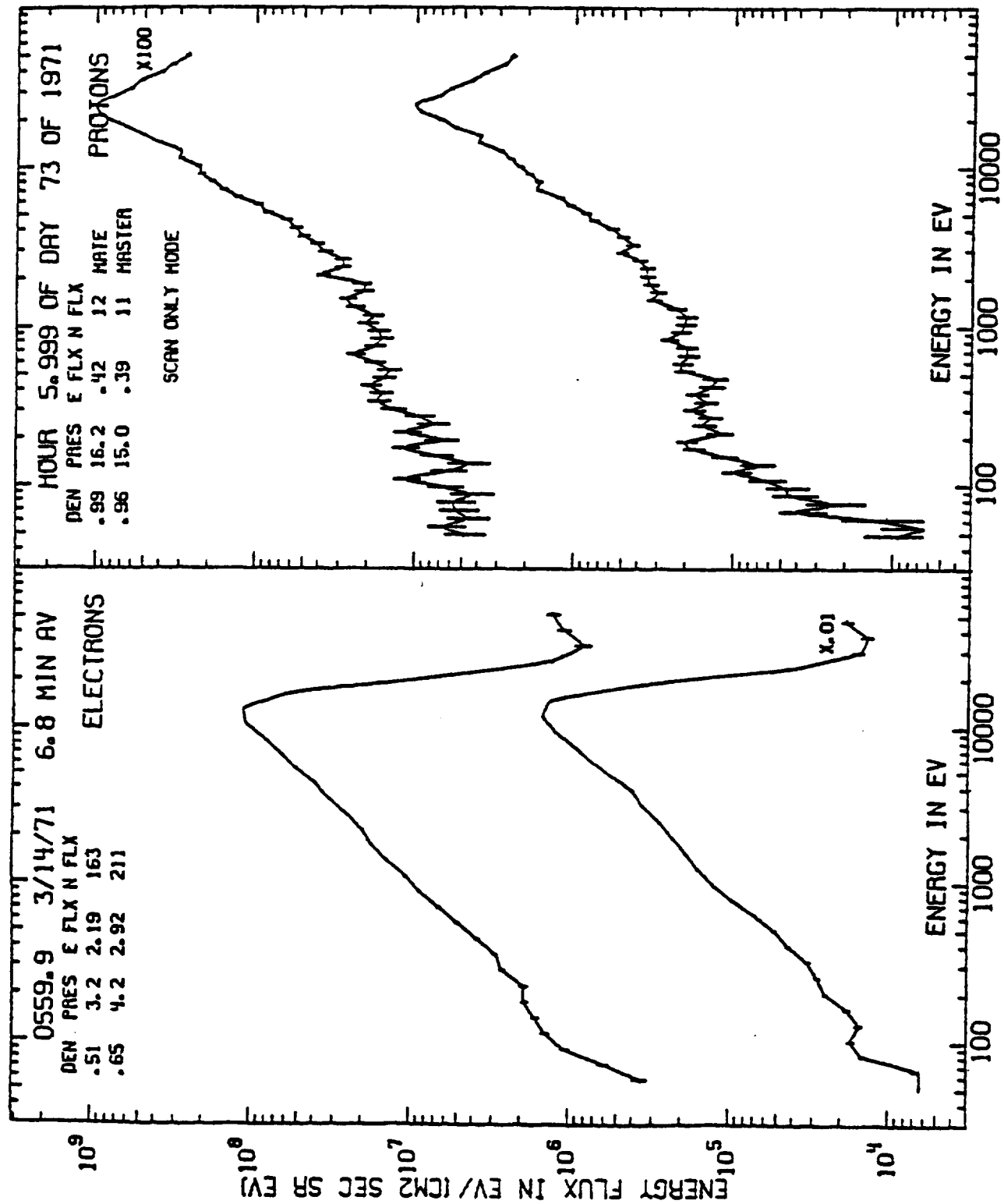


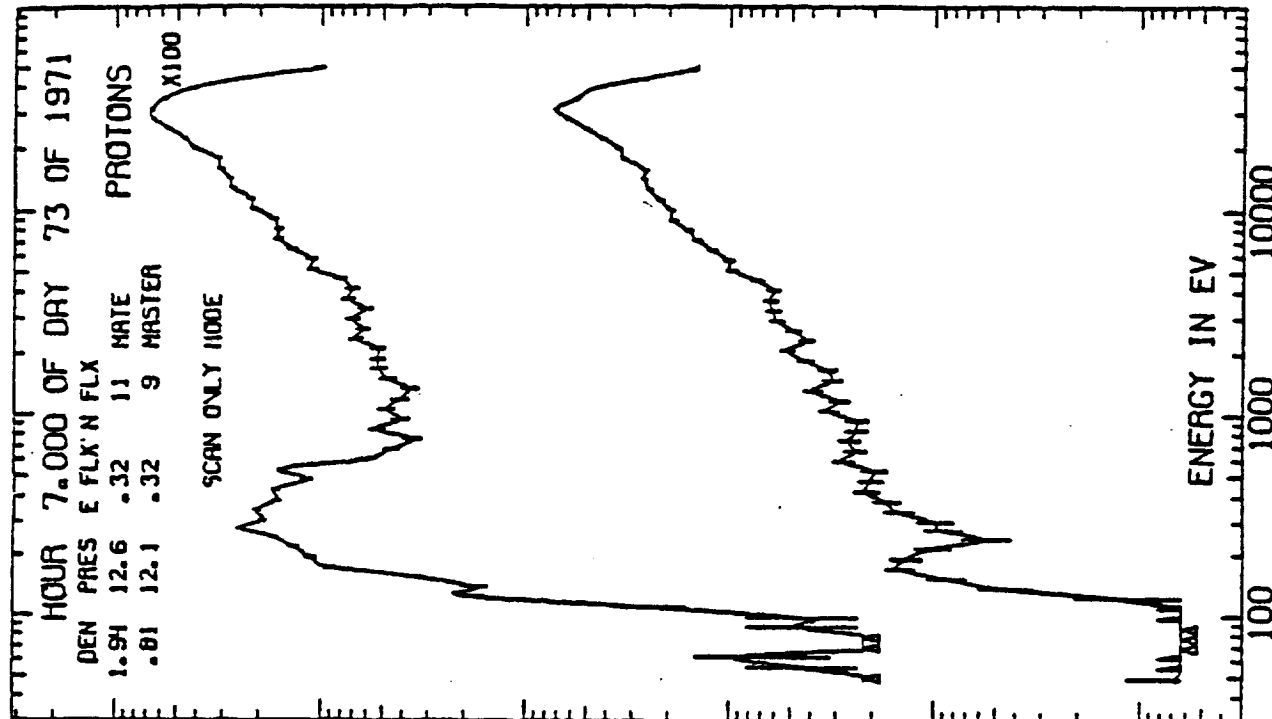
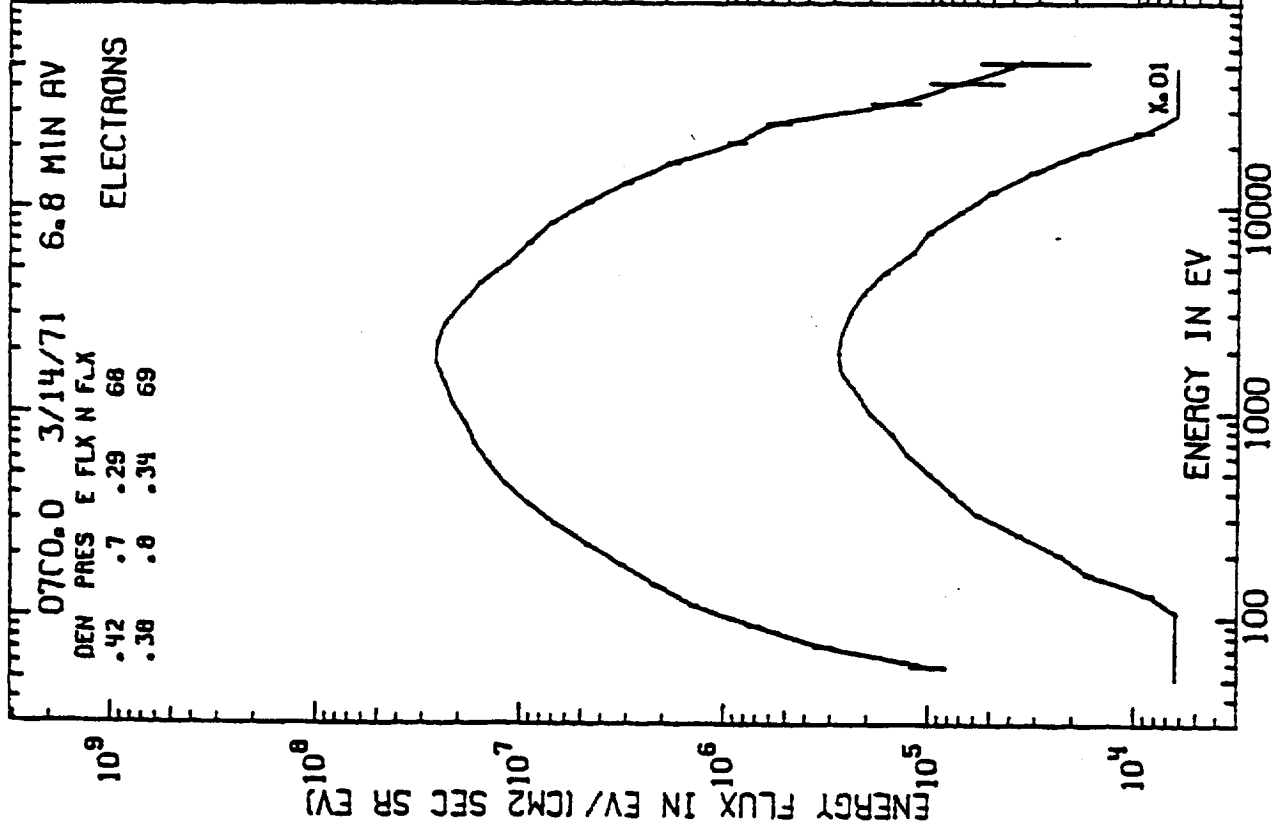
ORIGINAL PAGE IS  
OF POOR QUALITY



Spectrogram for 3/14/71 - Eclipse and sunlight charging.

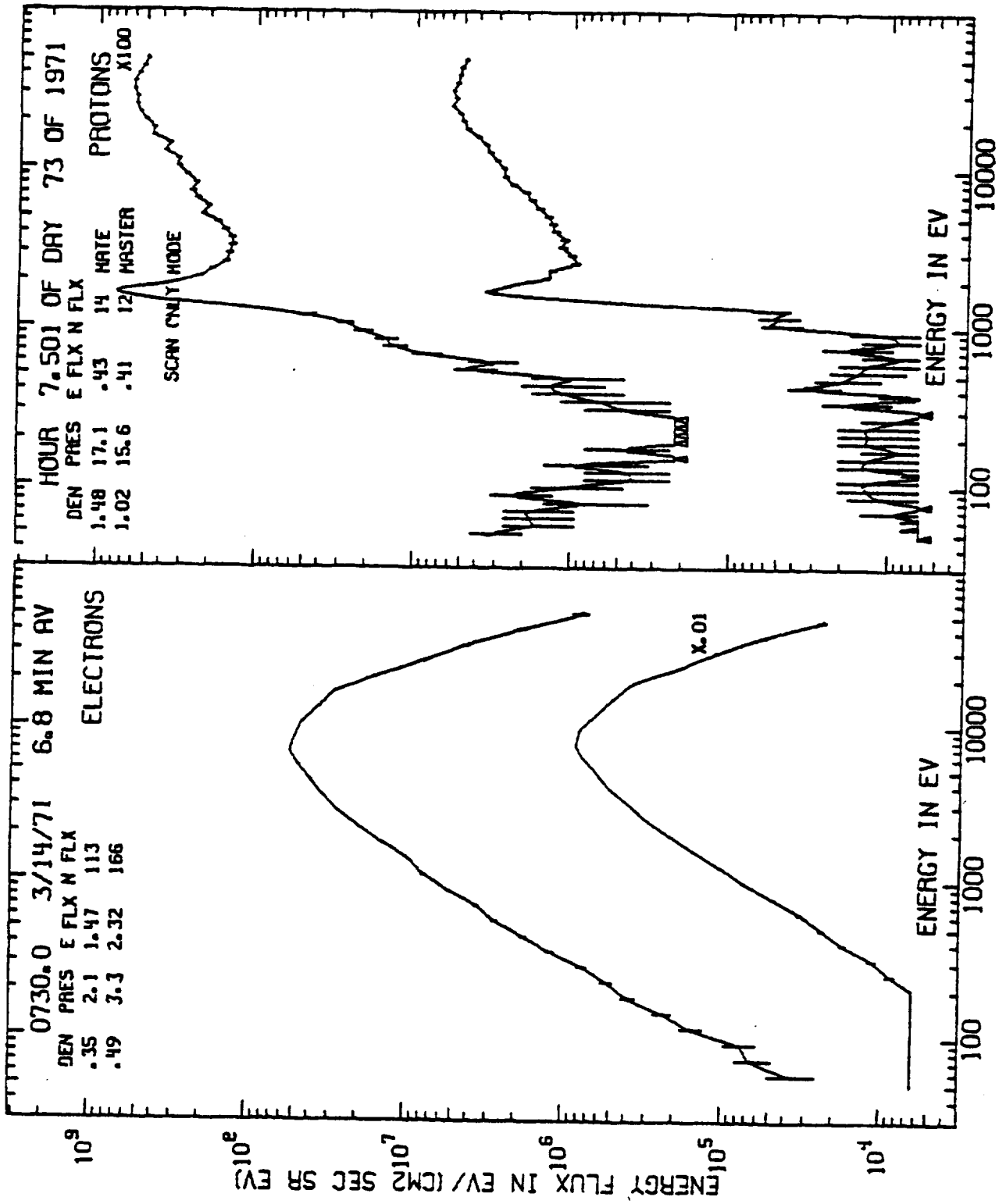
0.00 1.00 2.00 3.00 4.00 5.00

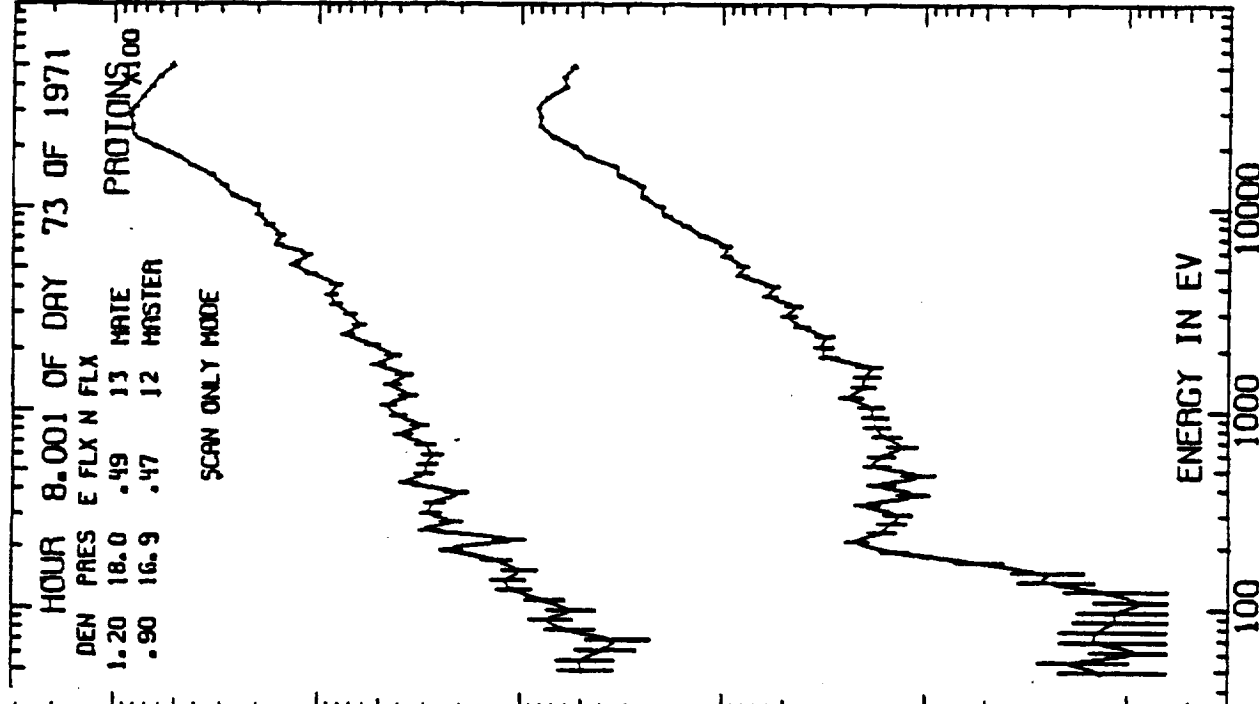
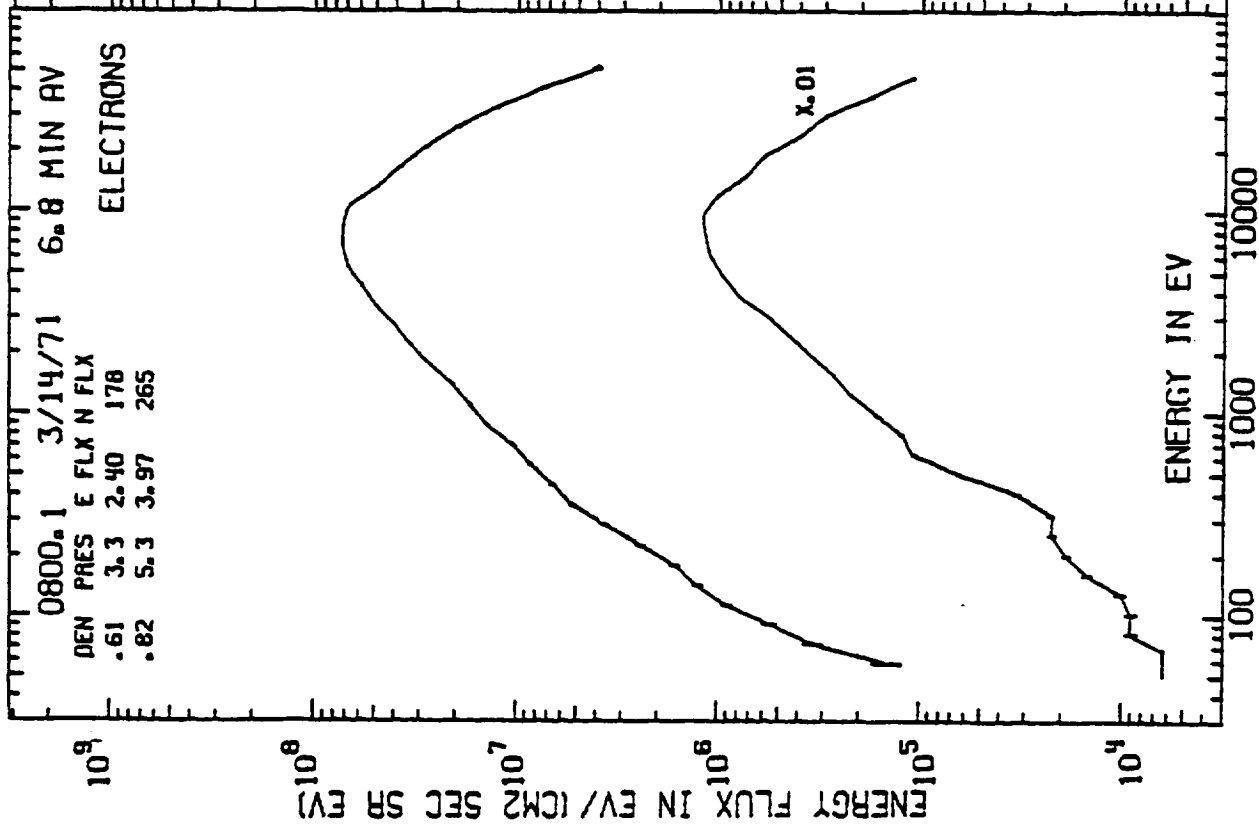




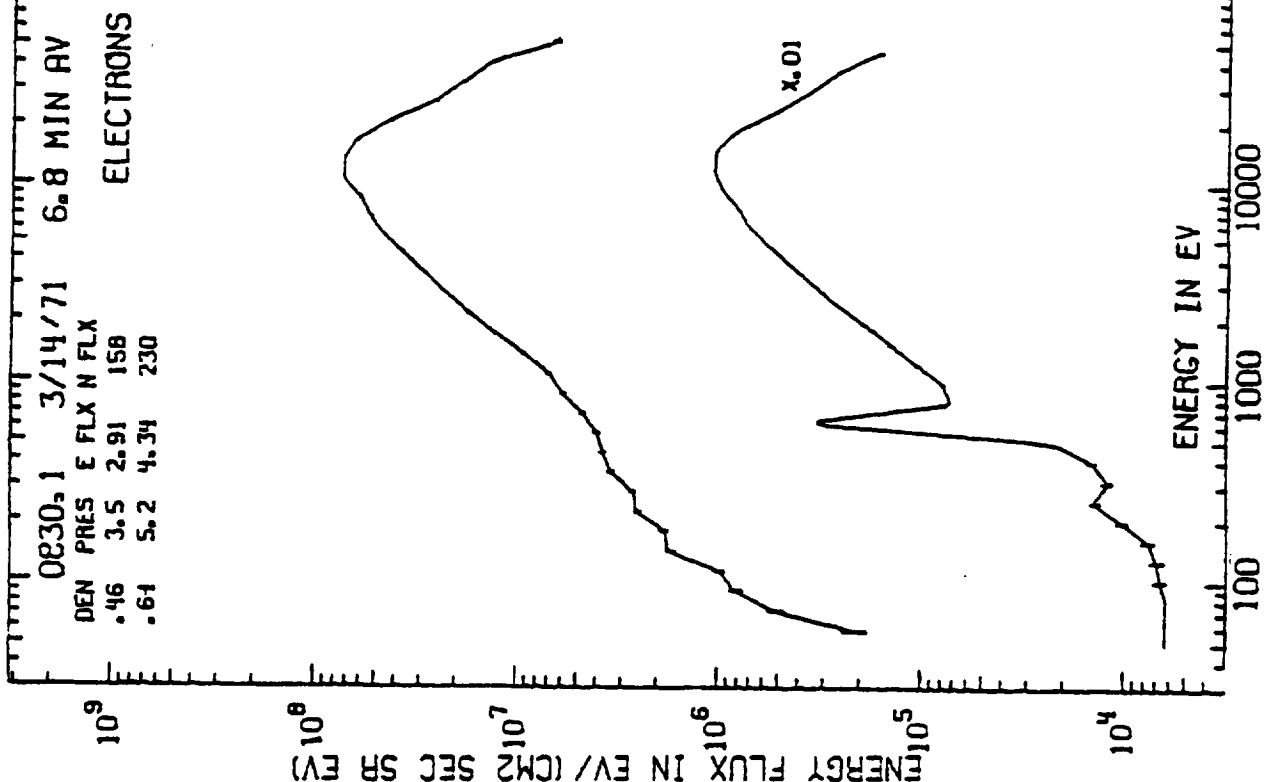
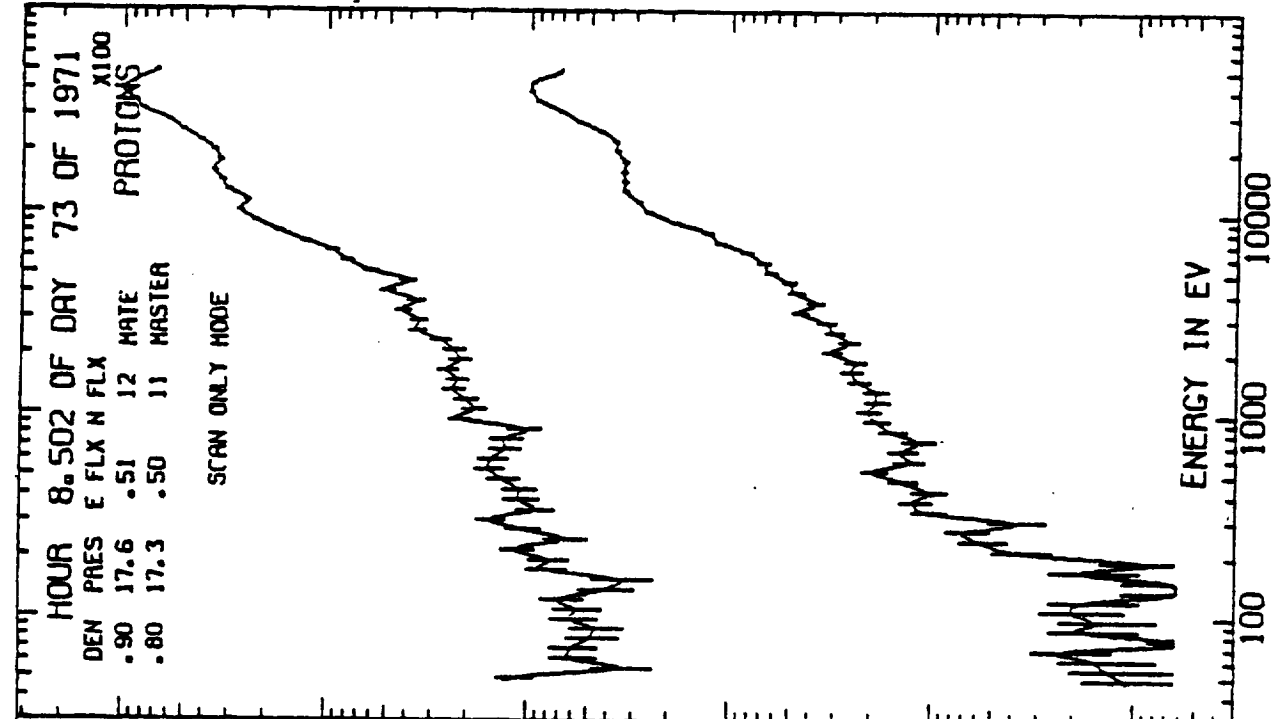
0.00 1.00 2.00 3.00 4.00 5.00

5.00  
4.00  
3.00  
2.00  
1.00  
0.00

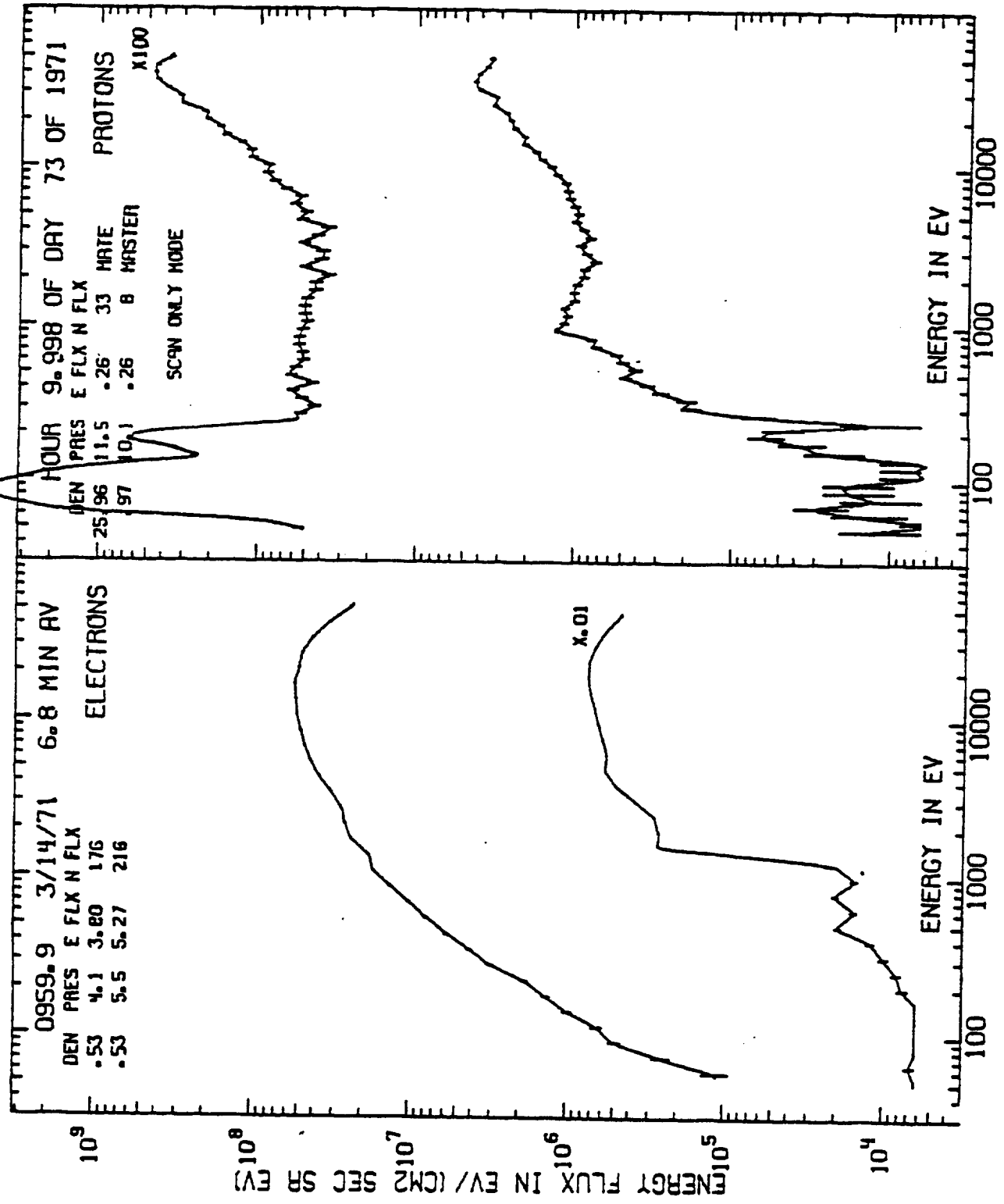




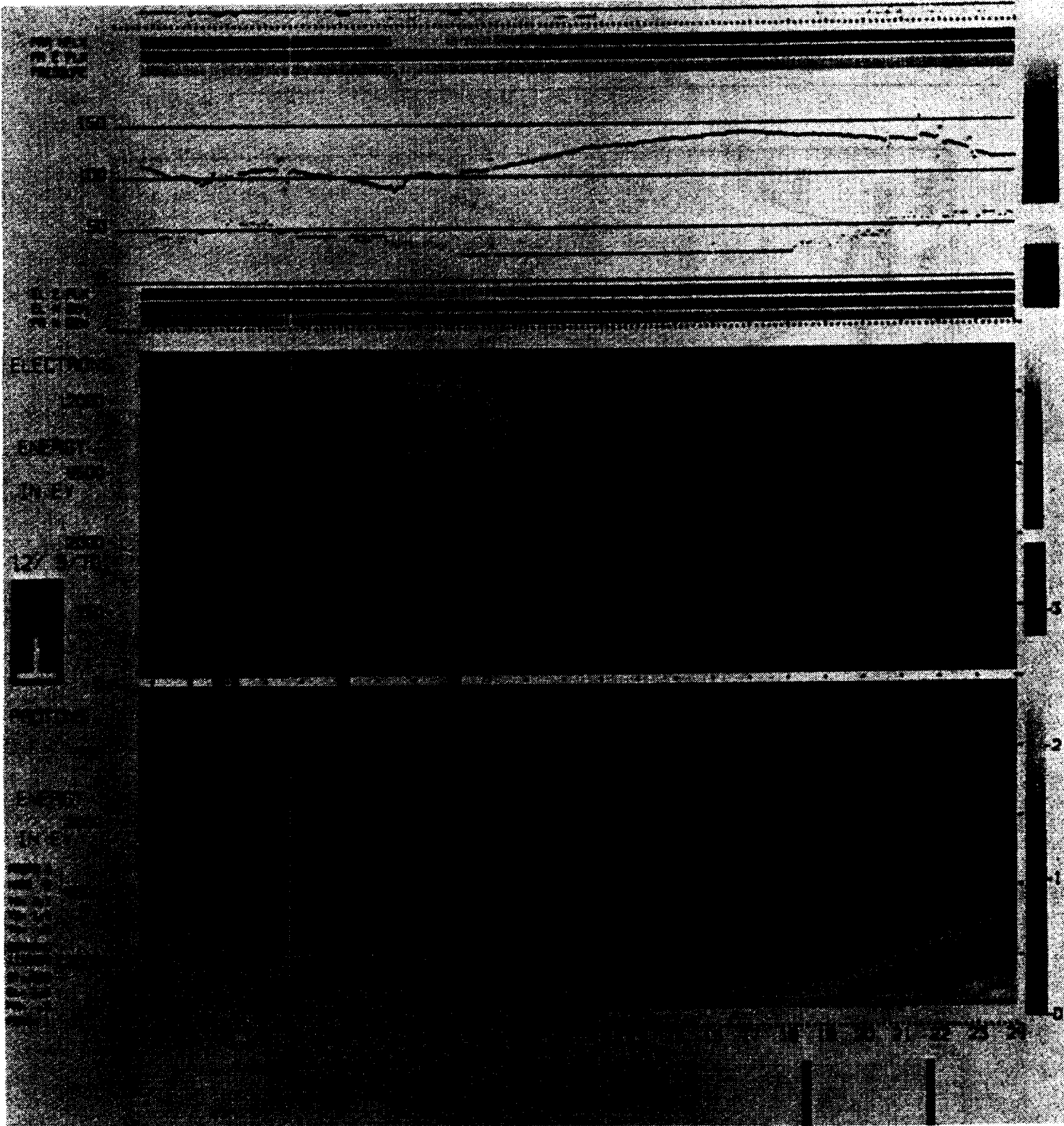
0.00 1.00 2.00 3.00 4.00 5.00



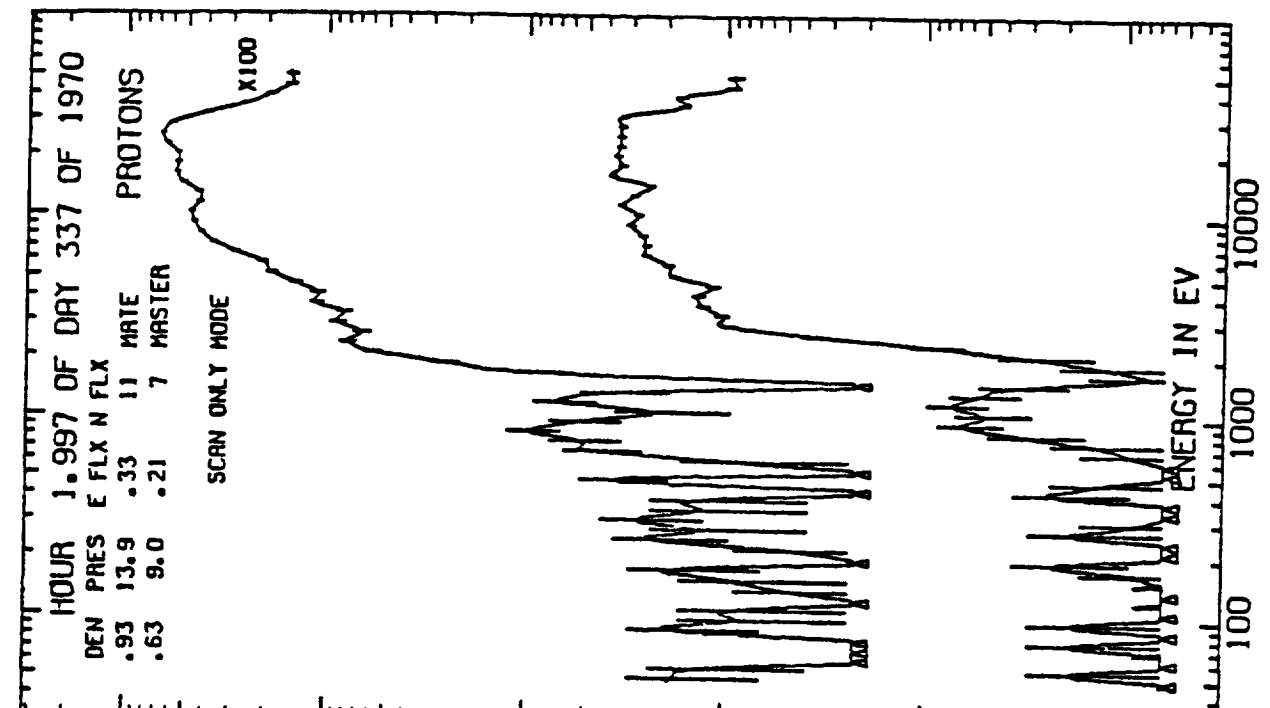
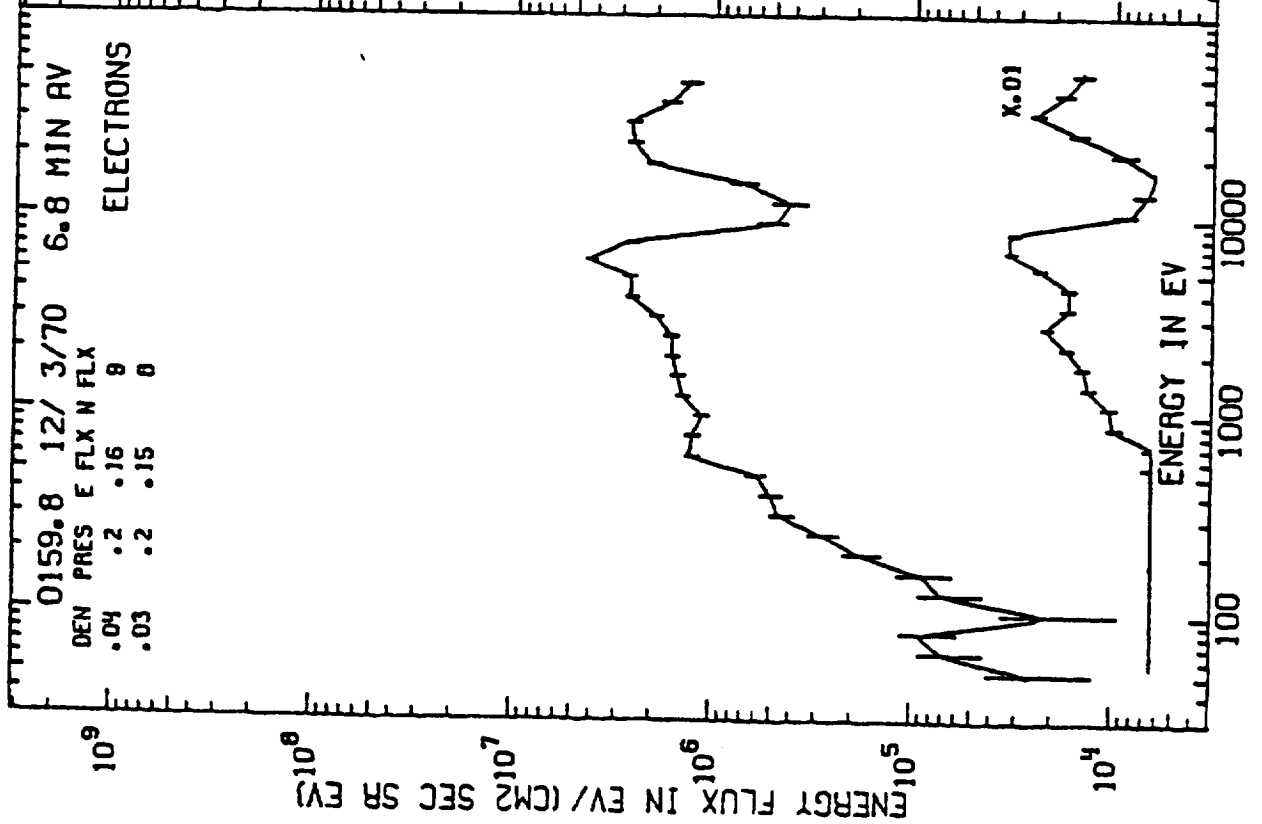
0.00 1.00 2.00 3.00 4.00 5.00



ORIGINAL PAGE IS  
OF POOR QUALITY

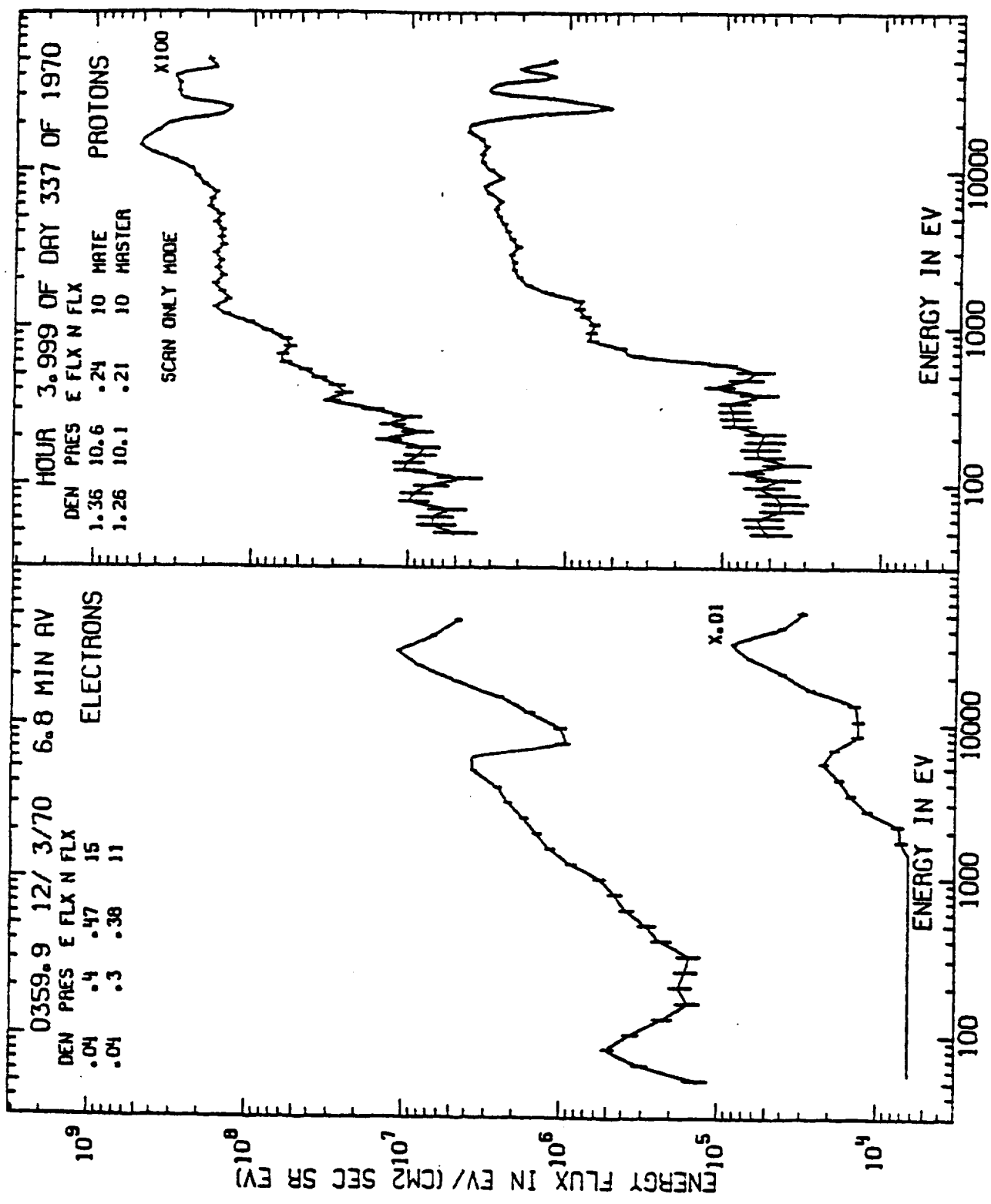


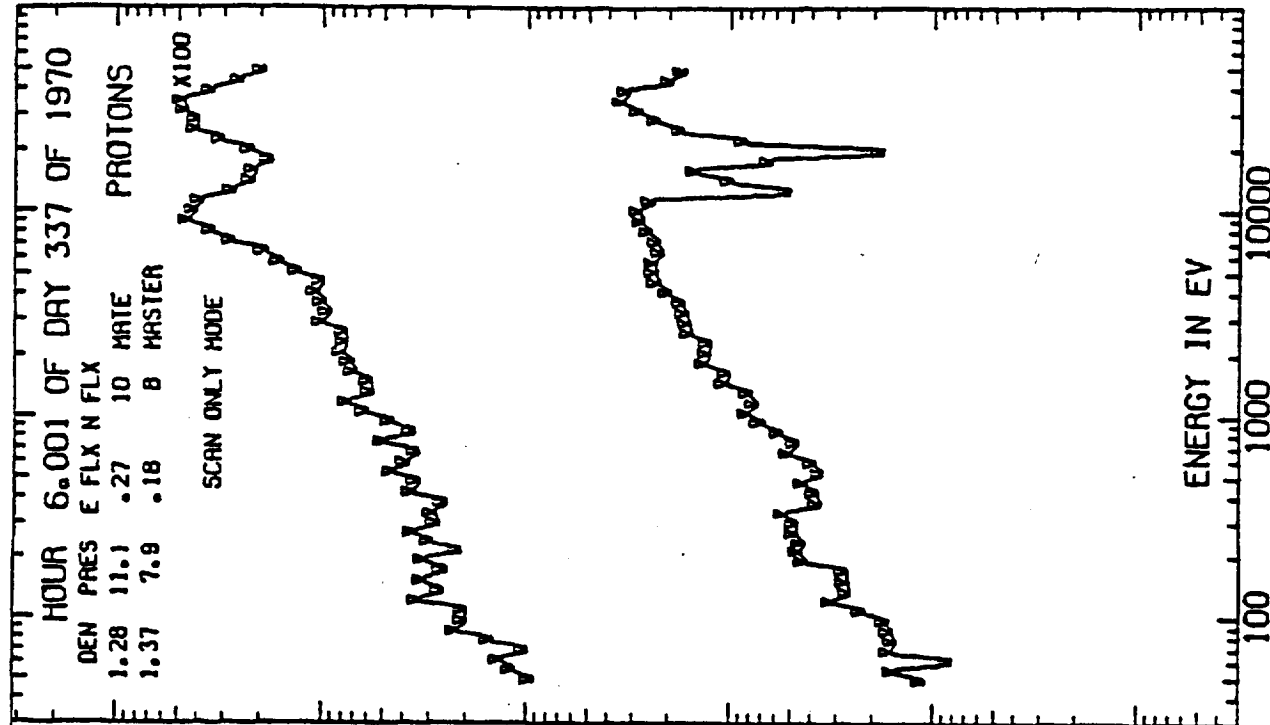
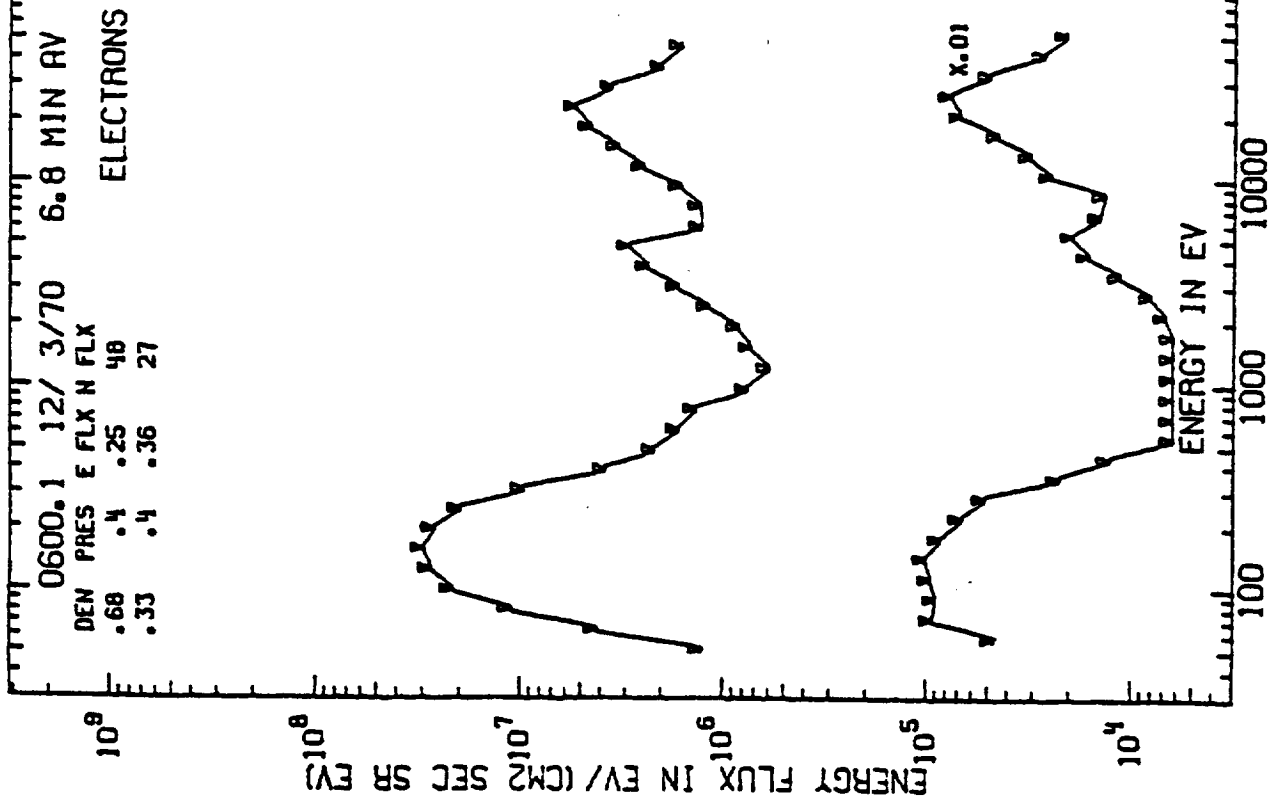
Spectrogram for 12/3/70 - Pre-midnight substorm.



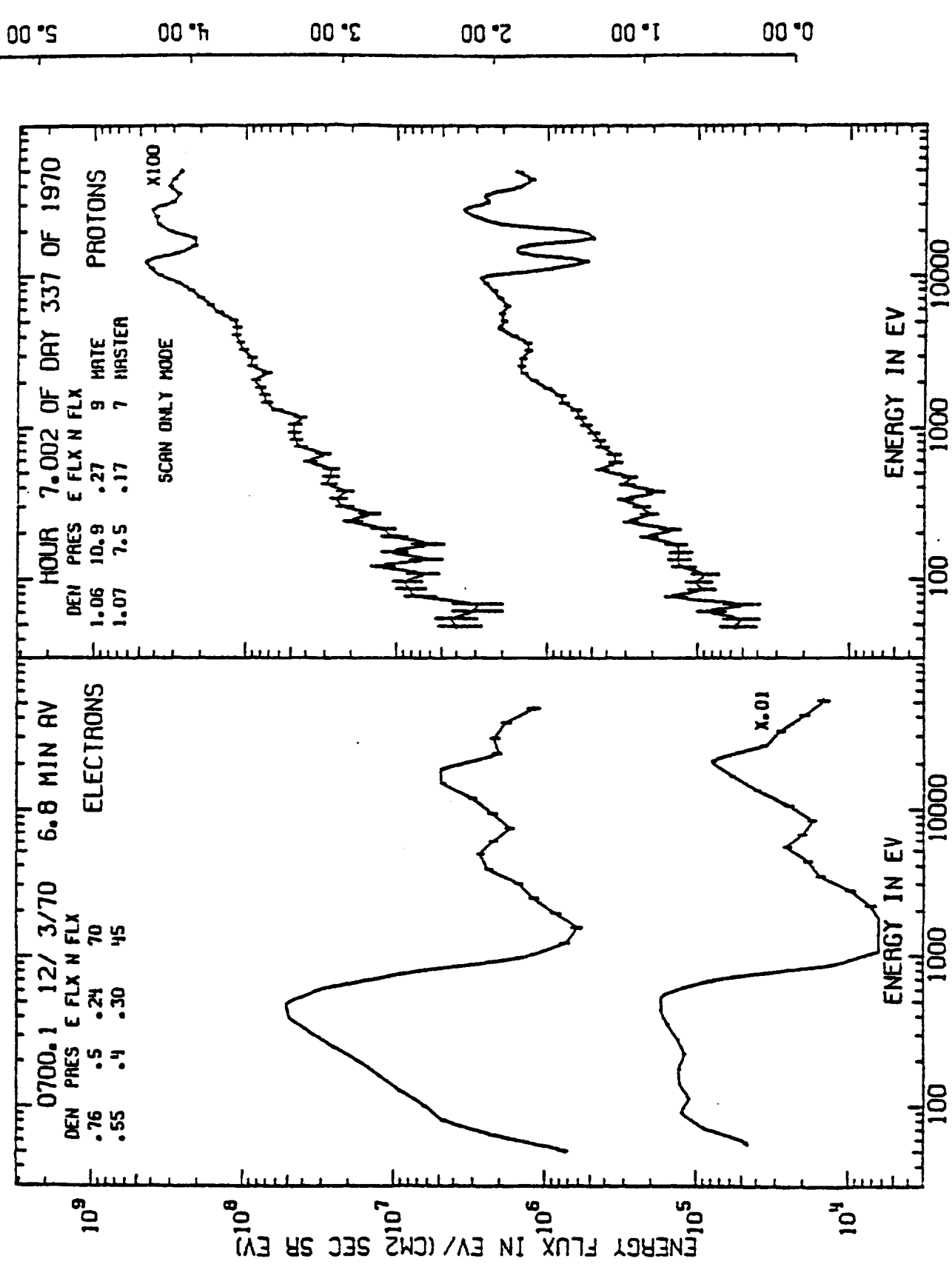
0.00  
1.00  
2.00  
3.00  
4.00  
5.00

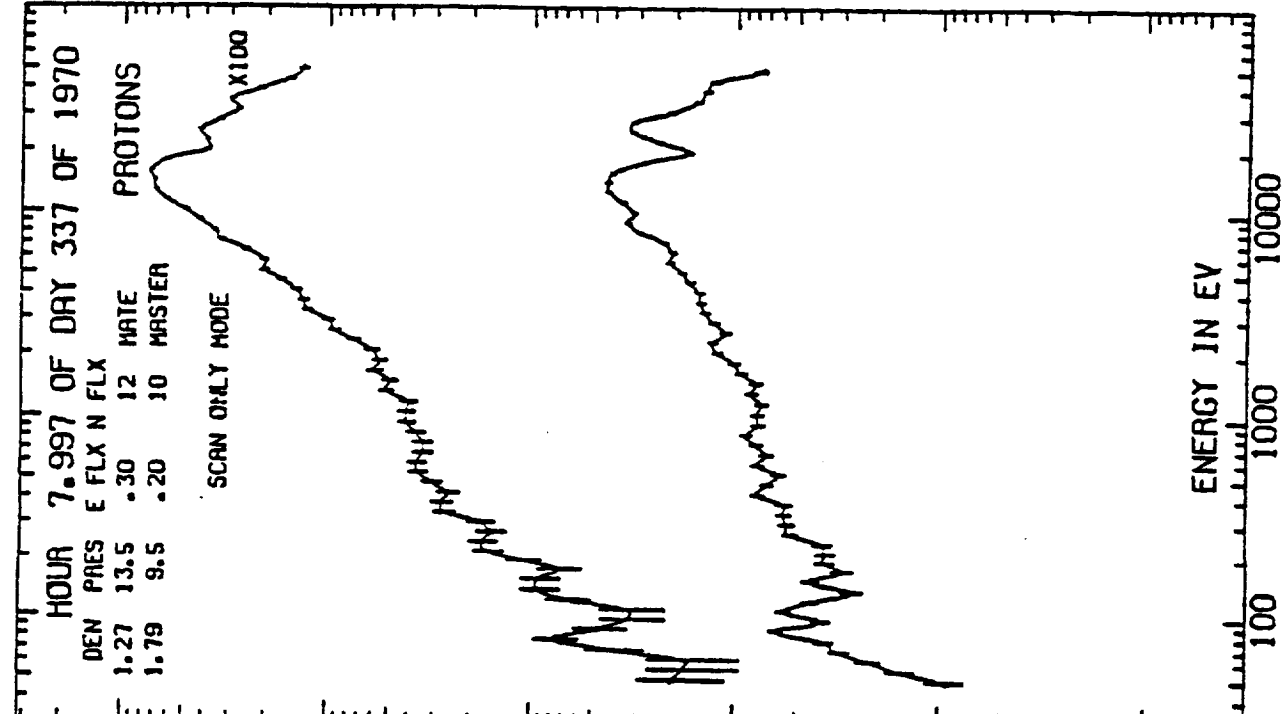
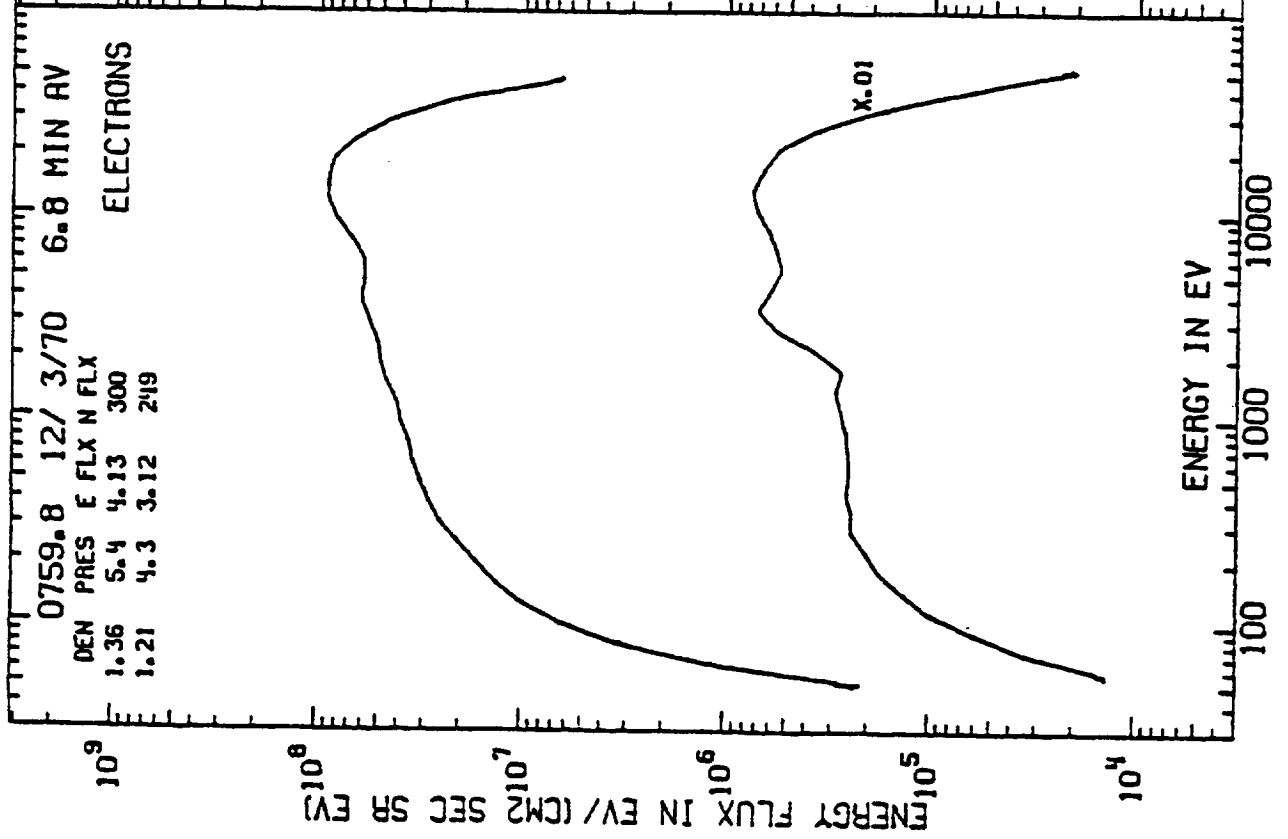
0.00 1.00 2.00 3.00 4.00 5.00





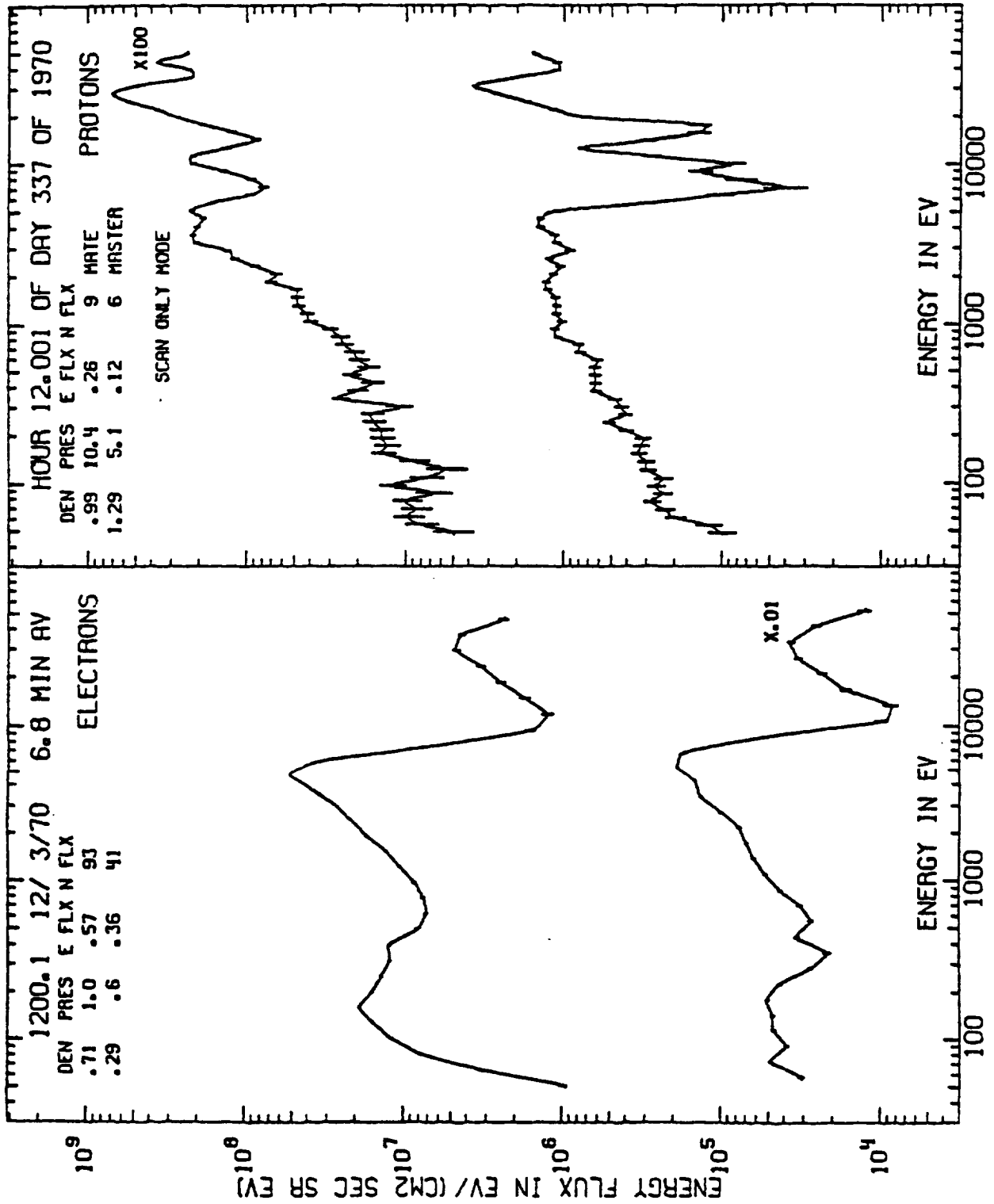
5.00 4.00 3.00 2.00 1.00 0.00



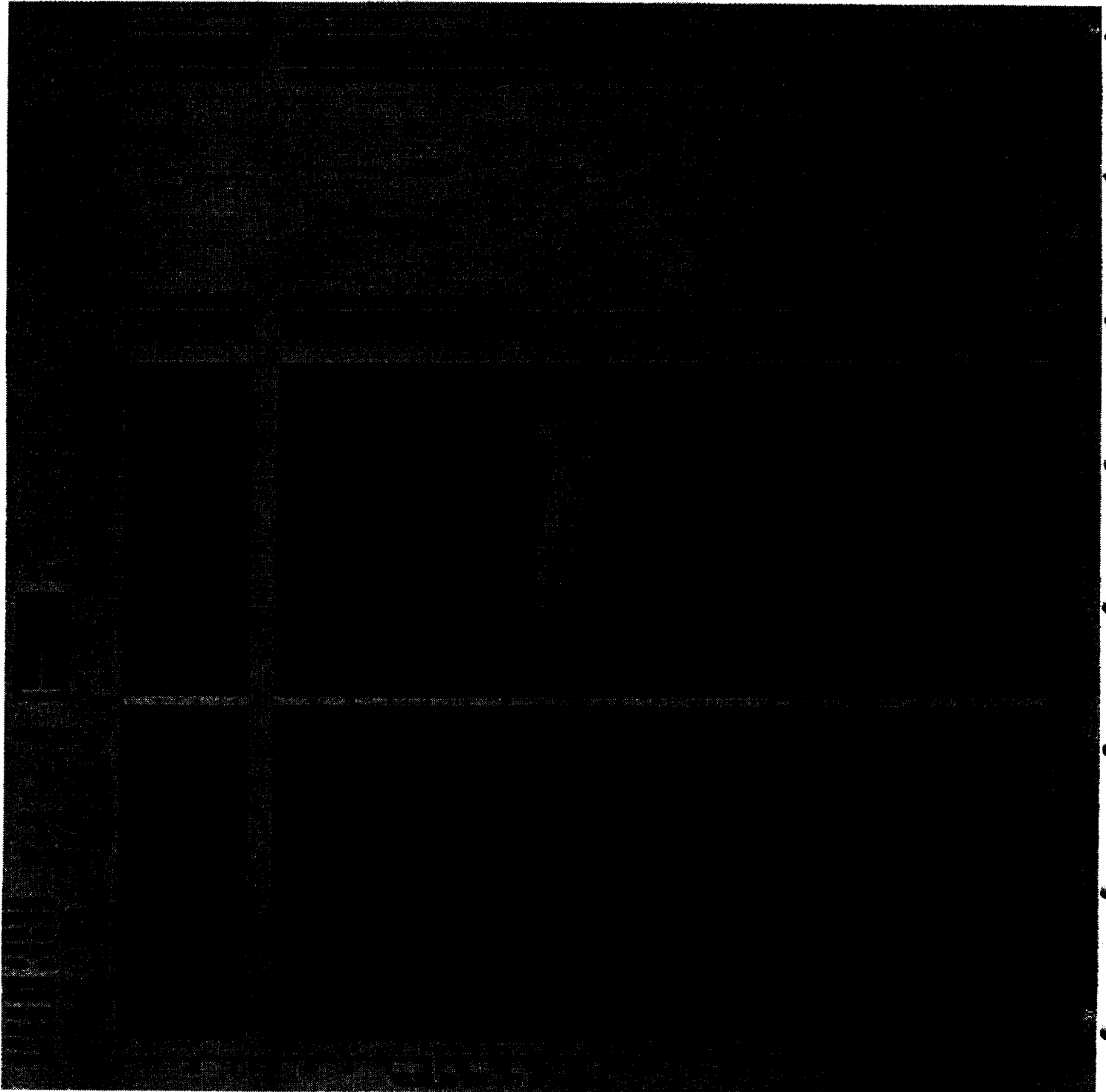


0.00 1.00 2.00 3.00 4.00 5.00

0.00 1.00 2.00 3.00 4.00 5.00

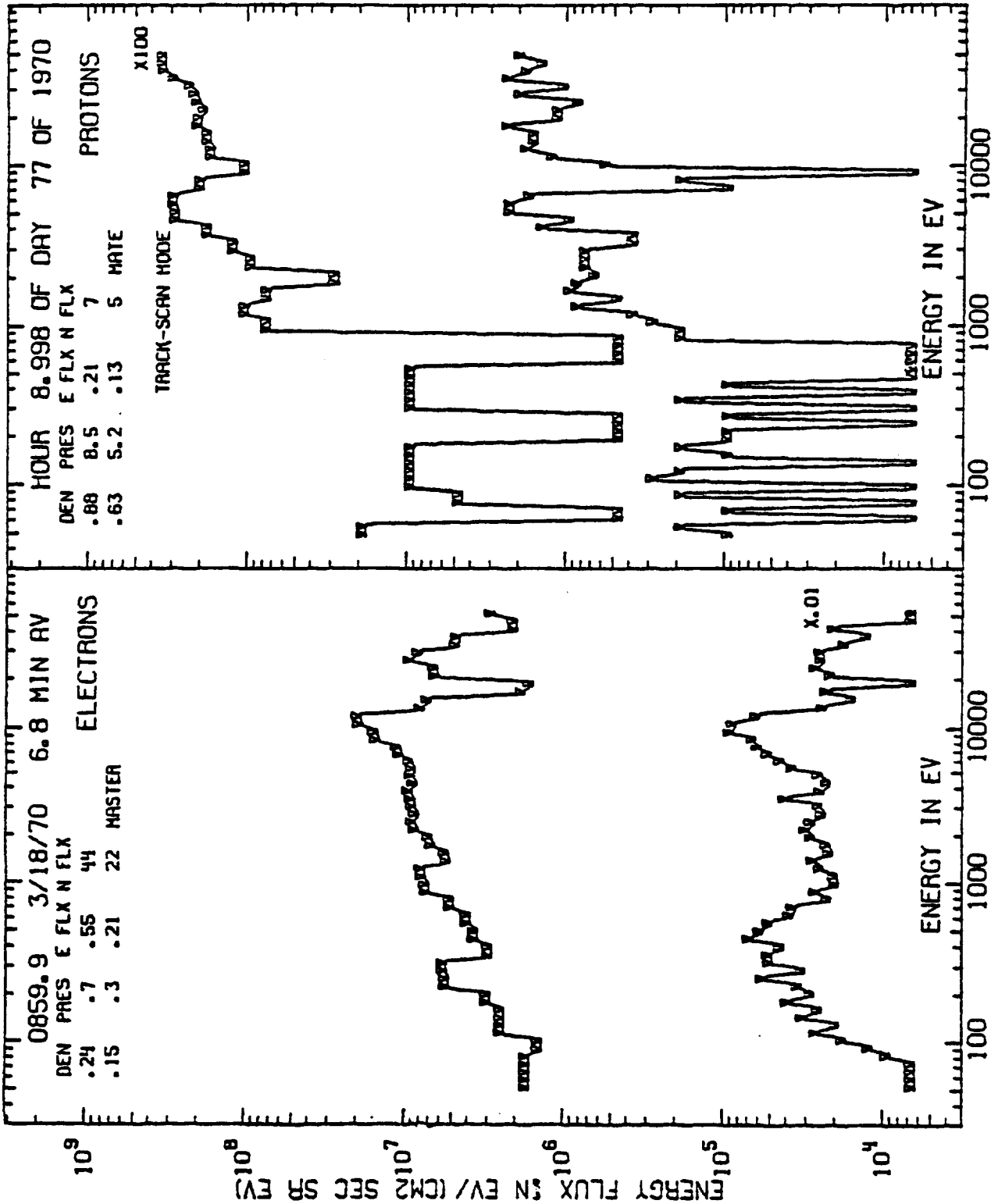


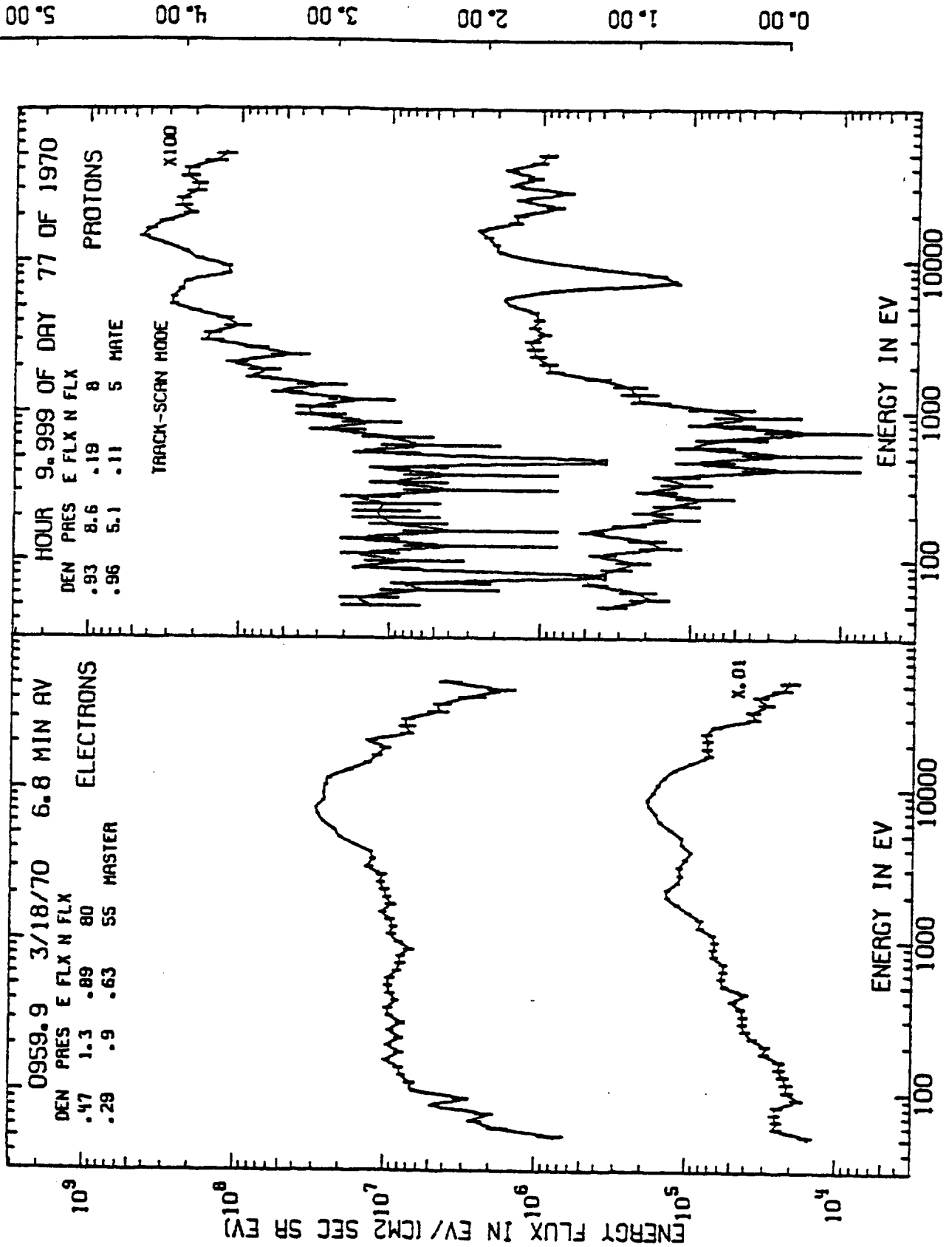
ORIGINAL PAGE IS  
OF POOR QUALITY



Spectrogram for 3/18/70 - Post-midnight substorm.

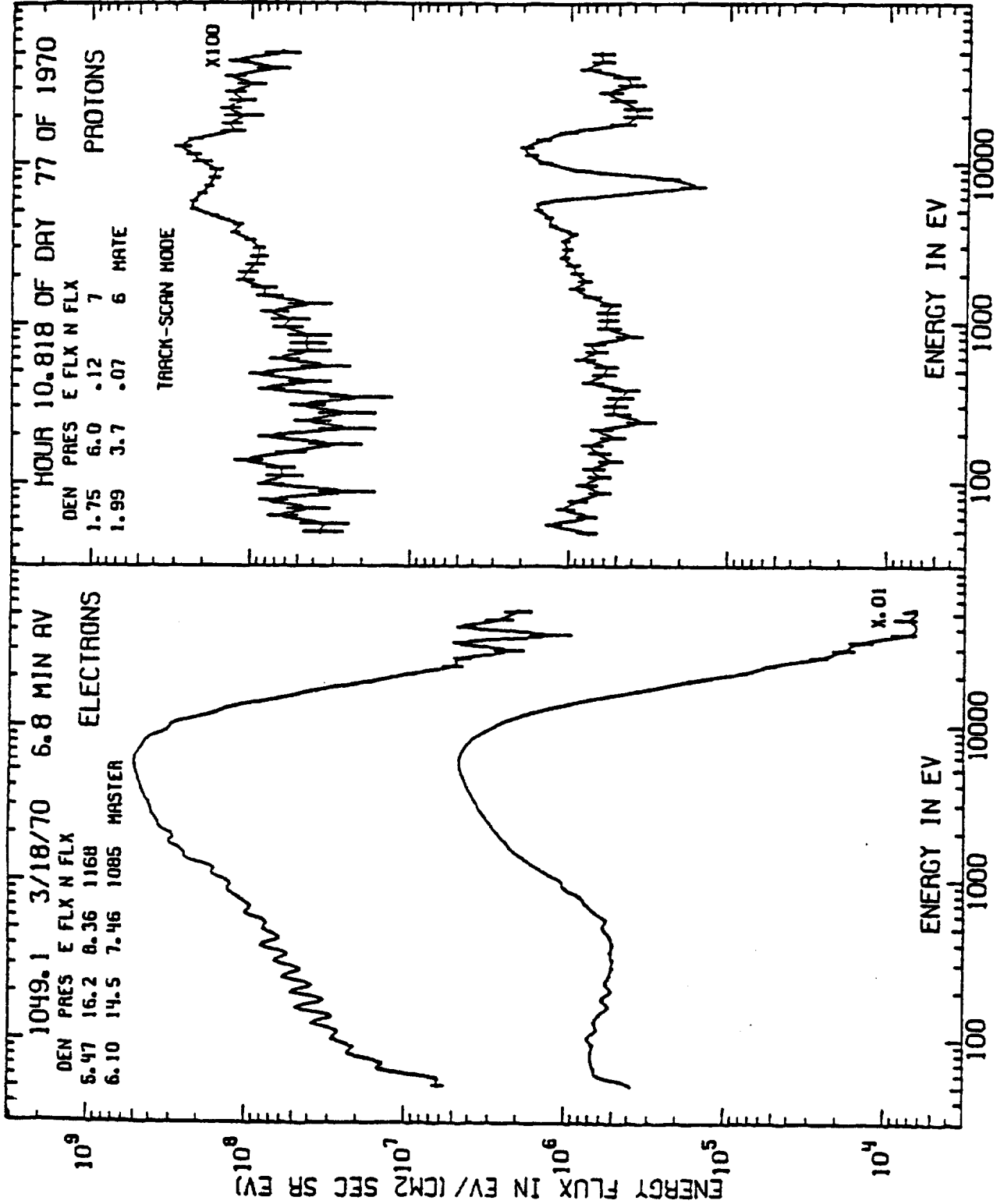
0.00 1.00 2.00 3.00 4.00 5.00

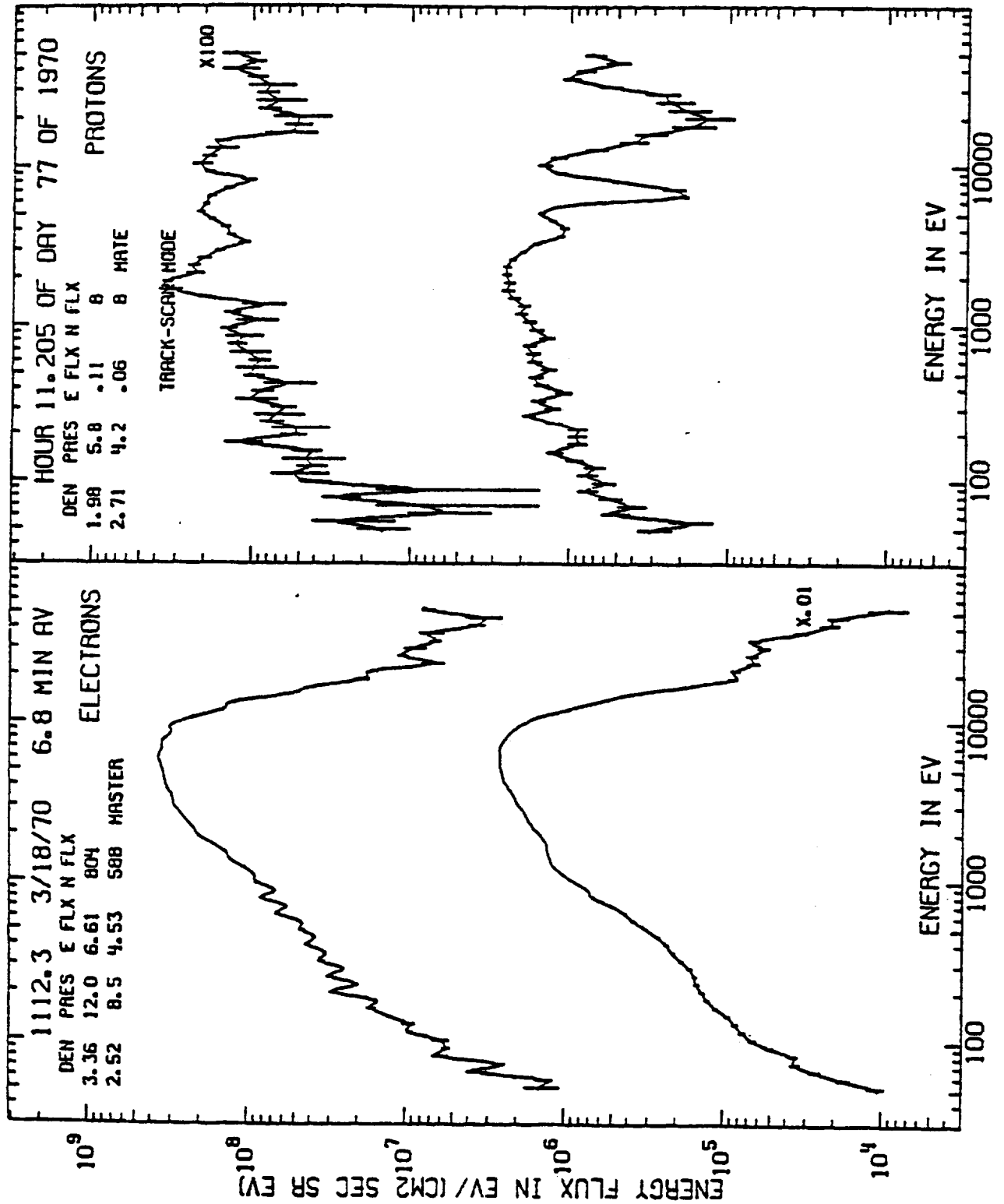




0.00  
 1.00  
 2.00  
 3.00  
 4.00  
 5.00

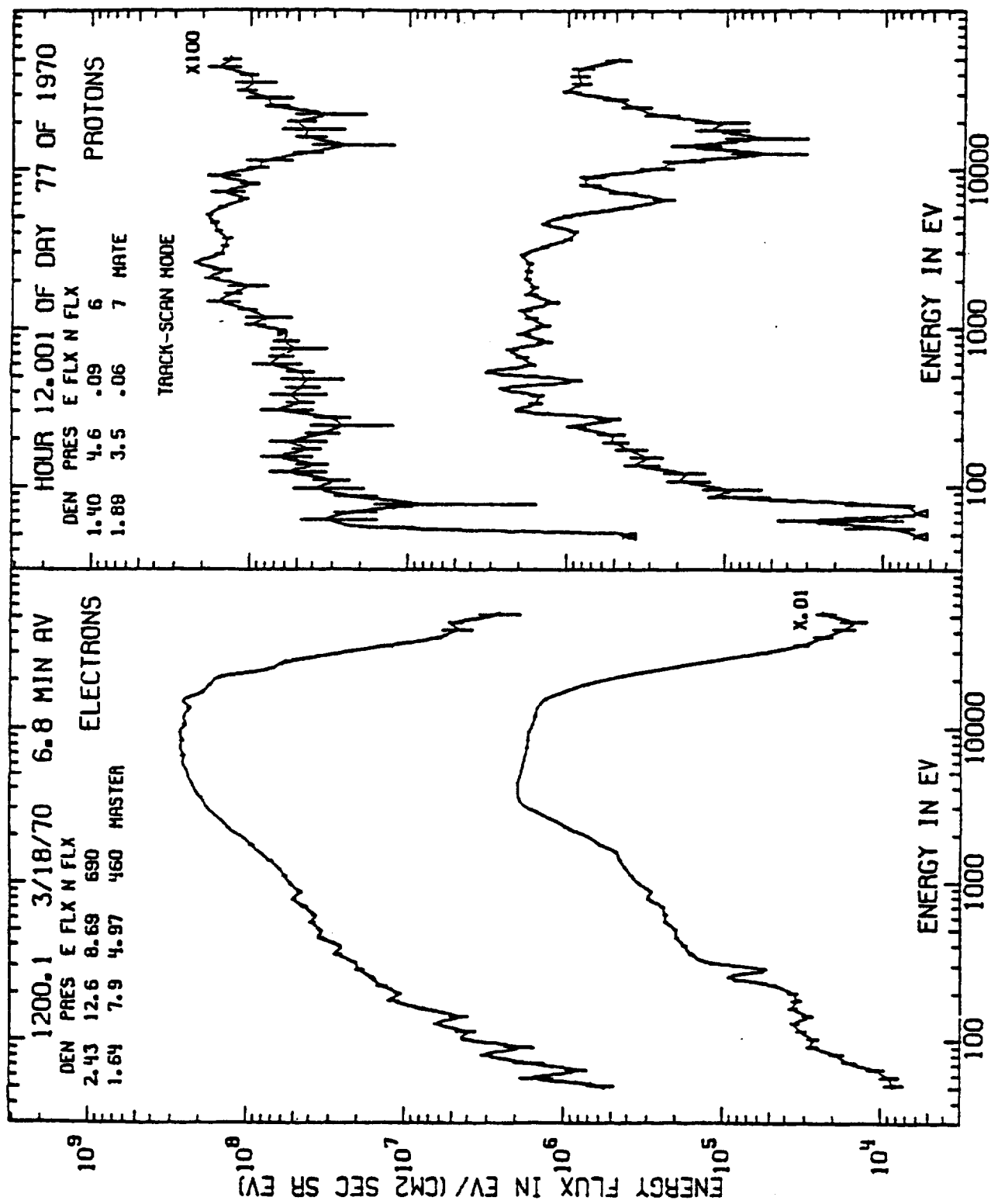
5.00  
4.00  
3.00  
2.00  
1.00  
0.00

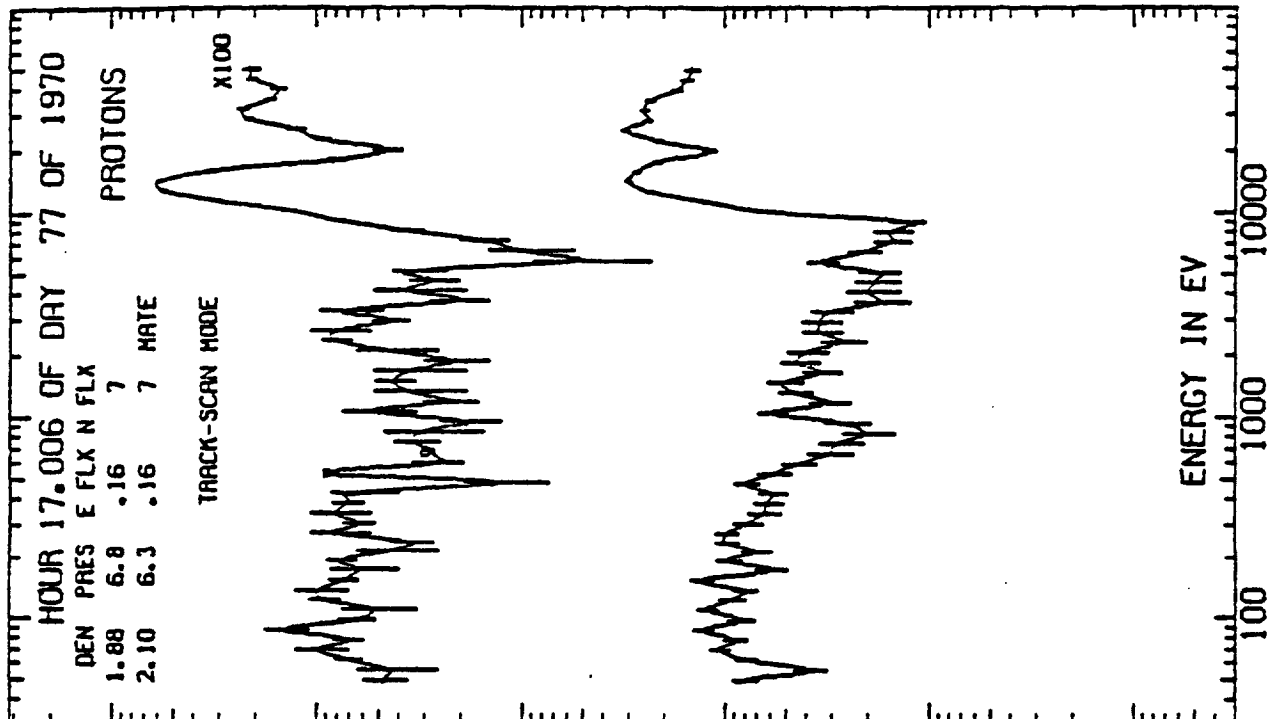
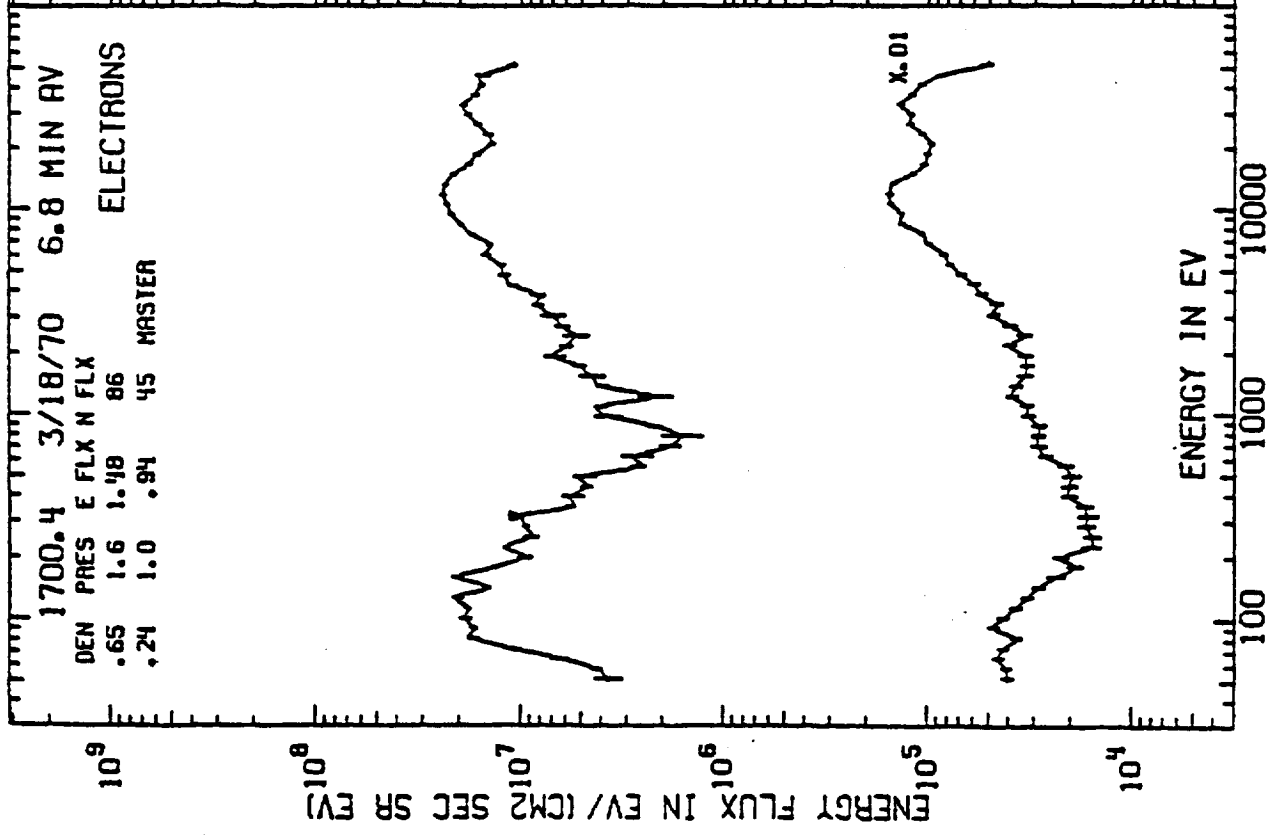




0.00 1.00 2.00 3.00 4.00 5.00

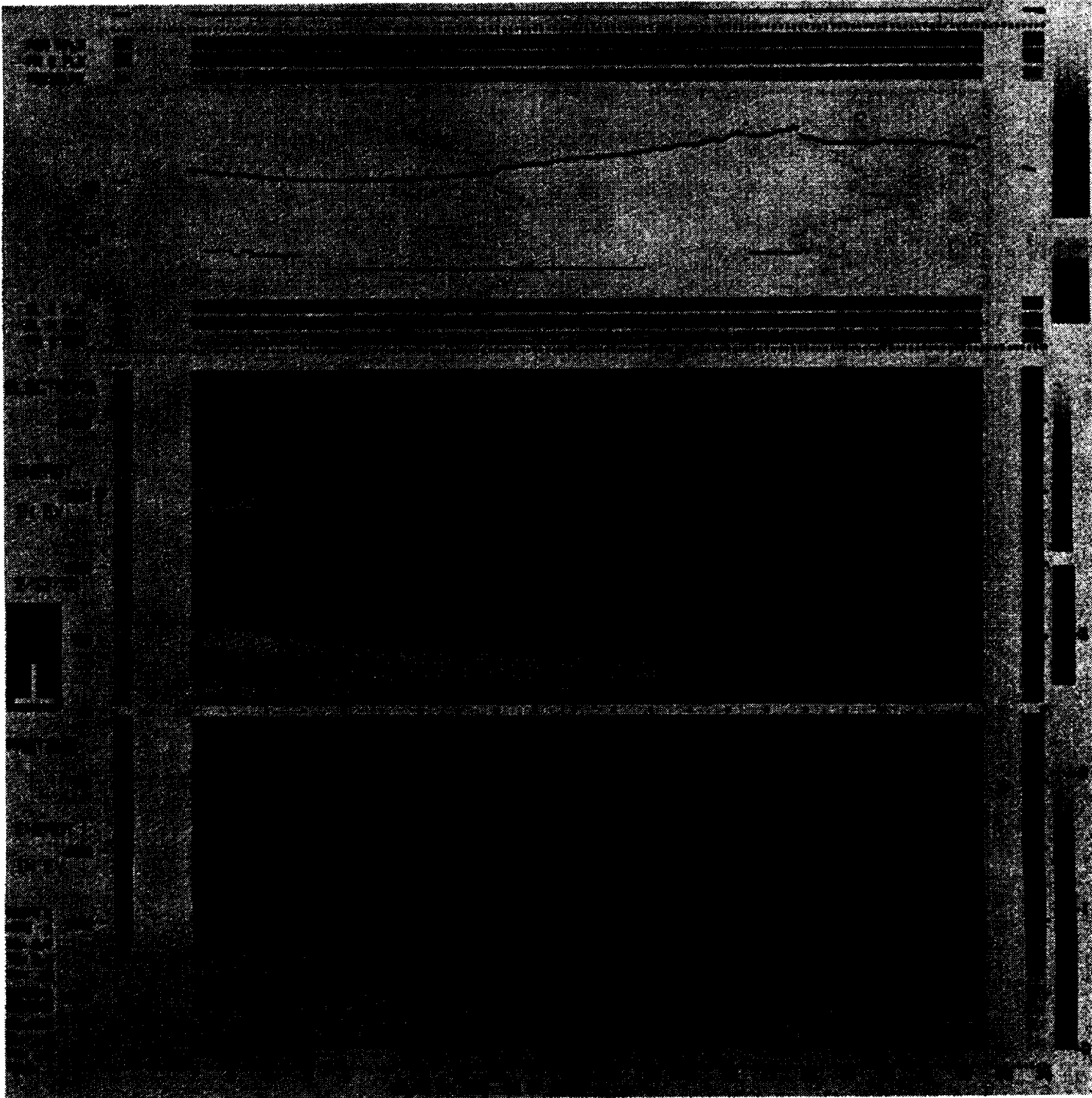
0.00 1.00 2.00 3.00 4.00 5.00



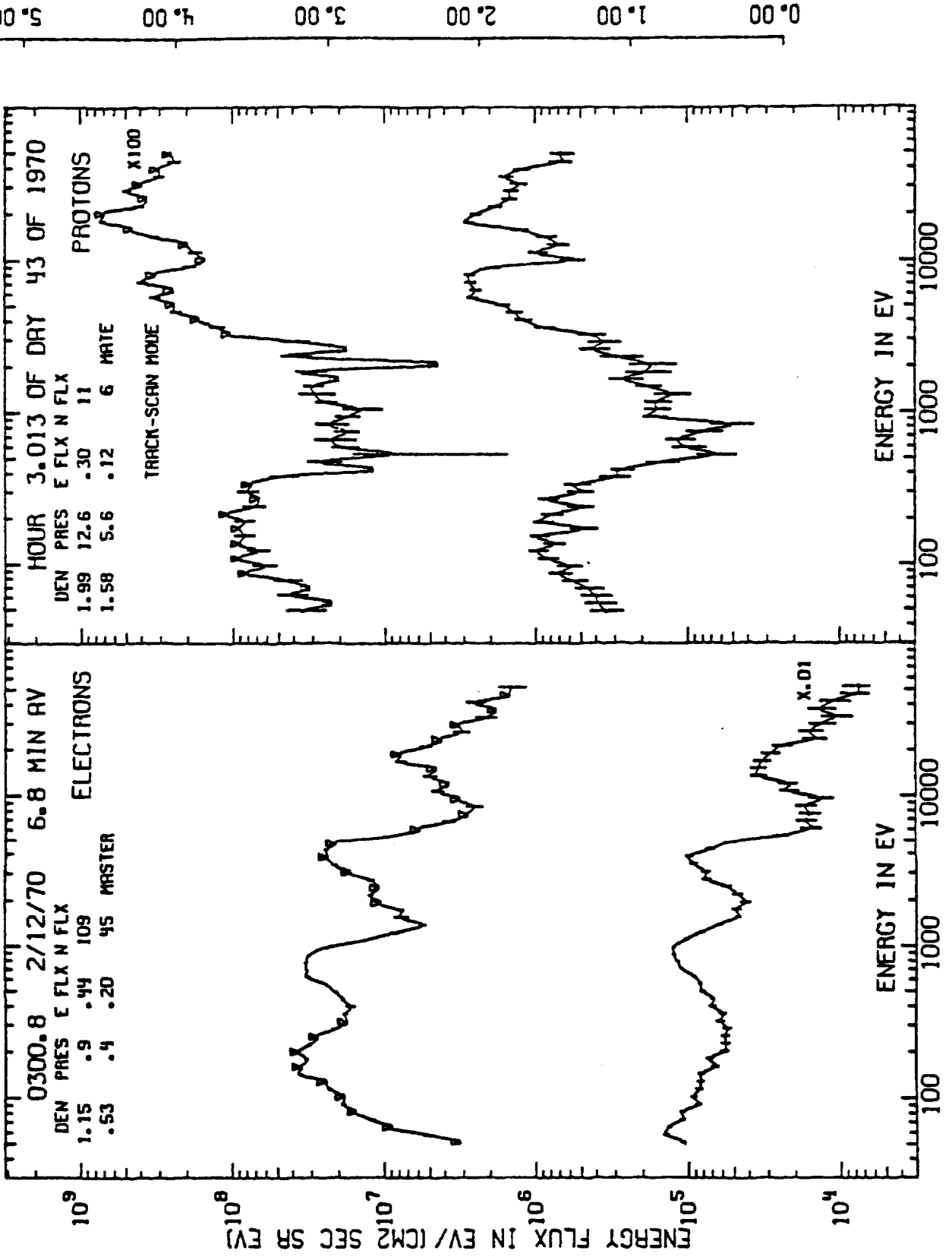


5.00  
 4.00  
 3.00  
 2.00  
 1.00  
 0.00

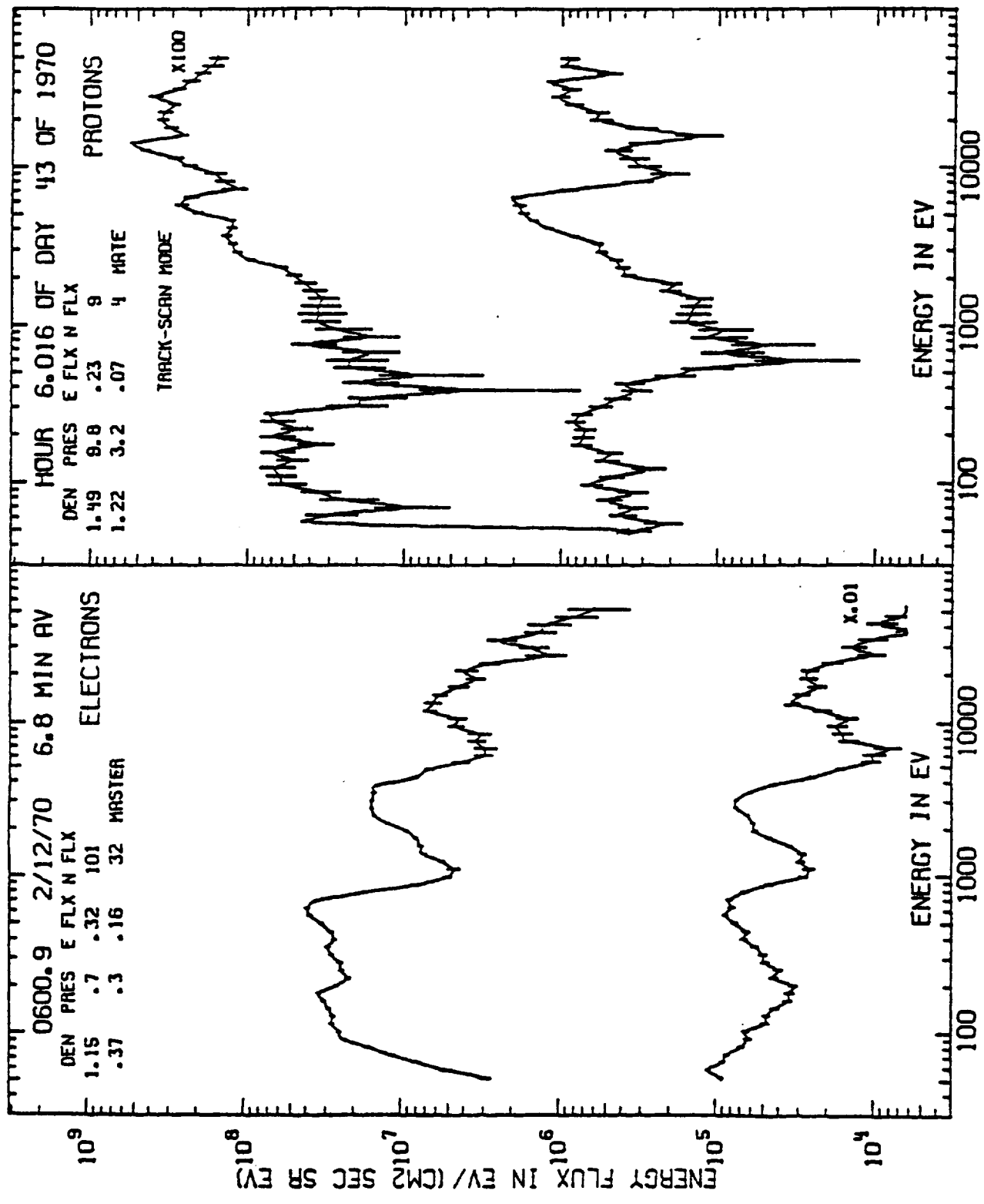
ORIGINAL PAGE IS  
OF POOR QUALITY

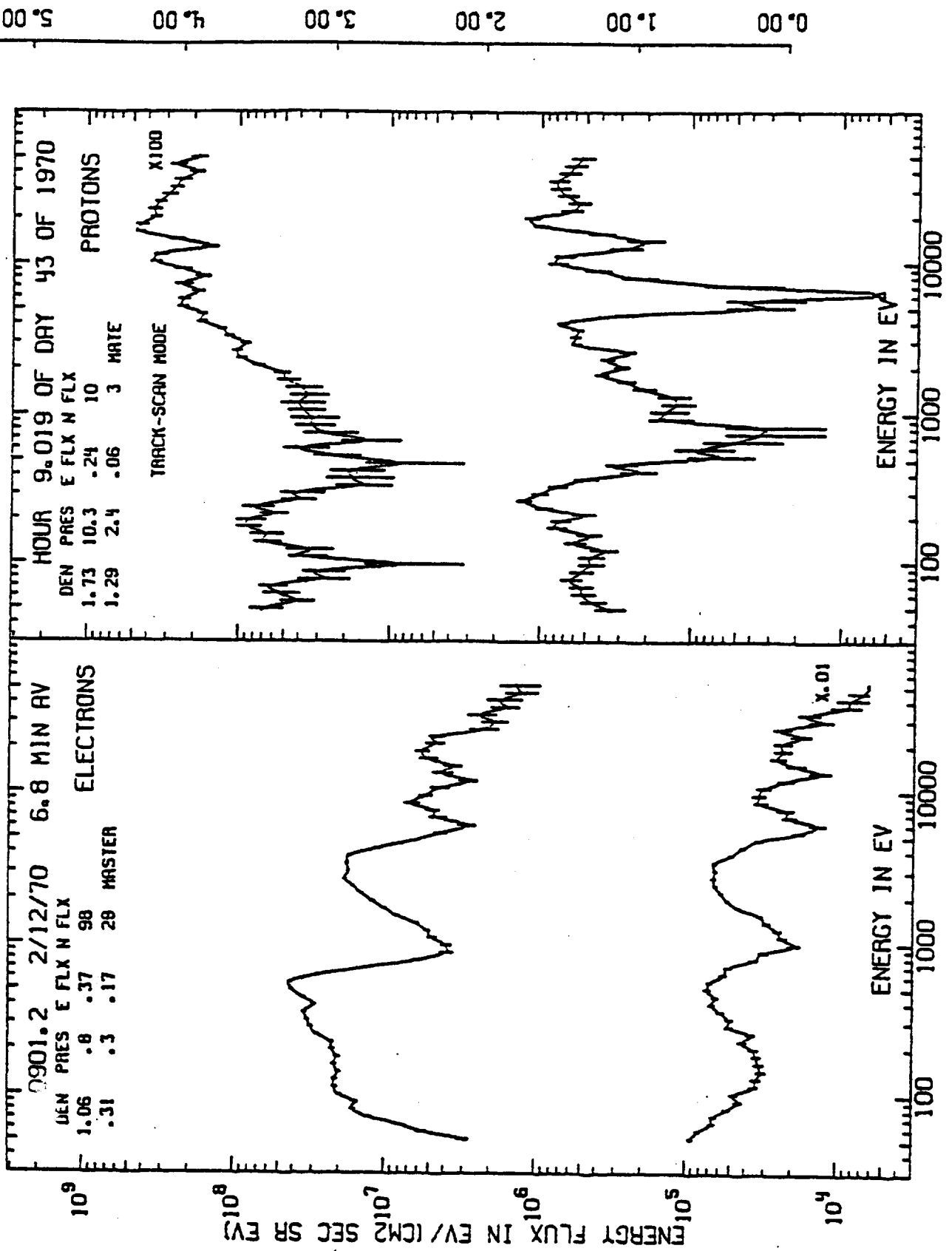


Spectrogram for 2/12/70 - Quiet day.



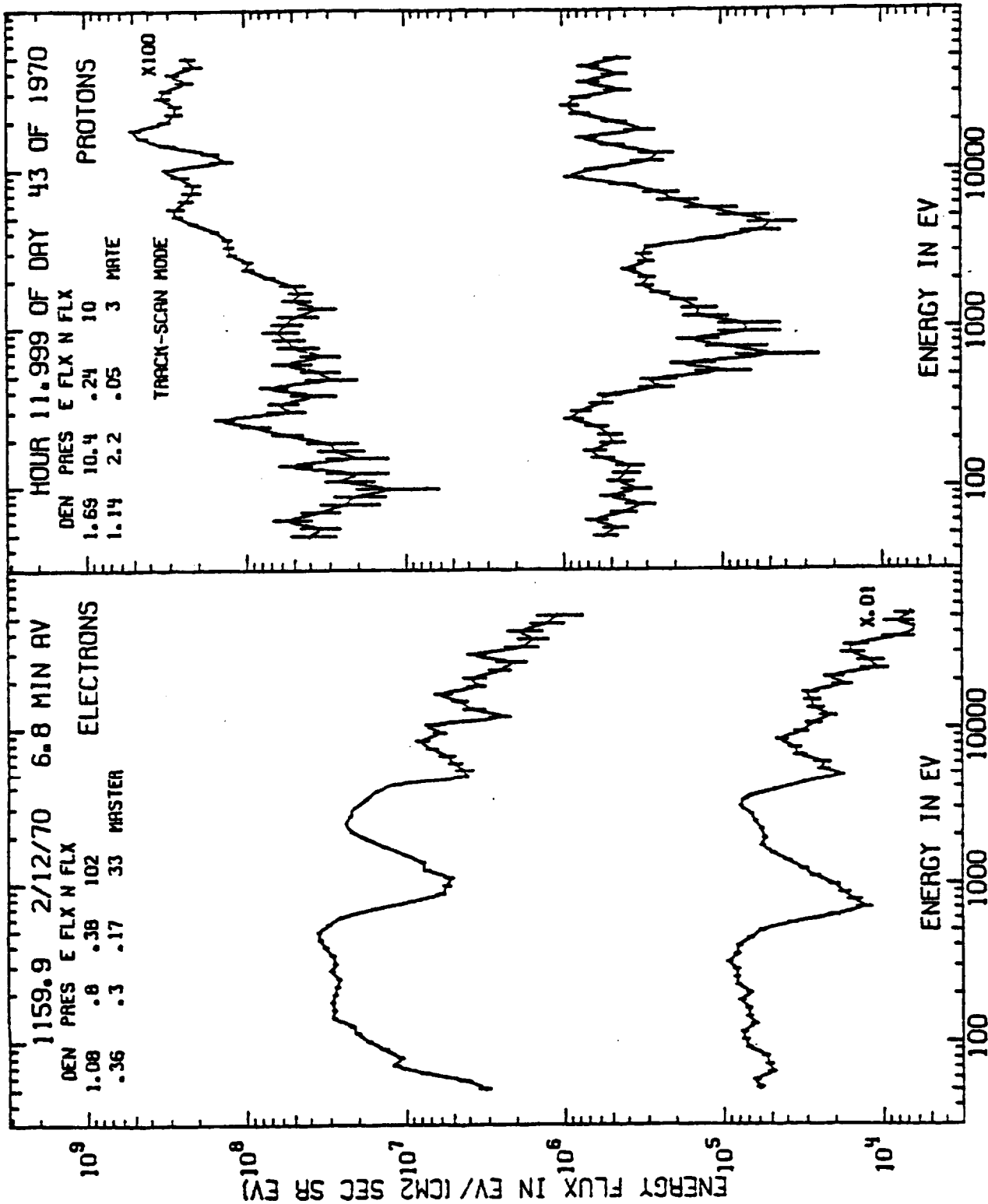
5.00  
4.00  
3.00  
2.00  
1.00  
0.00



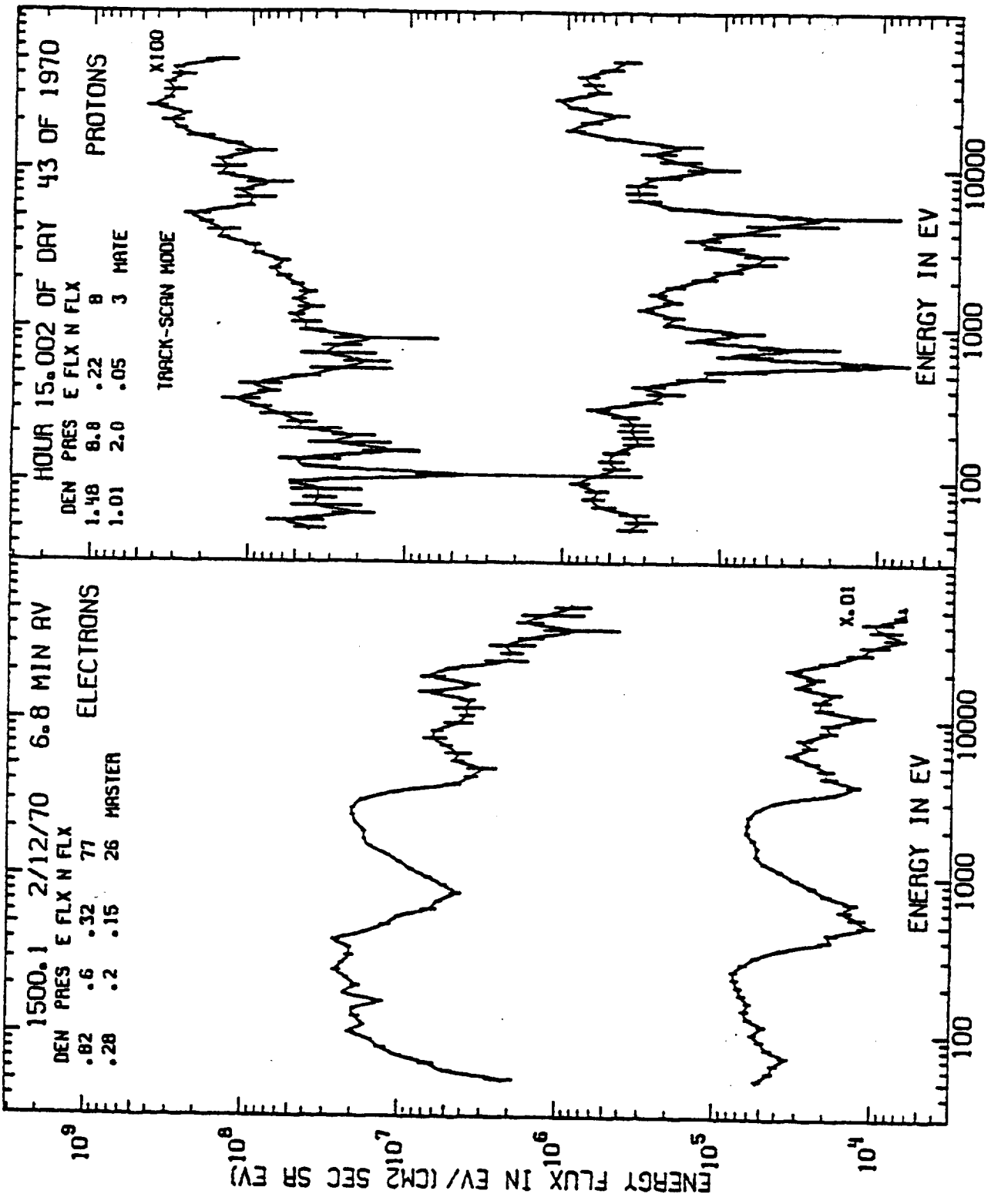


00.00 1.00 2.00 3.00 4.00 5.00

0-3

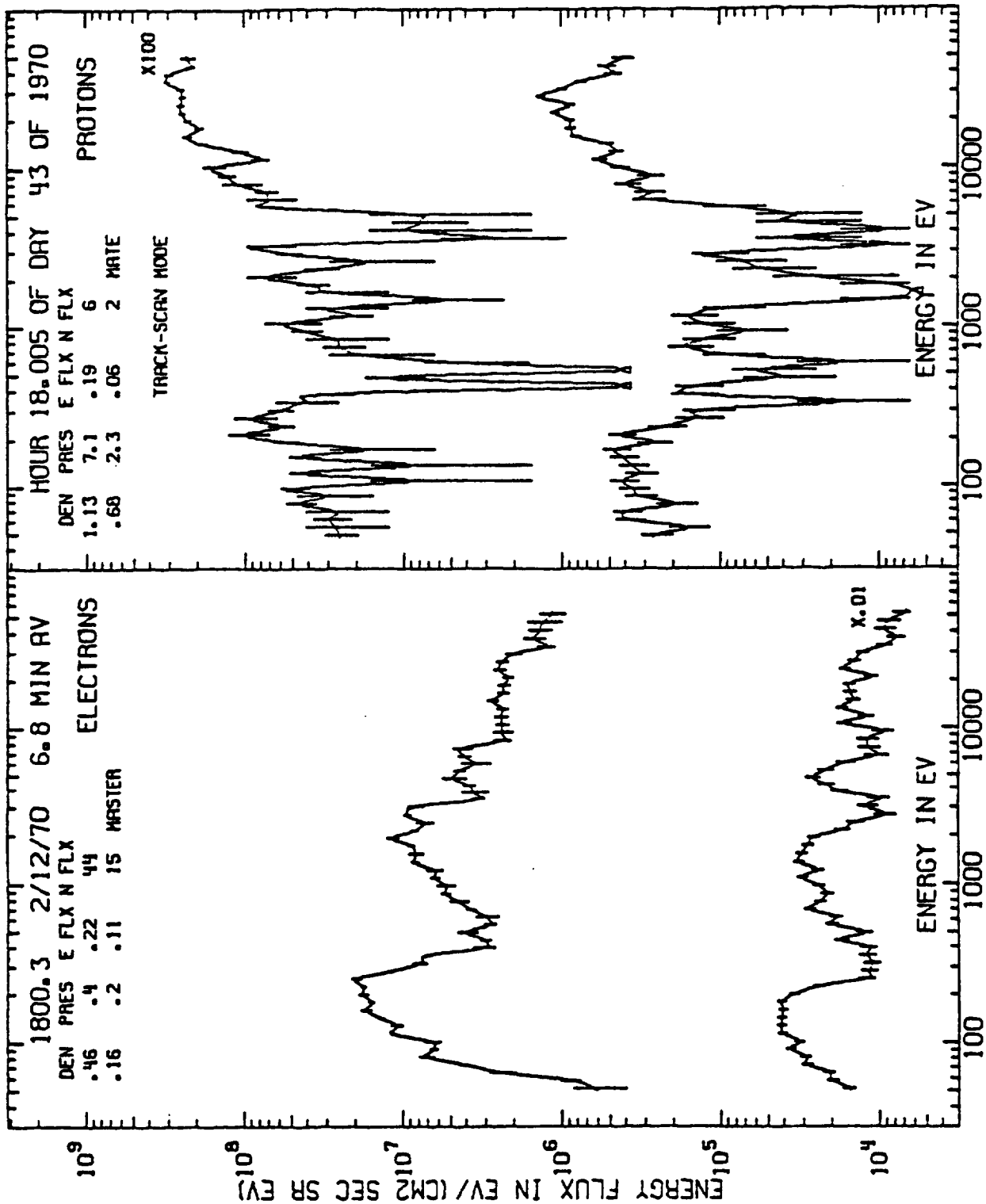


0.00 1.00 2.00 3.00 4.00 5.00

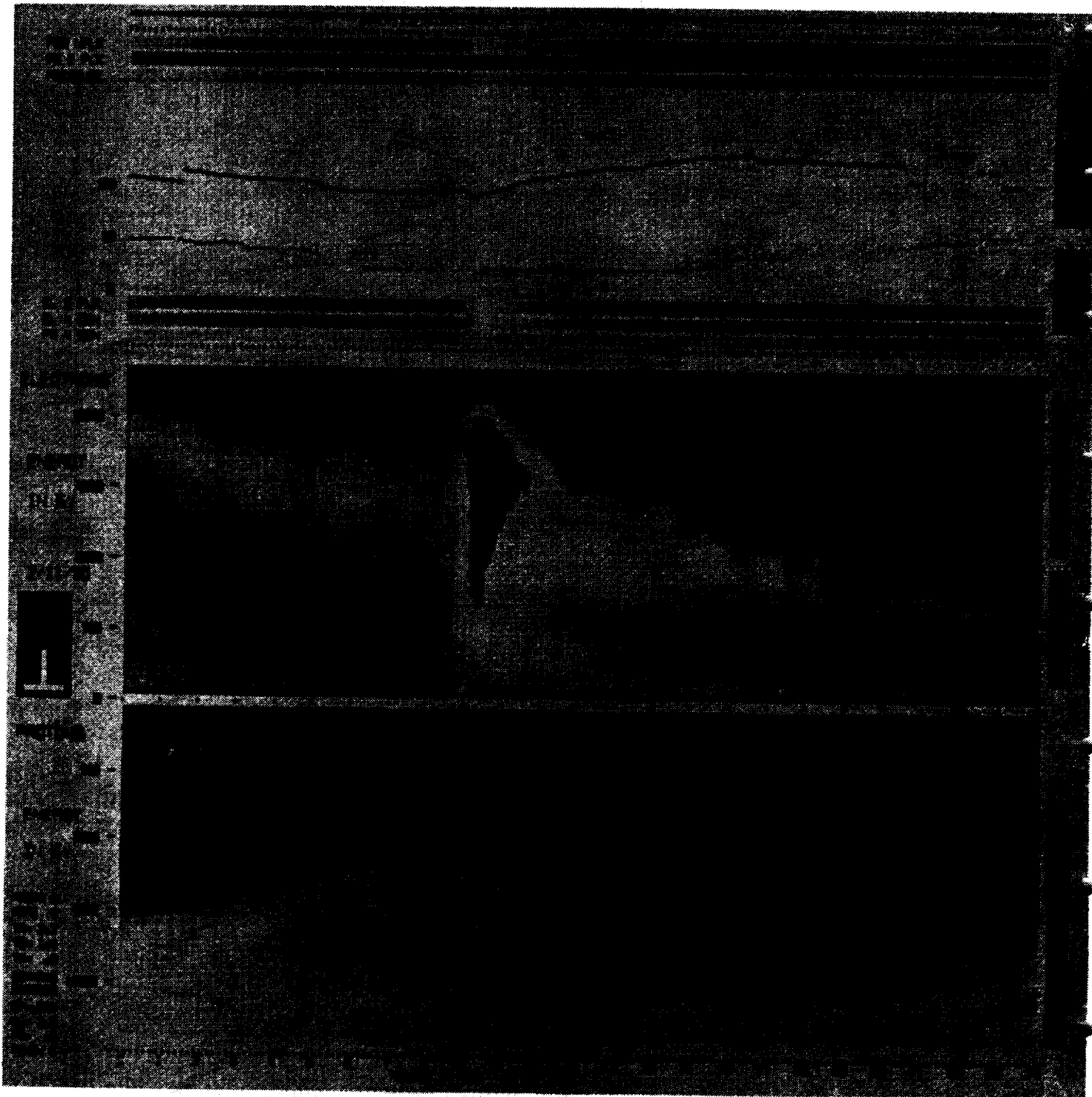


0.00 1.00 2.00 3.00 4.00 5.00

0.00 1.00 2.00 3.00 4.00 5.00

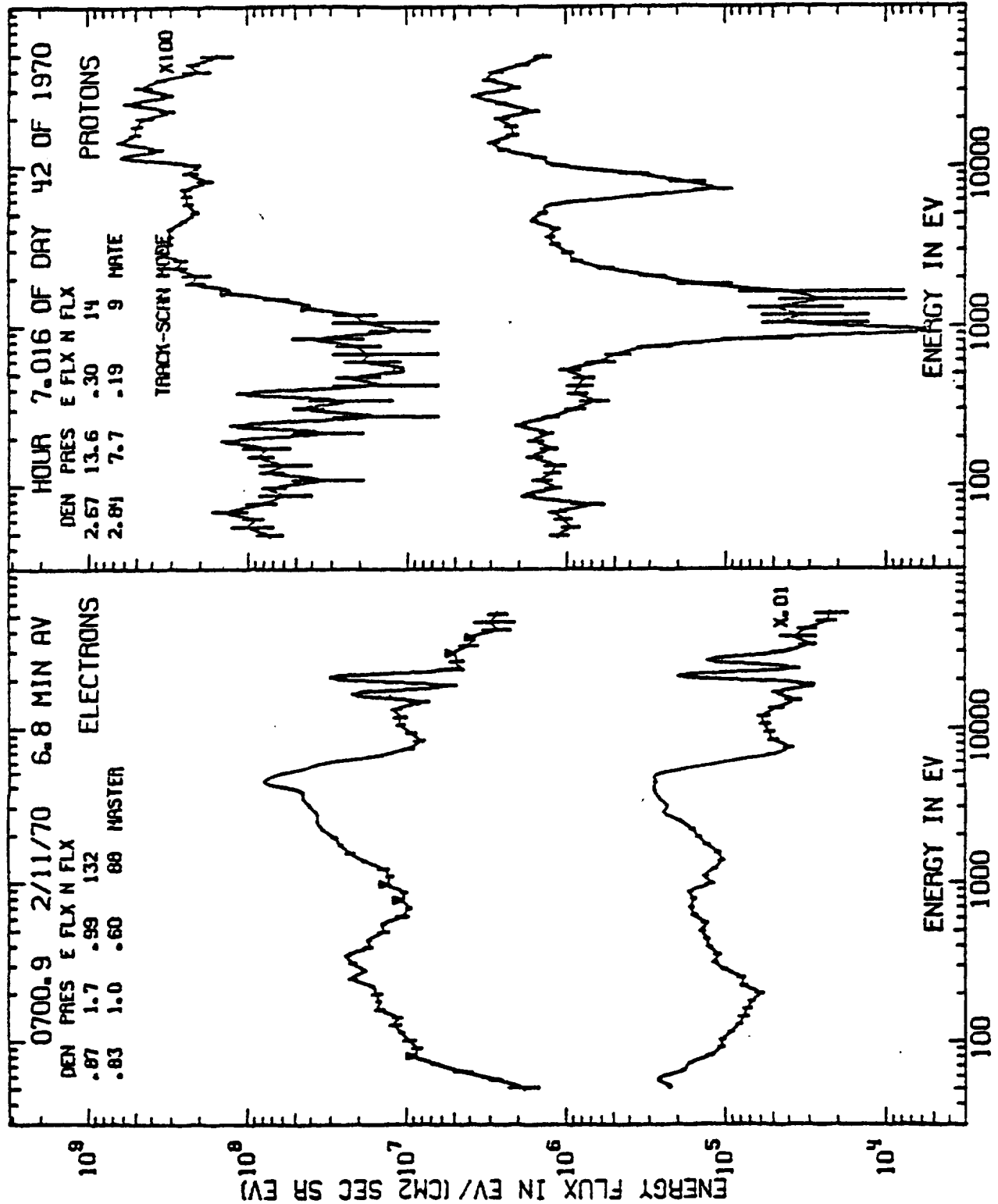


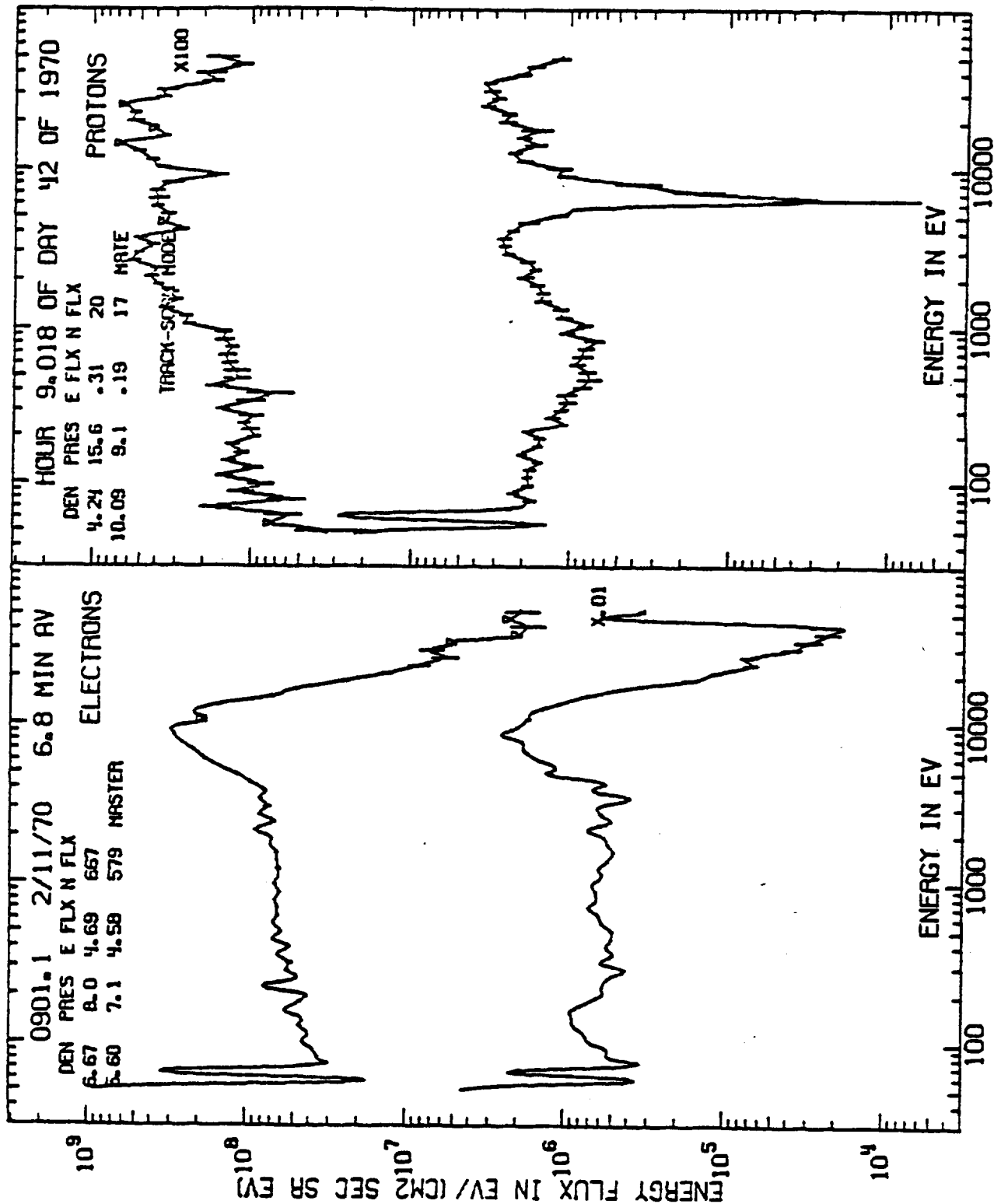
ORIGINAL PAGE IS  
OF POOR QUALITY



Spectrogram for 2/11/70 - Intense localized post midnight substorm.

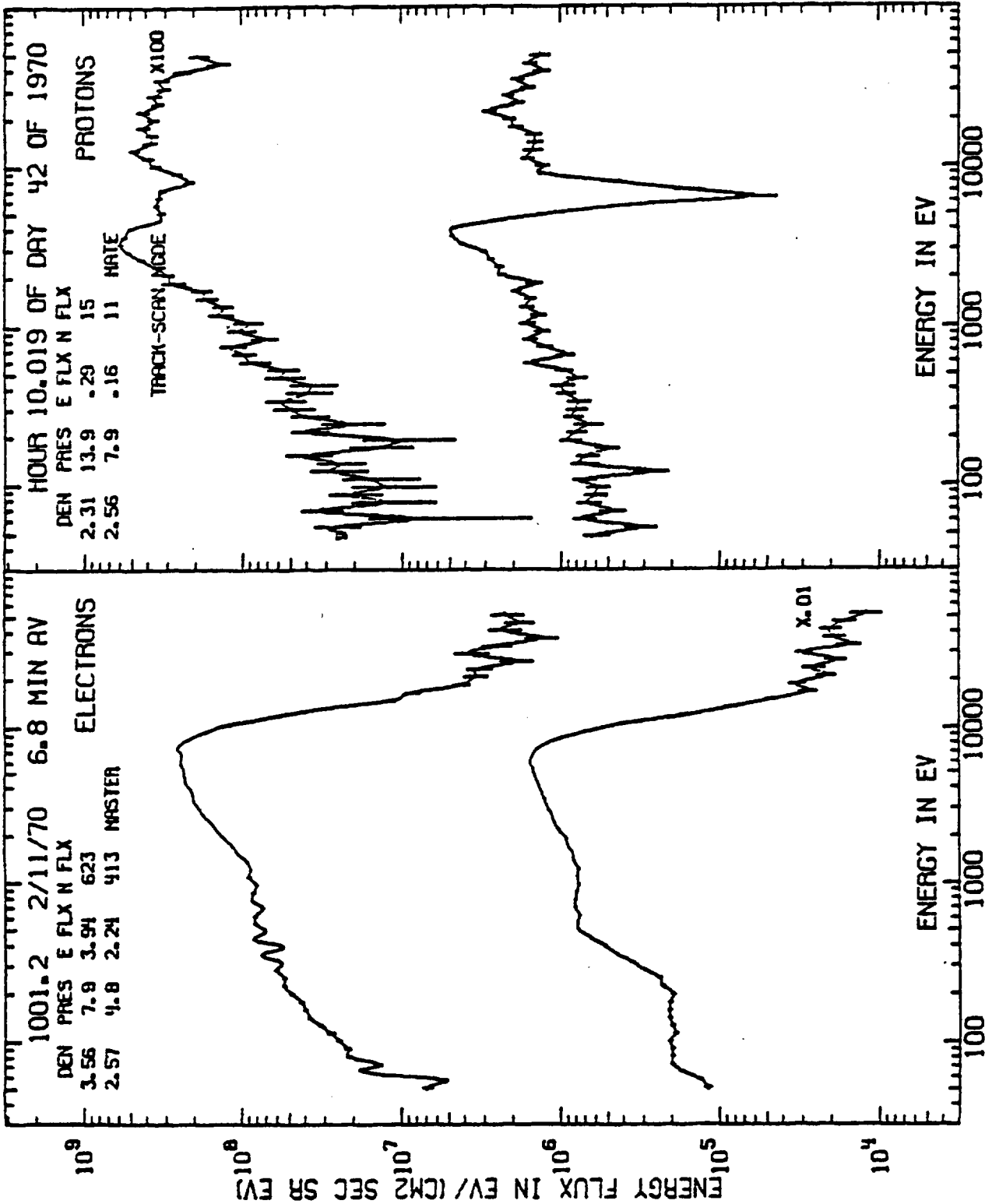
0.00 1.00 2.00 3.00 4.00 5.00

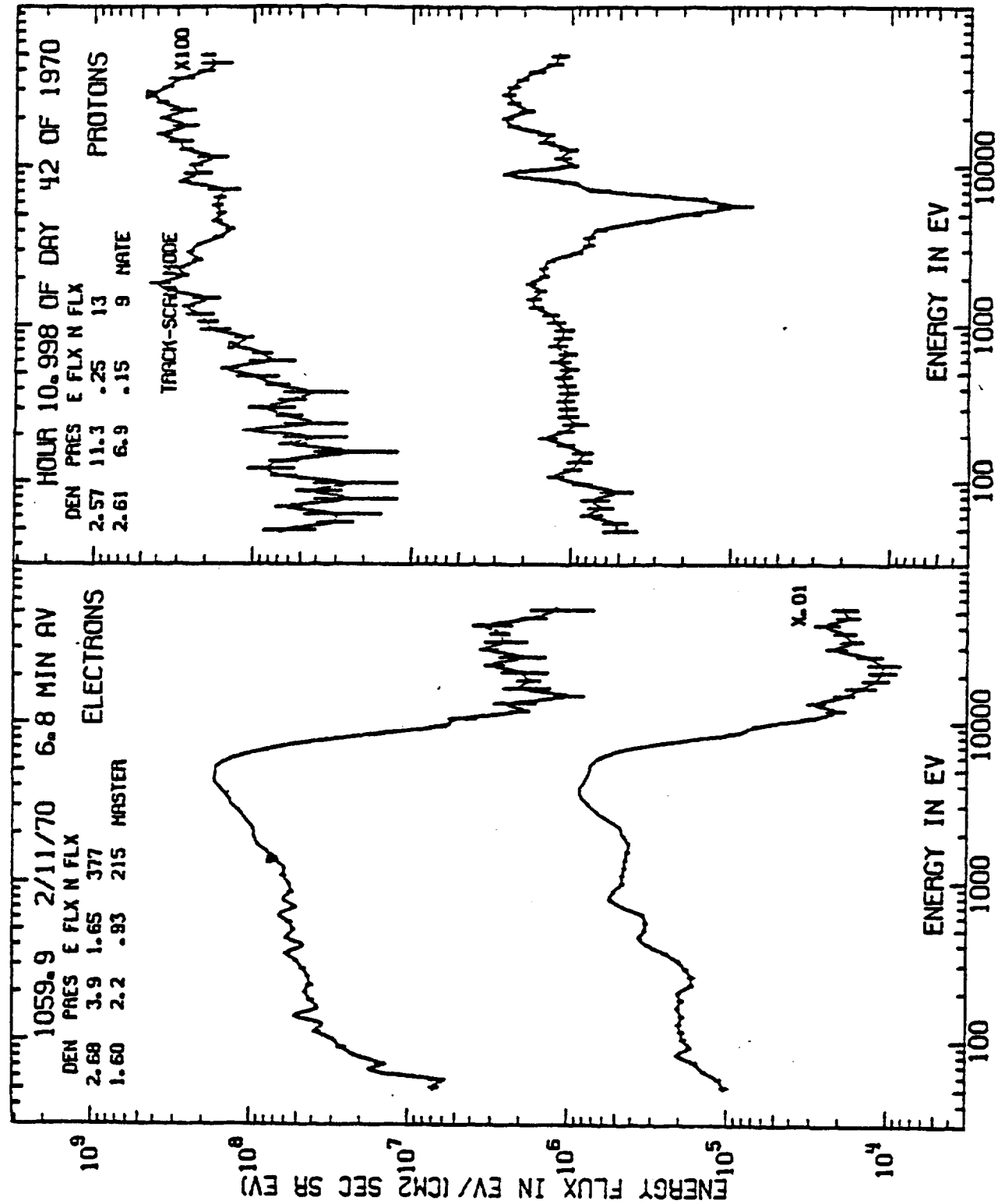




5.00  
4.00  
3.00  
2.00  
1.00  
0.00

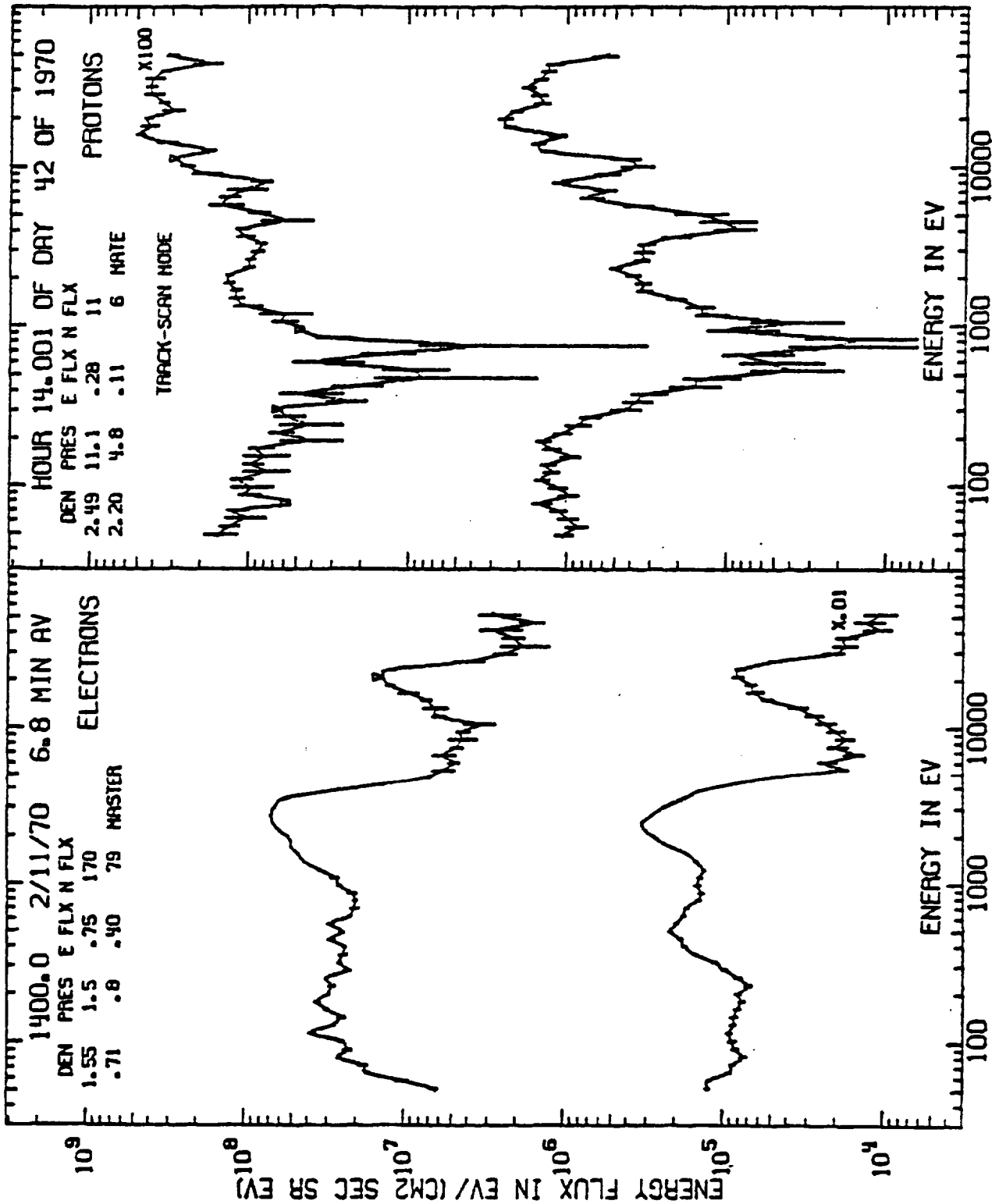
0.00 1.00 2.00 3.00 4.00 5.00

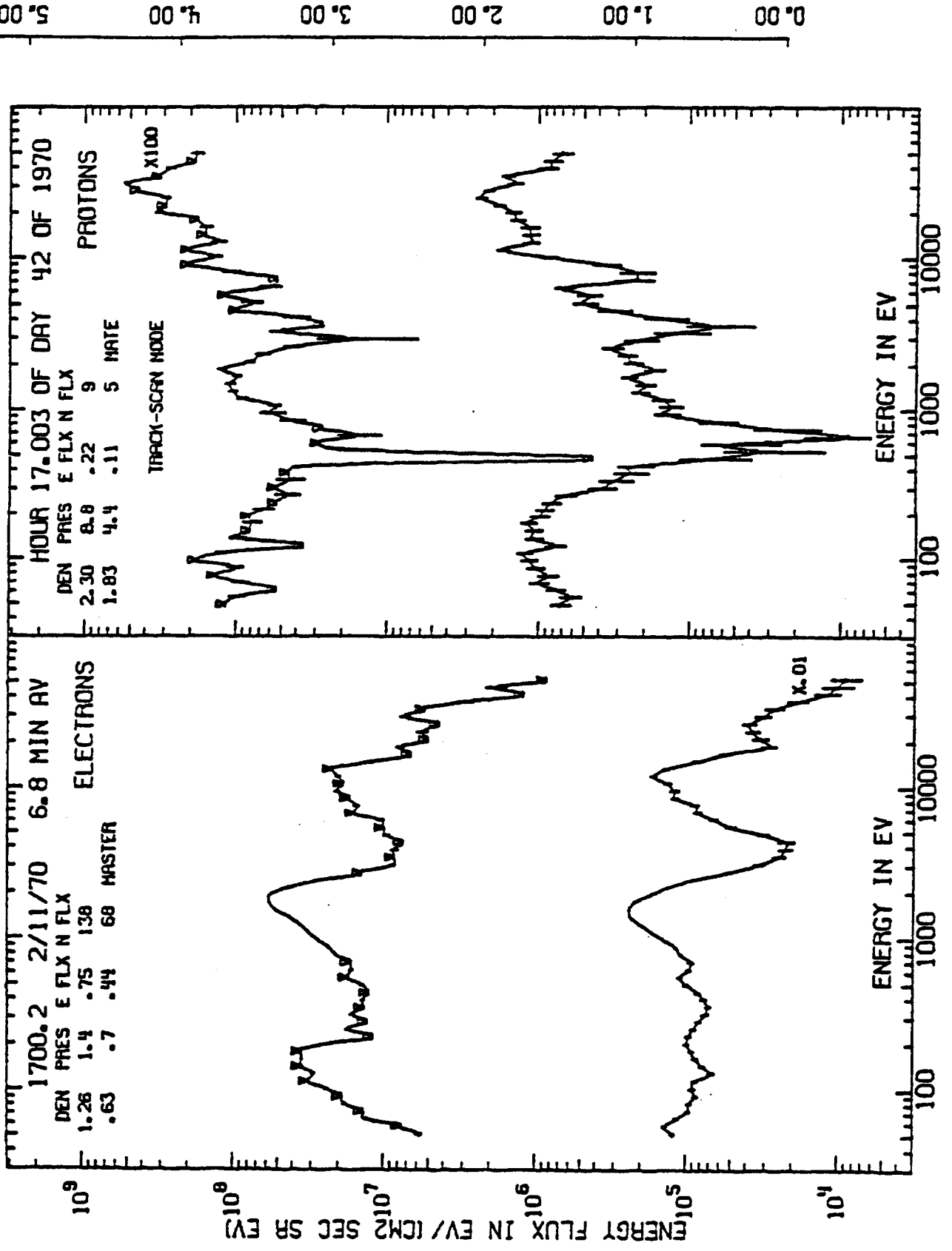




0.00 1.00 2.00 3.00 4.00 5.00

0.00 1.00 2.00 3.00 4.00 5.00





APPENDIX B

EXPERIMENTAL PLAN FOR THE TESTING OF  
SPACECRAFT CHARGING MODELS

by

MAYA DEVELOPMENT CORPORATION

for

SYSTEMS, SCIENCE AND SOFTWARE

August 1977



## TABLE OF CONTENTS

		Page
1.0	Introduction . . . . .	201
2.0	Experimental Strategy . . . . .	204
3.0	Ground Test Set Up . . . . .	215
3.1	Test Facilities . . . . .	217
3.2	Boundary Conditions . . . . .	219
3.3	Particle Source Characteristics. . . . .	223
3.3.1	Accelerator Characteristics . . . . .	224
3.3.2	Experimental Determination of the Source Particle Character- istics . . . . .	226
3.3.3	Programming of the Source Particle Characteristics . . . . .	227
3.3.4	Complications Caused by Electron Cyclotron Radius . . . . .	227
3.3.5	Photon Source . . . . .	231
3.4	Measured Quantities . . . . .	232
3.5	Diagnostic Instrumentation . . . . .	233
3.5.1	Field Mills . . . . .	234
3.5.2	Electrostatic Voltmeter (ESVM). . . . .	240
3.5.3	Diagnostic Electron Beam (DEB) and Beam Locator (BL) . . . . .	241
3.5.4	Retarding Potential Analyzer (RPA) . . . . .	243
3.5.5	Electrometer (EM) . . . . .	245
3.5.6	Magnetometer . . . . .	245
3.6	Procedures . . . . .	246
	Procedure 1 . . . . .	246
	Procedure 2 . . . . .	248
	Procedure 3 . . . . .	249
	Procedure 4 . . . . .	250
3.7	Data Processing and Display System . . . . .	254

	Page
Appendix 1 - Strut Design . . . . .	258
Appendix 2 - Distributed Source Ion Accelerator. . . .	261
Appendix 3 - Distributed Source Electron Accelerator . . . . .	265
Appendix 4 - Comparison Between the Ground Test and the Magnetospheric Environment . . . . .	269
References . . . . .	272

## LIST OF FIGURES

Figure No.		Page
2.1	Experimental matrix . . . . .	205
2.2	Experimental approach to computer code verification . . . . .	207
2.3	Flow diagram of the main program . . . . .	209
2.4a	Testing of subroutine POTENT . . . . .	211
2.4b	Testing of subroutine PUSHER . . . . .	212
2.4c	Testing of subroutine MATRIL . . . . .	213
3.1	Test object in vacuum tank . . . . .	216
3.2	Supporting strut . . . . .	221
3.3	Test object or satellite model . . . . .	222
3.4a	Electron cyclotron radii . . . . .	229
3.4b	Differential deflection of distributed Source Electron Beam . . . . .	230
3.5	Elementary field mill . . . . .	235
3.6	Rotating sensor field mill . . . . .	239
3.7	Block diagram of electrostatic volt- meter . . . . .	240
3.8	Block diagram of beam locator . . . . .	242
3.9	Retarding potential analyzer . . . . .	244
3.10	Test set-up for measuring and analyzing total currents . . . . .	252
3.11	Data processing and display system . . . . .	255
A-1	Supporting strut design for cylinders. . . . .	260
A-2	Distributed Source Ion Accelerator . . . . .	262
A-3	Distributed Source Electron Accelerator. . . . .	266

LIST OF TABLES

Table No.		Page
3.1	Characteristic Parameters for Particle Accelerators . . . . .	225
3.2	Measured Parameters and Diagnostic Instrumentation . . . . .	233
A-1	Characteristic Plasma Parameters and Scale Lengths . . . . .	270

## 1.0 Introduction

The purpose of this report is to develop plans for the experiments which must be conducted in order to verify the ground test mathematical model (GTMM) of spacecraft charging. Experiments will determine the ability of computer codes, which are being developed, to predict the electrostatic fields and charge distributions in the region around the GTMM. The verification tests consist of a matrix of experiments. The first experiments are simple. Later experiments are more complex culminating in a full scale test of an operational satellite.

The philosophy of this report is to establish the overall objectives in depth and then to explore the details of implementation. While the overall objectives are well-defined, the physical implementation as presented is flexible enough to allow a variety of engineering compromises and optimization.

Often during the development of this report a physical device or instrument was needed which was either not available commercially or had never been designed. Examples are the Distributed Source Accelerators (Discussed in Appendices 2 and 3) and the rotating sensor electric field mill illustrated in Figure 3.6. When this problem occurred our approach was to provide a rough conceptual design of the needed device and then indicate an estimated level of effort necessary to do detailed design and to construct the device. While the

conceptual designs are often sketchy they do provide a direction and provide a better response to the problem at hand than simply saying "There is no such device."

Facilities for the performance of these tests are available at NASA Lewis Research Center. The 15 ft. diameter tank described by Finke, et al. <sup>1</sup> is specifically designed for the testing of space packages and will, when adequately instrumented, make a superb facility for performing the FTMM verification tests. Preliminary tests of smaller test bodies can be performed in the 6 ft. x 6 ft. test tank which already contains substantial instrumentation (See Berkopec, et. al. <sup>2</sup>).

Section 2.0 contains a general description of the overall experimental strategy, and section 3.0 contains the description of specific experiments, including test set ups, procedures, and quantities measured.

In summary, the experimental plan presents a series of experiments, each repeating a prescribed procedure to measure an important physical parameter, which will enable the predictive ability of the computer codes to be determined. The ground test mathematical model (GTMM) will thus be verified by quantitative experiments. In addition, several extremely important spinoffs will result. The test facility which is

instrumented for an adequate GTMM verification will also be ideally instrumented (and calibrated) for a full scale operational satellite test. Tests of electrostatic properties can be performed. A new level of environmental simulation will be attained.

## 2.0 Experimental Strategy

The experimental strategy developed in this plan is as follows. Begin with as simple a situation as possible and attempt to understand it. Then in systematic steps increase the complexity of the situation. In this way, one can hope to progress from, for instance, a flat plate made of a single conductor irradiated by monoenergetic electrons toward a full scale test of an operational satellite being charged by distributed energy beams of electrons, ions and photons. The plan develops a matrix of experiments where complexity varies along three dimensions representing geometry, materials and irradiating sources. (See Figure 2.1).

For each experiment in the matrix the same instrumentation is employed, according to prescribed procedures, to measure the same physical parameters. Thus, as an example, a scan of an electrostatic voltmeter from the outer boundary to the surface of the test body along a prescribed path is a procedure which would be repeated for a number of different test bodies, each representing a different point in the experimental matrix. The data generated is then compared with that calculated using the computer codes, thus determining the predictive ability of the codes. A serious attempt has been made in this plan to develop experimental procedures which are a sensitive test of the computer code capabilities.

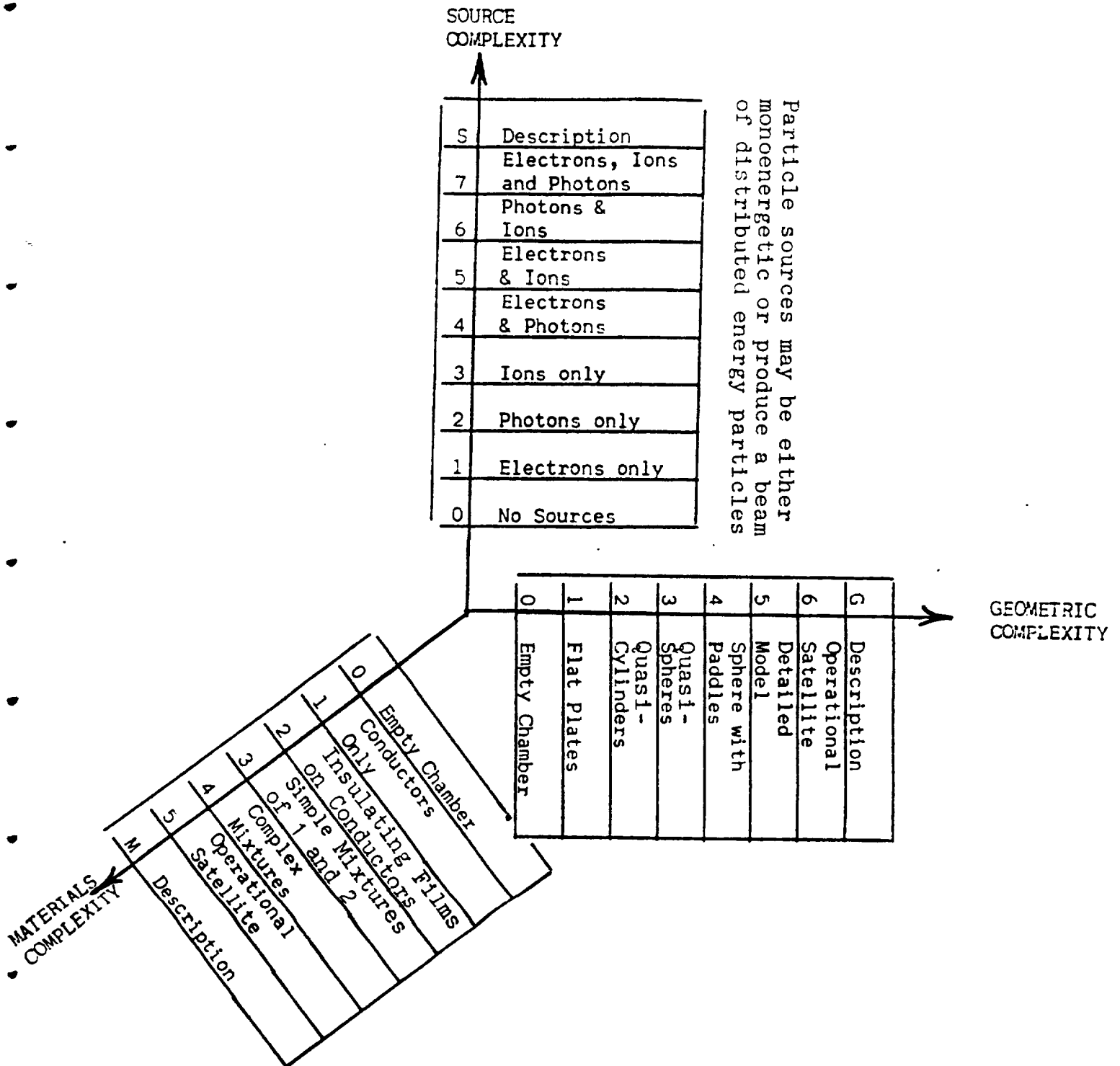


Figure 2.1. EXPERIMENTAL MATRIX .

All tests are assigned an experimental code (S, G, M) which defines the tests position within the experimental matrix. Large values of S, G, or M: signify more complex experimental situations.

A flow diagram indicating the overall experimental approach is shown in Figure 2.2. One begins by specifying a point in the experimental matrix, i.e. one must define the three parameters S. G. M. which specify the particle source, the geometry and the materials of the test object, respectively. Then one runs the computer codes and performs the experiments. Next the results are compared. We note that these experiments will generate a large amount of data, and that computer aided, on line, interactive reduction and presentation of this data should be seriously considered. The data output should, whenever possible, be formatted in such a way as to enable direct comparison with the output of the computer codes. After comparison of the data, it will likely be necessary to modify either the experiment or the computer code. One then repeats, as necessary, the process until the results of experimental and computer code agree. Finally, one selects a new point in the experimental matrix and repeats the entire procedure.

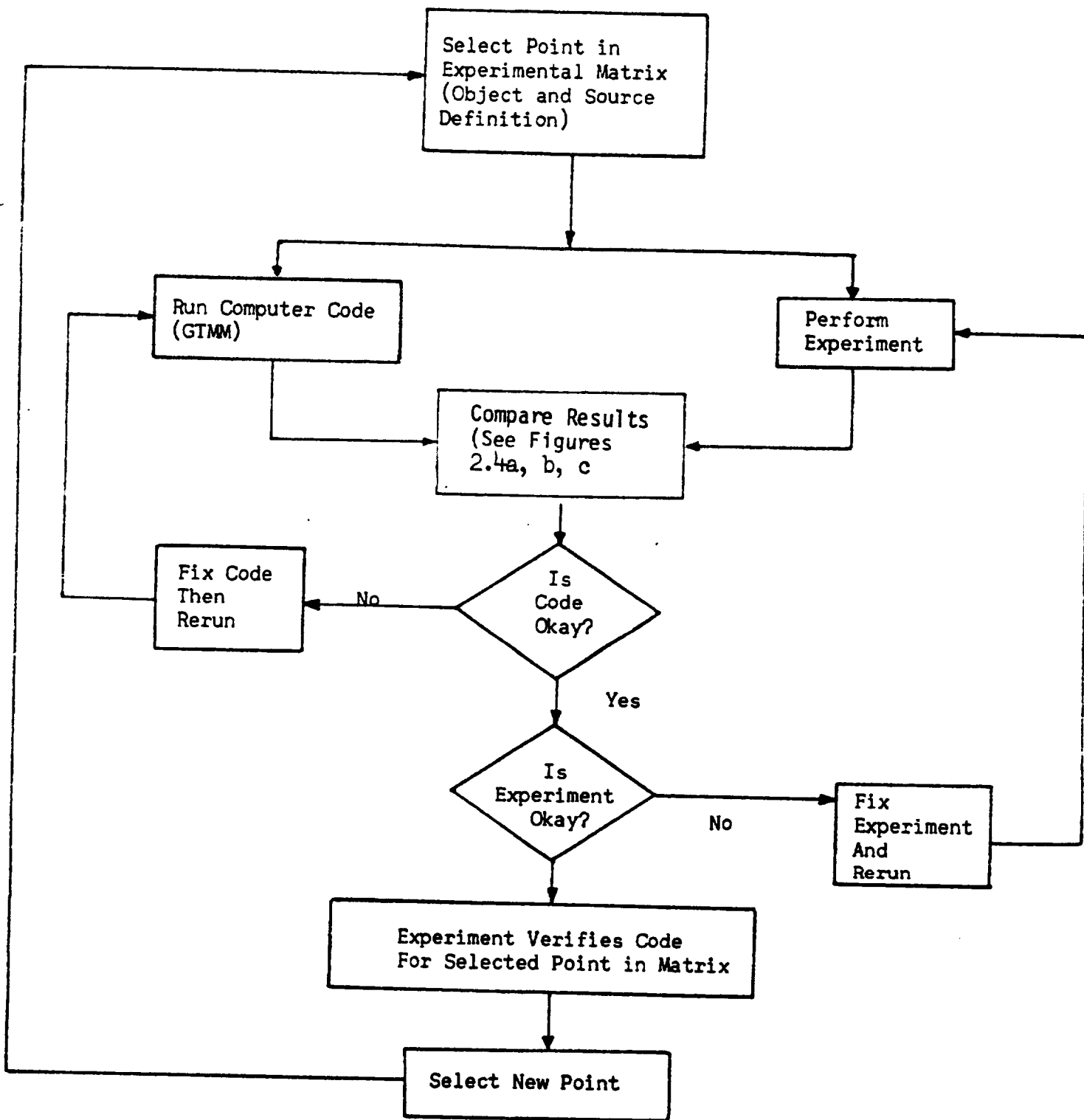


Figure 2.2.

Experimental approach to computer code verification.

As implied by the center box in Figure 2.2, a detailed examination of the comparison procedure is necessary. The comparison should take into account the structure of the computer codes and the difficulties of the experimental situation. Points to where the code predictions are sensitive and which can be experimentally examined with ease are sought out. Results of this examination follow as we present the details of the comparison procedure.

A review of the computer code development as presented in the Systems, Science and Software interim report (SSS-R-77-3124) provides the flow diagram shown in Figure 2.3. The code development has proceeded in "top down" fashion with each block being filled in with increasing detail. The experiments are similarly developed in a top down fashion with the plan structure paralleling the code structure. Both the computer code and the experiments accept as input data the specifications of the test object and particle source characteristics.

Thus to specify the input data to either the computer code or the code verification plan one must specify a point (S, G, M) in the experimental matrix. Verification consists of comparing the results of experiment and computer code then modifying one or the other until any differences are resolved.

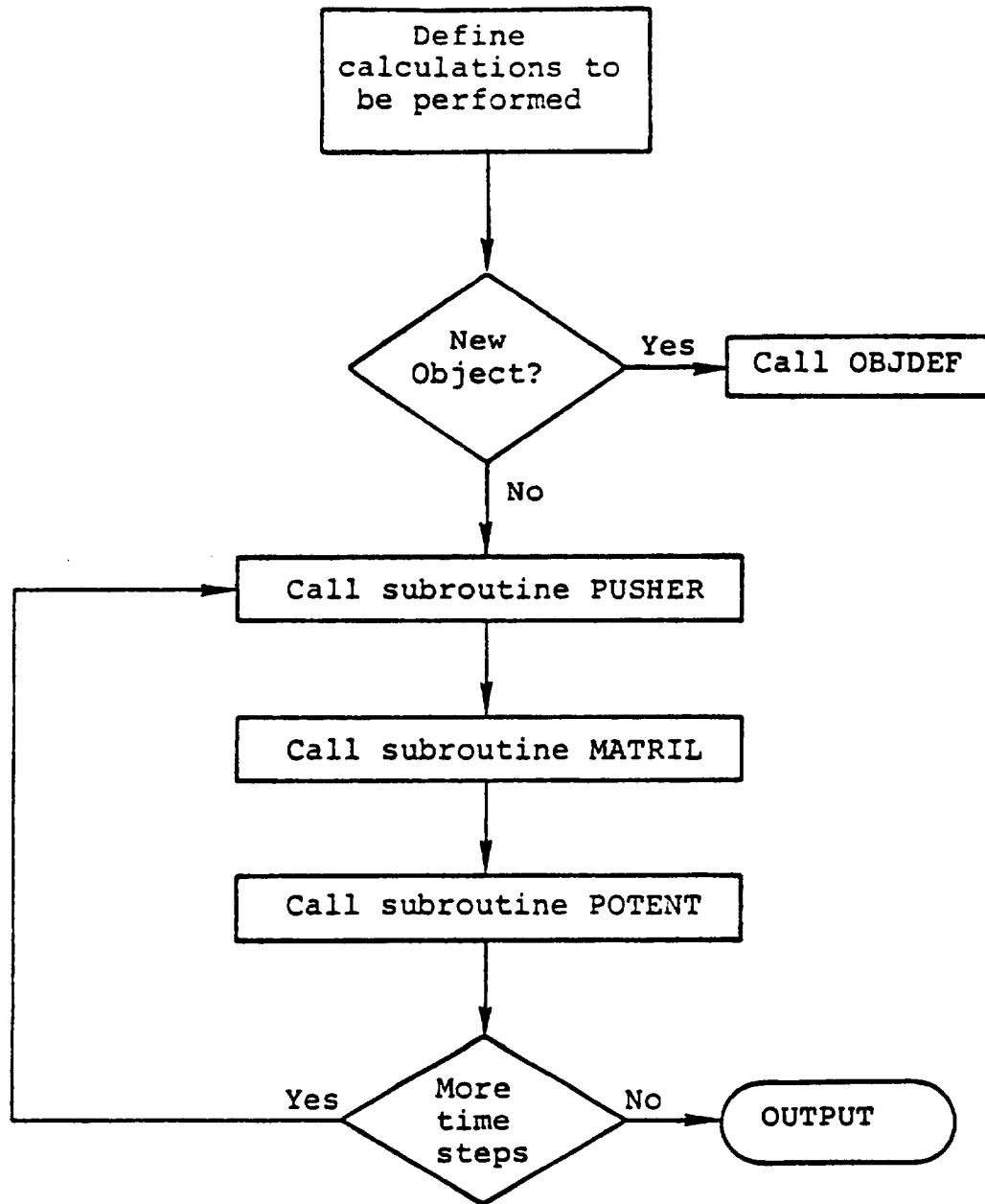


Figure 2.3. Flow diagram of the main program.

If possible, individual subroutines should be verified individually by experiments. The computer codes under consideration lend themselves well to this approach.

The subroutine POTENT, which calculates the electrostatic potential that results from a given geometric configuration of boundaries and charges, can be verified individually by experiments aimed at measuring potentials or alternatively capacitances. Figure 2.4a illustrates the approach. Trajectory measurements will provide a test of the capability of the subroutine PUSHER as indicated in Figure 2.4b. The verification of POTENT and PUSHER should be relatively straightforward.

MATRIL, the subroutine which treats charged particle interactions with the surface will be the most difficult to verify. The source of this difficulty lies in the difficulty of performing the experiments and in the wide range of variability of material surface properties. The approach is indicated in Figure 2.4c. An important result which should result from the implementation of this experimental plan is an improvement in the state of the art of materials measurements. The combination of computer codes with experiments will, once verified, create a powerful new tool for the study of material surface properties.

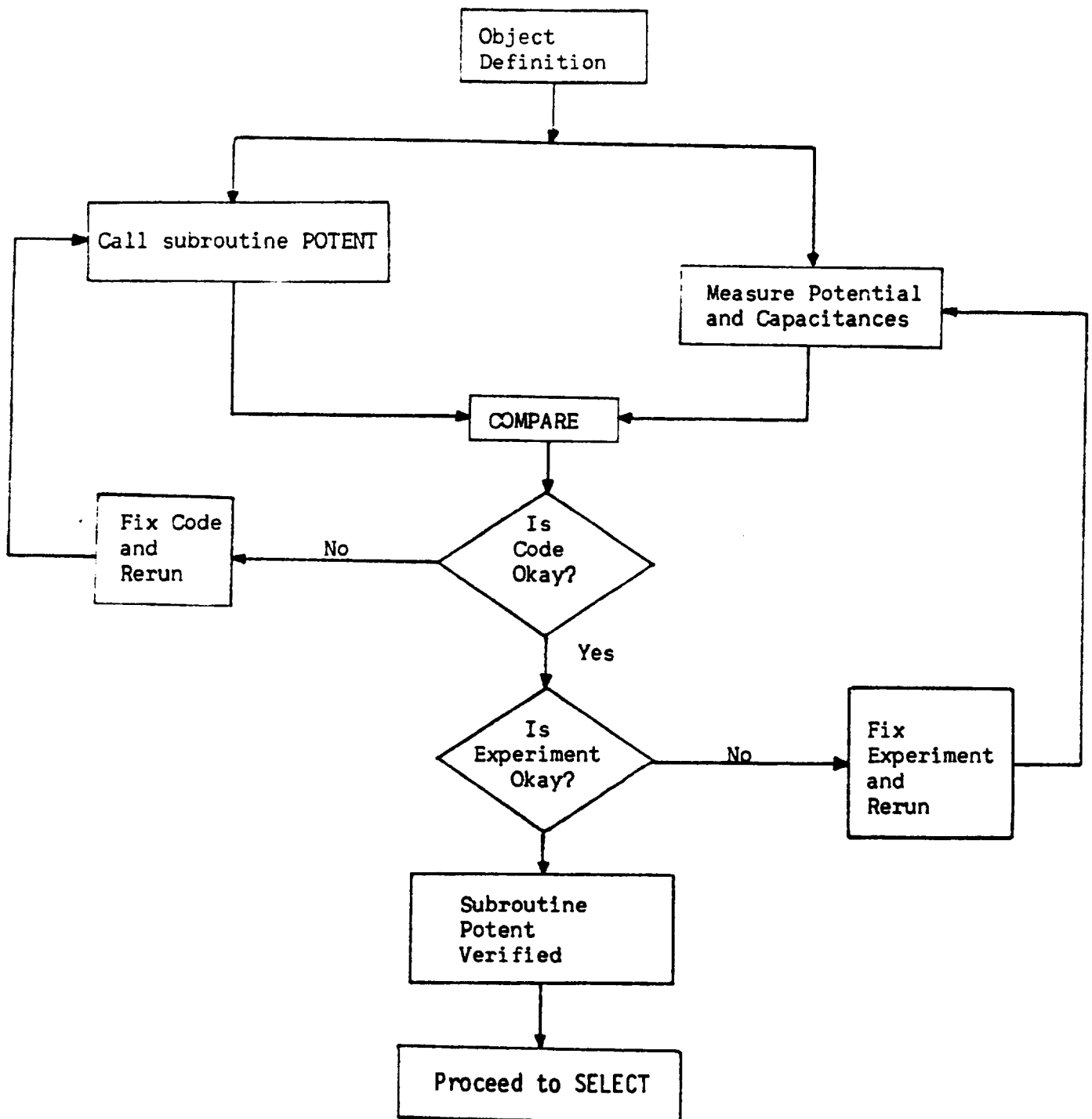


Figure 2.4a.

Testing of subroutine POTENT. Potentials or alternatively capacitances can be measured and compared with the results predicted by the code.

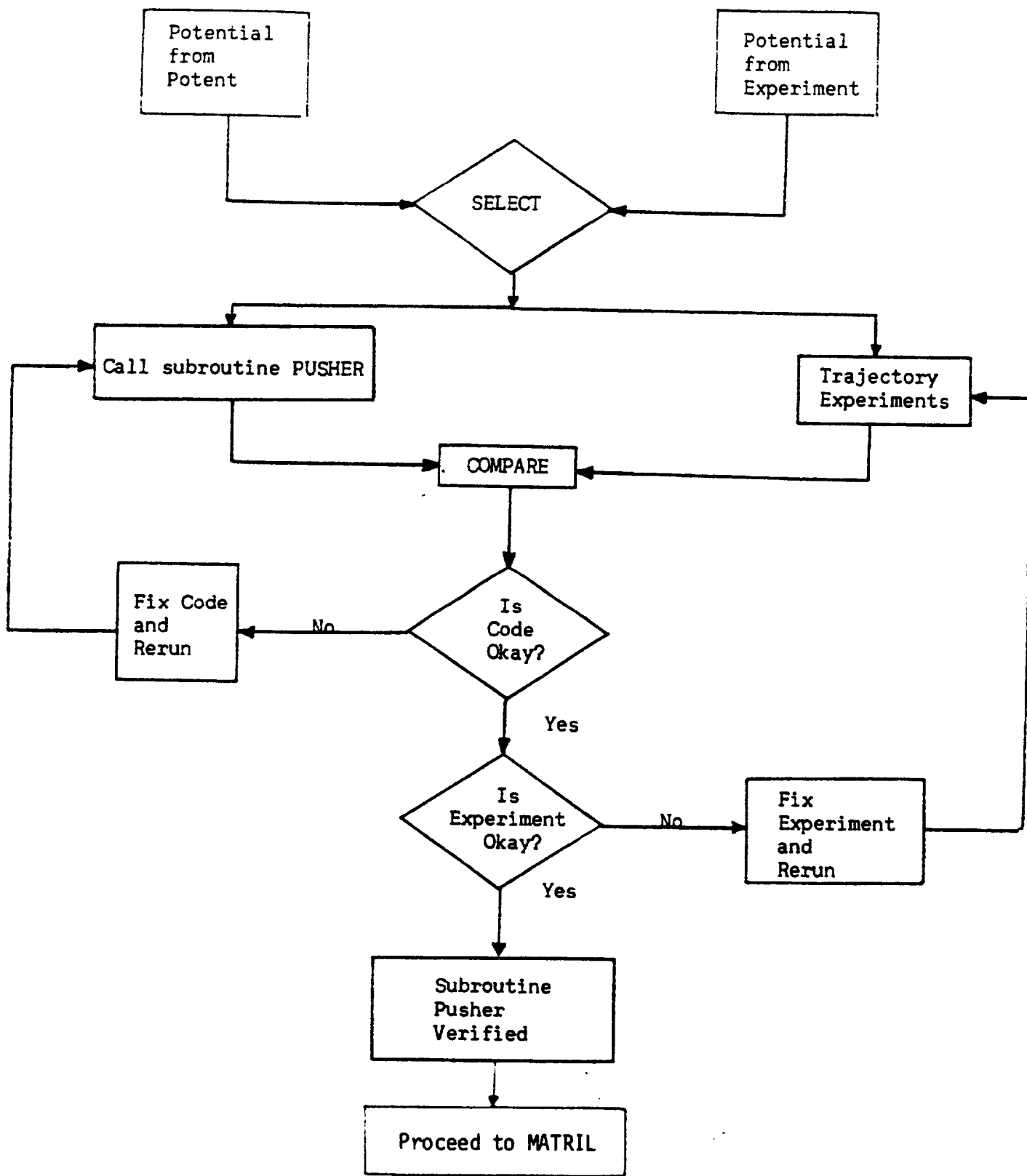


Figure 2.4b.

Testing of subroutine PUSHER. Charged particle trajectories in fields which are known from either measurement or calculation can be experimentally determined. Comparison with PUSHER trajectory calculations leads to verification.

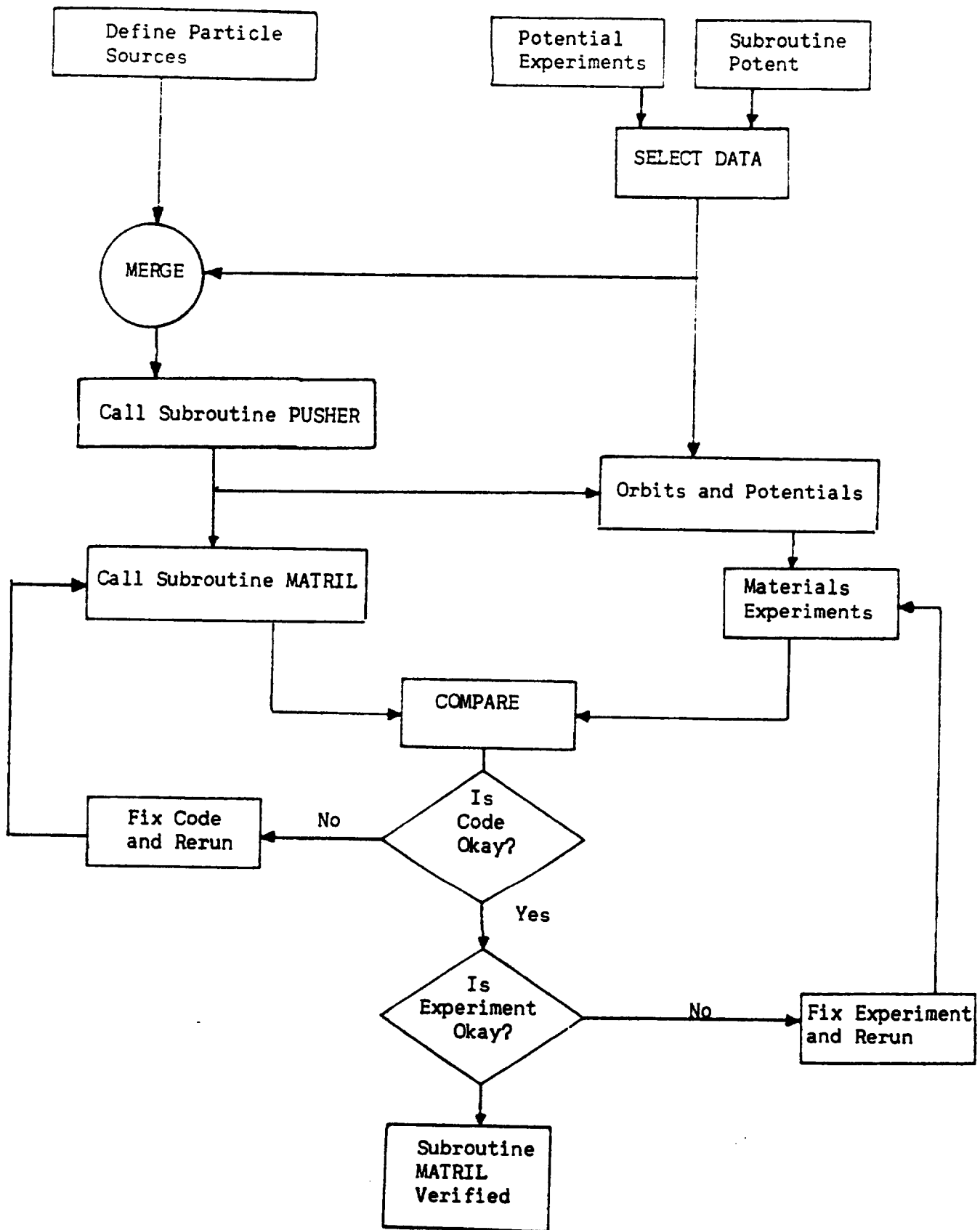


Figure 2.4c.  
 Testing of subroutine MATRIL. PUSHER is used to compute trajectories for materials experiments. Results are compared to verify MATRIL.

After verification of the individual subroutines the experiments should focus upon the verification of the overall code. (See Figure 2.2.) As a diagnostic procedure one may revert at any point during the overall verification of the GTMM to the procedures for testing an individual subroutine.

In summary, the experimental plan presents a series of experiments, each repeating a prescribed procedure to measure an important physical parameter. which will enable the predictive ability of the computer codes to be determined. The ground test mathematical model (GTMM) will thus be verified by quantitative experiments.

### 3.0 Ground Test Set UP

The purpose of this section is to describe a test facility which will be used to verify the Ground Test Mathematical Model (GTMM). Specifications for this test facility should determine the electrostatic boundary conditions and the source particle characteristics. To test the GTMM it is necessary to measure the electric charge distribution, the electric field intensity, the electric potential, the total current to the test object, (and leakage current) as well as current fluxes throughout the test space. These quantities are then to be compared with the results predicted by the GTMM.

In Figure 3.1 we indicate schematically the basic elements in an experimental facility designed to assess the GTMM. The facility supplies ion, electron and photon sources capable of simulating magnetospheric fluxes, establishes the appropriate electrostatic boundary conditions and provides the instrumentation required to measure the quantities stated in the previous paragraph. Data processing and display is incorporated into the facility in order to enable the large amounts of data which will be produced to be examined intelligently.

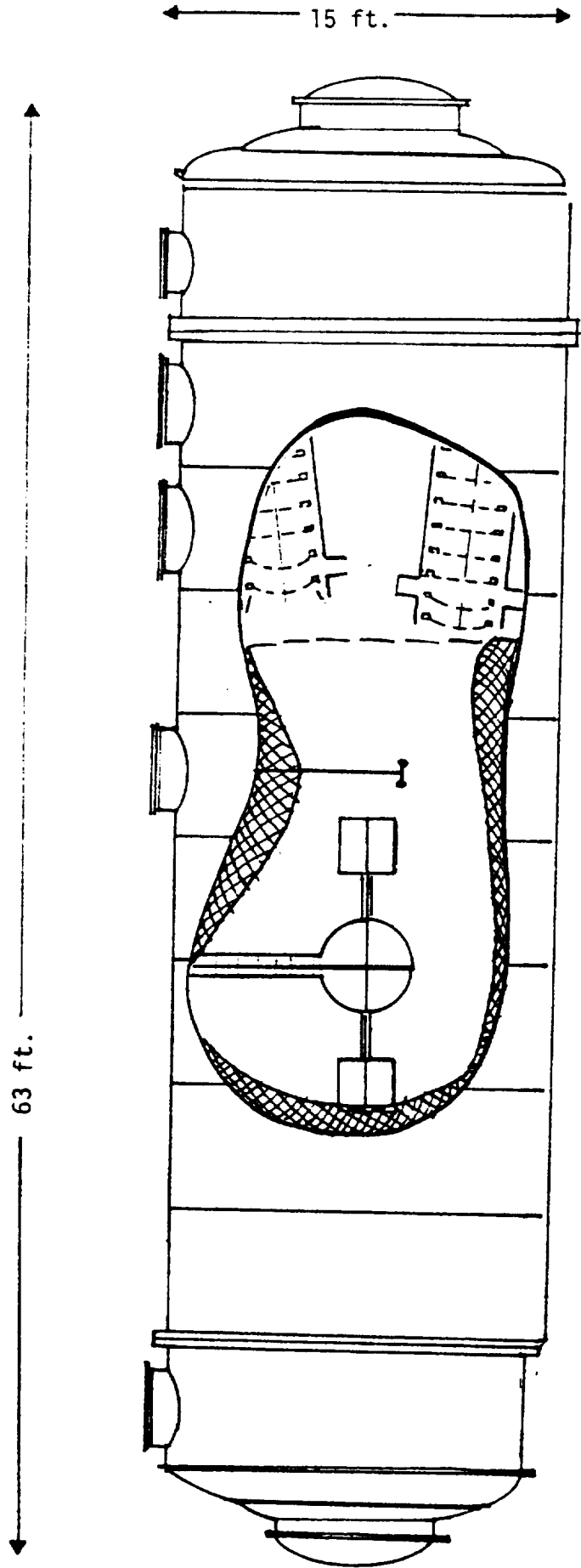


Figure 3.1. - A test object which might be a fullscale satellite is shown suspended in the 15 ft. x 63 ft. vacuum tank at LeRC. The entire assembly is contained within a Faraday cage. Data from the instruments is processed and displayed for comparison with the predictions of computer codes. Ion, electron, and photon beams illuminate the test object.

### 3.1 Test Facilities

Tests will be performed in two facilities which exist at NASA Lewis Research Center. The smaller of the two, a tank which is 6 ft. diameter by 6 ft. long, is described in NASA TM X-73602 by Berkopce, et al.<sup>2</sup>, is instrumented for use as a substorm simulation facility. This facility has been used by Stevens, et al. to measure the response of small samples of material to fluxes of electrons and photons comparable to those found at Geosynchronous Orbit (GSO). A larger facility measuring 15 ft. diameter by 63 ft. long is described in NASA TM D-2774 by Finke, et al.<sup>1</sup> This tank is designed primarily for environmental testing of space packages and plasma thrusters. It is large enough to perform full scale tests of an operational satellite. In this report we outline an instrument complement which, when installed in the large tank, will enable the experimenter to obtain the data necessary to verify a ground test mathematical model (GTMM) and to perform a full scale spacecraft charging test on an operational satellite.

The large LeRC tank is capable of high pumping speeds and ultimate vacuums approaching  $10^{-8}$  Torr thus it is suitable for use in this work. The high pumping speeds (e.g. Atmospheric to  $10^{-6}$  Torr in about 2 hours.) are important during the initial setting up of a test, when it may be necessary to pump down from atmospheric several times in order to work out

the details of a test set up. The ultimate high vacuums are important in the simulation of the hard vacuum of space. We note that a pressure of  $4 \times 10^{-7}$  Torr is obtainable in the empty tank without coolant in the pump traps, thus early tests could be run without using liquid nitrogen at a potential cost savings.

### 3.2 Boundary Conditions

An earlier MAYA report<sup>4</sup> (Appendix E of the S<sup>3</sup> Interim Report SSS-R-77-3124) specified boundary conditions and source particle characteristics for the ground test environment. An amplified version of this work, targeted for use in the large LeRC tank is presented here.

It is of great importance that the electrostatic boundary conditions be accurately defined in the ground test environment. If effort is not expended to do so, then stray fields can invalidate the test data. In order to obtain an accurate definition of the electrostatic potential at a large distance from the test object a Faraday cage should be constructed to contain a test volume within the vacuum tank. One might consider as an alternative simply allowing the vacuum tank to act as the Faraday cage. This alternative should be rejected. Despite the simplicity of implementation, using the vacuum tank as a boundary results in a geometrically and electrostatically irregular surface which will complicate test interpretation. Surrounding the test object with a Faraday cage will enable the experimenter to specify accurately the outer boundary condition for the electrostatic potential.

The satellite model or test object is suspended in the center of the cage. The supporting strut requires some care in its design in order to avoid seriously perturbing the

potentials. In Figure 3.2 we show an approach to the design. The strut is made of a number (say 10) of conducting cylinders, each of which is held at well-defined potential, chosen so as to minimize the perturbation caused by the strut. An example of the choice of strut potentials for a cylindrical test object at vacuum potential is given in Appendix 1. Voltages, currents and signals to and from the test object are conducted on wires contained within a shielding cable which runs through the strut.

A cross section through a typical test object is shown in Figure 3.3. The test object consists of two parts, an outer shell which represents the satellite surface and an instrument module contained within a Faraday cage. This Faraday cage establishes a solid reference potential and shields the outer shell from extraneous fields produced by the instrumentation. The outer shell can be changed to test different satellite configurations. The instrumentation module will be used with the different outer shells to establish potentials on the surface of the satellite and to operate those diagnostics which are located on the satellite model.

The inner and outer boundary conditions on the electrostatic potential are thus well defined by the experimental set up.

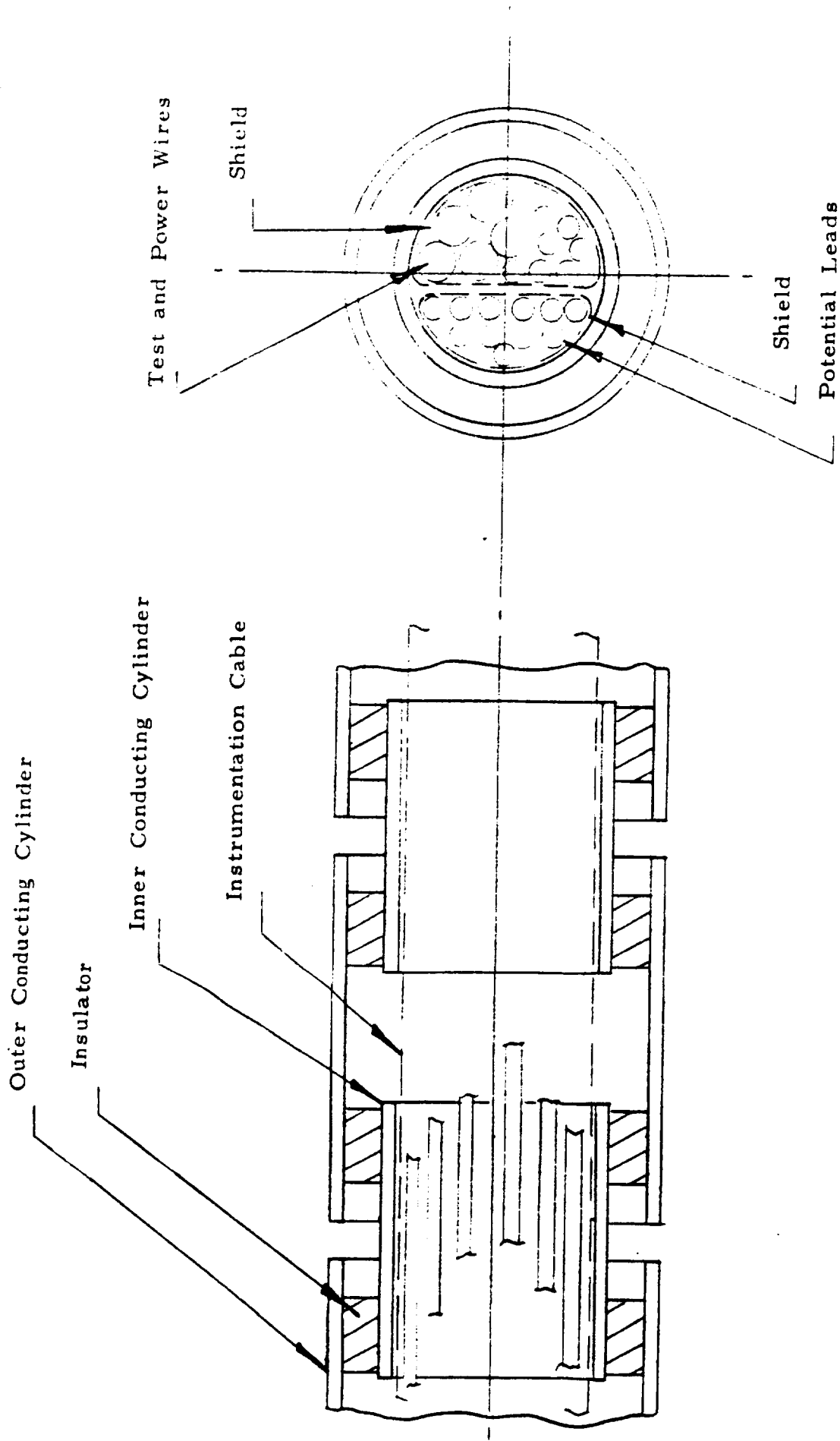


Figure 3.2 Supporting Strut

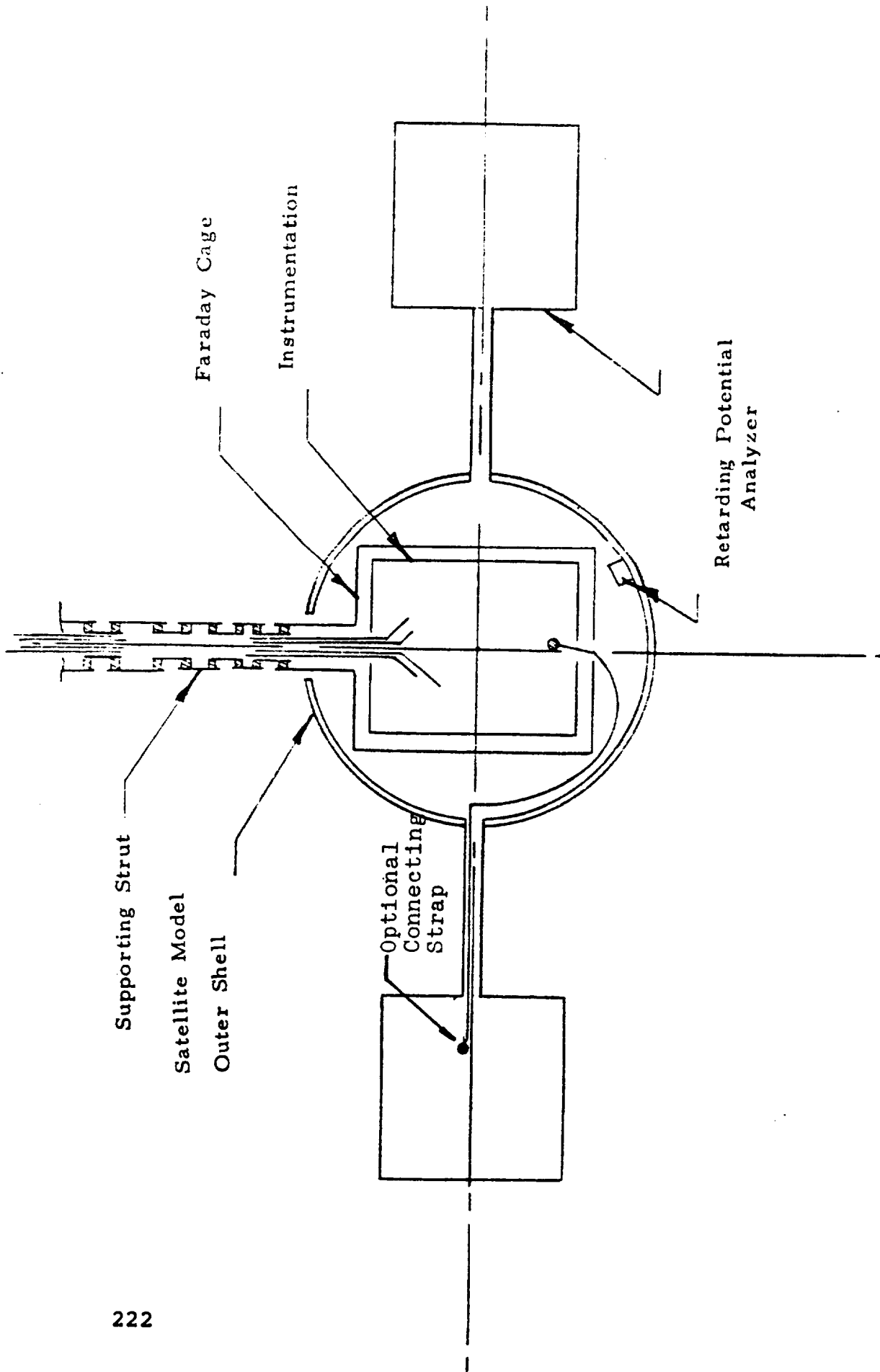


Figure 3.3 Test Object or Satellite Model

### 3.3 Particle Source Characteristics

The plasmas present in the magnetosphere at geosynchronous orbit are too hot and tenuous to be produced directly in a ground test environment. (See Appendix for a comparison of magnetospheric and ground test environment.) While it is possible to produce plasmas with the requisite number density ( $n \sim 1-100/\text{cm}^3$ ) it does not appear possible to heat these plasmas to kilovolt temperatures. We have therefore elected to simulate the magnetospheric environment with particle accelerators. The accelerators provide a directed, rather than a random, flux of energetic particles but have the advantages of ease of design, operation and characterization.

### 3.3.1 Accelerator Characteristics

The particle accelerators chosen for use in the ground test environment should be capable of producing fluxes which are comparable in intensity and in energy spectrum to the fluxes present in the magnetospheric environment. Data representing this environment have been previously presented in the MAYA report entitled "A Preliminary Specification of the Environment at Geosynchronous Orbit" (SSS-R-76-2996).<sup>5</sup>

The electron data given in this report are characterized by a high intensity number flux  $\Gamma_e \sim 1.5 \times 10^{10} / \text{cm}^2\text{-sec}$  with mean electron energy of 4.5 Kev seen on hour 10.8 of 3/18/70. This situation is typical of a post-midnight substorm and could produce hazardous charging. High proton fluxes occur on the day 2/11/70 during hour 9. These fluxes,  $\Gamma_i \sim 2.5 \times 10^8 / \text{cm}^2\text{-sec}$  are characterized by a mean particle energy greater than 10 Kev. The particle accelerators should be capable of producing fluxes with these properties over some large part of the test chamber.

With this background, after extensive review of the data, we have chosen parameters for the particle accelerators which will bracket the magnetospheric variations. These parameter choices are shown in Table 3.1.

Parameter	Electron Beam	Ion Beam
Directed Flux Intensity ( $\text{cm}^{-2} \text{sec}^{-1}$ )	$5 \times 10^6 < \Gamma_e < 5 \times 10^{10}$	$1 \times 10^6 < \Gamma_i < 1 \times 10^{10}$
Current Density (amps/cm <sup>2</sup> )	$8 \times 10^{-13} < J_e < 8 \times 10^{-9}$	$1.6 \times 10^{-13} < J_i < 1.6 \times 10^{-9}$
Particle Energy (Kev)	$1 < V_e < 40$	$1 < V_i < 40$
Energy Spread (Full Width at Half Maximum)	$10\% < \left( \frac{\Delta V_e}{V_e} \right) < 50\%$	$10\% < \frac{\Delta V_i}{V_i} < 50\%$

Table 3.1 Characteristic Parameters for Particle Accelerators

The flux densities are assumed to be delivered to an area of approximately one square meter. Thus the maximum total currents are approximately  $8 \times 10^{-5}$  amps and  $1.6 \times 10^{-5}$  amps for the electrons and ions respectively. The accelerators to be used should be low current large area devices. The beam area at the exit aperture of the gun should be at least  $0.05 \text{m}^2$ , and preferably larger, so that an area of  $1 \text{m}^2$  can be covered at a distance of approximately 1 meter from the gun without excessive beam divergence. A particle source of this size could be tested and debugged in the small 6 ft. vacuum tank with existing instrumentation. Note that the large vacuum tank is 15 ft. in diameter, hence has an area of  $16.7 \text{m}^2$ , so that multiple particle sources must be considered.

The energy spread indicated is optional but obviously desirable. The accelerators indicated for this work are of a rather peculiar sort. One usually seeks to make an accelerator with as monoenergetic a beam

as possible and often one seeks high current densities. For this application we are operating in the opposite limit, seeking a beam broadly distributed in energy with low current densities. Such beams are not currently commercially available, nor have they to the best of our knowledge designed or built in other research programs. We have thus undertaken to outline approaches to the design of such accelerators. In Appendix 2 "Distributed Source Ion Accelerator" we provide simple calculations which indicate that an ion accelerator based upon the use of crossed electron and neutral beams would provide the requisite currents. Such an accelerator has never been built and would require perhaps two man years to develop. A "Distributed Source Electron Accelerator" is discussed in Appendix 3. Again such a device has never been built, although MAYA personnel have used photoelectron source mono-energetic accelerators for the calibration and testing of auroral particle experiments on Advanced Technology Satellites 5 and 6. A distributed source electron accelerator would require more development, perhaps on the order of one man year by a qualified scientist.

### 3.3.2 Experimental Determination of the Source Particle Characteristics

The stability and accuracy of the particle accelerators may well be good but should not be trusted. Actual source particle characteristics should be measured experimentally, by examining

the beam with a retarding potential analyzer (RPA). The particle energy, variation of energy and current density across the beam and the angular spread of the beam should be defined. A series of scans with an RPA across the beam at different distances from the source will provide the requisite information. Using a MAYA RPA (See Section 3.5.4) energy analysis can be performed with an accuracy of at least 1% of the total beam energy and a spatial resolution of 0.1 cm.

### 3.3.3 Programming of the Source Particle Characteristics

Substorm simulation will be achieved by programming the temporal variation of the source intensity, mean energy and energy spread. This programming which should be controlled by the developing computer data link can be based upon the integrals computed as 2.3 minute averages from the ATS-5 data presented in the report SSS-R-76-2996.<sup>5</sup>

### 3.3.4 Complications Caused by Electron Cyclotron Radius

As has been noted in the Introduction, the electron cyclotron radius in the terrestrial experiments can be comparable to the dimensions of the test object. ( $r_e \sim 2.5m$  for a 1 Kev particle in a magnetic field of 0.3 gauss, See Figure 3.4a . Thus as a minimum provision should be made for pointing the electron accelerator through a range of angles. For a monoenergetic accelerator the beam may be deflected

electrostatically to compensate for the deflection by the magnetic field. Alternatively, the accelerator may be attached to a gimballed mount and thus pointed mechanically to compensate for the magnetic deflection.

An accelerator producing a beam distributed in energy will exhibit worse problems. Electrons with different energies will be deflected by different amounts. Neither electrostatic deflection nor mechanical pointing of a gimballed accelerator will compensate for this effect. Figure 3.4b illustrates the problem.

Photoelectrons are characterized by electron cyclotron radii of perhaps 10 cm. (See Figure 3.4.a.) The photoelectric sheath around a test object much larger than 10 cm would thus be substantially modified by the presence of the earth's field. While the computer codes can handle the effect of the magnetic field on the particle trajectories, the physics of the sheath may be changed profoundly. Some numerical and analytical work is needed to determine the impact of finite electron, cyclotron radii. Serious thought must therefore be given to constructing a Helmholtz coil system for the purposes of reducing the field within the test chamber.

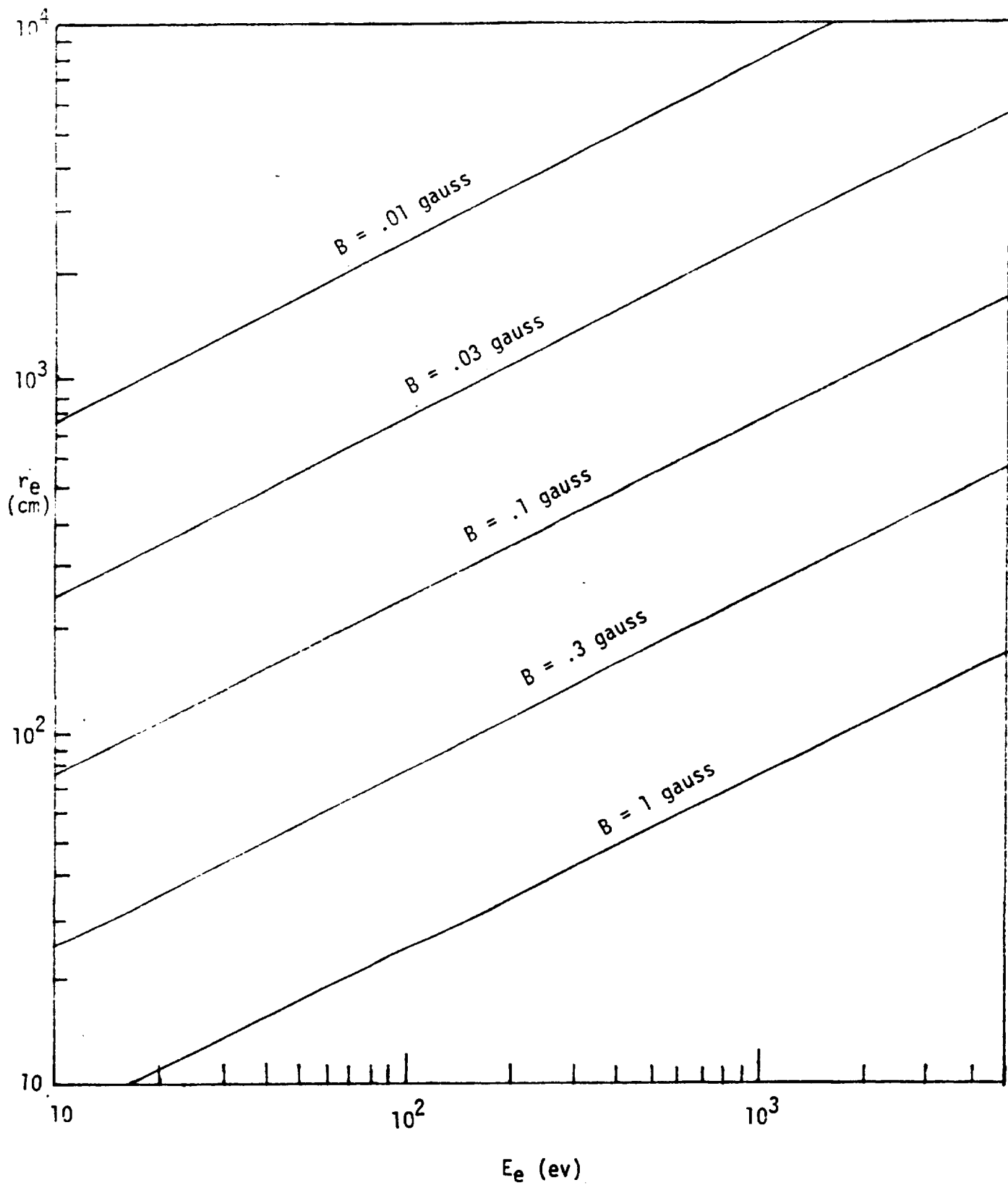
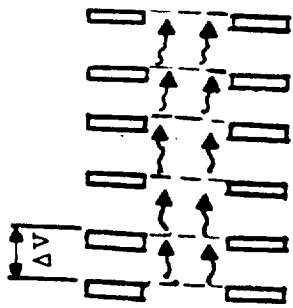


Figure 3.4a Electron Cyclotron Radii



DISTRIBUTED  
SOURCE  
ELECTRON  
ACCELERATOR  
(APPENDIX 3)

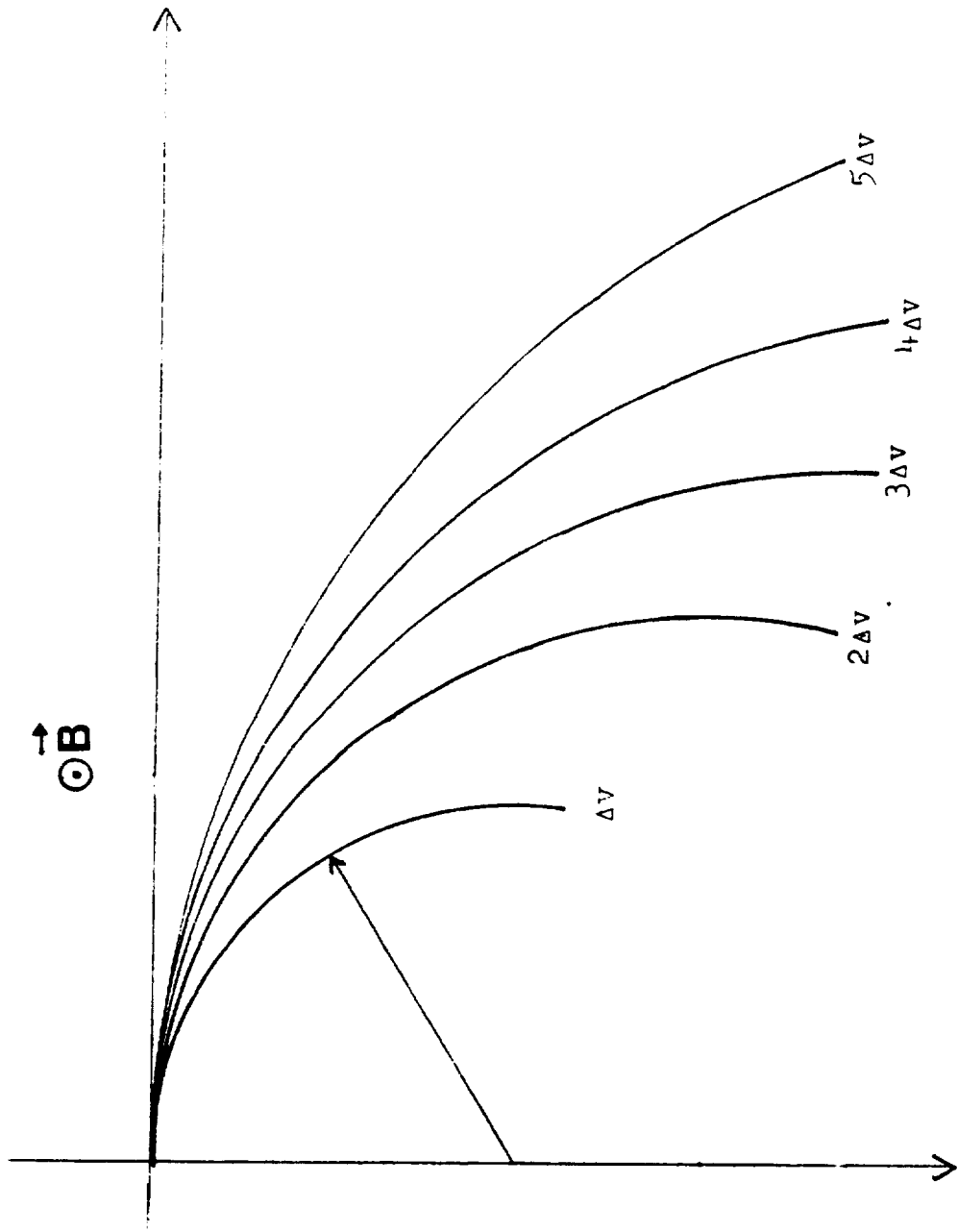


Fig. 3.4b.

DIFFERENTIAL DEFLECTION OF DISTRIBUTED SOURCE  
ELECTRON BEAM

Electrons with lower energies are deflected more. Thus the beam emerging from a distributed source electron accelerator (see Appendix 3) would be defocused at energies below 1 kev by the presence of the magnetic field of the earth.

### 3.3.5 Photon Source

Photons should be provided by a solar simulator. Since photoemission is very important in the determination of overall satellite potentials both the intensity and spectrum of the illuminating photons should be carefully matched to that of the sun. ORIEL Corporation of America, 15 Market St., Stamford, Conn. 06902 is a comprehensive source of solar simulation equipment.

### 3.4 Measured Quantities

The computer codes use as input the following:

- 1) specification of the boundary conditions far from the satellite
- 2) specification of the source particle characteristics far from the satellite
- 3) detailed geometry and materials of the satellite

The computer codes then calculate the following:

- 1) particle trajectories, interactions at the satellite surface, and resulting electric charge distributions
- 2) electric field intensity
- 3) electric potential
- 4) total current to the body and total leakages through the body
- 5) current fluxes

This experimental plan develops the methods of measuring items 1) to 5) so that direct comparison can be made between experimental measurements and the results of the computer codes. To do so we define an array of diagnostic instrumentation, a series of procedures for making the measurements and a method of reducing the resulting data. Of these parameters, the surface electrostatic potentials and the currents are perhaps the most important. These are also the most easily measured and so should provide a sensitive test of the computer codes.

### 3.5 Diagnostic Instrumentation

An array of instrumentation is needed in order to perform the measurements defined in the preceding section. These instruments should be interfaced to a data acquisition system (DAS) which is spelled out in more detail in Section 3.7. The instruments which are needed and the measurement which they perform are indicated in Table 3.2.

		Diagnostic Instrumentation				
		Field Mill	Electrostatic Voltmeter	E Beam/RPA	Electro-meters	Magneto-meters
MEASURED PARAMETERS	Charge/Trajectories	X				
	E Field	X				
	Potential		X	X		
	Total Current				X	X
	B Field					X

Table 3.2

Description of the instrumentation follows.

### 3.5.1 Field Mills

The electric field is best measured with a time varying capacitive probe, i.e. a field mill. The basic equation describing such a device is

$$Q = CV$$

whence the current

$$I = \frac{dQ}{dt} = C \frac{dV}{dt} \textcircled{1} + V \frac{dC}{dt} \textcircled{2}$$

Term  $\textcircled{1}$  is the usual term which one finds in ordinary circuit analysis of constant capacitance devices. Term  $\textcircled{2}$  is important whenever the capacitance varies in time. In order to understand how such a device can be used to sense electric fields we consider the situation illustrated in Figure 3.5.

For a plate of area  $A$  separated by a distance  $d$  one has a capacitance  $C = \epsilon_0 \frac{A}{d}$

And an electric field

$$E = V/d$$

where  $V$  is the potential difference across the plates

Thus the current associated with the time varying capacitor is

$$I = \epsilon_0 A \frac{dE}{dt} + \epsilon_0 E \frac{dA}{dt}$$

$A(t)$  varies periodically in time with a fundamental frequency

$\omega$  thus  $A(t) = \sum_{-\infty}^{\infty} a_n e^{in\omega t}$

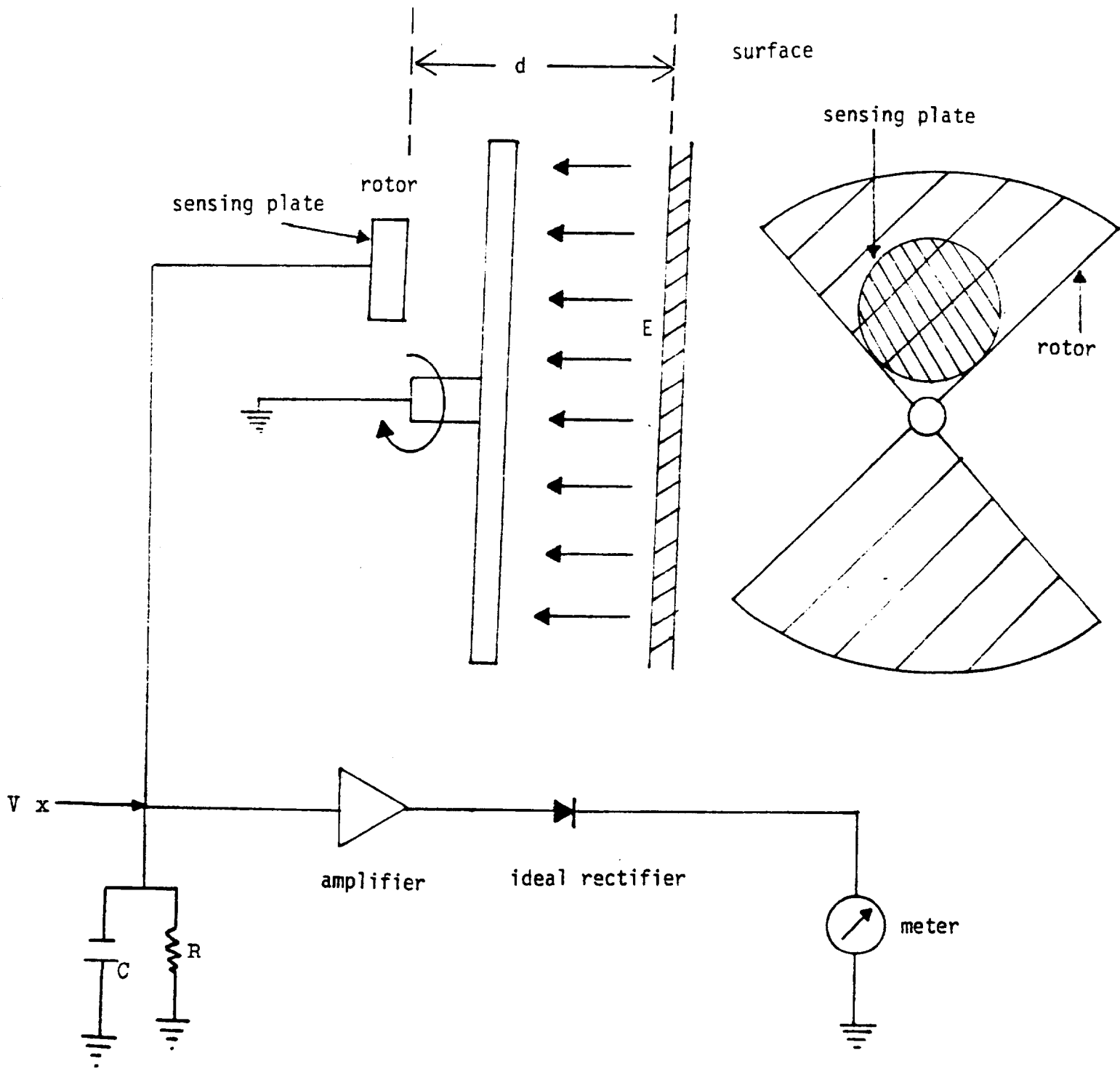


Figure 3.5. Elementary Field Mill

For purposes of illustration we take

$$A(t) = \frac{1}{2} a (1 + \sin \omega t)$$

and thus

$$I(t) = \epsilon_0 a \frac{dE}{dt} + \epsilon_0 E \frac{1}{2} a \omega \cos \omega t$$

For a static electric field  $\frac{dE}{dt} \rightarrow 0$

and the voltage at point x in Figure 3.5 is given by

$$V_x(\omega) = I(\omega)Z(\omega) = \frac{1}{2}\epsilon_0 E a(\omega)Z(\omega)$$

For an ideal integrator.

$$|Z| \rightarrow \frac{1}{\omega C} \text{ for } \omega RC \gg 1$$

thus

$$|V_x| \rightarrow \left( \frac{\epsilon_0 a}{2C} \right) E$$

The field mill therefore provides a simple way of measuring the electric field at a surface. In actual instruments one can use substantially more sophisticated filtering and phase sensitive detection techniques to improve the sensitivity and accuracy of the field mill. Also in practice one would calibrate the field mill using known fields. The analysis above is thus meant only to illustrate the principles involved and would not be used to determine actual field strengths. A simple analysis of field mills has been provided by Secker.<sup>6</sup> Field mills are commercially available from Monroe Electronics, Inc., 100 Housel Avenue, Lyndonville, New York, 14098. The Monroe units use a rather large sensing element and so it may well be necessary to design and fabricate a smaller sensor.

The device thus far discussed is useful for measuring the electric field strength near a flat surface. It must be modified however to measure the local electric field at a point in space well away from a surface. Our survey did not turn up a commercially available device which would perform this measurement, thus we have again, as in the case of the distributed source accelerators, been forced to propose a device which will require some development.

The device used to measure the electric field at a point in space well away from a surface is illustrated in Figure 3.6. A variation on the earlier theme is used to measure the electric field at a point in space well away from a surface. A rotating sensor consisting of two small spheres of radius  $a$  separated by a distance  $d$  is used to drive an integrating differential amplifier. The rotating sensor would be mounted on the end of an extensible shaft. This shaft could be extended from the top of the vacuum system downward into the measuring area. Alternatively the sensor would be extended outward from the wall. The mechanics of this one dimensional movement should not be too difficult.

As is shown in Figure 3.6 the potential on the spheres varies as they are rotated. Thus one senses a term like  $\textcircled{1}$  in the current equation. By integrating this term one finds  $\Delta\phi$  and hence can directly infer  $E = \Delta\phi/d$ . This device and the

conventional field mill previously discussed are both simple theoretically and easy to construct and calibrate. The rotating sensor device will require perhaps six months of developmental work.

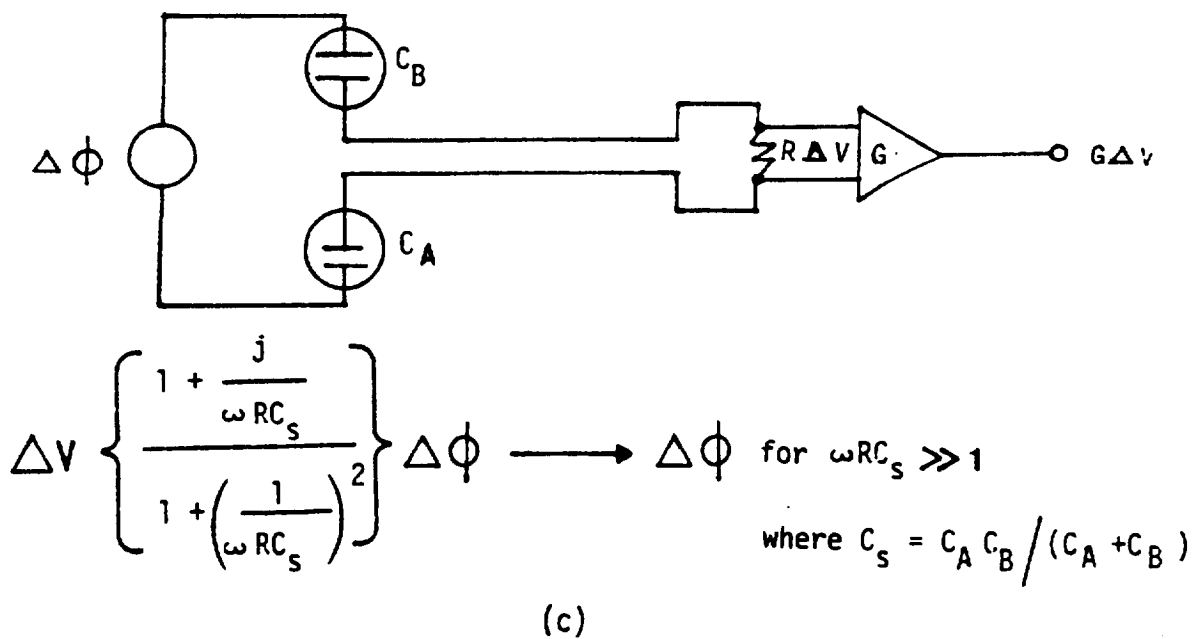
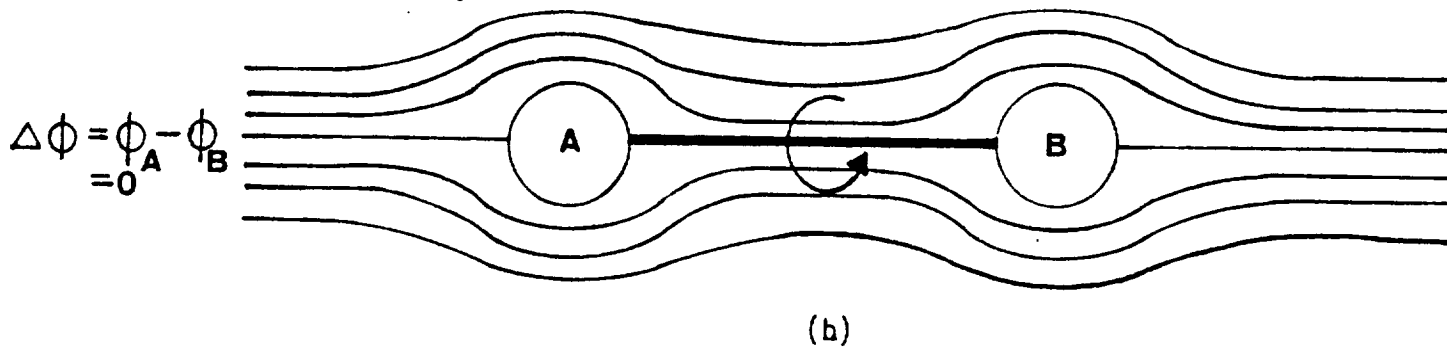
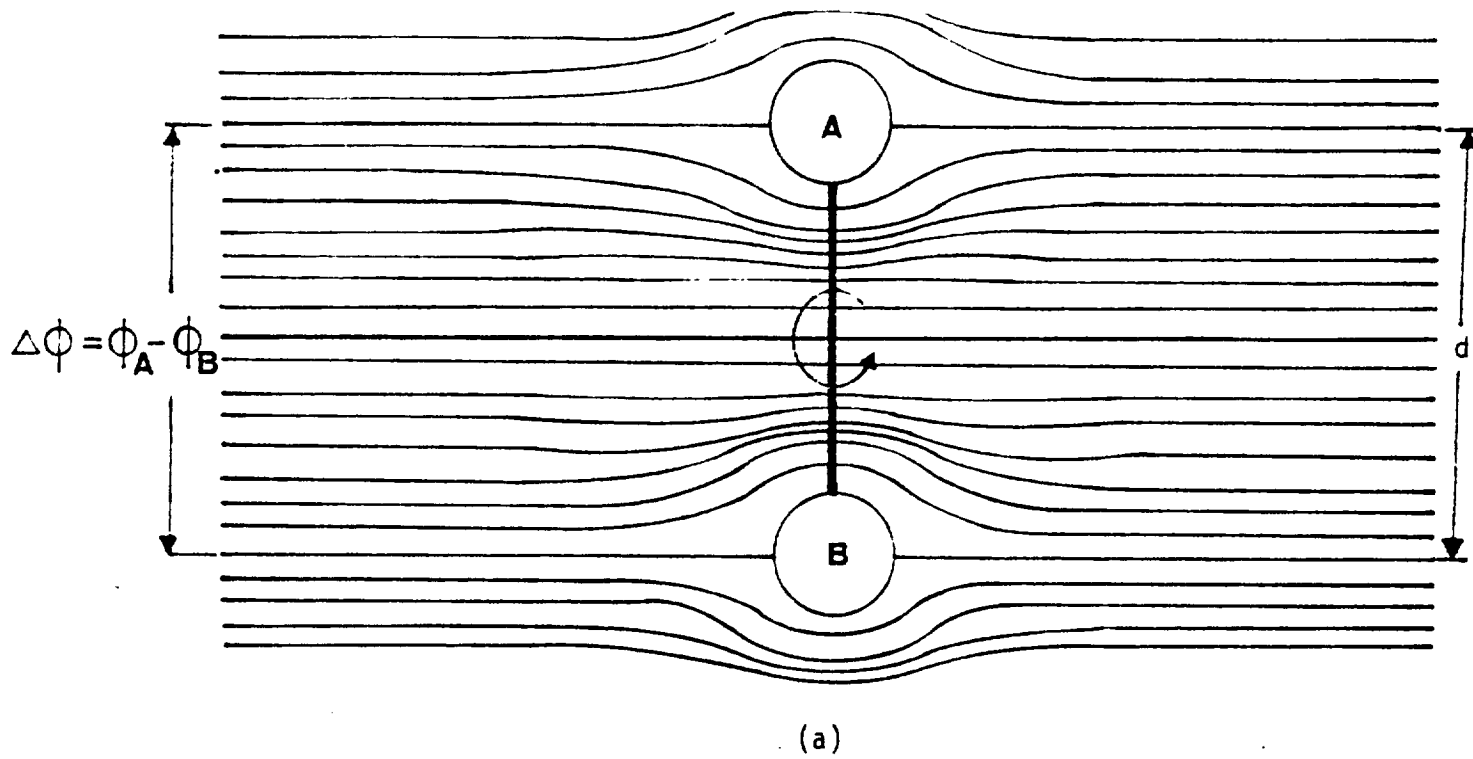


Figure 3.6 Rotating Sensor Field Mill - The potential  $\Delta\phi$  impressed between two small spheres rotating with frequency is measured with an electrometer. The local electric field  $E = \Delta\phi/d$  is thus determined.

### 3.5.2 Electrostatic Voltmeter (ESVM)

A field mill can be combined with a phase sensitive detector and a feedback amplifier to make a sensitive electrostatic

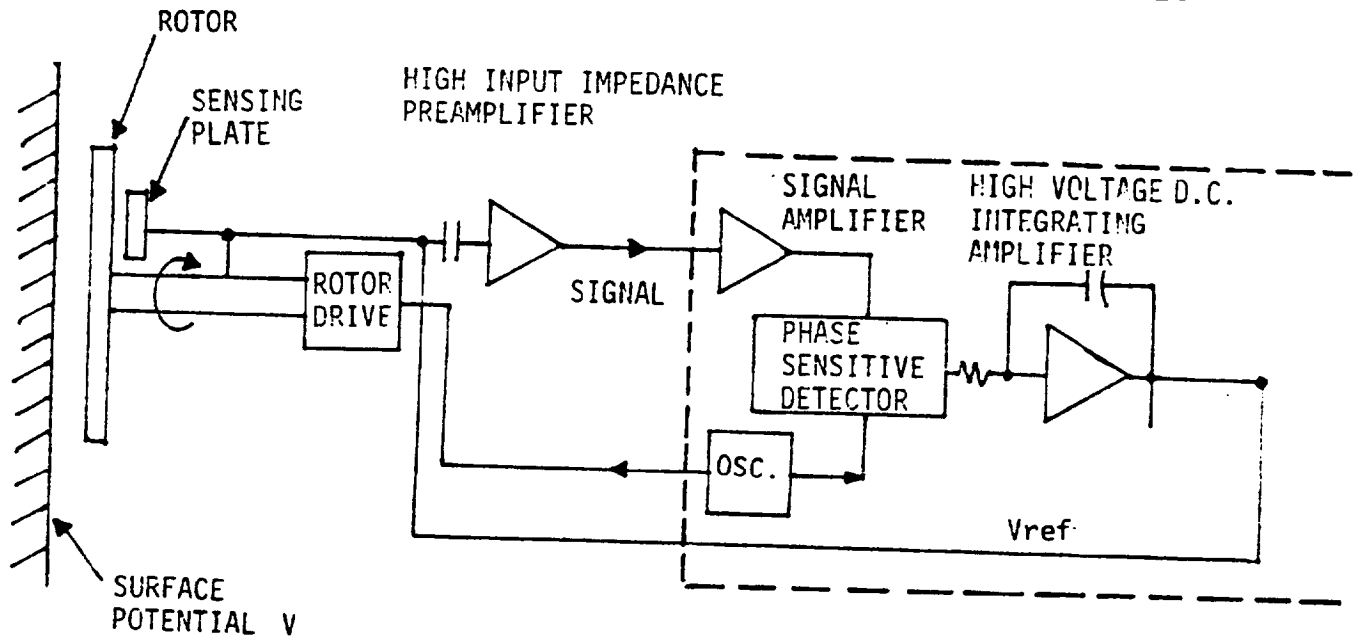


Figure 3.7. Block Diagram of Electrostatic Voltmeter  
voltmeter. A block diagram of such a system is shown in Figure 3.7. The voltage out of the field mill is proportional to the electric field  $E = (V - V_{ref})/d$  as has been demonstrated in the previous section. The voltage  $V_{ref}$  is served through the integrating amplifier to match  $V$  so as to reduce  $E$  to zero. Thus  $V_{ref}$  approaches  $V$ . Typical commercially available systems have an accuracy of 0.1% and will settle to within this accuracy in 10 milliseecs. Instruments of this type are manufactured by Monroe Electronics, Inc., 100 Housel Avenue, Lyndonville, New York and by Trek, Inc., 8460 Ridge Road, Gasport, N.Y. 14067.

The Trek unit uses a probe based upon a mechanically resonant reed which leads to a smaller sensor than is available from Monroe.

### 3.5.3 Diagnostic Electron Beam (DEB) and Beam Locator (BL)

In addition to the primary electron sources which simulate the magnetospheric fluxes an electron beam should be available for diagnostic purposes. Simple inexpensive guns designed for use in CRT's are available. These guns produce a small diameter beam of monoenergetic electrons and work well in the 100 ev to 20kev range. The CRT guns are provided with plates for x-y deflection of the beam and lenses for focusing. The Beam Locator consists of a four quadrant electrometer as shown in Figure 3.8. The beam is located when signals from the four quadrants are all equal. The electronic Beam Locator is not commercially available but should be relatively simple to develop. We estimate that three man months of engineering effort should be sufficient to produce a working unit. An alternative approach which is of particular use in debugging, is to use a photoemissive screen. With such a screen one simply observes a glowing spot where the beam is impacting on the screen.

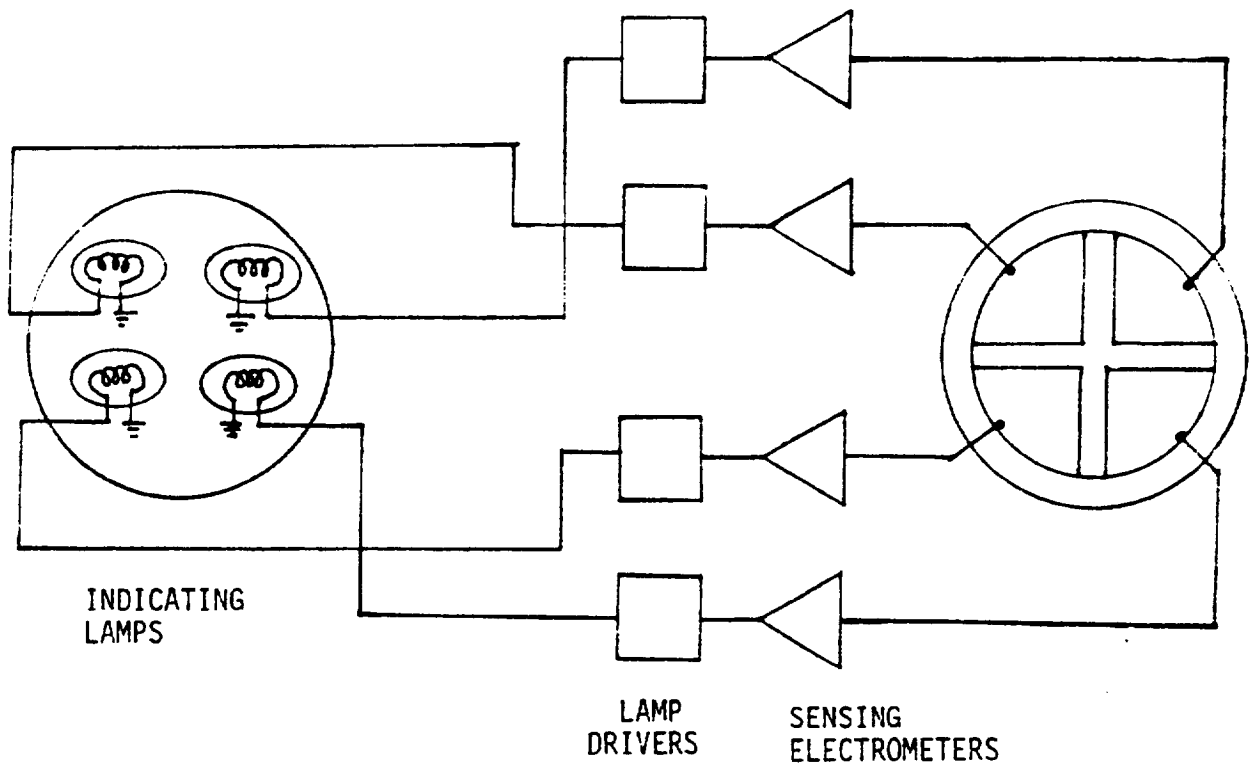


Figure 3.8. Block Diagram of Beam Locator

The sensing electrometers produce signals indicating which quadrant the beam is in and drive the lamps proportionately. Provision can easily be made for handling a large variation in beam current.

#### 3.5.4 Retarding Potential Analyzer (RPA)

Retarding potential analyzers have many uses in this program. A unit based upon development work done by MAYA personnel is shown in Figure 3.9. The RPA measures the flux of particles with energies  $E > V_R$  which enter the entrance aperture of the sensor. Used in conjunction with a diagnostic electron beam and beam locator, the RPA will provide detailed information on the particle trajectories and electrostatic fields.

An RPA must use a current sensor to detect the flux of charge particles. The MAYA RPA is based on a spiral electron multiplier which counts individual particles, and hence is capable of sensing very low fluxes of particles. An RPA can also be designed around an electrometer. (See Section 3.5.5.) The RPA based on the spiral electron multiplier will operate at approximately  $10^6$  times as low a current density as will an instrument based on a conventional electrometer.

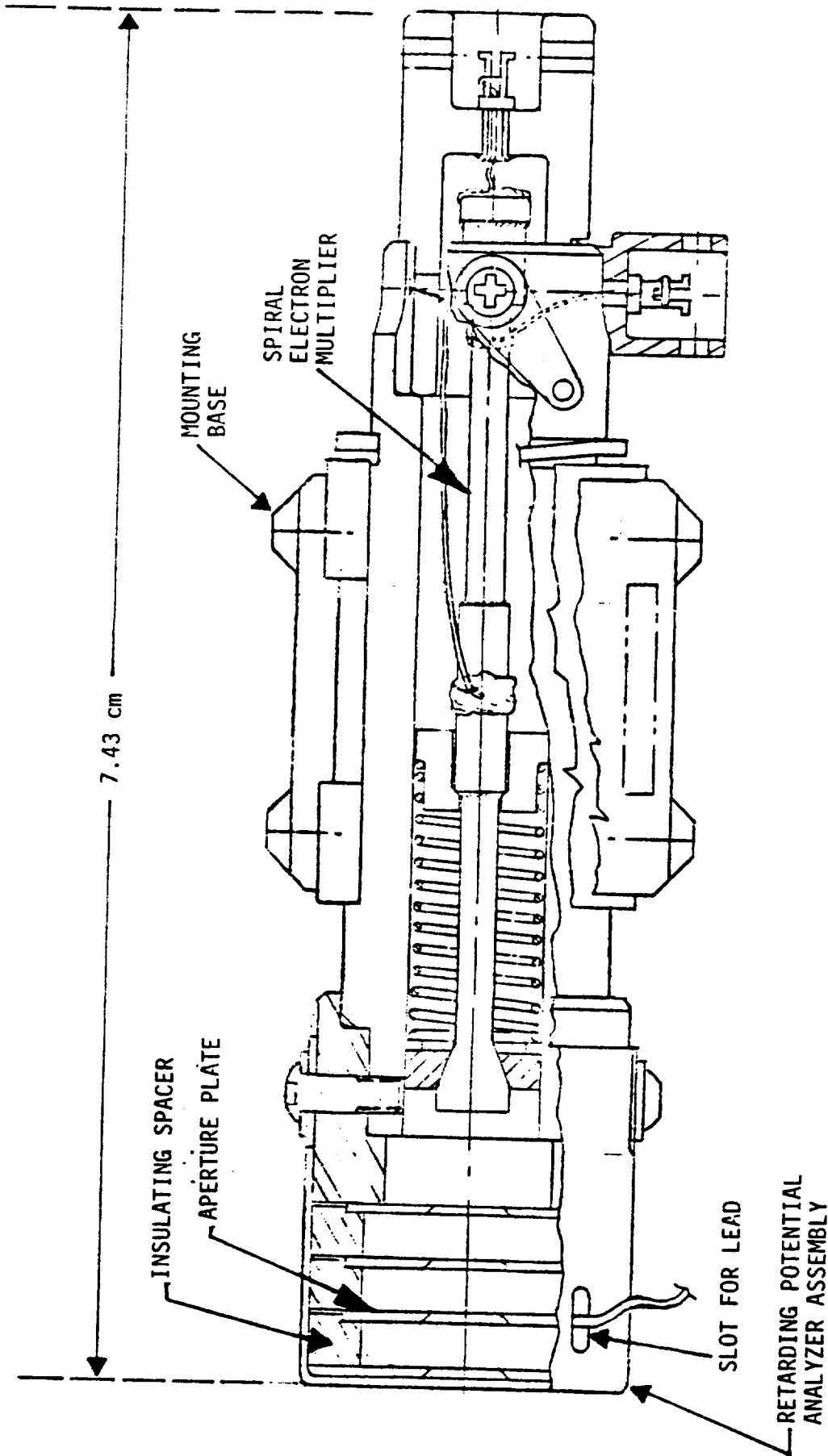


Figure 3.9 Retarding Potential Analyzer

A simple retarding potential assembly is fitted to the front of a spiral electron multiplier which senses electrons or protons that have energies greater than the retarding potential. MAYA is presently building most of the elements of such an analyzer under various contracts.

### 3.5.5 Electrometer (EM)

The direct measurement of current fluxes and of total leakage currents to surfaces on the test object is probably best accomplished with standard electrometers. An electrometer is simply a high input impedance amplifier which measures very low currents (less than  $10^{-9}$  amps) by the voltage which they produce in very large resistors (greater than  $10^9$  ohms). A number of electrometers suitable for specially designed electrometers, such as might be used in the test module, are also readily available.

### 3.5.6 Magnetometer (MM)

A survey of the magnetic field within the vacuum tank should be performed. An accuracy of 1% or 3 milligauss should be quite adequate. A number of commercially available magnetometers are capable of this accuracy.

### 3.6 Procedures

The diagnostic instrumentation outlined in Section 3.5 is used in standard procedures to make those measurements called for in Section 3.4. These procedures are outlined in this section.

#### Procedure 1 - Trajectory measurements

This procedure is used to investigate the charge distribution and to verify the predictions of subroutine PUSHER. This procedure makes use of the Diagnostic Electron Beam (DEB) and Beam Locator (BL). A Retarding Potential Analyzer (RPA) may also be used for detailed measurements of the electrostatic potential.

The procedure is:

- 1) Locate the DEB on an outer surface element. By an outer surface element we mean a place on the outer boundary of the region of interest, say at the faraday cage surrounding the test region. The nomenclature here is chosen to match that reported by S<sup>3</sup> in the interim tech report SSS-R-3124<sup>4</sup>.
- 2) Define the DEB energy and direction thus determining  $\tilde{v}(\theta, \phi, v_e)$ , the velocity vector characterizing the electrons from the DEB.
- 3) Place BL directly in front of DEB.
- 4) Trace trajectory outward from DEB with the BL.

The last two steps are conceptually straight forward, but may in practice, prove to be quite difficult. The Beam Locator must move along the three dimensional locus of a particle trajectory if the particle trajectory is to be traced. The mechanism required to make this movement within a vacuum system does not appear to be simple. What is required here is remote manipulator technology. Solution of this problem will require further developmental work.

To determine potentials using the RPA:

- 1) Perform the previous procedure.
- 2) Replace the BL with the RPA.
- 3) Perform energy analysis on DEB with RPA.
- 4) Process data to extract RPA charging effects. (This might be difficult and will require more study.)

Again the mechanical movement may well be a major problem, otherwise the approach is conceptually simple.

## Procedure 2. Electric Field Measurements

This procedure is used to investigate the electric field distribution and hence to determine the charge and potential distributions.

2.1 Surface Fields. The field mill discussed in Section 3.5.1. can be used to measure surface electric fields and hence to infer the surface charge. The procedure consists simply of placing the field sensor near the surface and making the measurement. To avoid shadowing of the bombarding particle beams it will be necessary to move the field sensor across the surface more rapidly than the charging time.

2.2 Electric Field Distribution. The direct measurement of the electric field distribution at points well away from surfaces requires an extension of the field mill techniques to make them applicable to free space. The rotating capacitive sensor described in Section 3.5.1 and illustrated in Figure 3.6 measures local electric fields. The rotating sensor probe would move on an extensible shaft through the measurement region of interest. This motion is essentially one-dimensional and thus should be far less difficult to implement than the troublesome three-dimensional movement required for the Beam Locator. The procedure would consist of simply extending the sensor to the appropriate point and reading its output.

### Procedure 3. Direct Measurement of Potential

This procedure systematizes the use of electrometer probes to measure the electrostatic potential.

3.1 Surface Potential Measurement. The procedure is essentially the same as for the measurement of surface electric fields, except the feedback amplifier system described in Section 3.5.2 is employed with the sensing element. Again care must be taken to avoid shadowing effects. Here the small probe provided by the Trek, Inc., Model 340, electrostatic voltmeter will help.

#### Procedure 4. Measurement of Total Current

The measurement of total current to the test body is accomplished by an electrometer which is connected to the test body through a variable resistor R. The procedure is analogous to that which would be applied to measure the characteristics of a vacuum diode with the particle source playing the role of the cathode and the test object that of the anode. (See Figure 3.10.)

The procedures described below will not work if the test object is a perfect insulator. If however the test object is a conductor or if leakage currents ( $10^{-10}$  amps) are present then the instrumentation should be relatively easy to implement. The resistor R should be attached to a conducting part of the test object. Insulators and other parts of the test object will each charge to equilibrium potentials which may be different from the potential at the point where the resistor R is attached, but which should be predicted by the S<sup>3</sup> computer codes. Similarly the total current collected through the resistor R should be predicted by the computer code. Care should be exercised in the choice of test objects so as to avoid absurd demands on the instrumentation. For instance, a conducting sphere completely coated with a very good insulator would yield too low a leakage current for useful measurements to be performed. Nonetheless the computer codes

should be able to predict, and the experimentalist reasonably measure the resulting leakage current through R for simple test objects consisting of mixtures of conductors and insulators. We note in passing that this technique is the generalization of existing work at Lewis as described in Berkopec, et. al.<sup>2</sup> and in Purvis, et. al.<sup>3</sup>

The procedures are:

A) Equilibrium I-V curve.

- 1) Define energy  $V_0$  of particle source(s).
- 2) Vary R from  $R_{min}$  to  $R_{max}$  and measure total current with an electrometer.
- 3) Plot I-V curve. V here is the voltage between the point of attachment of the resistor R to the test object and the outer faraday cage.
- 4) Repeat for new  $V_0$ .

B) Dynamic Response for small signals.

Several approaches are possible.

- 1) Define energy by  $V_0 = \hat{V}_0 + V_1 \sin \omega t$
- 2) Measure oscillatory component of current as function of  $\omega$ .
- 3) Plot normalized frequency response vs.  $\omega$  in order to estimate lumped parameter values.

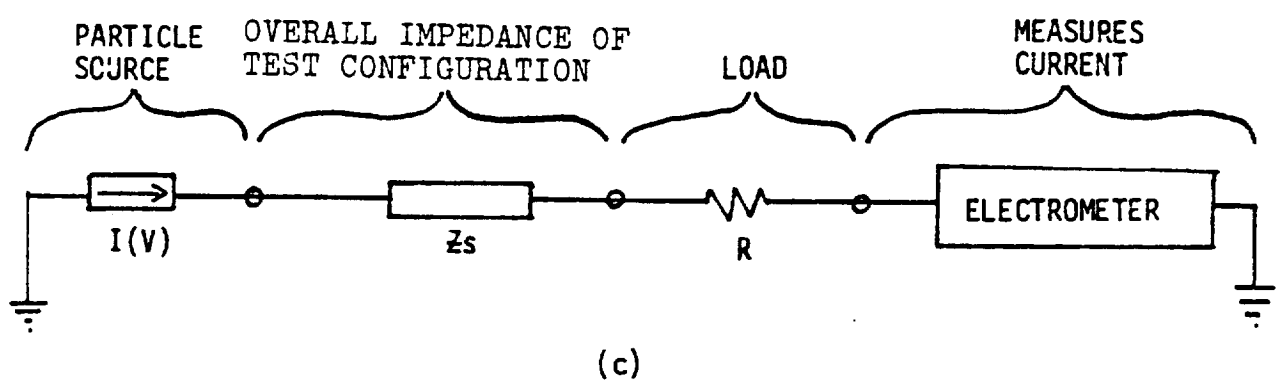
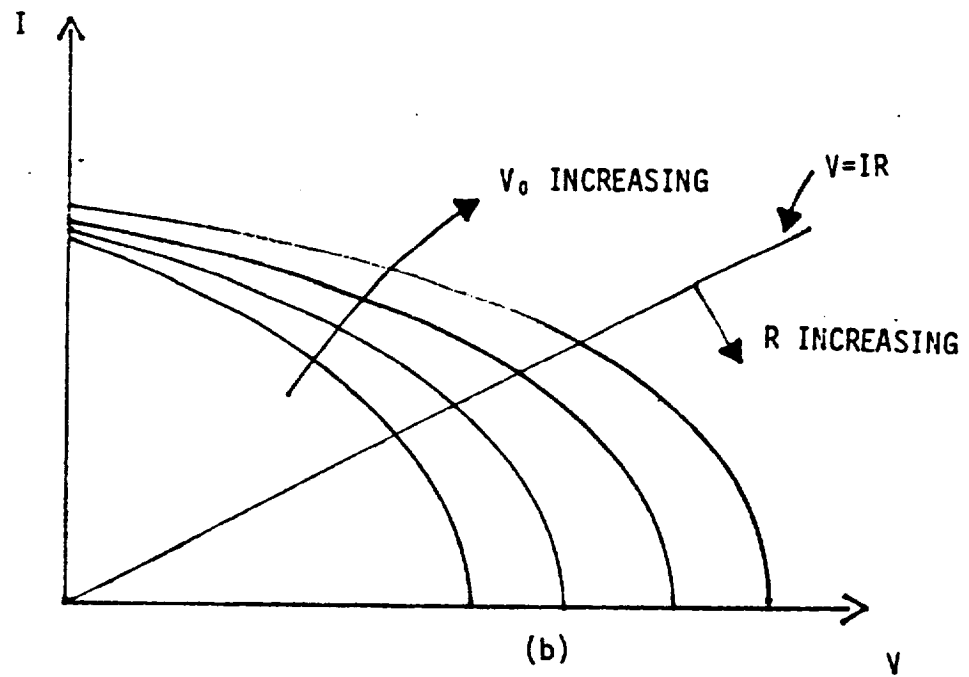
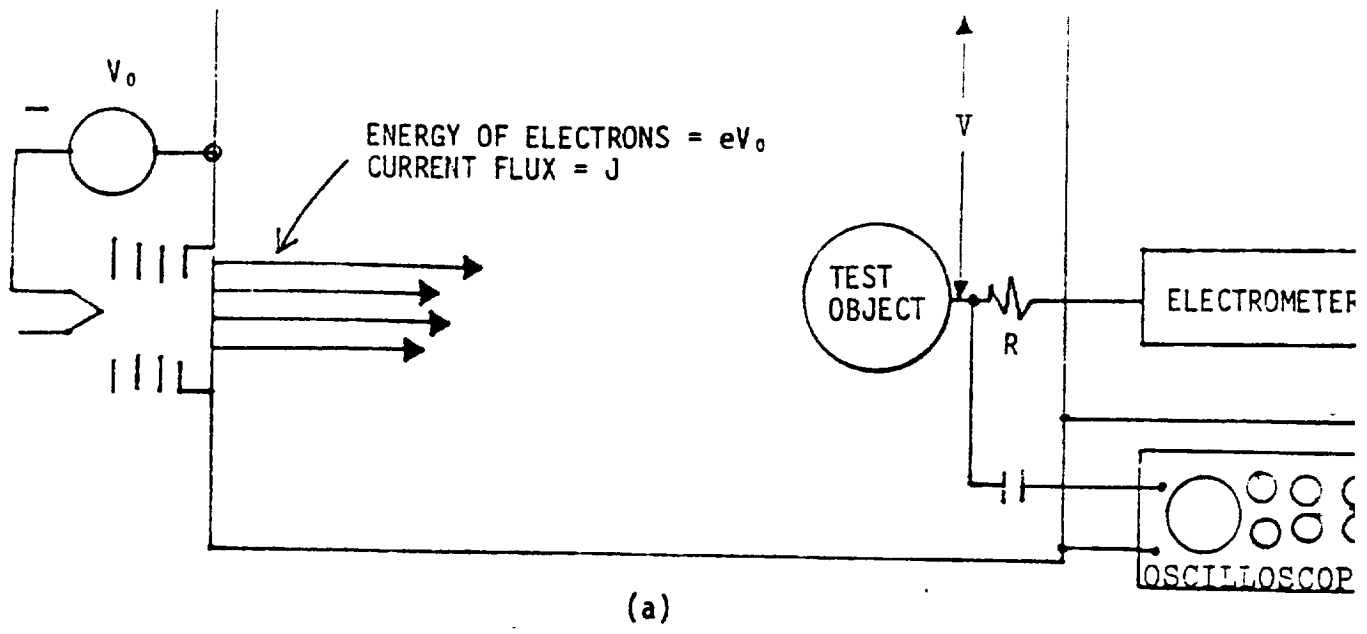


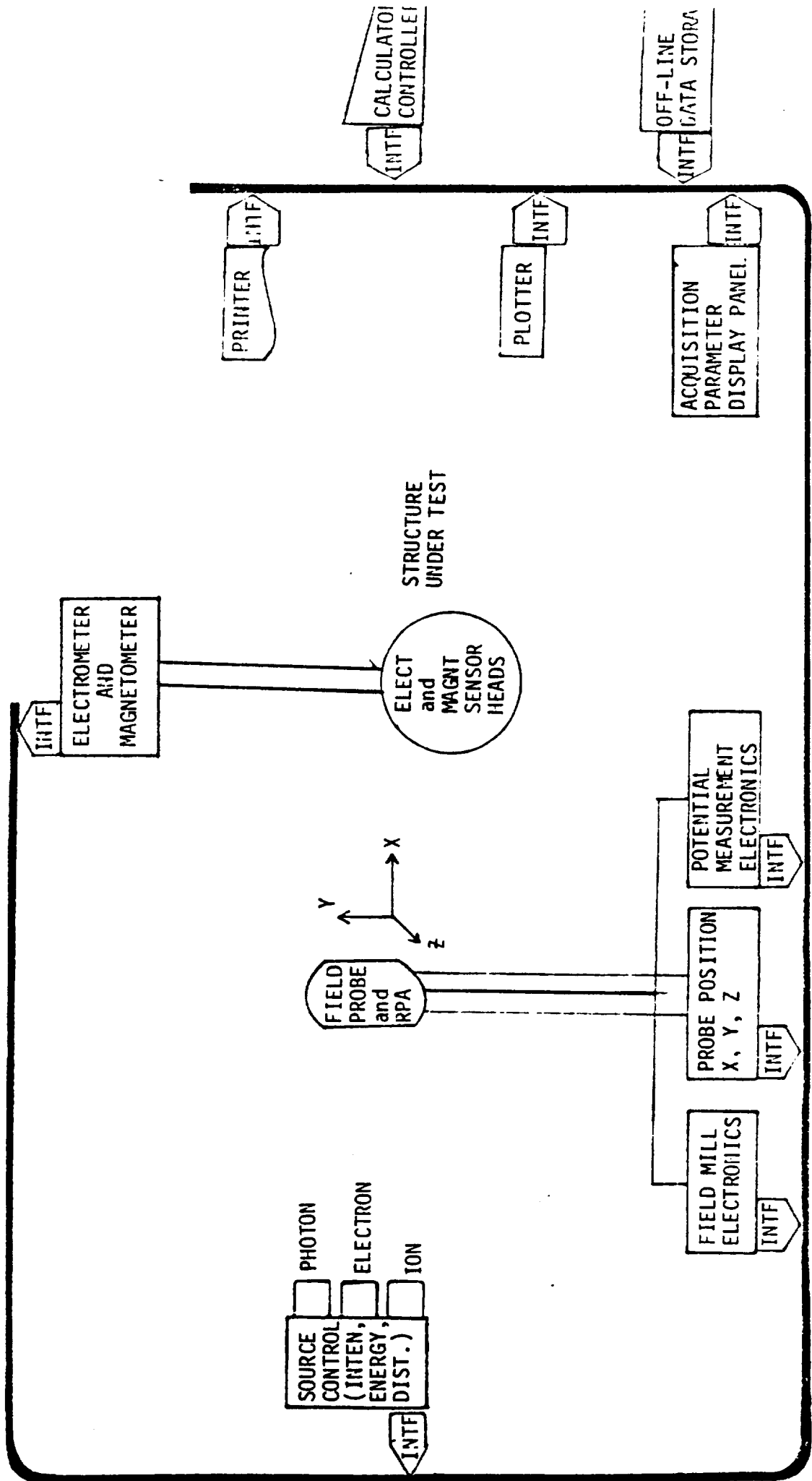
Figure 3.10 Test set-up for measuring and analyzing total currents a) A flux of charged particles is incident upon the test object b) I-V curve for test object in beam is analogous to that of a vacuum diode c) Equivalent circuit based upon either lumped parameter model (Inouye) or three dimensional computer code ( $S^3$ ).

Alternatively J or R may be varied in an oscillatory fashion to obtain frequency responses. From these responses one can determine the magnitude of the various circuit elements in a lumped parameter model of the system. Note also that the small signal dynamic response techniques can be extended to the study of small variations in parameters defining trajectories by employing the diagnostic electron beam and the retarding potential analyzer. For example, consider an instance where the test object is a metallic sphere charged by an electron beam to a negative 10 Kilovolts. Electrons from a diagnostic beam with energies greater than 10 Kev would penetrate to the test object. The electrons with energies less than 10 Kev would be reflected before reaching the test object. Detailed trajectories would be predicted by the S<sup>3</sup> computer code. If the Diagnostic Electron Beam current were modulated at frequency  $\omega$  and then the DEB energy was slowly swept through 10 Kev a signal at frequency  $\omega$  would suddenly appear on the oscilloscope when the electron energy was sufficient to enable them to reach the test object. An RPA could be positioned to detect the reflected DEB and thus provide another independent measurement of the test object potential and of the electron trajectories. Variations on these themes are endless and only the experimenters ingenuity need limit the possibilities. The equilibrium and dynamic I-V curves should be a sensitive test of the capabilities of the computer codes.

### 3.7 Data Processing and Display System

These experiments generate large volumes of data. If the data are to be interpreted meaningfully then the data must be processed intelligently and displayed in an easily interpretable form. The raw data from instruments should also be preserved for the purposes of checking any sophisticated analysis routines which might be built into the Data Processing and Display System (DPDS). Where possible the DPDS should present data from the experiments in a form which is directly comparable with the data from the computer codes. For example, a goal of the DPDS design would be to present trajectory plots derived from the experimental data in a format similar or identical to that of the spacecraft charging computer models.

The instruments should also have the ability to stand alone and be used meaningfully without the DPDS. A system which fulfills all of these requirements and which would be cost effective could be based upon the recently established general purpose instrumentation bus standardized by the IEEE. This standard IEEE-488<sup>7</sup> has been adopted by a number of the major U.S.A. instrument manufacturers, who are beginning to provide a wide variety of instruments and controllers compatible with IEEE-488. A block diagram of a DPDS based on the IEEE-488 standard is indicated in Figure 3.11.



IEEE 488  
INTERFACE BUSS

Figure 3.11 Data Processing and Display System

Should more versatility and higher data acquisition rates be desired for other experimental purposes then a DPDS system based upon the Computer Automated Measurement and Control or CAMAC standard (IEEE-583)<sup>8-10</sup>. As described in the CAMAC Tutorial Issue of the IEEE Transactions on Nuclear Science:<sup>10</sup> "The CAMAC system is a standardized assemblage of modular units and the dataway which interconnects them. Dimensions are specified for the "crates" (the containers for the modules) and the plug-in modules which supply the various logic functions contained within the system. Also detailed are the interconnection arrangement, including the sockets and the interconnecting "highway". These standards thus permit mechanical and electrical compatibility between equipments supplied by different sources." CAMAC has continued to grow in popularity and has gained wide international acceptance as a modular instrumentation system for the transmission of digital data between instruments and between instruments and computers, and computer peripherals.

The CAMAC system has much to recommend it. CAMAC has been used by all of the ERDA national laboratories for almost a decade. As a result of this use instrumentation for CAMAC is well developed and widely available. Another point of major importance for LeRC applications is the increasing interest

in CAMAC as a standard data system for use with Space Shuttle payloads. Trainer, et al.<sup>11</sup> discusses the use of CAMAC and NIM (Nuclear Instrumentation Modules which are CAMAC compatible systems developed under ERDA auspices) in the space program. Standardized equipment for space shuttle experiment payloads based upon CAMAC are discussed by More and Ebert<sup>22</sup>. NASA has let contracts to develop CAMAC hardware suitable for space flight thus there is reason to believe that the future will see the use of CAMAC in space. An environmental test facility which was compatible with the CAMAC standard would interface easily with experiments from any other group using the standard. All of these advantages suggest that CAMAC must be seriously considered for while initial costs might be higher than with IEEE-488 the operational costs could be substantially lower.

Whichever choice is made MAYA does most strongly recommend that either IEEE-488 or CAMAC be used. Developing a special purpose interface will almost certainly drive up costs, increase system design and fabrication efforts, result in reduced capability, and be incompatible with most other systems.

## APPENDIX 1 - STRUT DESIGN

The strut which supports the satellite model or other test object in the ground test environmental chamber should be designed to minimize electrostatic perturbations. An insulating rod would be a good choice were it not for the beams or charged particles which are present. These charged particle fluxes would charge up the insulator and thus create potential distortions which would be difficult to predict. So an insulating strut is ruled out.

A conducting strut is called for. If the strut were a single conducting rod, then it would create a potential surface which would not match closely to either the inner or the outer potential surface. We overcome this problem by making a strut of a series of conducting sleeves, each of which is run at a different potential. While this technique is somewhat more trouble, it will reduce substantially the inevitable perturbations of the electric potential by the strut.

As an example, and as a probable good approximation for use in more complex geometries, consider a strut with N segments which is designed for use in a cylindrical test system. The potential is held at ground on the inner cylinder and at  $\phi = V$  on the outer cylinder. The resulting potential is:

$$\phi(r) = V \left[ \frac{\ln\left(\frac{r}{a}\right)}{\ln\left(\frac{b}{a}\right)} \right]$$

The radius at which the potential is equal to  $\phi_\ell$  is

$$r_\ell = a^{-\alpha+1} b^\alpha$$

$$\text{where } \alpha = \frac{\phi_\ell}{V}$$

say  $\phi_\ell = \frac{\ell}{N} V$  where  $0 \leq \ell \leq N$ , both integers

$$\text{then } r_\ell = a^{-\left(\frac{\ell}{N} - 1\right)} b^{\left(\frac{\ell}{N}\right)}$$

The segments are chosen to extend between  $r_\ell$  and  $r_{\ell+1}$ , with the potential chosen as an average of  $\phi_\ell$  and  $\phi_{\ell+1}$ . An example with 10 segments is shown in the accompanying figure.

More generally when the general shape of the potential is known beforehand one chooses the strut segments to match the equipotential contours. In practice, for most purposes, the logarithmic strut indicated above should be quite adequate.

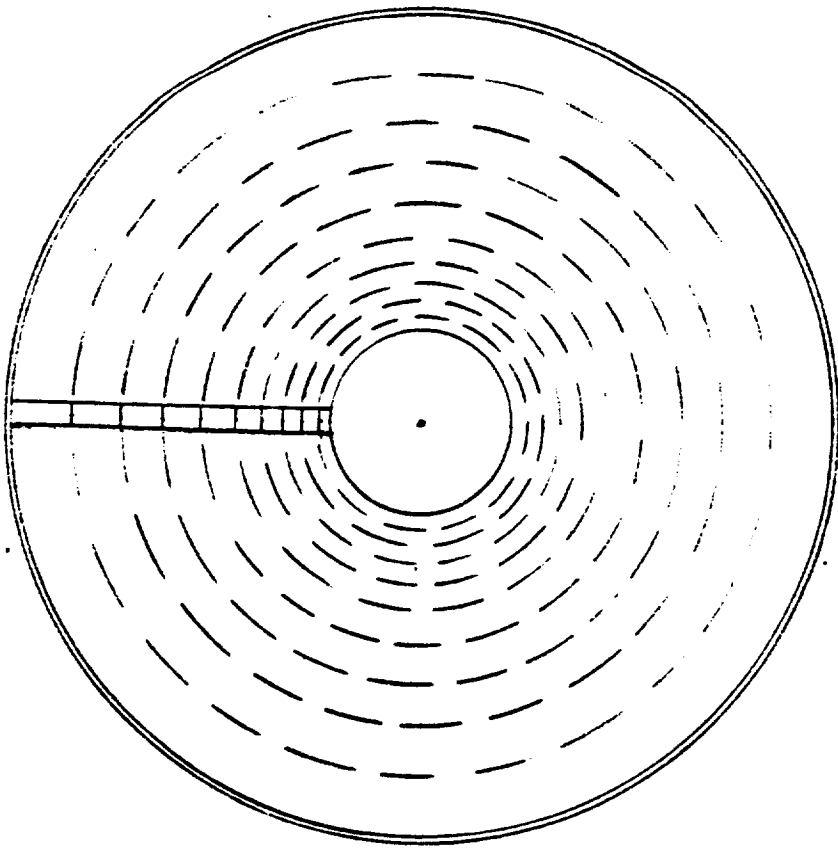


Figure A-1 Supporting Strut Design for Cylinders

## APPENDIX 2 - DISTRIBUTED SOURCE ION ACCELERATOR

An ion accelerator which produced a beam of particles with a finite and variable spread in energy would simulate the magnetospheric particle flux much more accurately than does a monoenergetic beam. In this appendix we outline a possible approach to the problem of designing such an accelerator.

The accompanying figure shows the approach. Ions are produced by electron impact on a crossed neutral beam. The ions are then accelerated (at right angles to the crossed electron and neutral beams) down a drift tube. Each modular stage in such an accelerator produces ions and accelerates ions from all of the preceding stages. The final output of the device would be a beam made up of a number of ion beams of differing energy. It should be possible by varying the electron and neutral beam currents to vary the number of particles at each energy. A final stage would post accelerate and diverge the entire beam.

Now let us analyze a single stage of the module. First consider the ionization process:

$$\frac{\partial n_i}{\partial t} = r_e Q n_n$$

where  $n_i$  = number density of ions  
 $r_e$  = number flux of electrons  
 $Q$  = ionization cross-section  
 $n_n$  = neutral beam number density

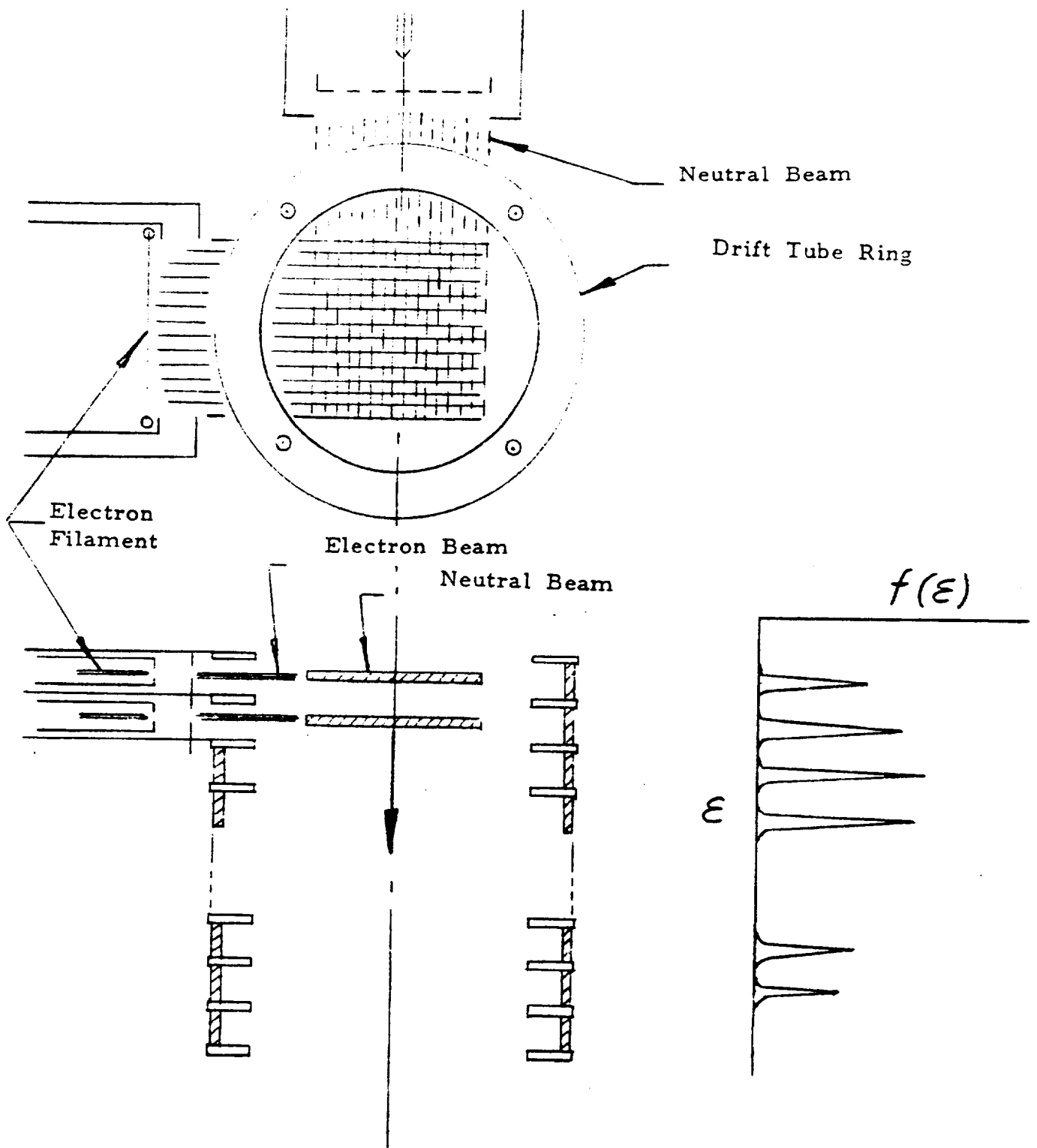


Figure A-2 Distributed Source Ion Accelerator

The ionization region, within which the crossed beams collide, is  $l_b$  wide on the electron side,  $l_n$  wide on the neutral side and  $d$  thick. So the volume is  $V = l_b l_n d$  and the rate of production of ions within the stage is

$$\frac{\partial N_i}{\partial t} = \frac{\partial n_i}{\partial t} V = l_b l_n d r e Q n_n$$

We consider the emission limited current from the ionization region for which:

$$I_i = q_i \frac{\partial N_i}{\partial t}$$

where  $I_i$  is the ion current

$q_i$  is the ion charge

and hence the ion current density is:

$$\begin{aligned} J_i &= \frac{I_i}{A} \quad , \quad A = l_b l_n \\ &= \frac{q_i}{e} (Qnd) J_e \end{aligned}$$

where  $J_e = e \Gamma_e$  is the electron current density.

A free jet can produce beams of neutrals with pressures  $p \sim 10^{-4}$  torr corresponding to number densities  $n \sim 10^{12}/\text{cm}^3$  (Anderson, 1974<sup>13</sup>).

From McDaniel<sup>14</sup>, we note that  $Q \sim 10^{-16} \text{cm}^2$  for 100eV electrons bombarding molecular hydrogen.

An electron number flux of  $10^{16}/\text{cm}^2\text{-sec}$  corresponding to a current density of 1.6 ma/cm<sup>2</sup> is easily obtained.<sup>15</sup>

Thus  $Qnd \sim 10^{-5}$  for  $d = .1\text{cm}$ , which should be easy to construct.

So that for singly ionized particles one has

$$J_i \approx 10^{-5} J_e$$

The desired ion current densities (See Table 3.1) should not be difficult to obtain.

Finally we note that the beam intensity might well be subject to drift induced by variations in the electron or neutral beam currents. An electrostatic retarding potential analyzer should be used as a sensor in a feedback control loop to stabilize the beam intensity at each energy. Such a stabilization loop should not be difficult to design and construct.

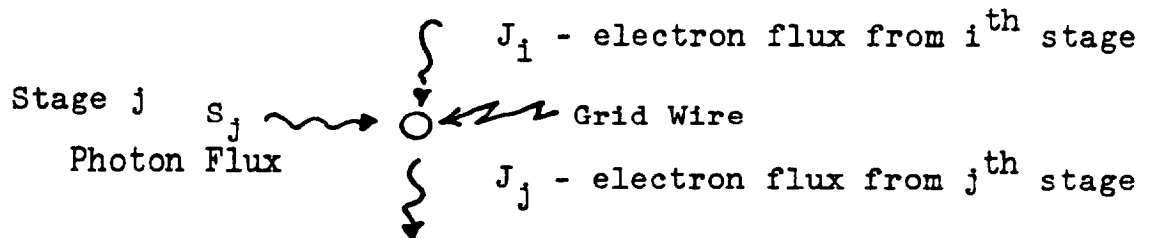
No Distributed Source Ion Accelerator of the type discussed in this appendix has ever been built. The physical principles are straightforward and well understood but the detailed engineering of such a device would be a substantial undertaking. At least two man years of scientific engineering effort would probably be required in order to build a working unit.

APPENDIX 3 - DISTRIBUTED SOURCE ELECTRON ACCELERATOR

An electron accelerator which produces a beam of particles with a distribution of energies is needed to simulate the magnetospheric electron flux. Such a gun could be constructed by reversing the extraction potential applied to the distributed source ion accelerator. We sketch here another alternative, based on the use of photoemission as a source of electrons.

U-V lamps are used to illuminate the back side of a wire grid. (See accompanying figure.) Photoelectrons produced in each stage are accelerated through each of the subsequent stages. A composite beam is thus made up of a number of beams of different energy. A final stage of post acceleration shifts the entire distribution to some mean energy.

Consider a single stage. The processes involved are:



One has:

$$J_j = \alpha_j S_j + \sum_{i < j} B_{ji} J_i$$

where

$\alpha_j$  is the effective photoyield of stage j

$B_{ji}$  is the effective secondary emission yield at the jth stage from electrons which are emitted at the ith stage

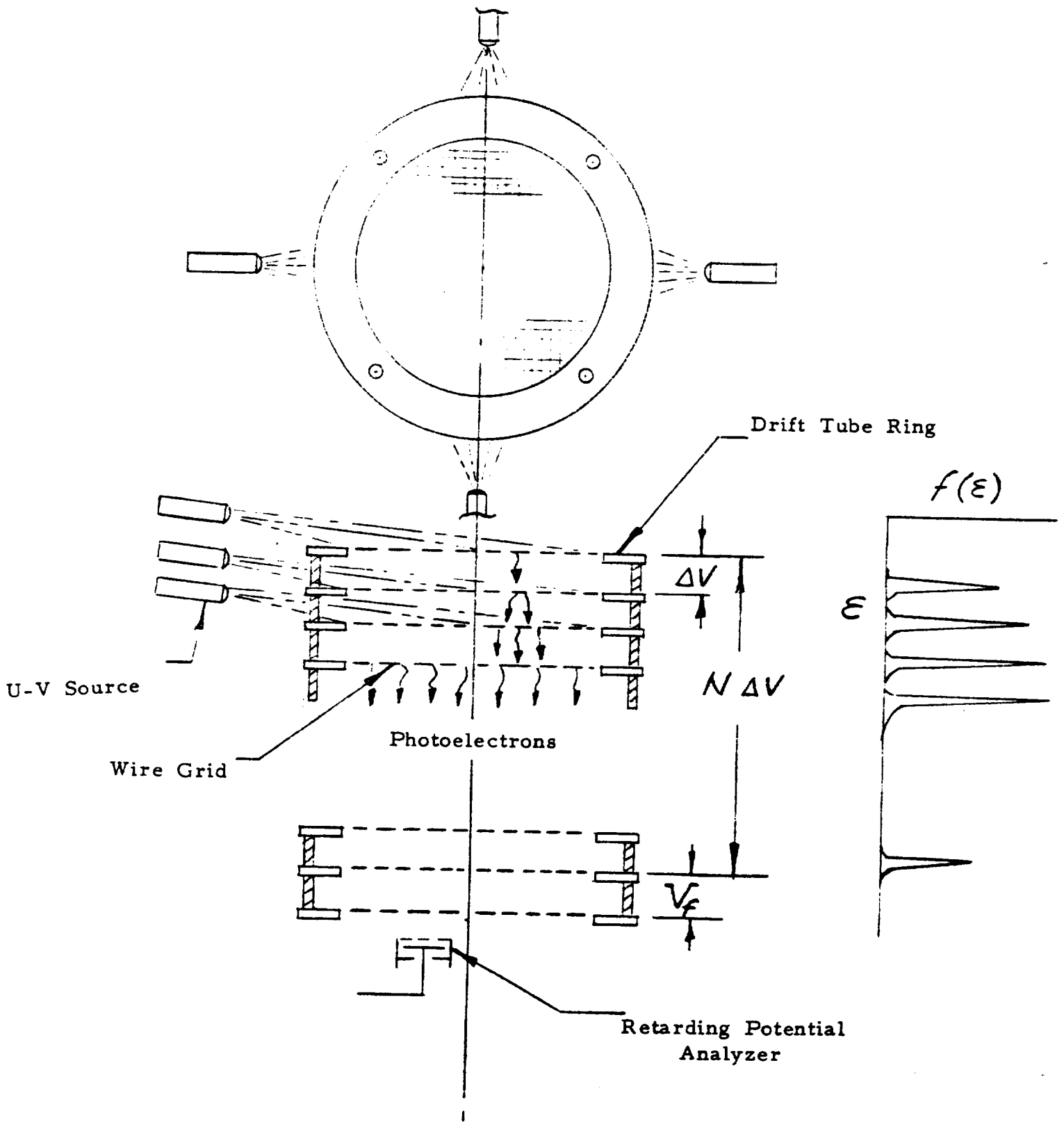


Figure A-3 Distributed Source Electron Accelerator

The second term in this expression represents the effects of electron multiplication. These effects should be kept small. The beam current will then be controlled primarily by the photon fluxes which are in turn easily controlled.

Now let us analyze the effect of electron multiplication. The worst case results from the final stage, N. The electron multiplication current is

$$J_n^* = \sum_{j < n} \beta^j J_j$$

$$= \beta^{(n-1)} J_1$$

Require that  $J_n^* \ll J_n \Rightarrow \left(\frac{J_n}{J_1}\right) \gg \beta^{(n-1)}$

Note that

$$\beta = \left(\frac{\Delta A}{A}\right) \delta$$

where  $\frac{\Delta A}{A}$  is the ratio of the grid area to the total area

$\delta$  is the secondary emission yield

thus

$$\frac{J_n^*}{J_1} = \left[ \left(\frac{\Delta A}{A}\right) \delta \right]^{(n-1)}$$

for gold  $\delta < \delta_{\max} = 1.45$  and  $\frac{\Delta A}{A} \sim 0.1$  should be easily realizable so that

$$\frac{J_n}{J_1} = (0.145)^{n-1} = 2.8 \times 10^{-8} \text{ for a system with } 10 \text{ stages}$$

∴ Electron multiplication is not a serious problem

We note that the Distributed Source Electron Accelerator discussed here has never been built. MAYA personnel have built mono-energetic electron sources using photoemission. These sources were used for calibration of the auroral particles experiments on the Advanced Technology Satellites 5 and 6. The photoemissive sources were easy to use and worked well. Should this concept be extended to build the Distributed Source Electron Accelerator discussed in this Appendix then approximately one man year of engineering science effort should be allocated to design, construct and test a prototype unit.

APPENDIX 4 - COMPARISON BETWEEN THE GROUND TEST AND THE MAGNETOSPHERIC ENVIRONMENT

The ground test environment is designed to simulate the magnetospheric environment and to test the predictive abilities of the computer codes which describe spacecraft charging. The first task, simulation of the magnetospheric environment, is a formidable problem, and admits to only a partial solution. The testing of the computer codes is a substantially more tractable problem.

The difficulty with simulation of the magnetospheric environment is one of scaling. The plasma surrounding a satellite at geosynchronous orbit has four important components: the background magnetospheric electrons (me), background magnetospheric ions (mi), electrons produced by secondary emission from the satellite surface (se), and the photoelectrons (pe) which result from solar illumination of the satellite surface. The Debye lengths associated with each of these components typically stand in the ratio

$$L_d(mi) : L_d(me) : L_d(se) : L_d(pe) = 1000:400:2:1$$

where typical values are as indicated in Table 1. Note that the photoelectric Debye length is by far the shortest ( $L_d(pe) \sim 2$  meters) and is the only one which is comparable to the dimensions of most present satellites. Thus for most purposes one can assume that except for the photoelectrons

the Debye length is much larger than the typical dimensions of the satellite. Thus it is not practical to attempt to simulate the Debye shielding of any of the particles except for the photoelectrons. Nor fortunately is it particularly important to do so.

	Lab ( $B \sim 3$ gauss)	Magnetosphere ( $B \sim 10^{-7}$ gauss)
1) Background Electrons		
$n \sim 6/\text{cm}^3$	$L_d(\text{me}) \sim 1 \times 10^4 \text{ cm}$	$L_d(\text{me}) \sim 1 \times 10^4 \text{ cm}$
$T \sim 5 \text{ Kev}$	$R(\text{me}) \sim 560 \text{ cm}$	$R(\text{me}) \sim 1.7 \times 10^5 \text{ cm}$
$r \sim 1.8 \times 10^{10} / \text{cm}^2\text{-sec}$		
2) Background Ions		
$n \sim 6/\text{cm}^3$	$L_d(\text{mi}) \sim 5.3 \times 10^4 \text{ cm}$	$L_d(\text{mi}) \sim 5.3 \times 10^4 \text{ cm}$
$T \sim 30 \text{ Kev}$	$R(\text{mi}) \sim 5.8 \times 10^4 \text{ cm}$	$R(\text{mi}) \sim 1.7 \times 10^7 \text{ cm}$
$r \sim 1 \times 10^2 / \text{cm}^2\text{-sec}$		
3) Secondary Emission Electrons		
$n \sim 125/\text{cm}^3$	$L_d(\text{se}) \sim 115 \text{ cm}$	$L_d(\text{se}) \sim 115 \text{ cm}$
$T \sim 3 \text{ ev}$	$R(\text{se}) \sim 14 \text{ cm}$	$R(\text{se}) \sim 4.1 \times 10^3 \text{ cm}$
$r \sim 0.9 \times 10^{10} / \text{cm}^2\text{-sec}$		
4) Photoelectrons		
$n \sim 450/\text{cm}^3$	$L_d(\text{pe}) \sim 50 \text{ cm}$	$L_d(\text{pe}) \sim 50 \text{ cm}$
$T \sim 2 \text{ ev}$	$R(\text{pe}) \sim 11 \text{ cm}$	$R(\text{pe}) \sim 3.4 \times 10^3 \text{ cm}$
$r \sim 2.6 \times 10^{10} / \text{cm}^2\text{-sec}$		

Table A-1 Characteristic Plasma Parameters and Scale Lengths

More severe problems arise when one considers the scaling with cyclotron radius,  $R$ . For the magnetospheric plasma one has  $L_D \ll R$  thus for all practical purposes the sheath may be considered unmagnetized. In the lab, if no provision is made for bucking out magnetic field of the earth, then one has  $L_D \gg R$ . Indeed for the photoelectrons, the cyclotron radius will be comparable to the size of the test object. This condition only occurs in the magnetosphere when the satellite becomes as large as one hundred meters, and even then, the Debye sheath should dominate. Thus if the background magnetic field of the earth is not reduced within the test chamber, simulation of the magnetospheric environment will be problematic.

We note though that the computer codes are being developed to include a magnetic field. Tests of the predictive ability of the codes do not require bucking out the magnetic field. The codes should be capable of computing the magnetized sheath structure.

## REFERENCES

- 1) Finke, Robert C., Arthur D. Holmes and Thomas A. Keller, "Space Environment Facility for Electric Propulsion Systems Research" NASA Technical Note TN-D-2774.
- 2) Berkopec, Frank D., N. John Stevens and John C. Sturman, "The Lewis Research Center Geomagnetic Substorm Simulation Facility" NASA Technical Memorandum TM-X73602.
- 3) Purvis, Carolyn K., N. John Stevens, Jon C. Oglebay, "Comparison of Experimental Results with Simple Analytical Models" NASA Technical Memorandum, TM-X-73606.
- 4) Katz, Ira and Donald E. Parks, Donald Brownell, Rozanne Bryson, James Harvey, Myron Mandell, Sang Wang, Andrew Wilson, "3-Dimensional Dynamic Study of Electrostatic Charging in Materials", SSS-R-77-3124.
- 5) Parks, Donald E. and Sang Wang "Preliminary Space Model for Spacecraft Charging Study." SSS-R-76-2996, See MAYA Development Corporation report contained within.
- 6) Secker, P.E. "The Design of Simple Instruments for Measurement of Charge on Insulating Surfaces." Journal of Electrostatics, 1 (1975), 27-36, Elsevier Scientific Publishing Co., Amsterdam
- 7) IEEE Std. 583-1975 "IEEE Standard Modular Instrumentation and Digital Interface System."  
  
References 7 and 8 are available from The Institute of Electrical and Electronics Engineers, Inc., 345 East 47 Street, New York, N.Y.
- 8) IEEE Std. 488-1975 also known as ANSI MC1.1-1975. "IEEE Standard Digital Interface for Programmable Instrumentation."
- 9) CAMAC. "A Modular Instrumentation System for Data Handling. AEC Committee on Nuclear Instrument Modules." July 1972. TID-25875.
- 10) CAMAC TUTORIAL - IEEE Nuclear Science. April 1973 Vol. NS-20 #2.

REFERENCES (Cont.)

- 11) J. H. Trainor, C. H. Ehrmann, and T. J. Kaminski,  
"CAMAC and NIM Systems in the Space Program,"  
IEEE Trans. NS-22, pp. 521-525.
- 12) K. A. More and D. Ebert, "Standardized Equipment for  
Space Shuttle Experiment Payloads," IEEE Trans.  
NS-22, pp. 582-586.
- 13) Anderson, J. B. Journal of Chemical Physics, V61, (1974)
- 14) McDaniel, Earl W., Collision Phenomena in Ionized  
Gases, p 185, John Wiley and Sons, New York, N.Y. (1964)
- 15) Reference Data For Radio Engineers, Chapter 17, Figure 1,  
Howard K. Sams and Co., Inc. New York, N.Y. (1975)



## APPENDIX C

### A VARIATIONAL/FINITE ELEMENT APPROACH FOR SATELLITE PROBLEMS OF ARBITRARY GEOMETRY

The following will describe a variational formulation for a certain class of charged satellite problems. Using a finite element approach to the solution of the variational problem, a symmetric system of linear equations results.

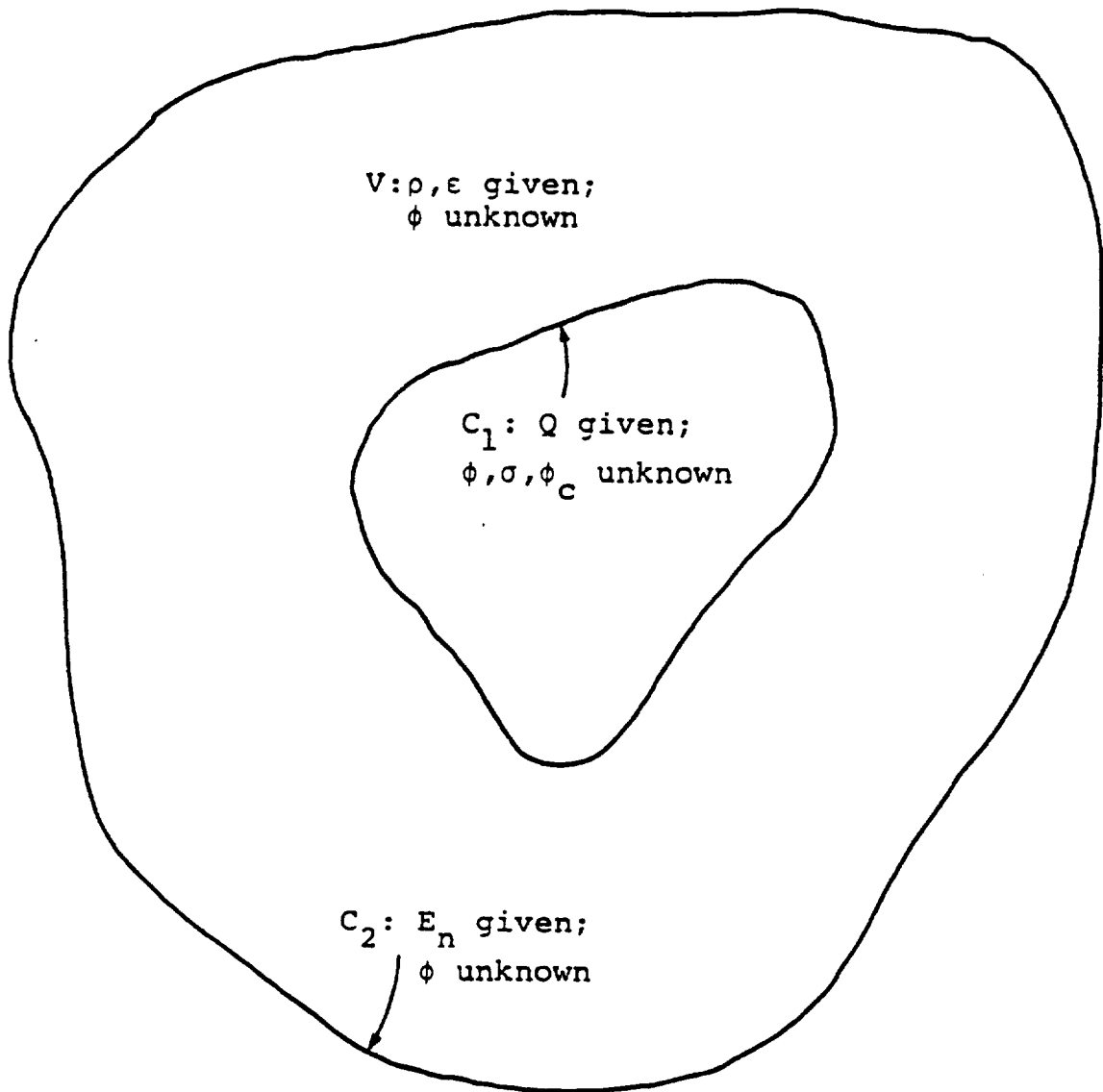
Consider a conductor with total surface charge  $Q$  and local surface charge density  $\sigma$  and at constant potential  $\phi_C$ , comprising surface  $C_1$ , surrounded by volume  $V$  with fixed charge density  $\rho$  and dielectric constant  $\epsilon$ , which is in turn bounded by surface  $C_2$  on which the outward normal component  $E_n$  of the electric field is specified (see figure). The only requirement on  $\rho$ ,  $\epsilon$  and  $E_n$  is that they be integrable; thus,  $\rho$  may have an (integrable) singularity representing a fixed surface charged distribution. After the equations are formulated, "geometric" boundary conditions - i.e., fixed potentials - may be applied on surface  $C_2$  by a simple modification of the equations.

Note that a dielectric layer on the conductor is considered here as part of volume  $V$  in which the potential  $\phi$  is unknown and to be solved for. Obviously, the volume integrals which must be evaluated in any finite element scheme will reduce to surface integrals in the elements comprising dielectric layer.

If one assumes a variational principle for the system, of the form

$$\delta \mathcal{L} = 0 \quad (C.1)$$

Preceding page blank



where

$$\begin{aligned}
 \mathcal{L} = & \int_V f(\underline{x}, \phi, \nabla\phi) \, dV \\
 & + \int_{C_1} g(\underline{x}, \phi, \sigma, \phi_c) \, dS \\
 & + \int_{C_2} h(\underline{x}, \phi) \, dS
 \end{aligned} \tag{C.2}$$

then one obtains

$$\begin{aligned}
 \delta\mathcal{L} = & \int_V \delta\phi \left\{ \frac{\partial f}{\partial \phi} - \frac{\partial}{\partial x_i} \frac{\partial f}{\partial \phi_{,i}} \right\} dV \\
 & + \int_{C_1} \left\{ \delta\phi \left[ \frac{\partial g}{\partial \phi} + \hat{n}_i \frac{\partial f}{\partial \phi_{,i}} \right] + \delta\sigma \frac{\partial g}{\partial \sigma} + \delta\phi_c \frac{\partial g}{\partial \phi_c} \right\} dS \\
 & + \int_{C_2} \delta\phi \left\{ \frac{\partial h}{\partial \phi} + \hat{n}_i \frac{\partial f}{\partial \phi_{,i}} \right\} dS = 0
 \end{aligned} \tag{C.3}$$

where  $\hat{n}$  is the unit normal vector (directed out of  $V$ ) and

$$\phi_{,i} \equiv \frac{\partial \phi}{\partial x_i} \tag{C.4}$$

Now  $\phi$  and  $\sigma$  may be varied independently in their respective domains; however, since  $\phi_c$  is constant, the variation  $\delta\phi_c$  is constant over  $C_1$ . Thus, the variational equations are

$$\frac{\partial f}{\partial \phi} - \frac{\partial}{\partial x_i} \frac{\partial f}{\partial \phi_{,i}} = 0 \quad \text{in } V \quad (\text{C.5a})$$

$$\frac{\partial g}{\partial \phi} + \hat{n}_i \frac{\partial f}{\partial \phi_{,i}} = 0 \quad \text{on } C_1 \quad (\text{C.5b})$$

$$\frac{\partial g}{\partial \sigma} = 0 \quad \text{on } C_1 \quad (\text{C.5c})$$

$$\int_{C_1} \frac{\partial g}{\partial \phi_c} dS = 0 \quad (\text{C.5d})$$

$$\frac{\partial h}{\partial \phi} + \hat{n}_i \frac{\partial f}{\partial \phi_{,i}} = 0 \quad \text{on } C_2 \quad (\text{C.5e})$$

Choosing

$$f = \frac{\epsilon}{2} \nabla \phi \cdot \nabla \phi - \rho \phi \quad (\text{C.6a})$$

$$g = \left( \frac{Q}{A} - \sigma \right) (\phi - \phi_c) - \frac{Q}{A} \phi \quad (\text{C.6b})$$

$$h = E_n \phi \quad (\text{C.6c})$$

where  $A$  is the area of surface  $C_1$ , the variational equations (C.5a) - (C.5e) become

$$\nabla \cdot (-\epsilon \nabla \phi) = \rho \quad \text{in } V \quad (\text{C.7a})$$

$$-\hat{n} \cdot (-\epsilon \nabla \phi) = \sigma \quad \text{on } C_1 \quad (\text{C.7b})$$

$$\phi = \phi_c \quad \text{on } C_1 \quad (\text{C.7c})$$

$$\int_{C_1} \sigma dS = Q \quad (\text{C.7d})$$

$$\hat{n} \cdot (-\epsilon \nabla \phi) = E_n \quad \text{on } C_2 \quad (\text{C.7e})$$

which are the desired governing equations of the system  
(in rationalized MKS units).

Suppose the volume  $V$  is divided into elements with nodes  $i$  and interpolation functions  $N^i$  at each node. The "surface" elements on  $C_1$  and  $C_2$  will be faces of elements of  $V$ . Expanding  $\phi$  and  $\sigma$  in the  $N^i$ , i.e.,

$$\phi = \phi^i N^i \quad (C.8a)$$

$$\sigma = \sigma^i N^i \quad (C.8b)$$

there results

$$\begin{aligned} \mathcal{L} = & \int_V \left\{ \frac{\epsilon}{2} \phi^i \phi^j \nabla N^i \cdot \nabla N^j - \rho \phi^i N^i \right\} dV \\ & + \int_{C_1} \left\{ \phi_c \sigma^i N^i - \phi^i \sigma^j N^i N^j - \frac{Q}{A} \phi_c \right\} dS \\ & + \int_{C_2} E_n \phi^i N^i dS \end{aligned} \quad (C.9)$$

Defining

$$\epsilon_{ij} \equiv \int_V \epsilon \nabla N^i \cdot \nabla N^j dV \quad (C.10a)$$

$$\rho_i \equiv \int_V \rho N^i dV \quad (C.10b)$$

$$S_{ij} \equiv \int_{C_1} N^i N^j dS \quad (C.10c)$$

$$s_i \equiv \int_{C_1} N^i dS \quad (C.10d)$$

$$E_i \equiv \int_{C_2} E_n N^i dS \quad (C.10e)$$

one has

$$\begin{aligned} \mathcal{L} = \frac{1}{2} \epsilon_{ij} \phi^i \phi^j - \rho_i \phi^i + s_i \sigma^i \phi_c - S_{ij} \phi^i \sigma^j - Q \phi_c \\ + E_i \phi^i \end{aligned} \quad (C.11)$$

Extremizing  $\mathcal{L}$  with respect to  $\phi^i$ ,  $\sigma^i$  and  $\phi_c$ , the resulting equations are

$$\epsilon_{ij} \phi^j - S_{ij} \sigma^j = \rho_i - E_i \quad (C.12a)$$

$$s_i \phi_c - S_{ij} \phi^j = 0 \quad (C.12b)$$

$$s_i \sigma^i = Q \quad (C.12c)$$

Of course, matrix elements  $S_{ij}$  can be nonzero only if nodes  $i$  and  $j$  are both on  $C_1$ ;  $s_i$  will be nonzero only if node  $i$  is on  $C_1$ ; and  $E_i$  can be nonzero only if node  $i$  is on  $C_2$ . Furthermore,  $\sigma$  is defined only on  $C_1$ , so the degrees of freedom  $\sigma^i$ , where node  $i$  is not on  $C_1$ , are to be removed from the system. Equation (C.12a) is the discretized analogue of the expression for the charge on  $C_1$ .

From the definitions of Equation (C.10a) and (C.10c), and the matrices  $\epsilon_{ij}$  and  $S_{ij}$  are symmetric.

The finite element equations (C.12a-c) can be reformulated in matrix-vector form; the writer begs the readers' indulgence with "civil engineering" notation.

The equations may be expressed as

$$[K] \{q\} = \{R\} \quad (C.13)$$

The matrix  $[K]$  is symmetric, but has some zero diagonal elements and, in general, is indefinite; the solution is not a minimum of  $\mathcal{L}$ , but a saddle point. However, this circumstance is easy to remedy, while at the same time reducing the number of degrees of freedom to be solved for.

Assume the interpolation functions obey the usual rule

$$\sum_i N^i = 1 \quad (C.14)$$

From Equations (C.10c-d)

$$\sum_j S_{ij} = s_i \quad (C.15)$$

Now the variational expression  $\mathcal{L}$  in Equation (C.11) may be written

$$\begin{aligned} \mathcal{L} = & \frac{1}{2} \{\phi\}^T [\epsilon] \{\phi\} - \{\rho\}^T \{\phi\} \\ & + \{s\}^T \{\sigma\} \phi_c - \{\phi\}^T [S] \{\sigma\} - Q \phi_c + \{E\}^T \{\phi\} \end{aligned} \quad (C.16)$$

where the dimensionality of vectors and matrices is  $N$  and  $N \times N$ , respectively, where  $N$  is the total number of nodes. From Equation (C.12b), assuming  $[S_{11}]$  is nonsingular,

$$\{\phi_1\} = [S_{11}]^{-1} \{s_1\} \phi_c \quad (C.17)$$

where the vector  $\{\phi\}$  has been decomposed as

$$\{\phi\} = \begin{Bmatrix} \{\phi_1\} \\ \{\phi_F\} \end{Bmatrix} \quad (\text{C.18})$$

$\{\phi_1\}$  is the vector of the  $\phi^i$ ,  $i$  on  $C_1$ , and  $\{\phi_F\}$  the vector of the  $\phi^i$ ,  $i$  not on  $C_1$ ; the decomposition of  $[S]$  and  $\{s\}$  is analogous to that of  $\{\phi\}$ . Equation (C.15) states that

$$\{s_1\} = [S_{11}] \{1\} \quad (\text{C.19})$$

where  $\{1\}$  is the vector, with all unit entries, of length  $N_1$ , where  $N_1$  is the number of nodes on  $C_1$ . Thus,

$$\{\phi_1\} = \{1\} \phi_c \quad (\text{C.20})$$

i.e., all  $\phi^i$ ,  $i$  on  $C_1$ , are equal to  $\phi_c$  in the finite element solution, as might have been anticipated. Since the solution obeys Equation (C.20), we may impose it on  $\mathcal{L}$  as a set of constraints:

$$\begin{aligned} \mathcal{L} = & \frac{1}{2} \{1\}^T [\epsilon_{11}] \{1\} \phi_c^2 + \{1\}^T [\epsilon_{1F}] \{\phi_F\} \phi_c \\ & + \frac{1}{2} \{\phi_F\}^T [\epsilon_{FF}] \{\phi_F\} \\ & - \{\rho_1\}^T \{1\} \phi_c - \{\rho_F\}^T \{\phi_F\} \\ & - Q \phi_c + \{E_F\}^T \{\phi_F\} \end{aligned} \quad (\text{C.21})$$

The  $\sigma^i$  and  $\phi_1^i$  do not appear in Equation (C.21). The variational equations for  $\mathcal{L}$ , Equation (C.21) are

$$\epsilon^* \phi_c + \{\epsilon_F\}^T \{\phi_F\} = \rho^* + Q \quad (\text{C.22a})$$

$$\{\epsilon_F\}\phi_C + [\epsilon_{FF}]\{\phi_F\} = \{\rho_F\} - \{E_F\} \quad (C.22b)$$

where

$$\epsilon^* \equiv \{1\}^T [\epsilon_{11}] \{1\} = \sum_{i,j \in C_1} \epsilon_{ij} \quad (C.23)$$

and

$$\{\epsilon_F\} \equiv [\epsilon_{1F}]^T \{1\} \quad (C.24)$$

i.e.,

$$\epsilon_{Fi} = \sum_{j \in C_1} \epsilon_{ij} \quad i \notin C_1 \quad (C.25)$$

and

$$\rho^* \equiv \{\rho_1\}^T \{1\} = \sum_{i \in C_1} \rho_i \quad (C.26)$$

The system of equations (C.22) is symmetric, and presumably positive definite and diagonal dominant, making for ease of solution.

After the system of Equation (C.22) has been solved for  $\phi_C$  and the  $\phi_F^i$ , the  $\sigma^i$  may be obtained from Equation (C.12a)

$$[S_{11}]\{\sigma_1\} = \{\epsilon_1\}\phi_C + [\epsilon_{1F}]\{\phi_F\} - \{\rho_1\} \quad (C.27)$$

where

$$\{\epsilon_1\} = [\epsilon_{11}]\{1\} \quad (C.28)$$

i.e.,

$$\epsilon_{1i} = \sum_{j \in C_1} \epsilon_{ij} \quad i \in C_1 \quad (C.29)$$



## APPENDIX D. POTENTIAL INTERPOLATION IN NASCAP

### D.1 LINEARLY BLENDED ELEMENTS

In the finite element solution of Poisson's equation, the requirement that the potential  $\phi$  be continuous is met by establishing unique conventions for the interpolation functions at element boundaries. For our case, we require that  $\phi$  be linear on any edge, bilinear on a square face, and linear on a triangular face. Subject to these restrictions, we must find the interpolation functions  $N$  and weights  $W$ , defined by

$$\phi(\vec{r}) = \sum_i N^i \phi_i$$

$$\int_{\text{cell}} |\nabla\phi|^2 dr = \sum_{ij} W_{ij} \phi_i \phi_j$$

for any cell.

An instructive example is the simple cube  $0 < x, y, z < 1$  having an extra edge drawn from (100) to (010). The potentials on the  $z = 0$  and  $z = 1$  planes are

$$\phi(x, y, 0) = \begin{cases} (1-x-y)\phi_{000} + x\phi_{100} + y\phi_{010} & x+y < 1 \\ (x+y-1)\phi_{110} + (1-y)\phi_{100} + (1-x)\phi_{010} & x+y > 1 \end{cases}$$

$$\phi(x, y, 1) = (1-x)(1-y)\phi_{001} + x(1-y)\phi_{101} + y(1-x)\phi_{011} + xy\phi_{111}$$

the total potential being

$$\phi(x, y, z) = (1-z)\phi(x, y, 0) + z\phi(x, y, 1)$$

This last step is an example of "linear blending".

Note that the electric field is discontinuous across the plane  $x+y = 1$ . However, within each of the regions,  $x+y < 1$  and  $x+y > 1$ , the functions  $N^i$  and  $\nabla N^i$  are simple.

In general, the problem is handled as follows:

1. Divide the cell into regions  $R_\alpha$  in which a differentiable potential function may be constructed by linear blending. This may be done in an asymmetric manner, the final result being obtained by averaging over equivalent functions.
2. In each  $R_\alpha$  write

$$\nabla N_\alpha^i(\vec{r}) = \sum_{\nu} a_{i_{\alpha\nu}} f_{\alpha\nu}(\vec{r})$$

3. Calculate

$$(f_{\alpha\mu}, f_{\alpha\nu}) = \int_{R_\alpha} d^3 \vec{r} f_{\alpha\mu} f_{\alpha\nu}$$

4. Finally, we have

$$M[\{\alpha\}] \phi(\vec{r}) = \sum_{\{\alpha\}} \sum_i N_\alpha^i(\vec{r})$$

$$M[\{\alpha\}] W_{ij} = \sum_{\{\alpha\}} \sum_{\alpha} \sum_{\mu\nu} (f_{\alpha\mu}, f_{\alpha\nu}) a_{i_{\alpha\mu}} a_{j_{\alpha\nu}}$$

where  $\{\alpha\}$  is the set of equivalent partitions of the cell, and  $M[\{\alpha\}]$  is the number of members in the set. We have found it convenient to perform steps 1 - 3 by hand, using a computer program to perform step 4.

## D.2 ELEMENT TABLE CODES

Code for Element Table [LTBL(NX,NY,NZ)].

54321 0987654321 0 9 8 765 432109876 5 43210  
           └──────────┘ | |           └──────────┘ └──────────┘  
                   E       D C                   B           A

<u>Field</u>	<u>Bits</u>	
A	4-0	Cell-type code (see Appendix D)
B	14-6	Orientation code (see Appendix D)
C	18	Set if cell is completely filled (interior)
D	19	Set for an empty special cell
E	30-21	Index used to reference PHOJ array to determine low energy electron currents

### ORIENTATION CODE

3x3 bits. Each group of 3 contains 1, 2 or 3 in the lower 2 bits, with the high bit set for negative.

$$\text{Code } \left[ (-)^{m_1} i_1, (-)^{m_2} i_2, (-)^{m_3} i_3 \right]$$

$$\text{takes } (r_1, r_2, r_3) \text{ to } \left[ (-)^{m_1} r_{i_1}, (-)^{m_2} r_{i_2}, (-)^{m_3} r_{i_3} \right]$$

e.g., the following codes take a point to (x,y,z):

<u>Octal Code</u>	<u>Dec. Code</u>	<u>Point</u>
123	1,2,3	(x,y,z)
365	3,-2,-1	(-z,-y,x)
532	-1,3,2	(-x,z,y)
176	1,-3,-2	(x,z,-y)
567	-1,-2,-3	(-x,-y,-z)
617	-2,1,-3	(y,-x,-z)

### D.3 STANDARD VOLUME CELLS

(Format)

Description

Standard Orientation

$$\text{Potential Function} = \sum_i N^i \phi_i$$

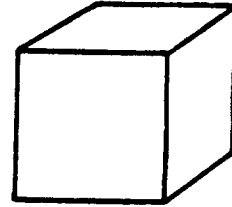
$$\text{Weight Matrix, } W_{ij}: \int d\Omega |\nabla \phi|^2 = \sum_{ij} W_{ij} \phi_i \phi_j$$

<u>Point Index</u>	<u>Cube Corner</u>
1	0 0 0
2	1 0 0
3	0 1 0
4	1 1 0
5	0 0 1
6	1 0 1
7	0 1 1
8	1 1 1

Standard Cell 0

Empty trilinear cube

Orientation: Arbitrary



Potential Function:

$i$	$N^i$
1	$(1-x)(1-y)(1-z)$
2	$(1-z)(1-y)x$
3	$(1-x)y(1-z)$
4	$(1-z)yx$
5	$z(1-y)(1-x)$
6	$x(1-y)z$
7	$zy(1-x)$
8	$xyz$

$W_{ij}$

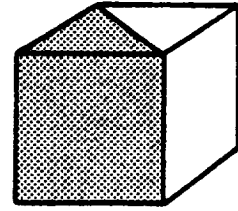
1/3								
0	1/3							
0	-1/12	1/3						
-1/12	0	0	1/3					
0	-1/12	-1/12	-1/12	1/3				
-1/12	0	-1/12	-1/12	0	1/3			
-1/12	-1/12	0	-1/12	0	-1/12	1/3		
-1/12	-1/12	-1/12	0	-1/12	0	0	1/3	

Standard Cell 1

Half-Empty Wedge

$$\begin{aligned} 1 < x + y < 2 \\ 0 < z < 1 \end{aligned}$$

Orientation: Right angle along  
line 7-8



Potential function:

i	$N^i$
1	0
2	$(1-y)(1-z)$
3	$(1-x)(1-z)$
4	$(x+y-1)(1-z)$
5	0
6	$(1-y)z$
7	$(1-x)z$
8	$(x+y-1)z$

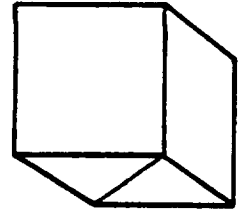
$W_{ij}$

0								
0	1/4							
0	1/24	1/4						
0	-1/8	-1/8	5/12					
0	0	0	0	0				
0	0	-1/24	-1/8	0	1/4			
0	-1/24	0	-1/8	0	1/24	1/4		
0	-1/8	-1/8	-1/12	0	-1/8	-1/8	5/12	

Standard Cell 2

Cube with diagonal line on one face

Orientation: Line from 2 to 3



Potential Function:

$i$	$N^i$
1	$(1-x-y)(1-z)\theta(1-x-y)$
2	$[x\theta(1-x-y)+(1-y)\theta(x+y-1)](1-z)$
3	$[y\theta(1-x-y)+(1-x)\theta(x+y-1)](1-z)$
4	$(x+y-1)(1-z)\theta(x+y-1)$
5	$(1-x)(1-y)z$
6	$x(1-y)z$
7	$(1-x)yz$
8	$xyz$

$W_{ij}$ :

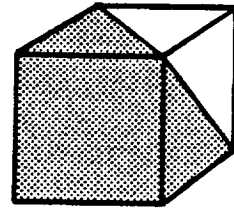
5/12								
-1/8	1/2							
-1/8	1/12	1/2						
0	-1/8	-1/8	5/12					
7/360	-37/360	-37/360	-23/360	1/3				
-11/180	-1/45	-19/180	-11/180	0	1/3			
-11/180	-19/180	-1/45	-11/180	0	-1/12	1/3		
-23/360	-37/360	-37/360	7/360	-1/12	0	0	1/3	

Standard Cell 3

Tetrahedron

$$2 < x + y + z < 3$$

Orientation: Empty corner at  
point 8



Potential Function:

i	$N^i$
1	0
2	0
3	0
4	1-z
5	0
6	1-y
7	1-x
8	x+y+z-2

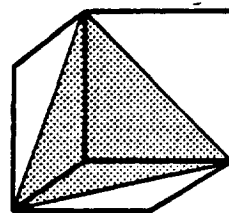
$W_{ij}$ :

0								
0	0							
0	0	0						
0	0	0	1/6					
0	0	0	0	0				
0	0	0	0	0	1/6			
0	0	0	0	0	0	1/6		
0	0	0	-1/6	0	-1/6	-1/6	1/2	

Standard Cell 4

Truncated Cube

Orientation: 000 corner (point 1)  
missing



Potential Function:

i	$N^i$
1	0
2	
3	exercise
4	for
5	reader
6	
7	
8	

$W_{ij}$ :

0								
0	5/12							
0	1/72	5/12						
0	-11/120	-37/360	13/36					
0	1/72	1/72	-1/9	5/12				
0	-37/360	-1/9	-7/180	-11/120	13/36			
0	-1/9	-11/120	-7/180	-37/360	-7/180	13/36		
0	-5/36	-5/36	1/45	-5/36	1/45	1/45	7/20	



## APPENDIX E

The following paper was presented at the IEEE Annual Conference on Nuclear and Space Radiation Effects, Williamsburg, Virginia, July 1977. (Note that the material properties used in this calculation differ somewhat from those used elsewhere in this report.)



NASCAP, A THREE-DIMENSIONAL CHARGING ANALYZER  
PROGRAM FOR COMPLEX SPACECRAFT

I. Katz  
D. E. Parks  
M. J. Mandell  
J. M. Harvey  
S. S. Wang

Systems, Science and Software  
La Jolla, California

J. C. Roche

National Aeronautics and Space Administration  
Lewis Research Center  
Cleveland, Ohio

ABSTRACT

A computer code, NASCAP (NASA Charging Analyzer Program), has been developed by Systems, Science and Software under contract to NASA-LeRC to simulate the charging of a complex spacecraft in geosynchronous orbit. The capabilities of the NASCAP code include a fully three-dimensional solution of Poisson's equation about an object having considerable geometrical and material complexity, particle tracking, shadowing in sunlight, calculation of secondary emission, backscatter and photoemission, and graphical output. A model calculation shows how the NASCAP code may be used to improve our understanding of the spacecraft-plasma interaction.

Preceding page blank

## 1. INTRODUCTION

Several anomalies observed on geosynchronous spacecraft have been attributed to differential charging caused by magnetospheric substorms. These substorms consist of hot plasmas with mean energies ranging from several thousands to tens of thousands of electron volts. The several physical processes taking place during a charging event include backscattering of incident particle fluxes, emission of secondary electrons, charge redistribution on the spacecraft, as well as modification of incident fluxes due to the charging itself. However, if spacecraft are to be optimally designed for operation under all magnetospheric conditions, it is important to understand how the different processes interact. To accomplish this, a charging analyzer program, NASCAP, has been developed. This code self-consistently simulates the three-dimensional charging of complex model spacecraft subject to magnetospheric conditions. NASCAP is also capable of treating objects in a ground test environment.

In the next section of this paper we will discuss very briefly the physical models employed in the code. Following that we will present a calculation of a moderately complex asymmetric spacecraft similar in size and materials to the body of the experimental satellite, SCATHA, which is being constructed to study Satellite Charging At High Altitudes. Conclusions drawn from this calculation concerning surface material properties on satellites are discussed in the last section.

## 2. COMPUTATIONAL TECHNIQUE

Magnetospheric substorms are encountered rather frequently by satellites in geosynchronous orbit. Under these conditions the hot plasma environment may be characterized by a temperature of  $10^4$  eV or greater, and a density of order  $1/\text{cm}^3$ . Such a plasma may charge a satellite negatively to

many kilovolts; also kilovolt potentials may develop between different parts of the satellite or across dielectric coatings, causing dielectric breakdown and various electronic malfunctions.

To simulate the charging phenomenon requires self-consistent calculation of the electronic and ionic fluxes to each surface element of the satellite, and the material response to the incident flux. Since the shortest times characterizing satellite charging  $[(V/4\pi Rne)(m/kT)^{1/2} \sim 10^{-3}$  seconds] are significantly longer than plasma dynamic response times  $[(m/4\pi ne^2)^{1/2} \sim 10^{-5}$  seconds] the plasma responds quasi-statically to charge accumulation on the satellite. NASCAP follows, therefore, an explicit timestepping procedure, each step consisting of a charge accumulation calculation and an electrostatic potential calculation. A flow chart of the NASCAP code is shown in Figure 1.

The net charge accumulation by each surface cell of the satellite is calculated in the presence of the electrostatic and magnetostatic fields about the satellite, and specified environmental characteristics. In the ground test case, the incident flux is provided by a monoenergetic electron gun of specified beam profile. In the space case the incident flux of electrons and ions at surfaces is determined using the reverse trajectory sampling method. The ambient plasma may be isotropic and Maxwellian, or may be represented by any of several sets of data from ATS-5 and -6 prepared for S<sup>3</sup> by MAYA Development Corporation. Alternatively, a spherical probe approximation may be used. Electron backscatter and secondary emission due to electron and ion impact, as well as photoemission and shadowing, are taken into account. The formulation of the various physical processes take into account their energy and angle dependence. Details may be found in Reference 1. Optionally, a first-order photosheath

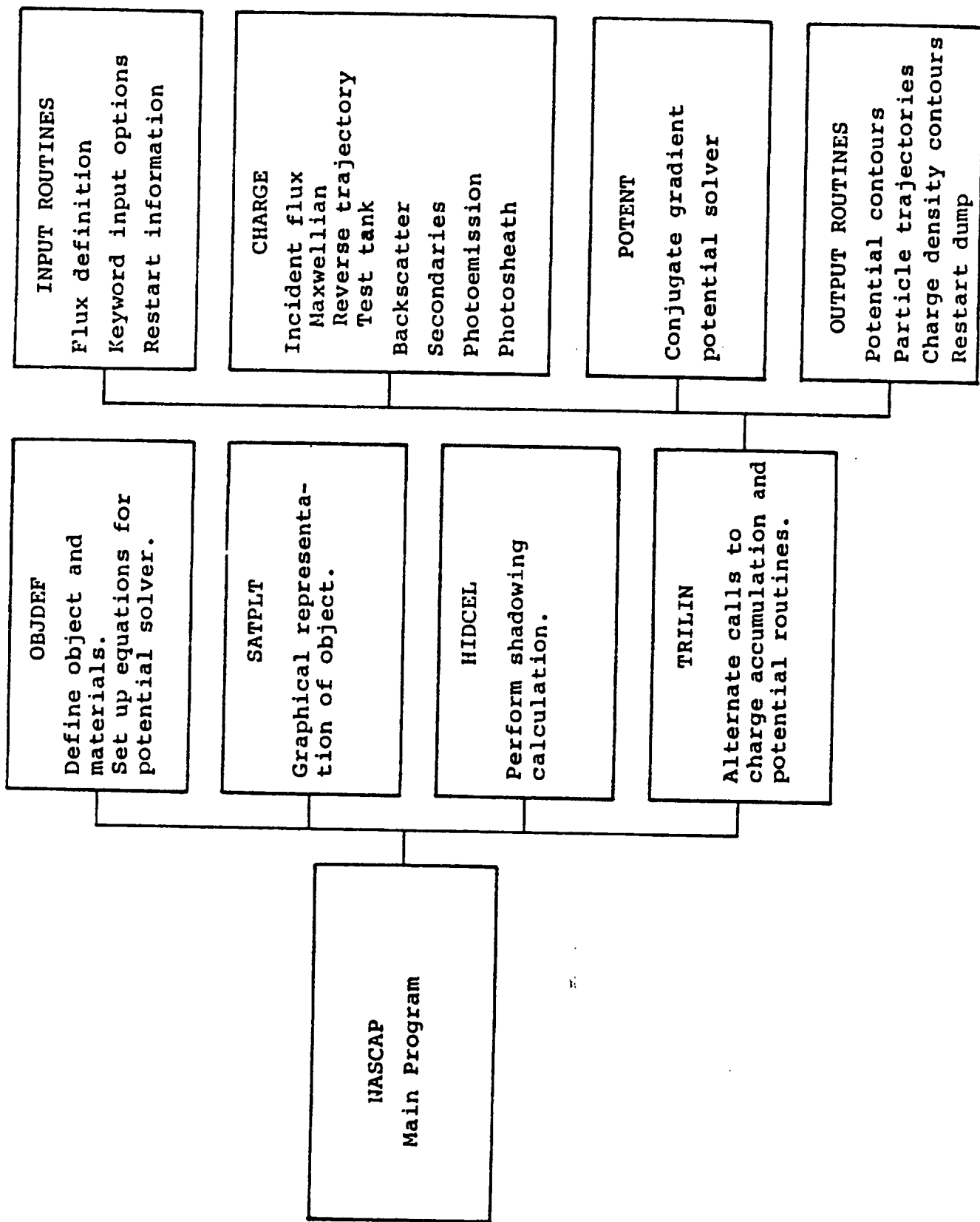


Figure 1. Flow chart of NASCAP code.

calculation may be performed, but in general, because magnetospheric Debye lengths are large compared with spacecraft dimensions, space charge is neglected.

The electrostatic potential about the satellite or in the test tank is calculated by NASCAP using a finite element formulation of Poisson's equation. Under magnetospheric conditions the Debye length  $\lambda_D = (kT/4\pi ne^2)^{1/2}$  is typically hundreds of meters, so that space charge can be ignored, except for a positively charged satellite which may develop a photoelectron sheath. The computational space consists of an arbitrarily large number of nested cubic meshes. The resulting set of several times  $10^4$  linear equations is solved using the Conjugate Gradient technique. The satellite or test object is defined within the innermost mesh, and may have surfaces normal to any of the twenty-six cubic symmetry directions. It consists of one or more conductors which may be covered with thin dielectric layers. The conductors may be floating, held at fixed potentials, or biased relative to one another.

### 3. CALCULATION OF DIFFERENTIAL CHARGING OF A MODEL SATELLITE

The calculation presented here is of a model satellite similar in size, shape and surface material to the experimental SCATHA satellite presently under construction. The purpose of this calculation is to examine how the various surfaces react to a fairly intense substorm environment. To the best of our knowledge this is the first such calculation to self-consistently incorporate three-dimensional geometry, complex material electrical boundaries, and realistic surface response effects. For computational ease the incident currents were assumed to be from an isotropic Maxwellian whose mean ion and electron densities and energies were chosen to be similar to those actually encountered by ATS-5 on March 14, 1971, during a magnetospheric substorm. At the end of the calculation, the self-consistent particle fluxes incident on

a material test patch on the top of the spacecraft were calculated using the reverse orbit technique and the reduced ATS-5 data. The fluxes agreed with analytical formulas within a factor of two.

The model satellite is shown in Figure 2 and its dimensions are given in Table 1. The satellite model consists of an aluminum right octagonal parallelepiped which forms spacecraft ground. All of the sides of the object are covered with a four mil layer of silicon dioxide, with the exception of a 35 cm band on which the aluminum is exposed. On opposite sides and on the top are kapton covered magnesium plates. The kapton is 4 mils thick while the plates are capacitatively coupled to spacecraft ground by 200 picofarads. The remainder of the top surface and all of the bottom surface are bare aluminum. Electrically we have four separate conducting structures and hundreds of separate dielectric surfaces. Coupling is purely capacitive except for the very small dielectric conductivity. In this calculation the dielectric conductivity was independent of the field strength and had a numerical value of  $10^{-14}$  mho/m.

The calculation of backscatter and secondary coefficients was performed as described in Reference 1.

Initially, the satellite is assumed to be in eclipse with all surfaces at zero potential. Table 2 shows a breakdown of the particle fluxes both incident and emanating from the four different types of material surfaces. It is most interesting to note that even though there is no photoemission, secondary emission from the insulators, in particular from  $\text{SiO}_2$ , exceeds the incident electron flux. Notice also the high electron secondary emission caused by incident protons. As such then, a satellite completely covered with  $\text{SiO}_2$  would actually charge a few volts positively with respect to the plasma. It is the aluminum surfaces that are charging

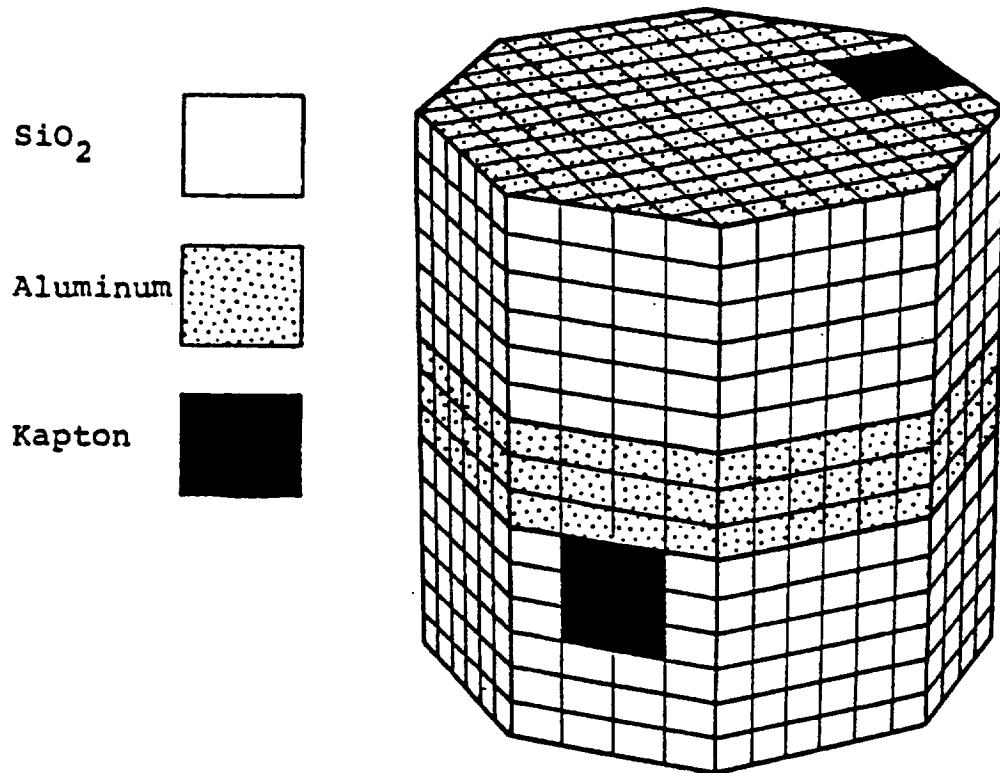


Figure 2. Model satellite used in sample calculation showing surface resolution and materials.

TABLE 1  
 Dimensions of Model Satellite and Comparison  
 with SCATHA Spacecraft

SCALE - 1 Zone = 11.5 cm

		Dimensions in Meters	
		MODEL	SCATHA
Octagon Mean Diameter	=	1.68	1.71
Height	=	1.73	1.77
Aluminum Band	=	0.35	0.25
SSPM	top	= .35 x .35	
	sides	= .35 x .33	.32 x .32

(For this calculation all SSPM are Kapton over Mg)

TABLE 2

Charging at Early Time  
(Satellite Potential = -80 V)

<u>Source of Flux</u>	<u>Fluxes (A/m<sup>2</sup>)</u>		
	Aluminum	SiO <sub>2</sub>	Kapton
Incident Electrons	-8.92 x 10 <sup>-7</sup>	-8.92 x 10 <sup>-7</sup>	-8.92 x 10 <sup>-7</sup>
Electron backscatter	2.13 x 10 <sup>-7</sup>	1.92 x 10 <sup>-7</sup>	1.53 x 10 <sup>-7</sup>
Electron-produced secondaries	3.29 x 10 <sup>-7</sup>	8.96 x 10 <sup>-7</sup>	5.55 x 10 <sup>-7</sup>
Incident Protons	9.22 x 10 <sup>-9</sup>	9.22 x 10 <sup>-9</sup>	9.22 x 10 <sup>-9</sup>
Proton-produced secondaries	1.19 x 10 <sup>-8</sup>	1.23 x 10 <sup>-8</sup>	1.23 x 10 <sup>-8</sup>
Net Flux	-3.29 x 10 <sup>-7</sup>	2.18 x 10 <sup>-7</sup>	-1.63 x 10 <sup>-7</sup>

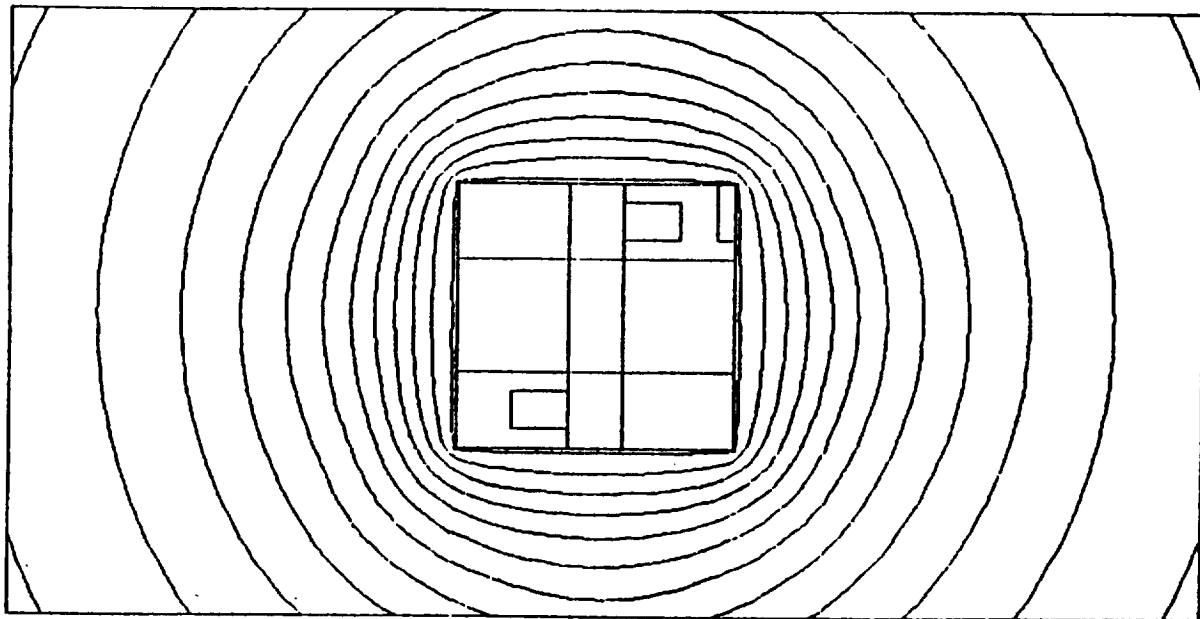
negatively and driving the overall satellite potential negative.

As one would expect, the overall body goes negative at about the same rate as an equivalent sphere with the same total net charge. However, the maximum potential achieved is only 575 volts, just over 10 percent of the mean plasma energy. The potential about the satellite is illustrated in the upper part of Figure 3. After developing this voltage, which takes less than 300 milliseconds (see Figure 4), the surfaces begin to develop differences of potential. The ratio in time scales between differential charging and overall charging is approximately the same as the ratio of the overall body size to the dielectric thickness. In this case that ratio is the order of  $10^4$ .

Figure 4 shows the highest differential charging rate is across the 4 mil  $\text{SiO}_2$  surface. This rate is only about 75 volts/cm-sec, or less than a volt per second. The actual potentials grow more quickly on the kapton surfaces in spite of a lower differential current. This is due to having less capacitance per unit area relative to the underlying metal. It is important to note that the  $\text{SiO}_2$  surfaces charge positive with respect to spacecraft ground but the kapton goes negative. This occurs because the net positive current to the  $\text{SiO}_2$  tends to "soak up" negative current to the aluminum. As a result the kapton has an effective higher negative current than the aluminum.

This calculation was run to 56 seconds. The fields in the dielectric have been increasing linearly to over  $3 \times 10^5$  volts/meter with only small changes in  $\text{SiO}_2$  fluxes. The flux to the top kapton surface had dropped to about two-thirds its initial value with the voltage differential less than 300 volts from spacecraft ground. The current balance at this time is indicated in Table 3, and the potentials are in the lower part of Figure 3.

Early potentials  
No differential charging



Late time potentials (56 seconds)  
SiO<sub>2</sub> covering charged positive  
Aluminum band charged to -575 volts  
SSPM in upper right charged to -650 volts

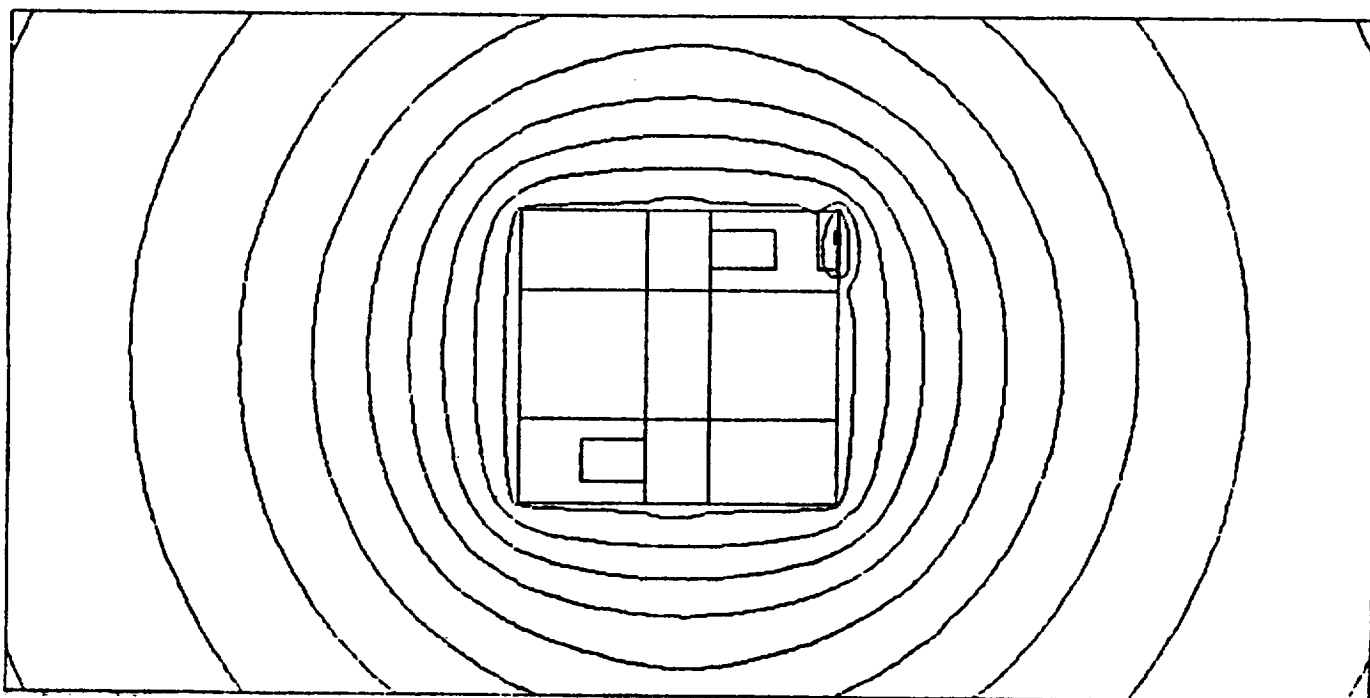


Figure 3. Potential contours about the satellite before (upper) and after (lower) differential charging.

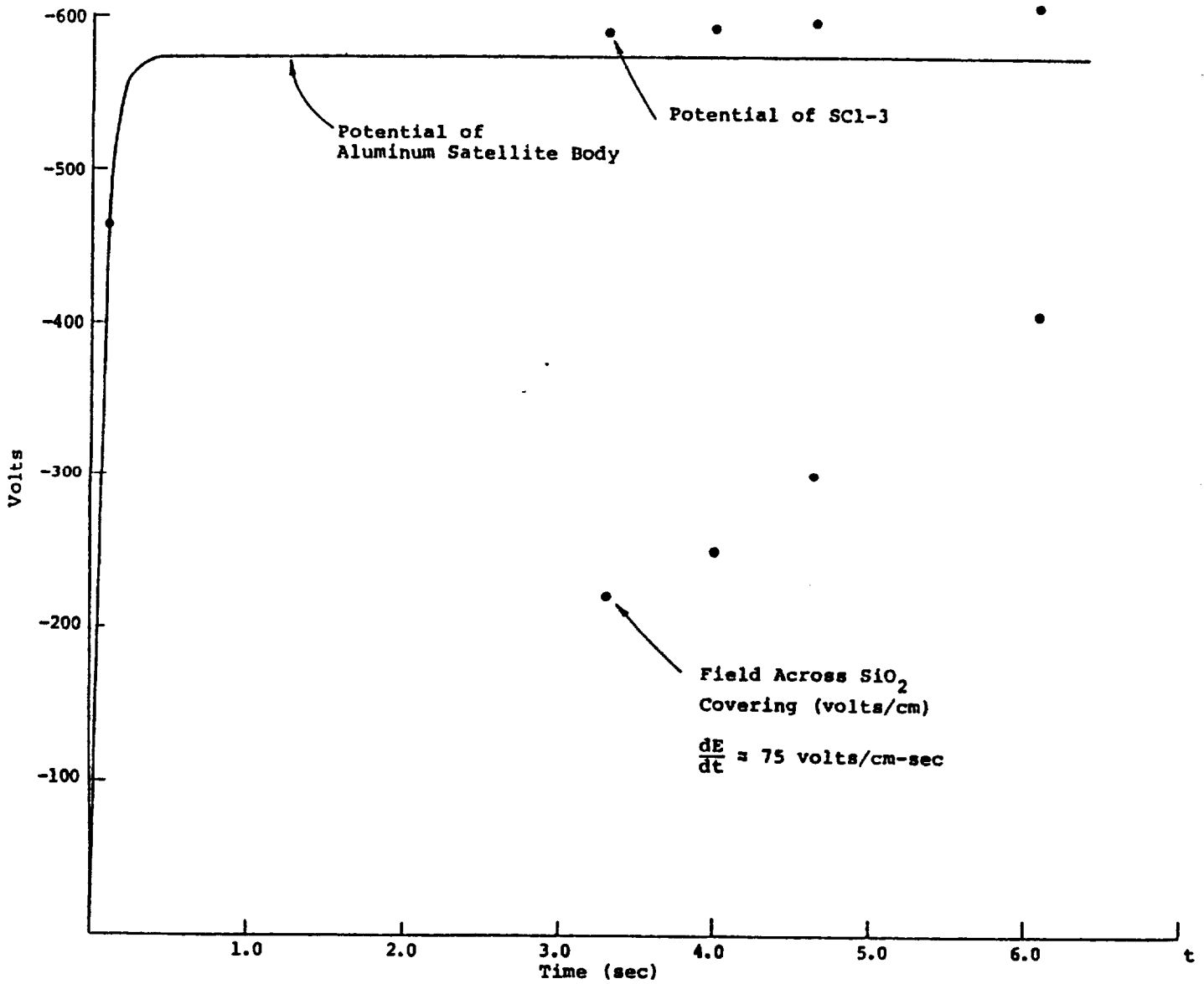


Figure 4. Time development of potentials on aluminum satellite body, on a kapton-coated sample, and the field across the SiO<sub>2</sub> cover cells.

It is useful to contrast the results presented here with those that would be deduced from a simplified theory based on complete current balance on every material of the satellite's surface. The simplified theory has been invoked, for example, by DeForest<sup>[2]</sup> to analyze charging observed on the ATS-5 experimental spacecraft. Complete current balance for each surface material, however, is expected only after charging in the given environment has proceeded for a sufficiently long time,  $t_{eq}$ , and assuming that the plasma environment in the vicinity of the satellite does not change for times to  $\lesssim t_{eq}$ .

In the present application, considering the secondary yields of aluminum, kapton and  $\text{SiO}_2$ , one should expect an equilibrium in which both  $\text{SiO}_2$  and kapton are positive with respect to spacecraft ground (aluminum), and in which  $\text{SiO}_2$  is slightly positive with respect to infinity. After approximately one minute of charging, the  $\text{SiO}_2$  is positive relative to the aluminum; the kapton, however, is negative with respect to spacecraft ground.

Based on the net charging currents in Table 3, this inversion of the relative potentials of kapton and aluminum is expected to persist for several minutes.

In the absence of dielectric conduction, complete equilibration, based on net charging current  $j$  of order  $10^{-7}$  amps/m<sup>2</sup> and a  $\Delta V \sim 600$  volts is attained in a time of order

$$t_{eq} = \frac{C\Delta V}{j} = \frac{600 \times 200 \times 10^{-12} \times 10^4}{4\pi \times 10^{-7}} \sim 20 \text{ min.}$$

Apart from dielectric relaxation times,  $t_{eq}$  is the longest time scale associated with differential charging. In many circumstances, it is longer even than the characteristic time for variations in the magnetospheric environment, so that full equilibration of differential potentials may not be achieved within the duration of a substorm. Such conditions clearly require a quasi-static as opposed to a fully equilibrium treatment of spacecraft charging.

TABLE 3  
Charging at Late Time

<u>Source of Flux</u>	Fluxes (A/m <sup>2</sup> )		
	Aluminum (-576 volts)	SiO <sub>2</sub> (-520 volts)	Kapton (-785 volts)
Incident Electrons	-7.91 x 10 <sup>-7</sup>	-8.01 x 10 <sup>-7</sup>	-7.51 x 10 <sup>-7</sup>
Electron backscatter	1.89 x 10 <sup>-7</sup>	1.73 x 10 <sup>-7</sup>	1.29 x 10 <sup>-7</sup>
Electron-produced secondaries	2.92 x 10 <sup>-7</sup>	8.06 x 10 <sup>-7</sup>	4.67 x 10 <sup>-7</sup>
Incident Protons	1.82 x 10 <sup>-8</sup>	1.72 x 10 <sup>-8</sup>	2.20 x 10 <sup>-8</sup>
Proton-produced secondaries	3.57 x 10 <sup>-8</sup>	3.38 x 10 <sup>-8</sup>	5.01 x 10 <sup>-8</sup>
Net Flux	-2.56 x 10 <sup>-7</sup>	2.28 x 10 <sup>-7</sup>	-8.33 x 10 <sup>-8</sup>

#### 4. CONCLUSIONS

The calculation presented here illustrates several features that are common to most magnetospheric charging situations. First is that all the surface potentials charge initially according to the overall net charge on the object, regardless of their local currents. For example, the silicon dioxide surfaces always have a net positive current, but at first their potentials rise along with the rest of the body to a negative 575 volts. In general, the potentials on all surfaces will initially remain constant with respect to each other, but change with respect to infinity in response to a sudden change in environment. Then, on a longer (minutes) time scale, the surface potentials will re-adjust with respect to each other while the integral net current to the satellite is almost zero.

Second, the insulators, in particular silicon dioxide, resist charging due to their high secondary yields and high secondary crossover points. This is very important since so much of the surface of satellites, particularly those which are spin stabilized, is covered with solar cell coverplates which are made of  $\text{SiO}_2$ . These materials keep the body potentials thousands of volts below a high plasma temperature. Indeed, it is the exposed conductors that collect the most charge. This implies that a high degree of active control may be possible just by discharging the spacecraft ground if the insulating surfaces are chosen for high secondary yield coefficients. While this will not solve all charging problems, it can certainly lower potential differences on the spacecraft.

The third point is that not only is the magnitude of the potential difference between two surfaces dependent upon what is happening on the entire vehicle, but even the direction of the difference depends on non-local effects. Comparing the current fluxes to the aluminum and kapton surfaces,

one would assume that kapton would not become as negative as the aluminum. While in the limit of long times this may be true, the very opposite occurs on a time scale of minutes. Since the environment can change in minutes, both situations are important. Indeed the system may not even approach the long time limit before substantial changes in the environment occur.

The calculation presented here has used just a few of the capabilities of the NASCAP code. By performing detailed simulations of a variety of both space and ground charging situations, we hope to better understand the interaction of geometry, environment, and material properties. It is this knowledge that should lead to simple design criteria to prevent charging induced anomalies from interfering with the operation of future satellites.

## REFERENCES

1. Katz, I., et al., "3-Dimensional Dynamic Study of Electrostatic Charging in Materials," Systems, Science and Software Interim Report, SSS-R-77-3124, January 19, 1977.
2. DeForest, Sherman E., "Spacecraft Charging at Synchronous Orbit," JGR, 77, 681, 1972.



APPENDIX F.1  
ELECTRON BACKSCATTER

Electron backscatter plays an important role in establishing current balance to a spacecraft. Quantities of interest are:

1. Backscattering coefficient for normal incidence.
2. Energy distribution (or, at least, mean energy) of backscattered electrons.
3. Angular distribution of backscattered electrons.
- 4.-6. Dependence of (1-3) on angle of incidence.

We have developed a modification of the theory of Everhart<sup>[18]</sup> and McAfee<sup>[40]</sup> which gives good agreement with available data for 1, 2, 4 and 5 above for  $\theta \lesssim 60^\circ$  and energies in the range 10 keV to 100 keV. The theory can be made to yield (3,6) and can be modified to yield results in the 1 keV to 10 keV energy range.

The backscattering theory of Everhart, which was extended by McAfee to yield an energy distribution, assumes (1) a single scattering in accordance with the Rutherford cross-section, and (2) the Thomson-Widdington slowing down law,  $\frac{dE}{dx} \propto E^{-1}$  (valid for most metals for  $E > 10$  keV). The single-scattering approximation is illustrated in Figure F.1a. All scatterings toward the surface are considered to deplete the beam, though only those in region I have sufficient energy to escape. For normal incidence, the backscattering coefficient is

$$\eta = \frac{a - 1 + (1/2)^a}{a + 1}$$

where  $a$  is (somewhat arbitrarily) taken to be  $0.045 Z$ .

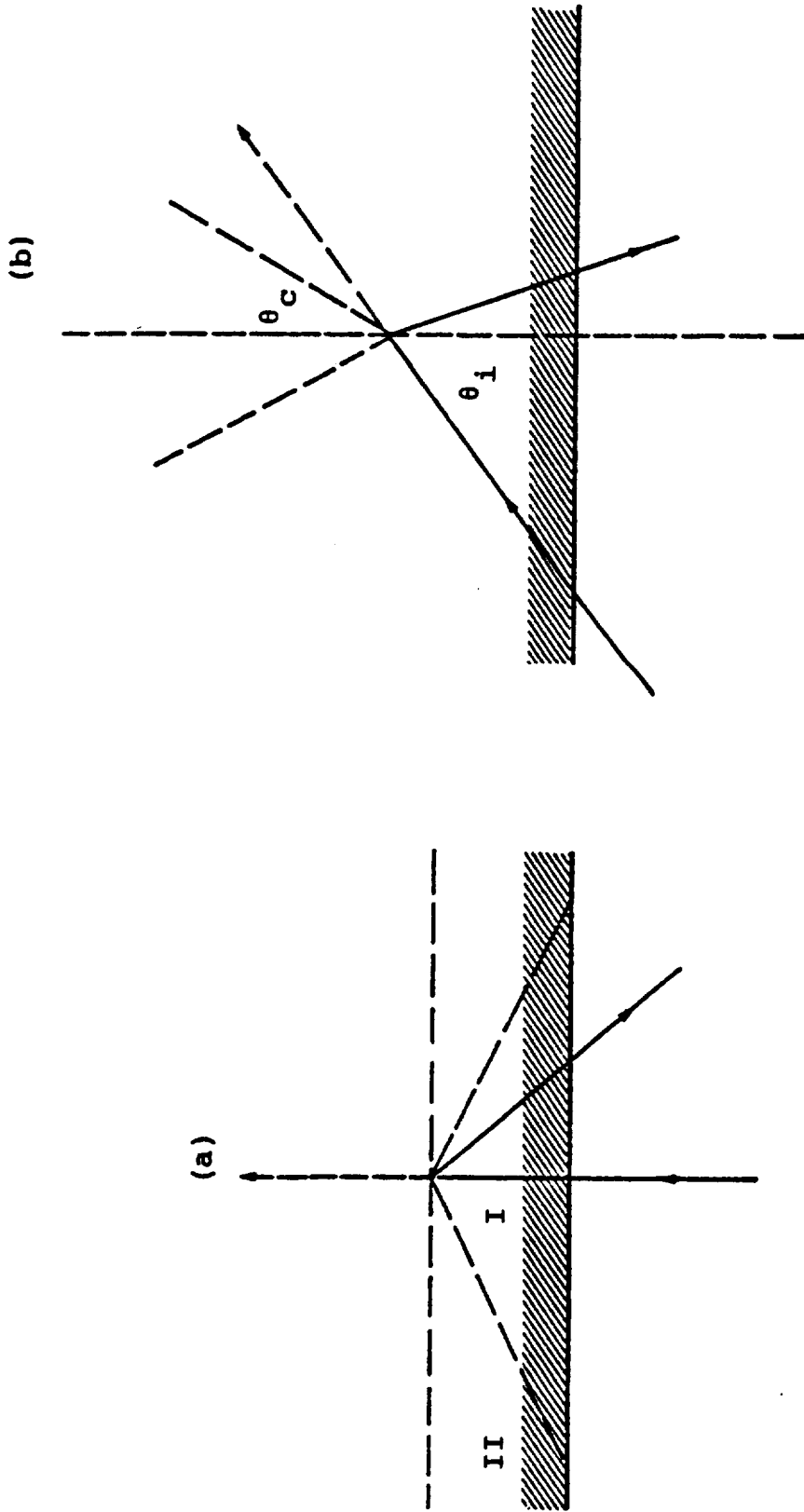


Figure F.1 - Single scattering schemes for electron backscatter: (a) Everhart's scheme (Refs. 2,3) for normal incidence, (b) scheme suggested here for oblique incidence.

For non-normal incidence, it becomes painfully apparent that scattering into region II is best ignored; these electrons are more likely to escape than those remaining in the beam. We adopt the model shown in Figure F.1b: the beam is depleted by escaping electrons and by electrons scattered inward into a cone of angle  $\theta_c < \theta$ . For normal incidence, this gives

$$\eta = 1 - \left(\frac{2}{e}\right)^a$$

where we take  $a = 0.037 Z$  to give backscatter coefficients whose agreement with experiment is similar to that of Everhart. The ELTRAN Monte Carlo results for backscattering coefficients appear to be somewhat lower than the experimental consensus.

Darlington and Cosslett<sup>[16]</sup> (to be referred to as DC) indicate that the angular dependence of the backscattering coefficient is well fit by

$$\frac{\ln[\eta(\theta)/\eta(0)]}{1 - \cos \theta} = F(Z, E) \quad , \quad (F.1)$$

where the right hand side depends only on the material and may be assumed independent of the incident energy if the Thomson-Widdington law holds. Figure F.1a shows this quantity as a function of angle for Al ( $Z = 13$ ) and for kapton ( $Z = 5$ ). For the theory curves, we have taken

$$\theta_c = \begin{cases} 0 & \theta < 30^\circ \\ \theta - 30^\circ & 30^\circ < \theta < 60^\circ \\ 30^\circ & 60^\circ < \theta \end{cases}$$

It is apparent that Equation (F.1) provides an adequate representation of the results, although the ELTRAN data show a systematic decrease of  $F$  with angle. Values of  $F$  are shown in Table F.1. It is apparent that  $F$  decreases with  $Z$ , and that

Table F.1. Angular Dependence of Backscattering Coefficient

<u>Substance</u>	<u>Z</u>	<u>E (keV)</u>	<u>F (a)</u>	<u>Method (b)</u>
---	4	10 - 100	2.54	Theory
Be	4	25	3.4	Experiment
Kapton	5	10 - 100	3.75	ELTRAN
---	5	10 - 100	2.5	Theory
C	6	1 - 3	1.8 - 2.3	Experiment
Teflon	8	10 - 100	3.3	ELTRAN
---	13	10 - 100	2.12	Theory
Al	13	10 - 100	2.24	ELTRAN
Cu	29	25	1.1	Experiment
Cu	29	1.5	0.75	Experiment
---	29	10 - 100	1.5	Theory

(a) For theory and ELTRAN,  $F(Z,E)$  is measured at  $\cos\theta = 0.75$ . For experiment, a line is "eyeballed" through the graph of  $\ln[n(\theta)/n(0)]$  and its slope is quoted.

(b) "Theory" is the modified Everhart theory described herein. "Experiment" data is taken from Darlington and Cosslett.[19]

for small  $Z$  the theory gives values for  $F$  which are too low, while the ELTRAN values are somewhat high.

Results for the mean energy of backscattered electrons are shown in Figure F.2. It is apparent that the theory does poorly near normal incidence, where it gives too small a dependence of mean energy on angle.

For  $E < 10$  keV, the Thomson-Widdington law does not hold and experiment (DC) indicates increased backscattering for low energies, at least for low- $Z$  materials. DC claim that the Everhart theory can be modified to give reasonable agreement for backscattering at normal incidence in the 1-10 keV range.

It is apparent that the theoretical framework can be made to yield the angular distribution of backscattered electrons. Such a calculation would, however, require a non-trivial effort, as this function is now integrated out at an early stage and the quality of such results would be questionable due to the single-scattering approximation.

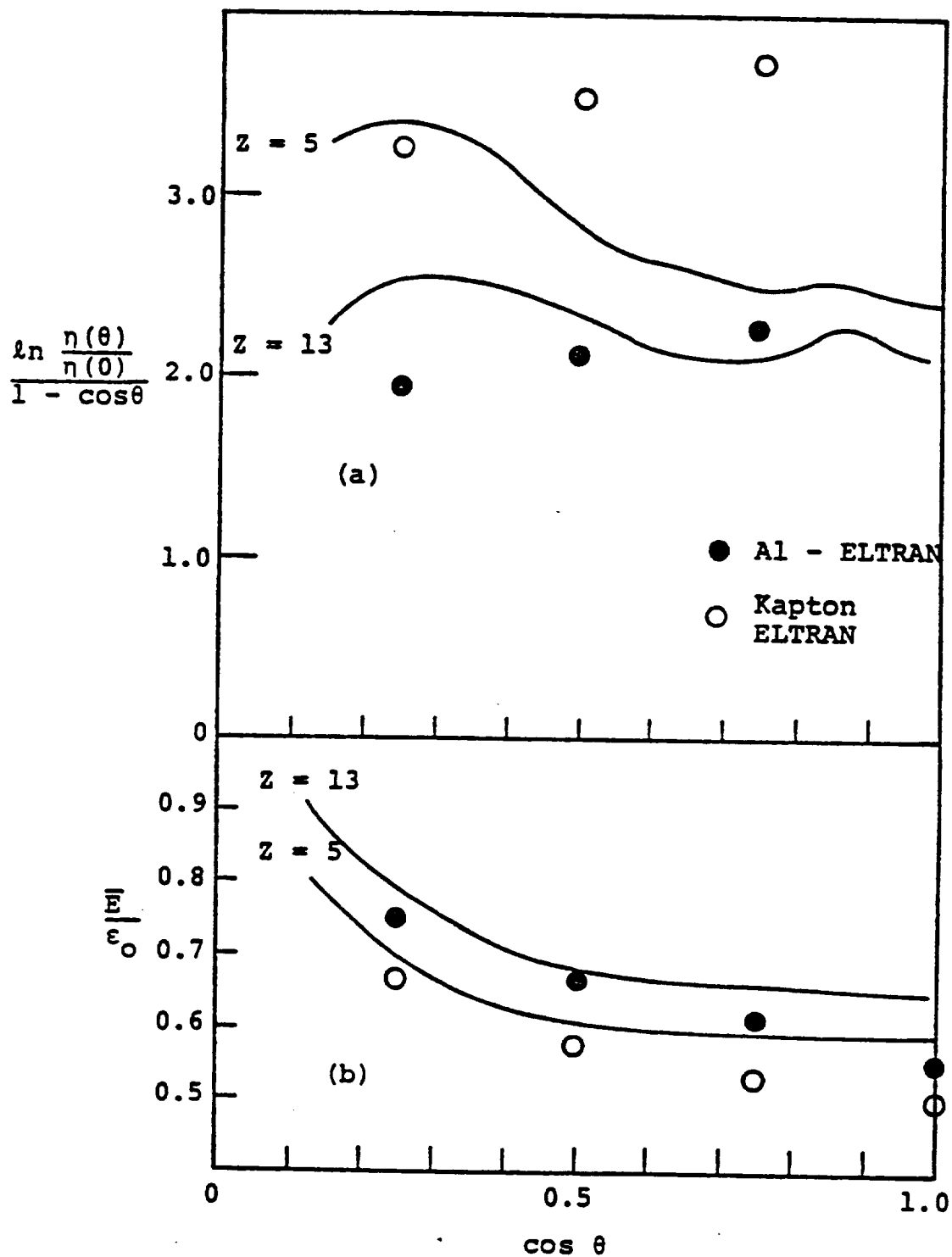


Figure F.2. Results for angular dependence of backscattering coefficients and mean backscattered energy compared with ELTRAN data.

APPENDIX F.2  
DEPOSITION OF ELECTRONS IN MATERIALS

We have developed a simple theory for deposition profiles and albedo (net reflection) for electrons characterized by a plasma temperature of 1-100 keV. We find that the deposition profile can be adequately represented by a simple exponential.

The underlying assumptions of our theory are:

1. The electron plasma is isotropic and characterized by a temperature, T.
2. An incident electron is either backscattered or travels in a straight line to its "maximum practical range."
3. The backscattering probability is taken to be energy-independent and given by (Appendix F.1)

$$\eta = \eta_0 \exp[\eta_1(1 - \cos\theta)]$$

$$\eta_0 = 1 - \left(\frac{Z}{e}\right)^{0.037Z}$$

$$\eta_1 = -\log \eta_0$$

It follows that the albedo  $A_0$  is given by

$$A_0 = (2\eta_0/\eta_1^2) [\exp(\eta_1) - (1 + \eta_1)]$$

4. The range is given by Feldman's<sup>[4]</sup> expression

$$R = bE^n$$

where, for R in angstroms and E in keV,

$$n = 1.2/(1 - 0.126 \log Z)$$

$$b = 250 A/\rho Z^{n/2}$$

A is the mean atomic weight and  $\rho$  the density in gm/cm<sup>3</sup>.

Numerical integration leads to a charge deposition profile

$$N(x) = 2\pi \int_0^1 du (1 - \eta(u)) f[\epsilon(x/u)] / R'[\epsilon(x/u)]$$

where  $u = \cos \theta$ ,  $\epsilon$  is the inverse function to the range R, R' is the derivative of R, and f(E) is the particle flux. The result appears to be adequately represented by

$$N(x) = \frac{1 - A_0}{\bar{x}} \exp(-x/\bar{x}) \quad .$$

Because of the simple expressions for range and backscatter,  $\bar{x}$  scales with temperature as  $T^n$ . Parameters are shown for various materials in Table 3.1. It should be stated that the deposition profile is not exactly represented by an exponential. In particular, low-Z materials (kapton) have a slight minimum in N(x) at  $x = 0$ . However, such behavior occurs only within a few hundred angstroms of the surface and will, in any case, be overwhelmed by charge depletion due to electron emission.

While it is our belief that the average over energies and angles ameliorates the crudeness of the assumptions of this theory, several improvements might be made: Assumption (2) could be relaxed to take account of range straggling; account could be taken of increased backscatter at low energy; and a more accurate range expression might be used.

APPENDIX F.3  
ANGULAR DEPENDENCE OF PHOTOEMISSION

It has been known for some time (Weissler<sup>[41]</sup> and references therein) that there could be a strong dependence of photoelectric yield on the incidence angle of the incident light, and that, at least in some cases, this dependence could be well explained by the optical (or dielectric) properties of the material. We suppose that the yield per photon incident relative to normal incidence is given by

$$\frac{Y(\theta)}{Y(0)} = \sec \theta \frac{E(\theta)^2}{E(0)^2} \times \frac{1 + 2\alpha(0)L}{1 + 2\alpha(\theta)L}$$

Here,  $E(\theta)$  is the electric field just inside the solid calculated using the appropriate electromagnetic boundary conditions,  $\alpha(\theta)$  is the  $\vec{E}$ -field attenuation coefficient normal to the surface, and  $L$  is the escape depth for photoelectrons which may be estimated from low energy electron transport studies.<sup>[6]</sup>

We have applied this theory to aluminum using the known dielectric constant<sup>[42]</sup> and compared the results to the measurements of Samson and Cairns<sup>[43]</sup> on 94 percent aluminum alloy having undergone "routine polishing and cleaning" (see Figure F.3). Below the plasma frequency, the agreement is excellent, indicating little angular dependence until fairly glancing angles are reached. Above the plasma frequency, we predict a much sharper angular dependence than was measured, although we agree on the general form of the curve. The difference may be due to surface roughness and/or contamination and/or differences in the optical constants of the alloy from those of pure aluminum.

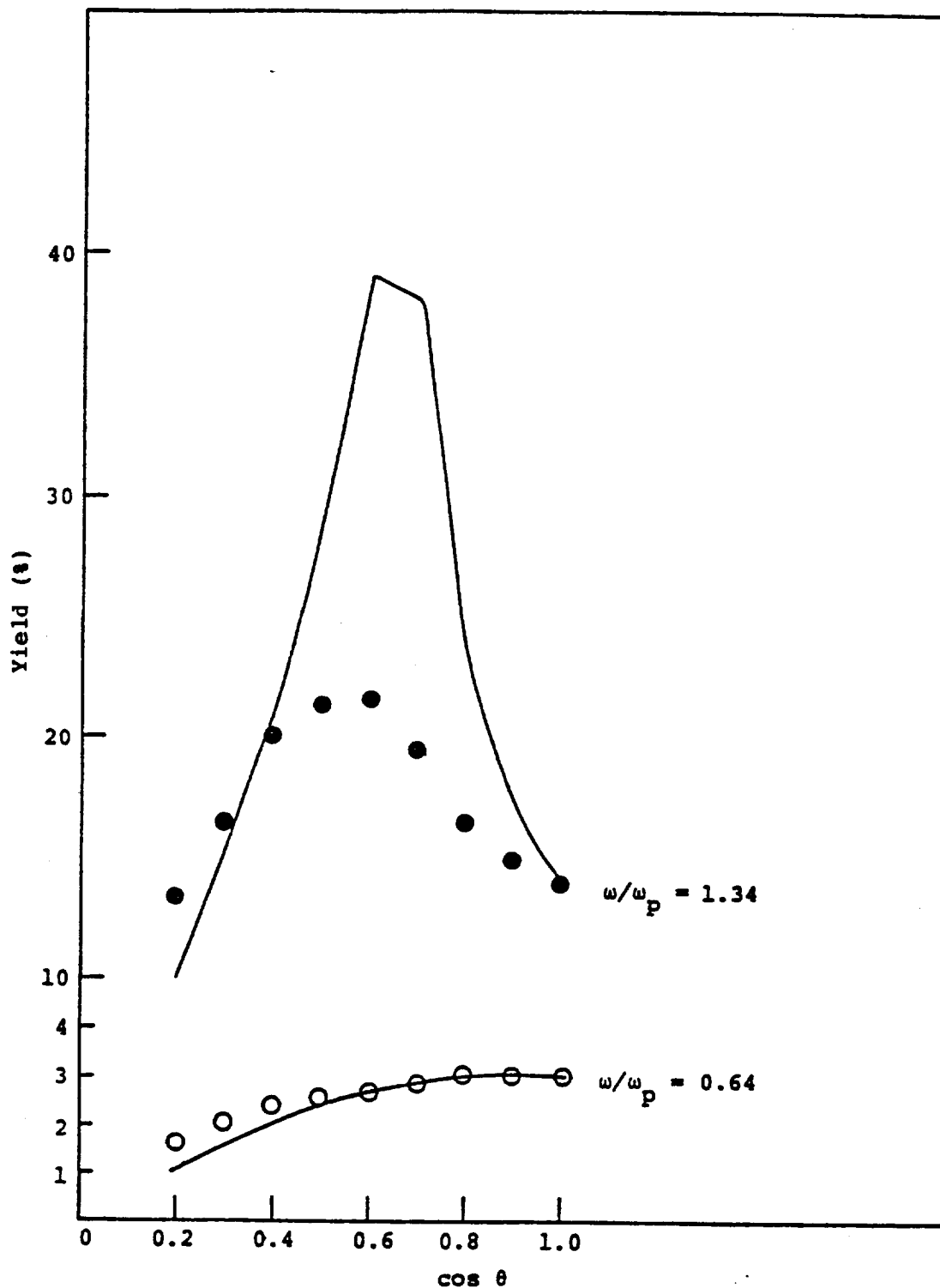


Figure F.3. Angular dependence of photoemission compared with data for 94 percent Al (Ref. 43). [NOTE: Data for pure, clean aluminum (Ref. 44) is in good agreement with the theoretical curve.]

## REFERENCES

1. Mandell, M. J., J. M. Harvey and I. Katz, "NASCAP User's Manual," Systems, Science and Software Report SSS-R-77-3368, August 1977.
2. Birkhoff, G., J. C. Cavendish and W. J. Gordon, Doc. Nat. Acad. Sci., USN, 71, 3423 (1974).
3. Cavendish, J. C., J. Comp. Phys., 19, 211 (1975).
4. Feldman, C., "Range of 1-10 keV Electrons in Solids," Phys. Rev. 117, 455 (1960).
5. Dekker, A.J., "Secondary Electron Emission," Solid State Physics 6, 251 (1958).
6. Hackenberg, O. and W. Brauer, Advances in Electronics and Electron Physics 16, 145 (1962).
7. Gibbons, D.J., "Secondary Electron Emission," Handbook of Vacuum Physics, Vol. 2, p. 299, Pergamon (1966).
8. Willis, R.F. and D. K. Skinner, "Secondary Electron Emission Yield Behavior of Polymers," Sol. St. Comm. 13, 685 (1973).
9. Tung, C.J., J. C. Ashley, V. E. Anderson and R. H. Ritchie, "Inverse Mean Free Path, Stopping Power, CSDA Range, and Straggling in Si and SiO<sub>2</sub> for electrons of energy  $\leq$  10 keV," RADC-TR-76-125.
10. Ashley, J. C., C. J. Tung, R. H. Ritchie and V. E. Anderson, "Calculations of Mean Free Paths and Stopping Powers of Low Energy Electrons in Solids Using a Statistical Model," IEEE Trans. Nucl. Sci., December 1976.
11. Katz and Penfold, Rev. Mod. Phys. 24, 28 (1962).
12. Kaminsky, M., Atomic and Ionic Impact Phenomena on Metal Surfaces, Berlin: Springer (1965).
13. Aarset, B., R. W. Cloud and J. G. Trump, "Electron Emission from Metals Under High-Energy Hydrogen Ion Bombardment," J. Appl. Phys. 25, 1365 (1954).
14. Hill, A. G., W. W. Buechner, J. S. Clark and J. B. Fisk, "The Emission of Secondary Electrons Under High-Energy Positive Ion Bombardment," Phys. Rev. 55, 463 (1939).

15. Sternglass, E. J., "Theory of Secondary Electron Emission by High-Speed Ions," Phys. Rev. 108, 1 (1957).
16. Foti, G., R. Potenza and A. Triglia, "Secondary-Electron Emission from Various Materials Bombarded with Protons at  $E_p < 2.5$  MeV," Lett. al Nuovo Cim. 11, 659 (1974).
17. Cousinie, P., N. Colombie, C. Fert and R. Simon, "Variation du coefficient e'emission électronique secondaire de quelques métaux avec l'énergie des ions incidents," Comptes Rendus 249, 387 (1959).
18. Everhart, T. E., "Simple Theory Concerning the Reflection of Electrons from Solids," J. Appl. Phys. 31, 1483 (1960).
19. Darlington, E. H. and V. E. Cosslett, "Backscattering of 0.5-10 keV Electrons from Solid Targets," J. Phys. D5, 1969 (1972).
20. Shimizu, R., "Secondary Electron Yield with Primary Electron Beam of Kilo-electron-volts," J. Appl. Phys. 45, 2107 (1974).
21. McCracken, G. M., "The Behavior of Surfaces Under Ion Bombardment," Rep. Prog. Phys. 38, 241 (1975).
22. Hinteregger, H. E. and L. A. Hall, "Solar XUV Radiation and Neutral Particle Distribution in July 1963 Thermosphere," Space Research 5, 1175 (1964).
23. Tousey, R., "The Radiation from the Sun," in Green, A.E.S., Ed., The Middle Ultraviolet: Its Science and Technology, Wiley (1966).
24. Feuerbacher, B. and B. Fitton, "Experimental Investigation of Photoemission from Satellite Surface Materials," J. Appl. Phys. 43, 1563 (1972).
25. Schottky, W. Z., Phys. 15, 872 (1914).
26. Frenkel, J., Phys. Rev. 54, 647 (1938).
27. Adamec, V. and J. H. Calderwood, "Electrical Conduction in Dielectrics at High Fields," J. Phys. D8, 351 (1975).
28. DuPont Kapton Technical Bulletin H-4, Electrical Properties.
29. DuPont Teflon FEP Fluorocarbon T-4E, Electrical Properties.
30. Corning Bulletin, Low Expansion Materials, 1969.

31. Johnscher, A. K., Thin Solid Films 1, 213 (1967).
32. Mead, C. A., Phys. Rev. 128, 2088 (1962).
33. Hoffmaster, D. K. and J. M. Sellen, Jr., "Spacecraft Material Response to Geosynchronous Substorm Conditions," in Progress in Astronautics and Aeronautics, 47: Spacecraft Charging by Magnetospheric Plasmas, A. Rosen, ed. MIT Press (1976).
34. Electrets, Charge Storage and Transport in Dielectrics, Martin M. Perlman, ed., The Electrochemical Society, Inc., Princeton, New Jersey, 1973.
35. Lilly, A. C., Jr. and J. R. McDowell, "High-Field Conduction in Films of Mylar and Teflon," J. Appl. Phys., 39, 141 (1968).
36. Monteith, L. K. and J. R. Hauser, "Space-Charge Effects in Insulators Resulting from Electron Irradiation," J. Appl. Phys. 38, 5355 (1967).
37. Gross, B., G. M. Sessler and J. E. West, "Charge Dynamics for Electron-Irradiated Polymer-Foil Electrets," J. Appl. Phys. 45, 2841 (1974).
38. O'Dwyer, J. J., The Theory of Electrical Conduction and Breakdown in Solid Dielectrics, Clarendon Press, Oxford, p. 136, 1973.
39. Fowler, J. F., "X-ray Induced Conductivity in Insulating Materials," Proc. Roy. Soc. A 236, 464 (1956).
40. McAfee, W. S., "Determination of energy spectra of back-scattered electrons by use of Everhart's theory," J. Appl. Phys., 47, 1179 (1976).
41. Weissler, G. L., "Photoionization in Gases and Photoelectric Emission from Solids," Handbuch der Physik XXI, pp. 360-363 (1956).
42. Powell, C. J., "Analysis of Optical- and Inelastic-Electron-Scattering Data, II: Application to Al," J. Opt. Soc. Am. 60, 78 (1970).
43. Samson, J. A. R. and R. B. Cairns, "Photoelectric Yield of Aluminum from 300 to 1300 A," Rev. Sci. Inst. 36, 19 (1965).
44. Arakawa, E. T., R. N. Hamm and M. W. Williams, "Optical Properties and Electron-Attenuation Lengths from Photoelectric Yield Measurements," J. Opt. Soc. Am., 63, 1131 (1973).

DISTRIBUTION LIST

National Aeronautics and Space Administration  
Washington, D.C. 20546  
ATTN: W. R. Hudson/Code RP 1 copy  
D. P. Cauffman/Code ST 1 copy  
A. F. Timothy/Code ST 1 copy

National Aeronautics and Space Administration  
Ames Research Center  
Moffett Field, CA 94035  
ATTN: H. Lum, Jr./M.S. 244-7 1 copy

National Aeronautics and Space Administration  
Goddard Space Flight Center  
Greenbelt, MD 20771  
ATTN: R. O. Bartlett/Code 408.0 1 copy  
A. Kampinsky/Code 715.0 1 copy  
E. G. Stassinopoulos/Code 601.0 1 copy

Jet Propulsion Laboratory  
4800 Oak Grove Drive  
Pasadena, CA 91103  
ATTN: R. Goldstein/M.S. 122-123 1 copy

National Aeronautics and Space Administration  
Lyndon B. Johnson Space Center  
Houston, TX 77058  
ATTN: J. E. McCoy/Code TN2 1 copy

National Aeronautics and Space Administration  
Langley Research Center  
Hampton, VA 23665  
ATTN: J. D. DiBattista/M.C. 158B 1 copy

National Aeronautics and Space Administration  
Lewis Research Center  
21000 Brookpark Road  
Cleveland, OH 44135  
ATTN: Head, Contract Section B/M.S. 500-313 1 copy  
Technical Utilization Office/M.S. 7-3 1 copy  
Report Control Office/M.S. 5-5 1 copy  
Office of Reliability and Quality Assurance/M.S. 500-211 1 copy  
AFSC Liaison Office/M.S. 501-3 2 copies  
Library/M.S. 60-3 2 copies  
J. C. Roche/M.S. 501-8 20 copies